Velocity measurements and free-shear-layer instabilities in a rotating liquid metal

Austin Hayes Roach

A Dissertation
Presented to the Faculty
of Princeton University
in Candidacy for the Degree
of Doctor of Philosophy

Recommended for Acceptance
by the Department of
Astrophysical Sciences
Program in Plasma Physics

January, 2013

Abstract

The dynamics of rotating flows in magnetohydrodynamics (MHD) are expected to play an important role in astrophysical accretion disks, specifically via the generation of the magnetorotational instability (MRI). The Princeton MRI experiment, a Taylor-Couette device with split axial endcap rings and with a gallium-indium-tin working fluid, was constructed to study rotating MHD flows in the laboratory. This work uses an ultrasound Doppler velocimetry (UDV) diagnostic to measure internal fluid velocities of the mean background flow and also of fluctuations driven by instabilities in this experiment.

Mean azimuthal velocities have been measured to show the effect of an applied axial magnetic field. For moderate magnetic field strengths, with the Elsasser number $\Lambda = B_0/\sqrt{4\pi\rho\eta\Omega} < 1$, the normalized azimuthal velocity at a point, v_θ/v_1, with v_1 the inner cylinder velocity, is constant for a given v_A/v_1, the Alfvén speed normalized to v_1. In the $\Lambda \gg 1$ regime, the shear at the split in the endcaps extends axially as a free Shercliff layer through the full height of the experiment.

When the inner endcap ring rotates faster than the outer endcap ring, the free shear layer produces a Kelvin-Helmholtz instability with an eigenmode that fills the experimental volume when $\Lambda = B_0/\sqrt{4\pi\rho\eta\Delta\Omega} > 1$, with $\Delta\Omega$ the angular velocity jump across the split endcap rings, or when there is sufficient background rotation so that the Rossby number $Ro = \Delta\Omega/\Omega > 2.35$, with Ω the background rotation. When the inner endcap ring rotates slower than the outer endcap ring, the Kelvin-Helmholtz instability is present in the absence of an applied magnetic field or background rotation.

Using a linear eigenmode analysis of a free shear layer, the threshold for the appear-

ance of the Kelvin-Helmholtz instability is presented as a competition between Rayleigh's centrifugal instability, which is driven by a negative radial gradient in the specific angular momentum, and the Kelvin-Helmholtz instability, which is driven by the velocity shear. Both instabilities act to smooth out the shear layer. While the eigenmodes of the centrifugal instability are confined to the free shear layer, allowing quiet flow in the bulk of the fluid when that instability dominates, the eigenmodes of the Kelvin-Helmholtz instability fill the fluid volume, creating large-amplitude coherent velocity fluctuations throughout.

Acknowledgements

While this work bears the name of a single author, it is the result of the help, support, and guidance of a vast number of people for whom I am deeply grateful.

Thanks first to my advisor, Hantao Ji, whose expertise and high standards served as an inspiration to always push for better results and more detailed explanations.

Thank you to my thesis readers Jeremy Goodman and Phil Efthimion for reviewing this manuscript. Particular thanks is due to Professor Goodman, whose guidance throughout my tenure as a graduate student, though infrequent, was outsized in its impact.

Thanks to the postdocs with whom I had the honor of working: Mark Nornberg, Eric Edlund, Christophe Gissinger, and especially Erik Spence. Their daily guidance was an invaluable part of my growth as a scientist. Thanks also to Ethan Schartman, whose mechanical expertise was essential to the progress of the experiment.

I am hugely appreciative of the technical support provided by Peter Sloboda, who consistently accomplished every task in the laboratory not only better than I expected, but better than I knew it could be done.

Thanks to John Rhoads for being an ideal labmate. We managed to never fight once over our shared liquid metal, even on the occasions that I delivered it to his experiment in an unconventional manner.

I am very thankful for the help of Barbara Sarfaty. Without her aid in navigating the graduate program, I am certain that graduation would be impossible.

And finally, I cannot express enough gratitude to my family in supporting me throughout.

Contents

List of Figures

List of Tables

Chapter 1

Introduction

The work presented is this thesis is relevant to two topics in magnetohydrodynamics (MHD): the magnetorotational instability (MRI), an instability that is suspected to be important in astrophysical accretion disks, and instabilities of free shear layers. These topics are explored using fluid velocity measurements in the Princeton MRI experiment, a modified Taylor-Couette device with a liquid metal working fluid. Background information on each of these topics is given in the sections below.

1.1 Astrophysical accretion disks

Accretion disks are astrophysical structures formed by matter that is accreting onto a central object. They are common features in the universe, found in protostellar systems, in binary star systems, and in active galactic nuclei. Disks in binary star systems and active galactic nuclei have significant ionization fractions, so magnetic fields can play an import role in the dynamics of these disks.

1.1.1 Angular momentum transport in accretion disks

In order to fall onto the central object, matter must lose both its energy and its angular momentum. Energy can be radiated away, but the angular momentum must be transported radially through the disk.

The transport of angular momentum in a rotating flow can be described by multiplying the azimuthal component of the momentum equation in nonideal MHD in cylindrical coordinates, found in Appendix C, by $r\rho$ to find the time evolution of the specific angular momentum, where r is the radial coordinate and ρ is the fluid density. This results in the equation

$$\frac{\partial}{\partial t}\rho r v_\theta + \nabla \cdot \rho r \left[v_\theta \vec{v} - \frac{B_\theta \vec{B}}{4\pi\rho} + \frac{1}{\rho} P \hat{\theta} \right] - \nabla \cdot \nu \left[r^2 \nabla \frac{v_\theta}{r} \right] = 0 \tag{1.1}$$

in the incompressible limit with spatially constant ρ and ν, the kinematic viscosity. (This analysis is performed in the more general, compressible case in Balbus and Hawley [1998].) The rate of change of specific angular momentum can therefore be described as the divergence of fluxes of angular momentum. In the steady state, the divergence of these fluxes is zero, even though the fluxes themselves may be nonzero.

If we consider the case of steady, laminar, axisymmetric rotation with $v_r = v_z = 0$, the angular momentum is transported entirely by the last term in Equation 1.1, the viscous stress. This would be the case for the simplest models of matter in Keplerian rotation. But the molecular viscosity in many accretion disks is far too small to account for the angular momentum transport that must be associated with observed accretion rates.

But small scale, turbulent fluctuations can also lead to angular momentum transport. To see this, consider writing each dynamic variable as the sum of a mean part, denoted by a bar, and a fluctuating part, denoted by a tilde, *e.g.* $v_\theta = \bar{v}_\theta + \tilde{v}_\theta$. We can rewrite Equation 1.1 in terms of these mean and fluctuating components, and then take an average over an interval large compared to the scale of the fluctuations, with an average being indicated by a quantity in angle brackets, $\langle\rangle$. The average may be performed over an appropriate spatial or time interval.

By definition, the average of any fluctuating quantity is zero, *e.g.* $\langle \tilde{v}_\theta \rangle = \langle \tilde{v}_r \rangle = 0$. The average of a mean quantity multiplying a fluctuating quantity is also zero, *e.g.* $\langle \bar{v}_\theta \tilde{v}_r \rangle = 0$. But the average of two fluctuating quantities may not be zero if there is a correlation between the two. We can describe the average transport of angular momentum in terms of

mean and fluctuating components. The radial angular momentum flux is then

$$r\rho\left[\bar{v}_r\bar{v}_\theta - \frac{\bar{B}_r\bar{B}_\theta}{4\pi\rho} + \langle\tilde{v}_r\tilde{v_\theta}\rangle - \frac{\langle\tilde{B}_r\tilde{B}_\theta\rangle}{4\pi\rho}\right] - \nu r^2\frac{\partial}{\partial r}\left[\frac{\bar{v}_\theta}{r}\right] \tag{1.2}$$

The contributions from correlated velocity fluctuations and correlated magnetic field fluctuations arise from components of the Reynolds stress tensor and Maxwell stress tensor, respectively.

For decades it has been accepted that turbulence must be invoked to account for the observed accretion rates, although the mechanism and saturation of the turbulence were not understood. Instead, the effect of the turbulence was simply parametrized by an observationally determined coefficient corresponding to an enhanced viscosity, such as in the widely used α-disk model [Shakura and Sunyaev, 1973].

1.2 Potential instability mechanisms in accretion disks

There are two primary candidates for the source of the necessary turbulence in accretion disks: subcritical hydrodynamic turbulence and the magnetorotational instability. Each of these will be discussed separately in the subsections below.

1.2.1 Subcritical hydrodynamic turbulence

Rotating flows are known to be linearly unstable if the specific angular momentum decreases with radius, $\partial(r^2\Omega)/\partial r < 0$ for positive Ω [Lord Rayleigh, 1917]. Flows in this regime are known to be "Rayleigh-unstable" or "centrifugally unstable". For Keplerian rotation, where $\Omega \propto r^{-3/2}$, this inequality is not satisfied, so the flows are linearly stable.

In the absence of a linear hydrodynamic instability, some have turned to the idea of a subcritical transition to instability in accretion disks [Lynden-Bell and Pringle, 1974]. Some sheared flows are known to be subcritically unstable at large Reynolds numbers $Re = vL/\nu$, where v and L are characteristic velocity and length scales. This means that they are linearly stable but that finite amplitude perturbations can still lead to turbulence. Pipe flow, for instance, is known to break down into turbulence at Re of a few thousand even though the

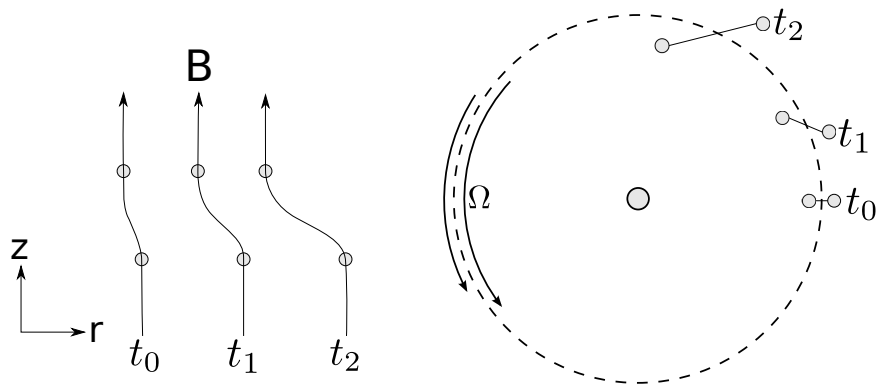

Figure 1.1: Cartoon of the MRI mechanism, showing two fluid elements linked by a common magnetic field line. *Left:* Projection of the motion on the $r - z$ plane. *Right:* Projection of the motion on the $r - \theta$ plane.

flow is linearly stable. Accretion disks would seem at the outset to be an ideal candidate for such subcritical transitions, since the Reynolds numbers are often greater than 10^{12}.

In support of this theory, there have been several reports of enhanced turbulence at large Reynolds numbers in Taylor-Couette devices [Richard and Zahn, 1999, Paoletti and Lathrop, 2011], in which sheared flow is developed in the gap between two coaxial, differentially rotating cylinders. But experiments performed during the hydrodynamic phase of this experiment suggest that quasi-Keplerian rotating flows are particularly resistant to such subcritical transitions when axial boundary conditions are controlled better than in the experiments that claimed to have demonstrated the subcritical transition [Ji et al., 2006, Schartman et al., 2012].

1.2.2 Magnetorotational instability

Magnetic fields are frequently associated with the damping of turbulence. But an axial magnetic field can lead to a robust, local, linear, ideal MHD instability in sheared rotating systems, called the magnetorotational instability (MRI). This instability was first discovered by Velikhov [Velikhov, 1959] and Chandrasekhar [Chandrasekhar, 1961], but its relevance to accretion disks was not realized until the work by Balbus and Hawley [Balbus and Hawley, 1991].

The mechanism of the MRI is often explained by considering the axial magnetic field to be a massless spring connecting fluid elements in a rotating flow with angular velocity decreasing with radius, illustrated in Figure 1.1. If a small radial disturbance with some axial wavelength is given to two fluid elements connected by a common field line (t_0), a fluid element that moves radially inward will begin rotating faster because the angular velocity of the flow is larger there, with the opposite being true of the fluid element that moves radially outward. This results in azimuthal separation of the fluid elements, stretching the magnetic "spring" that links them (t_1). The spring tugs back on the fluid element that moved radially inward, decreasing its angular momentum, and tugs forward on the fluid element that had moved radially outward, increasing its angular momentum. This transfer of angular momentum causes the inner fluid element to fall further radially inward, and the outer fluid element to move further radially outward (t_2). This is a runaway process, in the form of a linear instability, that transfers angular momentum outward through the fluid.

In contrast to the centrifugal instability, which required that the specific angular momentum decrease with radius, the MRI requires that the *angular velocity* decrease with radius, a condition that is satisfied for Keplerian rotation with $\Omega \propto r^{-3/2}$.

The MRI is commonly referred to as a "weak field" instability, because if the magnetic field, and its associated spring force, is too strong, the radial force is large enough to pull the fluid elements back toward their initial radius, leading to oscillatory motion about that radius. But a weak field can transfer angular momentum between the fluid elements while still allowing runaway radial separation.

The MRI is easily found in the linearized equations of ideal MHD, assuming axisymmetry and periodic variation in $\hat{r}$ and $\hat{z}$ [Balbus and Hawley, 1991, Balbus and Hawley, 1998]. In ideal MHD, instability occurs for $k_z^2 B_z^2/4\pi\rho < -d\Omega^2/d\ln r$. Keplerian rotation can always be destabilized for sufficiently large axial wavelengths and/or sufficiently weak magnetic fields.

There was quick recognition of the potential importance of the MRI in the dynamics of accretion disks, where the differential rotation and often significant ionization fractions pro-

duce the necessary conditions for this relatively simple instability mechanism. Its popularization by Balbus and Hawley led to a considerable interest in its study [Balbus and Hawley, 1998, Balbus, 2003], particularly through computation [Hawley et al., 1995, Balbus and Hawley, 2003, Julien and Knobloch, 2010], where the nature of the full MRI-driven turbulent spectrum, the saturation mechanism of the instability, and the effects of the MRI on the global dynamics of accretion disks are all topics of great interest.

1.3 Experimental studies of MRI

While the simplicity of the MRI mechanism and the near ubiquity of the ingredients required for its generation have left many with little doubt that the MRI is a physical phenomenon that exists and that plays an important role in accretion disks, direct observation of the instability would be an important confirmation of its validity and would provide a useful benchmark of the computer codes used for simulations of accretion disks.

Because the direct observation of the instability in an astrophysical system is currently not possible, a number of efforts have been undertaken in an attempt to generate the instability in the laboratory.

There are some differences in the expected behavior of the MRI in the laboratory, where the combination of limits on the axial wavenumber due to an experiment's finite height and dissipation due to fluid viscosity and resistivity places further restrictions on the MRI instability space [Ji et al., 2001, Goodman and Ji, 2002]. Namely, a critical magnetic Reynolds number $Rm = vL/\eta > O(1)$ is required for instability, where v and L are characteristic velocity and length scales, and η is the magnetic diffusivity. The magnetic Reynolds number describes the ratio of magnetic field induction due to the fluid motion to dissipation due to the magnetic diffusivity. The induced magnetic field is required for the transfer of angular momentum between fluid elements.

While the linear instability in ideal MHD suggests a *maximum* magnetic field above which there is stable oscillation, finite resistivity also leads to a *minimum* magnetic field relative to the dissipation, which can be expressed in terms of a minimum Lundquist number

$S = |B_z k_z|/\eta(k_z^2+k_r^2)$ [Ji et al., 2001], where k_z and k_r are the axial and radial wavenumbers. Once the minimum Rm has been reached, the MRI therefore is unstable for a range of magnetic field strengths between some minimum and maximum values.

The experiments that have been developed to study the MRI all share the common features of forcing sheared, rotating flow in a conducting fluid with an applied magnetic field. But there are variances among the choice of fluids, the mechanism of driving the flow, and the nature of the applied magnetic field.

A Russian experiment planned to drive sheared flow in a liquid metal by forcing a radial current between inner and outer cylinders in a Taylor-Couette like geometry. The interaction of the radial current with the applied axial magnetic field would give rise to a $\vec{j} \times \vec{B}$ force that would drive the fluid rotation [Velikhov et al., 2006].

An experiment currently being developed at the University of Wisconsin-Madison will attempt to destabilize the MRI in a cylindrical, sheared, rotating plasma [Collins et al., 2012]. The flow is driven locally at the walls by $\vec{j} \times \vec{B}$ forces in a magnetic cusp field that contains the plasma and that falls off rapidly with distance from the boundaries. The plasma in the bulk of the device is coupled viscously to the plasma that is driven at the boundary. An additional axial magnetic field applied throughout the plasma volume will provide the conditions for the instability. The choice of a plasma instead of a liquid metal as a working fluid allows the viscosity and the resistivity of the fluid to be varied, as well as allowing the examination of effects that are not present in liquid metals, such as the effect of the Hall term in Ohm's law on the instability.

An experiment in Germany called PROMISE (and later succeeded by PROMISE-2) uses a GaInSn alloy in a cylindrical Taylor-Couette device. This experiment generated a variant of the MRI called the helical MRI, or HMRI, which removes the requirement of a critical Rm for instability by supplying not only an externally applied axial magnetic field, but also an externally applied azimuthal magnetic field, rather than relying on induction to create it [Hollerbach and Rüdiger, 2005, Stefani et al., 2007, 2008, 2009]. The HMRI can be generated in this experiment at very low speed. But the instability takes the form of an

axial traveling wave and has specific conditions on the radial boundaries, leading some to question its relevance to accretion disks [Liu et al., 2006, 2007]

A spherical Couette experiment, in which a fluid is confined between an inner sphere and outer sphere in differential rotation, produced unstable nonaxisymmetric modes in a liquid sodium working fluid with an applied magnetic field. These modes were attributed to the MRI [Sisan et al., 2004], although results from computational modeling of that experiment suggest that these observations may have been of hydrodynamic shear flow instabilities [Hollerbach, 2009, Gissinger et al., 2011], similar to the results that will be presented in the second half of this thesis.

1.4 Expected behavior of the MRI in the Princeton MRI experiment

The Princeton MRI experiment was built to investigate the MRI in a Taylor-Couette device with a GaInSn working fluid and with an applied axial magnetic field. The behavior of the MRI in the experiment has been investigated through linear analysis [Ji et al., 2001, Goodman and Ji, 2002], and through nonlinear MHD simulations [Liu, 2008a, 2007, Gissinger et al., 2012]. It is expected to produce an eigenmode that drives two counter-rotating poloidal circulation cells, resulting in significant Maxwell and Reynolds stresses. The instability saturates by suppressing the shear in the bulk of the fluid.

Nonlinear 3-D MHD simulations by Christophe Gissinger [Gissinger et al., 2012] using a modified version of the `HERACLES` code [Gonzalez et al., 2007] represent the most up-to-date understanding of the expected behavior of the MRI in the experiment. These simulations predict a critical $Rm = \Omega_1 r_1 (r_2 - r_1)/\eta \approx 10$, where Ω_1 is the angular velocity of the inner cylinder, r_1 is the inner cylinder radius, and r_2 is the outer cylinder radius. This suggests $\Omega_1 > 2500$ rpm, which is slightly more than 60% of the designed maximum speed of 4000 rpm. The instability takes the form of an imperfect bifurcation from residual Ekman circulation, which has a common eigenmode structure of two dominant counter-rotating

poloidal circulation cells. So the MRI can perhaps be identified by a change in the fluid velocities that otherwise occur in magnetized Couette flow, namely a further suppression of the shear in the azimuthal velocity and an increase in the radial velocity.

These simulations also indicate an unfortunate scaling of the saturated MRI amplitude, which goes as $Re^{-1/4}$. Full saturation of the MRI in these simulations results only in about a 2% change to the azimuthal velocity as compared to cases below the critical Rm. As we will see in this work, this is near the threshold of what can be successfully resolved by the current set of diagnostics.

1.5 Free shear layer instabilities

Because of the split endcaps in our experiment, described more fully in Chapter 2, strong shear in the azimuthal velocity at an axial boundary can be produced. Under the appropriate conditions, shear at these surfaces can be extended into the bulk of the fluid, making our experiment a platform for the study of free MHD shear layers and their instabilities.

Shear layers are common at the boundaries of fluid dynamics experiments, where they are typically called "boundary layers". Hartmann studied the effect of a magnetic field on boundary layers where the field is perpendicular to the boundary [Hartmann, 1937]. Magnetized boundary layers of this sort are called "Hartmann layers". Shercliff extended that analysis to boundary layers with the magnetic field parallel to the boundary [Shercliff, 1953], which are called "Shercliff layers".

Free shear layers, which exist in the bulk of the fluid rather than at a boundary, are somewhat rarer than boundary layers. The classic example of a free shear layer is the Stewartson layer, which arises from small differences in the rotation speeds at axial boundaries of rapidly rotating systems [Stewartson, 1957a]. For small departures from rapid solid body rotation, the fluid velocity becomes invariant in the axial direction, a result known as the Taylor-Proudman theorem [Proudman, 1916, Taylor, 1917]. The large shear at the axial boundary extends into the bulk of the fluid, where a free shear layer is established. Such shear layers can form in cylindrical systems with split endcaps, or in spherical Couette sys-

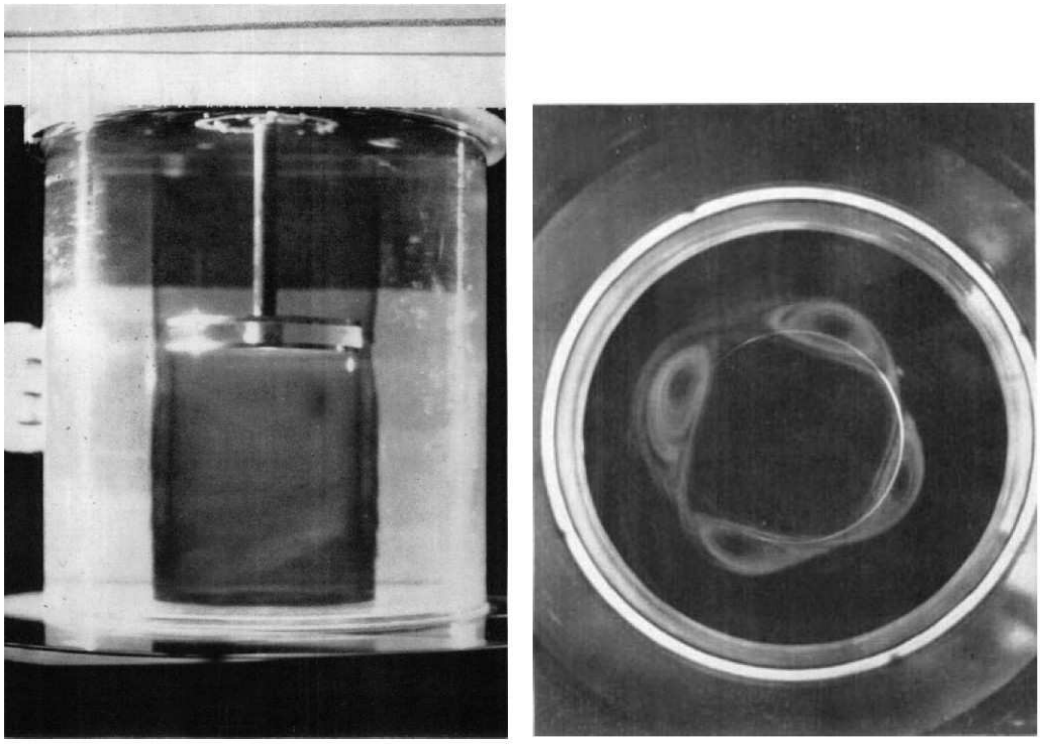

Figure 1.2: Pictures of a Stewartson layer produced in a cylindrical system with a suspended disk rotating at a slightly different rate than the cylindrical container, reproduced from Hide and Titman [1967]. *Left:* Picture from the side, with ink injected to show the volume of fluid corotating with the disk. *Right:* Picture from above showing the destabilization of the Stewartson layer by a Kelvin-Helmholtz instability

tems, where they may be present at the tangent cylinder. A picture of a Stewartson layer in cylindrical geometry is shown in Figure 1.2

Free shear layers can also arise in systems with a strong axial magnetic field, where the shear at the axial boundary is communicated to the bulk of the fluid by the tension of magnetic field lines. In this case, they can be referred to as magnetized Stewartson layers or as free Shercliff layers, in analogy to the magnetized boundary layers that share similar properties. Such free shear layers were first observed experimentally by Lehnert [Lehnert, 1955], with analytic descriptions of these free shear layers coming first from Stewartson [Stewartson, 1957b], and later from Braginskii [Braginskii, 1960] and Vempaty and Loper [Vempaty and Loper, 1978].

A recent computational work focused on the effects of background rotation and magnetic

field on the development of free shear layers in the Princeton MRI experiment [Spence et al., 2012]. An illustration of a free Shercliff layer from a 2-D nonlinear MHD simulation of this experiment is shown in Figure 1.3, showing the currents induced by axial shear in the presence of an axial magnetic field that act to extend azimuthal velocity shear at the axial boundaries into the bulk of the fluid.

1.5.1 Centrifugal instability

The centrifugal instability, or Rayleigh instability, is a thoroughly studied topic in the Taylor-Couette literature for globally unstable configurations, which are typically established with the inner cylinder rotating and the outer cylinder at rest. At marginal stability in the narrow-gap limit, the eigenmodes of the instability take the form of Taylor vortices: large-scale axisymmetric rotation cells with a large amount of poloidal circulation in addition to the azimuthal velocity perturbation [Taylor, 1923]. Beyond marginal stability, the parameter space is rich with features, including nonaxisymmetric perturbations to the Taylor vortices, leading eventually to fully developed turbulence at sufficiently large Re [Andereck et al., 1986]. Pictures of Taylor vortices in a narrow-gap Taylor-Couette experiment are shown in Figure 1.4.

Free shear layers can be unstable to the centrifugal instability in flows that are otherwise stable if there is a local negative angular momentum gradient large enough to overcome viscous damping, although much less attention has been devoted to this topic than to the globally unstable cases. The centrifugal instability of a free shear layer has been noted in simulations of Taylor-Couette experiments, including simulations of this experiment [Liu, 2008b, Hollerbach and Fournier, 2004], where its effect is to limit the extension of a free shear layer from the axial boundaries.

1.5.2 Kelvin-Helmholtz instability

The Kelvin-Helmholtz instability is driven by velocity shear and is a very common instability in fluid dynamics. The instability takes the form of velocity perturbations of some

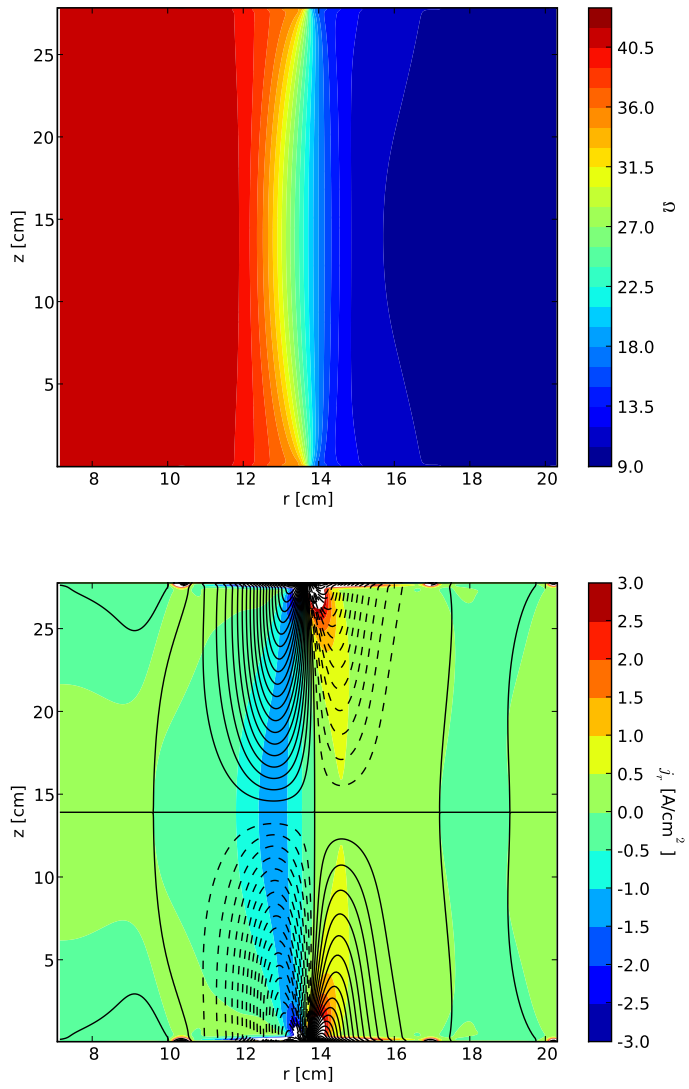

Figure 1.3: Illustration of a free Shercliff layer from a simulation with the ZEUS-2D code [Stone and Norman, 1992a, Liu, 2007] performed by Erik Spence in the geometry of the Princeton MRI experiment. The boundaries are fully insulating, $B_z = 16000$ Gauss, $Re = 3836$, and $Rm = 3.836$. The inner half of each axial endcap rotates with the inner cylinder ($\Omega_1 = 400$ rpm), and the outer half of each endcap rotates with the outer cylinder ($\Omega_2 = 100$ rpm). *Top:* Contour plot of the angular velocity, Ω, showing large shear throughout the fluid volume at the radial location of the split in the endcaps. *Bottom:* Color contour plot of the radial current density, with streamlines of B_θ overlaid. Solid lines indicate positive B_θ and clockwise current flow. Dashed lines indicate negative B_θ and counterclockwise current flows. The currents return in a Hartmann layer at the axial boundaries. The Lorentz force from these currents act to reinforce the free shear layer.

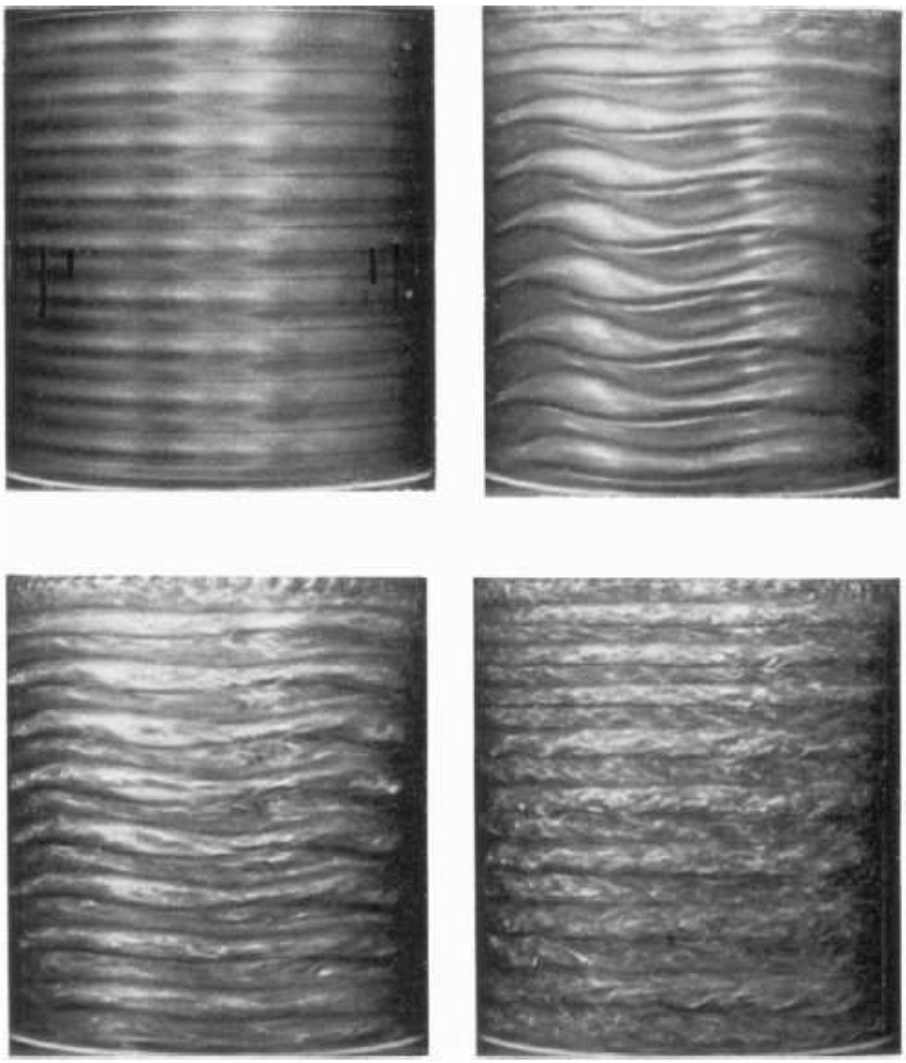

Figure 1.4: Pictures of Taylor vortices taken through the transparent outer cylinder of a narrow gap Taylor-Couette experiment, reproduced from Fenstermacher et al. [1979]. The centrifugal instability forms a series of axisymmetric rolls, which become nonaxisymmetric and eventually transition to turbulence at large Re.

wavelength in the direction of flow, and uniform in the direction along the shear layer but perpendicular to the flow. The nonlinear evolution of the Kelvin-Helmholtz instability typically results in swirls along the shear layer, features that are observed in an extremely broad range of systems.

Kelvin-Helmholtz instability of free shear layers can occur when the shear is sufficient to overcome the viscous damping. A picture of the Kelvin-Helmholtz destabilization of a shear layer in cylindrical geometry with small Ro is shown in Figure 1.2. The destabilization of Stewartson layers and free Shercliff layers to Kelvin-Helmholtz instabilities has been studied experimentally [Hide and Titman, 1967, Früh and Read, 1999, Hollerbach et al., 2004, Schaëffer and Cardin, 2005], analytically [Busse, 1968, Nagata, 1985] and computationally [Hollerbach and Skinner, 2001, Hollerbach et al., 2004, Wei and Hollerbach, 2008]. Most of the work has focused on the transition where the instability overcomes viscous damping. For Stewartson layers this transition occurs in the small Rossby number regime, where the Rossby number $Ro = \Delta\Omega/\Omega$ describes the ratio of inertial forces to Coriolis forces. $\Delta\Omega$ is the angular velocity differential across the shear region, and Ω is the overall rotation of the system, typically the outer cylinder velocity. There is a critical minimum Rossby number for generation of the Kelvin-Helmholtz instability. For free Shercliff layers, a minimum Reynolds number Re is typically required to overcome viscous stabilization for a given Hartmann number $Ha = BL/\sqrt{4\pi\rho\eta\nu}$, where L is a characteristic length.

By contrast, in this work we will show a *maximum* finite Rossby number for the appearance of a Kelvin-Helmholtz instability of a Stewartson layer, and a *maximum* Reynolds number required for the Kelvin-Helmholtz instability of a free Shercliff layer with a given B_0 when the inner endcap ring rotates faster than the outer endcap ring. Rather than resulting from sufficient inertial forces to overcome viscous stabilization, these thresholds are consistent with a competition between Rayleigh's centrifugal instability and the Kelvin-Helmholtz instability for the free energy in the shear layer. When the centrifugal instability is unstable, its growth rate typically dominates that of the Kelvin-Helmholtz instability. The most unstable eigenmodes of the centrifugal instability have large radial and axial

wavenumbers, so the associated velocity fluctuations are confined to the shear layer region. But an axial magnetic field and overall rotation can damp the centrifugal instability, allowing the growth of the Kelvin-Helmholtz instability. The eigenmodes of the Kelvin-Helmholtz instability are characterized by relatively small radial and axial wavenumbers, making it capable of producing large-amplitude radial and azimuthal velocity fluctuations throughout the fluid volume, far from the location of the unstable shear layer.

3-D nonlinear MHD simulations have exhibited the Kelvin-Helmholtz instability of the free Shercliff layer that will be described here [Gissinger et al., 2012]. This work therefore provides a good benchmark for nonlinear 3-D MHD codes.

1.6 Organization of thesis

Chapter 2 gives an overview of the experimental apparatus, including changes to the mechanical aspects of the experiment since previous published descriptions. It includes information about the liquid metal working fluid. It also describes how an experimental shot is executed.

Chapter 3 is dedicated to describing the ultrasound Doppler velocimetry diagnostic, a new addition to the experiment for this work. It includes a brief description of the mechanism of operation, parameters relevant to the operation of the diagnostic, and a description of the diagnostic installation. It also includes information about the calibration of the beam geometries and speed of sound, and gives information about the performance of the diagnostic in measuring various aspects of the fluid flow.

Chapter 4 describes measurements of mean velocity profiles in the unmagnetized, slightly magnetized ($\Lambda < 1$) and strongly magnetized ($\Lambda \gg 1$) regimes, where $\Lambda = B_0^2/4\pi\rho\eta\Omega$ is the Elsasser number, describing the ratio of $\vec{j} \times \vec{B}$ forces to inertial forces arising from rotation. This chapter describes how the application of a magnetic field results in increased coupling of the axial boundaries to the fluid through the induced Hartmann current. It also describes how the experiments so far relate to the search for the MRI.

Chapter 5 describes measurements of a Kelvin-Helmholtz instability of a free shear layer

observed with $\Lambda = B_0^2/4\pi\rho\eta\Delta\Omega > 1$ or $Ro < 2.35$ when the inner endcap ring rotates faster than the outer ring. It presents measurements of the instability near marginal stability and explains how the instability differs in the region far from marginal stability ($\Lambda \gg 1$).

Chapter 6 shows the results from calculations of the linear stability of a free shear layer, using a nonaxisymmetric global stability code described in Appendix D. It provides an explanation of the experimentally determined threshold for the appearance of the Kelvin-Helmholtz instability as a competition between the centrifugal instability and the Kelvin-Helmholtz instability for the energy in the free shear layer.

Chapter 7 gives a summary of the conclusions from this work and discusses ideas for future work.

Appendix A provides a quick reference for symbols and dimensionless parameters used in this thesis.

Chapter 2

Experimental apparatus

The experimental apparatus is well described in Ethan Schartman's thesis concerning hydrodynamic results from the Princeton MRI experiment [Schartman, 2008]. This chapter will summarize the key features of the experiment, and point out any modifications that have been made since that description was written.

2.1 Mechanical apparatus

The Princeton MRI experiment is a modified Taylor-Couette device consisting of a fluid which is forced to rotate between two concentric cylinders. The dimensions of the experiment are listed in Table 2.1. The experiment has a wider radial gap and is shorter than typical Taylor-Couette experiments, design decisions motivated by the necessity of a large radial wavenumber for easier destabilization of the MRI and by the high cost of the working fluid.

The novelty of this device lies in its axial boundaries, which are divided into two differentially rotatable end rings, as shown in Figure 2.1, minimizing the effect of the endcaps on the bulk flow dynamics. The benefits of this arrangement in hydrodynamic experiments have been written about many times [Kageyama et al., 2004, Burin et al., 2006, Ji et al., 2006, Schartman, 2008, Schartman et al., 2012], and will be revisited in Chapter 4.

The inner cylinder and outer cylinder of the experiment are made of stainless steel, and

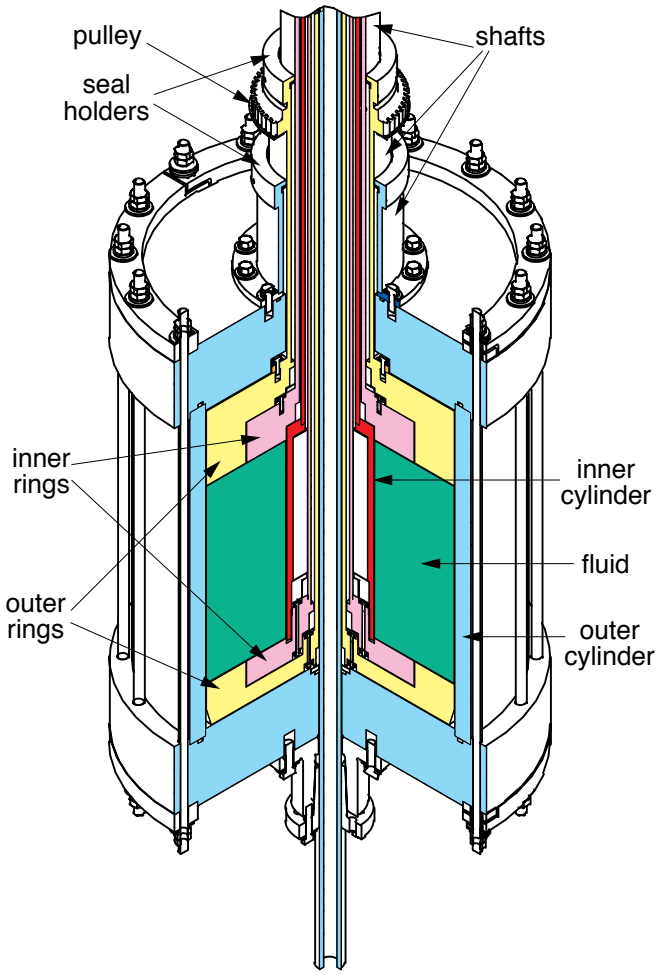

Figure 2.1: Schematic of the Princeton MRI experiment showing the four differentially rotatable components: the inner cylinder, inner rings, outer rings, and outer cylinder.

Quantity	Symbol	Value
Inner cylinder radius	r_1	7.06 cm
Outer cylinder radius	r_2	20.3 cm
Inner/outer ring transition radius	r_l	13.3 cm
Height of fluid volume	h	28 cm

Table 2.1: Nominal dimensions of the experimental apparatus.

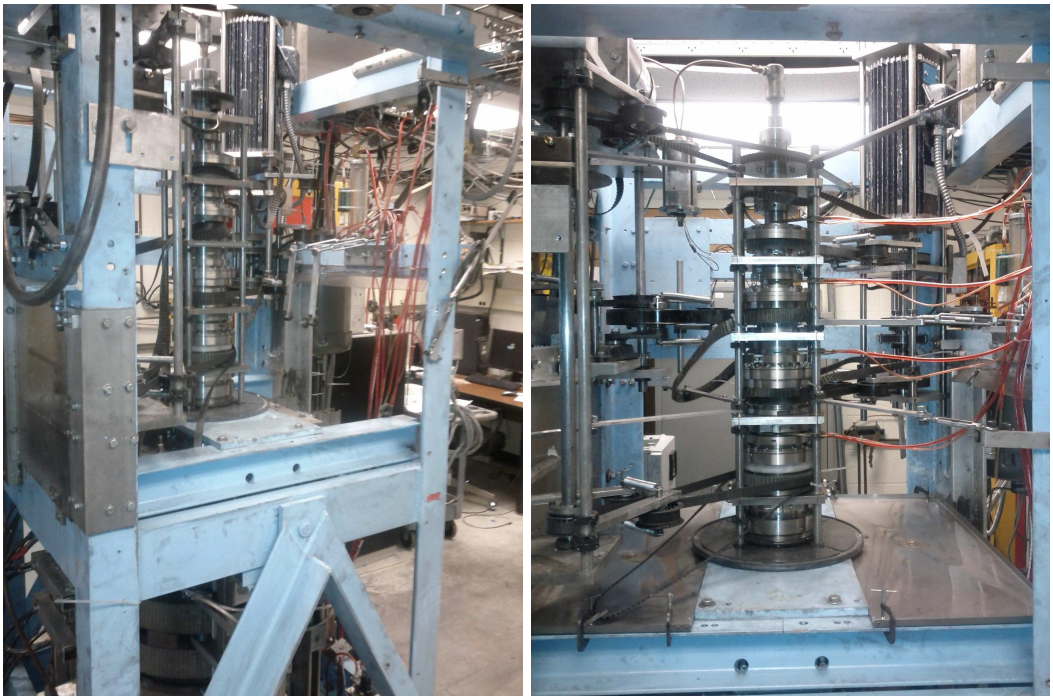

Figure 2.2: Photographs of the full experiment (*left*) and closeup of the seal stack (*right*). The experimental volume is at the bottom, surrounded by the magnetic field coils.

the inner ring and outer ring are made of acrylic. Each rotating component is fixed to a stainless steel shaft, which are nested and which exit the top of the experiment. Each shaft has a drive pulley, and a dynamic seal is made between each pair of shafts to avoid ejection of the fluid or exposure of the fluid to air during operation.

2.1.1 Motor modifications

The rotating components were driven by four motors: one for the inner cylinder, one for the outer cylinder, one for the pair of inner rings, and one for the pair of outer rings. The increased seal friction associated with higher-speed runs necessitated more powerful motors than those that had previously been used. For this work, the inner cylinder was driven by a 30 horsepower AC motor, the inner ring was driven by a 10 horsepower AC motor, the outer ring was driven by a 1 horsepower DC motor, and the outer cylinder was also driven by a 1 horsepower DC motor. The motors were controlled as before by a computer running LabVIEW^{TM}. For the AC motors, the computer output a DC voltage corresponding to the

desired speed, with the variable frequency drive for each motor enforcing that speed. The feedback for the DC motors was provided by a motor control board, as before, with output to the motor drives controlling the torque of the motors.

Braking during operation

During high-speed operation, the large differential rotation between the outer rings and inner rings resulted in the need to strongly brake the outer rings. The braking force at times exceeded that which could applied by the DC motors, causing the outer rings to spin faster than the desired speed. To address this, a pneumatically operated disc brake was added to the outer ring slave shaft. The brake could be applied manually during a shot when it was observed that the control system was demanding a large negative torque from the outer ring motor. The brake supplied a steady negative offset to the torque, with the control system continuing to provide feedback for fine control of the outer ring speed using the torque from the DC motor.

2.1.2 Modifications to seal designs

Energized lip seals were used to seal the concentric shafts that led to each of the rotating components. One of the issues plaguing the experiment was the difficulty in maintaining the concentricity of the seals, which were fixed to the outer shaft at each sealing junction, and of the differentially rotating inner shaft against which the dynamic seal was made. The lip seals allow radial runout of only a few thousandths of an inch, a tolerance that was difficult to maintain since the bearings locating the shafts radially are typically 8 inches or more apart.

This problem was addressed by a technique originating from Ethan Schartman, in which the seals were held in a seal holder which was coupled to the outer shaft of each nested pair by a flexible urethane bellows. The seal was thus allowed to move with respect to the outer shaft, but its position with respect to the inner shaft was fixed by a ball bearing between the two. A pin fixed to the seal holder inserted into a larger diameter hole in a part fixed to

the outer shaft, allowing the parts some freedom of movement, but also allowing torque to be transmitted from the outer shaft to the seal holder through a path that did not include the bellows. This free-floating seal design was able to maintain the runout tolerance much more effectively, decreasing seal friction and extending the lifetime of the seals.

The modified seal design made access to the seals for lubrication more difficult, rendering the automated oiling system that was used in hydrodynamic experiments ineffective. Instead, the seals were lubricated manually between shots with about 1 cm^3 of automatic transmission fluid per seal. As high speed shots lasted at most a little over three minutes, this procedure provided sufficient lubrication.

2.1.3 Modifications to accommodate hydrodynamic pressure

The centrifugal force of the rotating fluid is balanced by a radial pressure gradient. As discussed in Ethan Schartman's thesis, this can lead to substantial hydrodynamic pressures at high speed. The problems encountered during the hydrodynamic phase of the experiment are exacerbated with the liquid metal working fluid, which has a density six times greater than water, leading to pressures that are six times larger.

To relieve the axial pressure gradients across the rotating rings during the hydrodynamic experiments, a number of holes were drilled axially through these components. While this modification was sufficient to allow successful operation during the hydrodynamic phase, experiments at high speed with the liquid metal still encountered pressure-related problems. In particular, axial pressure gradients across the outer rings produced a force pulling the outer rings into the fluid which, depending on the specifics of the azimuthal velocity profile, might reach more than 10 tons of force. The method of locating and fixing the components axially was not able to withstand these forces, causing the outer rings to slip until they contacted the inner rings, leading to a premature end to the experiment and damage to both components.

The solution to this problem was to seal the outer rings to the outer endcaps of the experiment, eliminating the path by which the high pressure at the outer cylinder radius

Figure 2.3: Picture of gasket used to minimize axial pressure loads on the outer ring. The gasket is the black rubber piece fitted into the groove machined near the outer diameter of the component.

was communicated to the back side of each outer ring. A groove was machined in each outer ring, and a rubber gasket was placed into this groove, as shown in Figure 2.3. Each outer ring was positioned during assembly so that this gasket was pressed tight against the outer endcap. A small gap was left in the gasket so that gas could pass through as the experiment is filled with fluid, eliminating gas pockets that might otherwise have formed.

2.1.4 Sacrifice of differential outer ring rotation

The addition of the gasket between the outer ring and endcap eliminated the possibility of differential rotation between these components. But even before that modification was made, there seemed to be rubbing problems between the outer ring and outer cylinder, and the decision was made to eliminate the differential rotation between them. This removed one degree of freedom in controlling the boundary condition. But as it was noticed that the outer ring speed had a much smaller effect on the measured velocity profile at the midplane of the experiment compared to the inner ring speed, this seemed a reasonable sacrifice to

Property	Symbol	Value
Density	ρ	6.36 g/cm^3
Kinematic viscosity	ν	2.98×10^{-3} cm^2/s
Magnetic diffusivity	η	2.57×10^3 cm^2/s
Melting point		10.5 °C

Table 2.2: Nominal material properties of the GaInSn eutectic, reported in Morley et al. [2008].

make.

2.2 Liquid metal

The liquid metal used for these experiments is a gallium-indium-tin eutectic, sometimes called Galinstan, which is liquid at room temperature. The properties of this material have been described elsewhere [Morley et al., 2008], and are summarized in Table 2.2.

The liquid metal oxidizes quickly when exposed to even small amounts of oxygen. In the presence of oxygen and vigorous mixing, the solid oxides and remaining liquid metal can quickly form a thick sludge. This fact drives the strict sealing requirements of the experiment.

The liquid metal is stored in a tank under a high-purity argon cover gas. The experiment is backfilled with argon when it is assembled and drained of the liquid metal. The liquid metal is transferred between the tank and the experiment by means of a hose that is connected to the bottom of the tank and which may be connected to the bottom of the experiment with a quick-disconnect fitting. Gas pressure of up to 15 psi can be applied to the tank or to the experiment to force the liquid metal into one or the other.

2.2.1 The effects of gallium on aluminum

Gallium can corrode many metals at high temperatures [Luebbers and Chopra, 1995]. At room temperature, it remains highly corrosive to aluminum. Gallium disrupts the passivating oxide layer that normally forms on aluminum and penetrates into the solid aluminum, allowing oxidation at all of the grain boundaries throughout the volume. This transforms

a block of aluminum into a brittle structure with such poor mechanical properties that it sometimes simply crumbles.

The amount of damage and time to damage depend on a number of factors, including the volume of gallium to which an aluminum part is exposed and the surface condition of that part. For an aluminum part with a clean surface and a scratch in its oxide layer, penetration of gallium can occur within minutes, with visible damage to the part. The addition of water, for example in the application of a water-based cleaner, speeds up the destruction, since the aluminum is sufficiently chemically active to crack water, oxidizing itself and releasing hydrogen gas. This reaction is vigorous and exothermic, leading to bubbling and fuming from the released hydrogen gas, and noticeable warming of the part.

Aluminum can be protected by painting it or by an oily or greasy film on its surface. But if an aluminum part with a protected surface is exposed to gallium, the gallium will eventually find a defect and lead to damage to the part. Any part that could potentially be exposed to gallium and cannot fail or cannot be easily replaced should be made of something other than aluminum, like stainless steel, plastic, or titanium.

2.2.2 Reclaiming liquid metal from spills

Small spills of the liquid metal in the course of experiments are not infrequent. The liquid metal often becomes mixed with the oil used for seal lubrication. Large drops or puddles can be scooped up and deposited in a container, where the bulk of the oil and liquid metal will naturally separate. For more finely dispersed droplets of liquid metal in oil, the cleaner Simple Green is quite effective in disrupting the oil layer separating droplets of liquid metal, allowing those droplets to coalesce into larger ones. It can even help in the absence of large amounts of oil. For surfaces that have been smeared with a drop of gallium, scrubbing the surface with a cover of Simple Green often results in the microscopic drops of liquid metal reforming into a macroscopic ball.

2.3 Diagnostics

The experiment's diagnostics consisted of an array of 72 magnetic pickup coils measuring $\dot{B}_r$ [Schartman, 2008], as well as several saddle coils intended to be sensitive only to axisymmetric magnetic fluctuations.

The results presented in this thesis are of the fluid velocity, which was measured using an ultrasound Doppler velocimetry system, described separately in Chapter 3.

2.4 Anatomy of a shot

One experimental shot consists of a spin-up phase during which the rotating components of the experiment are brought up to speed and the fluid is allowed to reach a steady state, normally followed by the application of a magnetic field during which the experiment is diagnosed, followed by a spin-down phase where the rotating components are brought back to rest. The control of the experiment is performed by two computers running LabVIEW$^{\text{TM}}$. The first computer controls the motors and sends a trigger at the appropriate time to the second computer, which controls the magnetic field and the diagnostics. Each phase of the shot is described in the subsections below.

2.4.1 Fluid spin-up

A shot begins with a fluid spin-up time, during which the rotating components are brought up to full speed and the hydrodynamic flow profile develops. The ramp-up time for the rotating components can be as fast as a couple of seconds for very low speed shots, to a bit less than a minute for higher speed shots. The total time between when the components start rotating and when the magnetic field is applied is typically two minutes. This provides sufficient time for the fluid spin-up, as illustrated by the velocity measurement made by a UDV transducer in Figure 2.4.

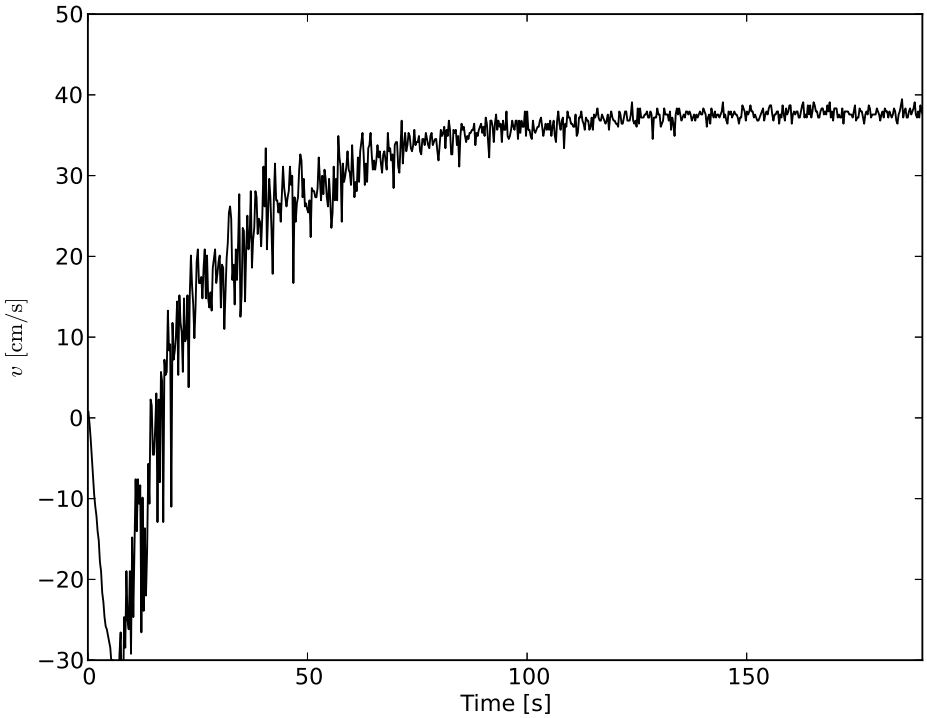

Figure 2.4: Raw UDV measurement of velocity at $r = 12.5$ cm, near the midplane, illustrating fluid spin-up at the beginning of a shot. $t = 0$ s corresponds to the time that the outer cylinder begins moving. The measured velocity is relative to the outer cylinder on which the transducer is mounted. The velocity is initially negative since the outer cylinder has started rotating but the fluid is still stationary.

Nomenclature of rotating component configurations

The angular velocity of the inner cylinder and outer cylinder are indicated by Ω_1 and Ω_2, respectively, as is common in the fluid dynamics literature for Taylor-Couette devices with only two rotation speeds. The additional velocities for the differentially rotating axial boundary components in this device are indicated by Ω_3 for the inner ring and Ω_4 for the outer ring.

Because it is cumbersome to list all of the component rotation speeds when describing the configuration used for a shot, a naming scheme was devised for many of the common component speed ratios used. "`MRI-Z`" is a configuration optimized to produce a nearly ideal Couette azimuthal velocity profile at the midplane with an effective exponential dependence on the angular velocity $\Omega(r) \sim r^{-1.9}$, in principle allowing destabilization of the MRI at sufficiently large Rm while avoiding centrifugal instability. The "`Ekman`" profile has the same inner and outer cylinder speeds as the "`MRI-Z`" configuration, but the inner ring and outer ring corotate with the outer cylinder. "`Split`" indicates any configuration in which the inner cylinder and inner ring corotate, and the outer cylinder and outer ring corotate: $\Omega_3 = \Omega_1$ and $\Omega_4 = \Omega_2$. "`Split-unstable`" is a special case of the "`split`" configuration with the outer components at rest.

The component speed ratios for several configuration names are summarized in Table 2.3. In all cases except for the generic "`split`" configuration, the name of the configuration may be followed by a number indicating the rotation speed of the inner cylinder as a percentage of the maximum design speed of $\Omega_{1,\max} = 4000$ rpm. Thus, the profile `MRI-Z 10%` would have component speeds of $(\Omega_1, \Omega_3, \Omega_4, \Omega_2) = (400, 220, 53, 53$ rpm).

2.4.2 Application of magnetic field

The axial magnetic field B_0 is supplied by six solenoidal electromagnetic coils. Magnetic fields up to 5000 Gauss can be applied. The application time of the field is limited by the resistive heating of the coils, which must be kept under 60 °C. For fields less than 800 Gauss, the field can be run steady state, as the water coolant is sufficient to keep the coil

Configuration name	Speed ratios
`Ekman`	(1.0, 0.1325, 0.1325, 0.1325)
`Split`	(Ω_1, Ω_1, Ω_2, Ω_2)
`Split-unstable`	(1.0, 1.0, 0, 0)
`MRI-Z`	(1.0, 0.55, 0.1325, 0.1325)

Table 2.3: Component speed ratios for several rotating component configurations. The component speeds are written in terms of increasing radius of the components: (Ω_1, Ω_3, Ω_4, Ω_2). The `split` configuration is used to describe any configuration with $\Omega_3 = \Omega_1$ and $\Omega_4 = \Omega_2$.

temperature below the threshold. A field of 2300 Gauss can be applied for 50 seconds, a field of 3400 Gauss can be applied for 30 seconds, and a field of 4600 Gauss can be applied for only 15 seconds.

The voltage from the rectifier that powers the coils is chosen by moving a tap within the rectifier by means of a remotely operated motor. This tap is positioned before a shot and does not move during the shot. The coils are therefore supplied with a constant voltage. But as the coils are heated during a shot, their resistance increases, leading to a drop in current over the course of a shot. It is not uncommon for the field to drop by more than 10% over the course of a shot, as shown in Figure 2.5.

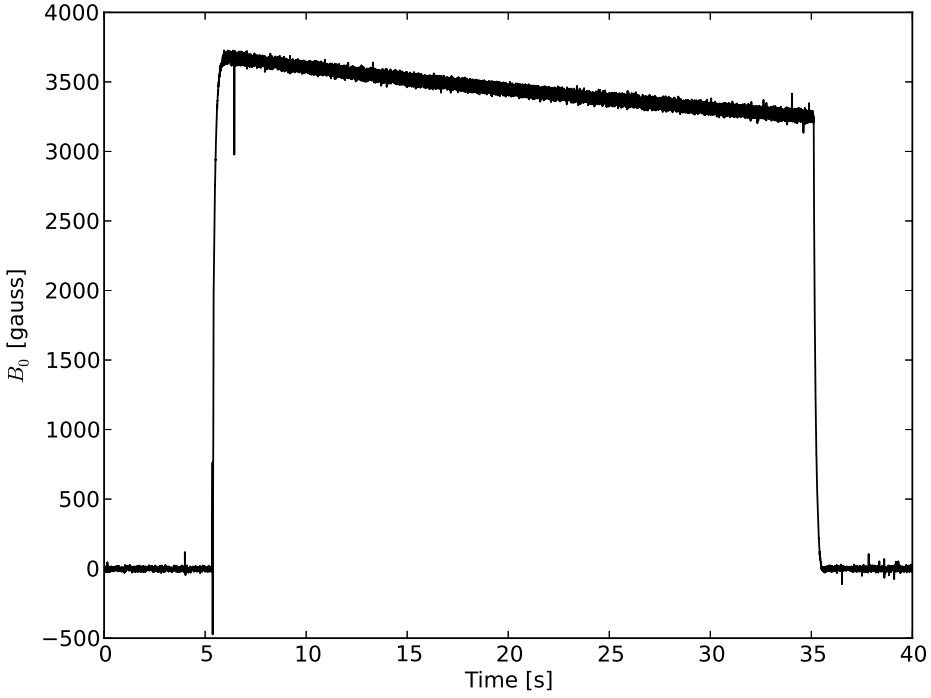

Figure 2.5: Magnetic field as calculated from the measured currents through the leads to the field coils during a typical shot with a nominal field of 3400 Gauss.

Chapter 3

Ultrasound Doppler Velocimetry

3.1 UDV overview

Ultrasound Doppler Velocimetry (UDV) is a technique for non-perturbatively measuring velocities in liquids using pulses of sound waves scattered from particles entrained in the fluid [Takeda, 1991, 1995, Sig, 2012]. The most common non-perturbative velocity measurement techniques in fluid dynamics, Laser Doppler Velocimetry (LDV) and Particle Image Velocimetry (PIV), make use of tracer particles in optically transparent media. While Laser Doppler Velocimetry was used on the Princeton MRI experiment in the first round of experiments with water as a working fluid, the change to liquid metal required a different velocity measurement technique.

UDV has been used in a number of applications similar to our experiment. Takeda *et al.* used UDV to measure axial velocity fluctuations in a Taylor-Couette device with a stationary outer cylinder [Takeda et al., 1993a,b]. Axial velocities in Couette systems were also made by Cramer *et al.*, who measured magnetic-field-driven flow in a cylinder of mercury and GaInSn [Cramer et al., 2004], and by Stefani *et al.*, who measured axial velocities in a rotating Taylor-Couette device with a GaInSn working fluid [Stefani et al., 2007]. Brito used UDV for azimuthal velocity measurements in a vortex of liquid gallium, with the UDV beam passing through the stationary copper outer cylinder [Brito et al., 2001]. UDV has

also been used in non-rotating liquid metal flows in sodium [Eckert and Gerbeth, 2002] and gallium [Tasaka et al., 2008].

3.1.1 Principles of operation

In pulsed UDV, a single transducer acts as both an emitter and a receiver. The transducer is resonant at an emitter frequency f_e. Pulses consisting of several oscillations of the emitter frequency are emitted by the transducer, with a time between these pulses t_{prf} determined by the pulse repetition frequency. These pulses scatter off of particles in the flow that have a different acoustic impedance than the fluid. Between pulse emissions, the transducer acts as a receiver, listening to these echos.

For a distribution of particles along the UDV beam, the transducer will receive a series of echos, with the time delay τ between emission and reception of an echo determined by d, the depth of the particle relative to the transducer,

$$\tau = \frac{2d}{c}, \tag{3.1}$$

where c is the speed of sound in the fluid. The maximum depth at which a measurement can be made before another pulse is emitted is therefore $d_{max} = ct_{prf}/2$.

In principle, the component of the velocity of the reflecting particle along the beam, v, could be found by measuring the Doppler shift f_D from the emitter frequency in the received echo,

$$f_D = 2f_e\frac{v}{c}. \tag{3.2}$$

But in practice, the number of ultrasonic oscillations in a single received echo is too small to make a good, direct measurement of the small Doppler shift to the emitter frequency. Instead, information from multiple received echos is used. A received echo is compared to the signal from the oscillator at the emitter frequency to find the phase shift of each echo relative to the oscillator signal. The change in phase, $\Delta\phi$, between echos off of the same scattering particle from two successive pulses is

$$\Delta\phi = 2\pi f_e(\tau_2 - \tau_1), \tag{3.3}$$

where the change in the echo reception time is $\tau_2 - \tau_1 = 2vt_{\mathrm{prf}}/c$. So, we find

$$\Delta\phi = 4\pi f_{\mathrm{e}} \frac{v}{c} t_{\mathrm{prf}} = 2\pi f_{\mathrm{D}} t_{\mathrm{prf}}. \tag{3.4}$$

By this technique, a quantity proportional to the Doppler shift f_{D} is measured. But it should again be emphasized that despite the name of the technique, the small Doppler frequency shift is not being directly measured. Rather, it is the change in the depth of a particle along the ultrasound beam between pulse emissions that is measured.

The fact that these measurements rely on phase measurements between multiple pulses rather than a direct measurement of f_{D} from a single pulse has a number of implications. First, not all values of the Doppler frequency can be measured unambiguously. Any velocity that would yield a phase shift $|\Delta\phi| > \pi$ will be aliased. This implies a maximum velocity $v_{\max} = c/(4f_{\mathrm{e}}t_{\mathrm{prf}})$ that can be unambiguously measured. The pulse repetition frequency also provides a constraint on the maximum measurable depth, $d_{\max}$, so that the product $v_{\max}d_{\max} = c^2/8f_{\mathrm{e}}$ is fixed for each emitter frequency. As will be seen later, aliasing of the measured velocity can often be removed when the data is processed, allowing velocities above $v_{\max}$ to be measured.

If a particle is not resident in the beam for more than t_{prf}, the time to interact with two emitted ultrasound pulses, a measurement of its velocity cannot be made. This implies a maximum velocity perpendicular to the beam $v_{\perp\max} = w/t_{\mathrm{prf}}$ for a beam of width w. For our setup, the beam width ($\approx$ 1 cm) is about 15 times greater than the ultrasound wavelength (0.068 cm), so $v_{\perp\max} \approx 15 v_{\max}$.

3.2 Implementation of UDV in the MRI experiment

3.2.1 UDV hardware

The UDV appliance used for this work is a DOP 3010, manufactured by Signal Processing, S.A. of Lausanne, Switzerland. The appliance supports 10 multiplexed transducers, meaning that there is one set of electronics that is used in turn by each transducer to make a

measurement. The appliance supports a range of emitter frequencies from 0.45 MHz to 10.5 MHz.

Signal Processing, S.A. also provided the ultrasonic transducers for use in this experiment. The transducers are stainless steel cylinders with epoxy faces that make up a resonant cavity for a piezoelectric crystal driven at the emitter frequency. Transducers are available with a range of face diameters. The geometry of the face has an effect on the shape of the ultrasound field emitted by the transducer.

The transducer face can be ideally modeled as a uniform disk of spherical sound emitters. The problem of calculating the acoustic field emitted by a cylindrical transducer is equivalent to the familiar problem of diffraction of a wave by a circular aperture. The solution for the wave field is then characterized by a near-field (Fresnel) region of depth r_{t}^2/λ, where r_{t} is the radius of the transducer face, and λ is the ultrasound wavelength. At 4 MHz, $\lambda = 0.068$ cm for GaInSn. So for the 8 mm and 12 mm diameter transducers used in this work, the near field extends 2.35 cm and 5.3 cm, respectively. In the near-field region, the sound intensity field is approximately cylindrical with a cross-section matching the shape of the transducer. The acoustic field has oscillations in the intensity parallel to the propagation direction.

In the far-field (Fraunhofer) region, the intensity falls off as $1/r^2$ along the centerline of the beam, but there are also variations perpendicular to the propagation direction. The directivity function, D, describes the acoustic field pressure at an angle ζ relative to the acoustic field pressure on axis:

$$D(\zeta) = \frac{2J_1(kr_t \sin\zeta)}{kr_t \sin\zeta} \tag{3.5}$$

where $k = 2\pi/\lambda$, and J_1 is a Bessel function of the first kind of order 1. This function is plotted for the 8 mm and 12 mm transducer diameters in GaInSn in Figure 3.1. Note that most of the energy is in the primary lobe, but side lobes are present. The full-width of the primary lobe from zero-crossing to zero-crossing is 11.9° for the 8 mm diameter transducer, and 7.92° for the 12 mm diameter transducer.

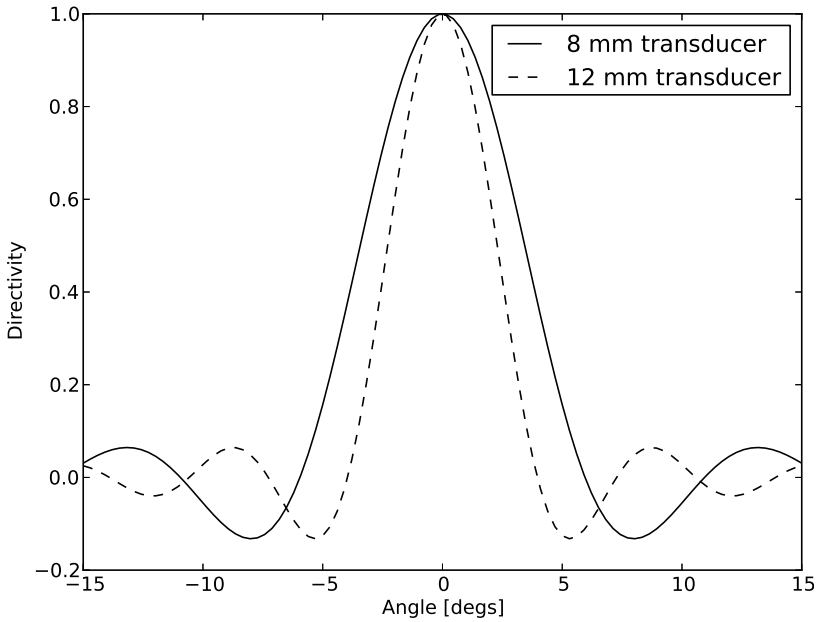

Figure 3.1: Directivity of the acoustic field in the far-field limit for 8 mm and 12 mm diameter transducers at 4 MHz in GaInSn ($c = 2.72 \times 10^5$ cm/s).

3.2.2 Reflecting particles

While most fluids must be seeded with tracer particles to reflect the ultrasound pulses, GaInSn is seeded naturally with solid oxides that form when the fluid is exposed to oxygen. Some previous work with UDV in gallium used a powder of ZrB_2 to seed the flow [Tasaka et al., 2008], however others noted that using only the natural oxide particles resulted in measurements that were just as good [Brito et al., 2001]. All of the measurements presented here used only the natural oxides as tracer particles.

The concentration of particles plays a critical role in the performance of the UDV system. If there are too few oxide particles, ultrasound pulses can bounce around the metal cylinders, leading to loud echos that interfere with velocity measurements. If there are two many oxide particles, the ultrasound pulse is dispersed quickly by the large amount of scattering, limiting the depth of measurement of the diagnostic. The effect of differing oxide concentrations in two shots can be seen in Figure 3.2.

Since the oxide particles are formed naturally and the concentration of particles is not controlled directly, it can be challenging to ensure that the concentration is within the range

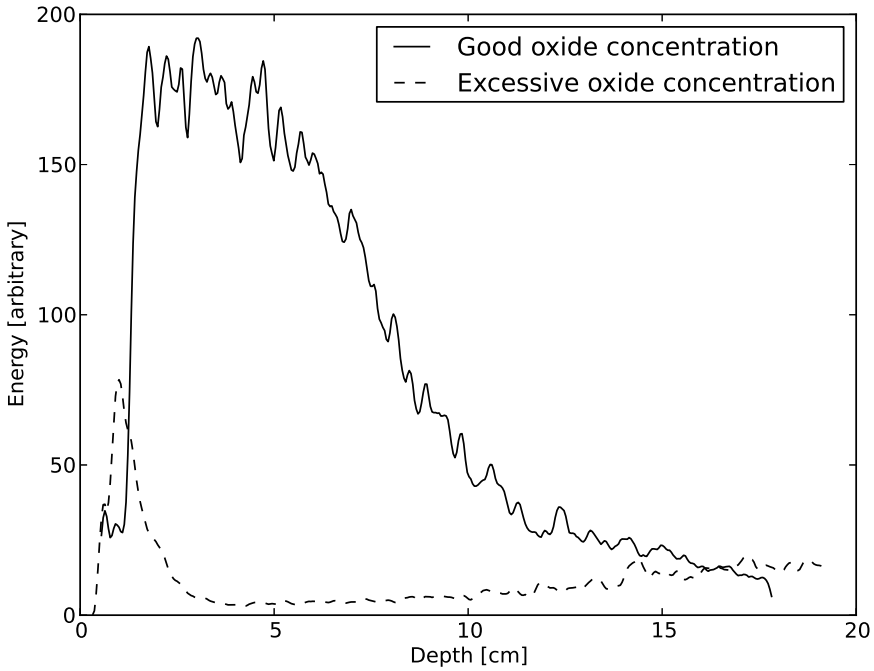

Figure 3.2: A comparison of the Doppler energy measured by the UDV diagnostic for a shot with a good concentration of oxides and a shot with excessive oxide concentration. The Doppler energy is a measure of the energy of the total power in the Doppler frequency spectrum at each depth, with the stationary (zero frequency) component removed. With a good concentration of oxides, the energy falls off roughly as $1/r^2$ in the far-field region, with a finite level of energy throughout the measurement region. When the oxide concentration is too high, the oxides dissipate the beam. The energy falls off quickly, restricting measurements to within a few centimeters of the transducer.

required for good measurements. Nonetheless, we have developed techniques to exercise some control over the oxide concentration.

It has been observed that because the oxide particles are very slightly buoyant, if the fluid is left still for several hours the clarity of the fluid improves. Agitating the fluid remixes the particles, quickly increasing its opacity. A strategy was developed to manage the oxide particle concentration based on the particle buoyancy. When the fluid becomes too opaque to the ultrasound pulses, the fluid in the experiment is agitated to ensure mixing of the oxide particles and then transferred to a holding tank, where it is allowed to sit overnight. With many of the oxides concentrated in the top part of the tank, fluid is transferred from the bottom of the holding tank back to the experiment, leaving some of the oxide-rich fluid in the holding tank.

If the oxide concentration needs to be increased, some of the fluid can be transferred from the experiment to the holding tank and mixed with the oxide-rich fluid there by bubbling argon through it. Some of this fluid can then be returned to the experiment, carrying with it an extra dose of oxides.

3.2.3 Choice of frequency

The choice of emitter frequency presents a number of trade-offs. Higher frequencies have better spatial resolution along the beam because of their smaller wavelengths, whereas lower frequencies can unambiguously measure larger velocities and tend to have larger penetration depths.

An emitter frequency of 4 MHz was chosen after testing showed adequate operation with the natural oxide particles. The constraints on maximum measurement depth and maximum unambiguous velocity measurement for this frequency in GaInSn is shown in Figure 3.3, along with some experimental parameters for reference.

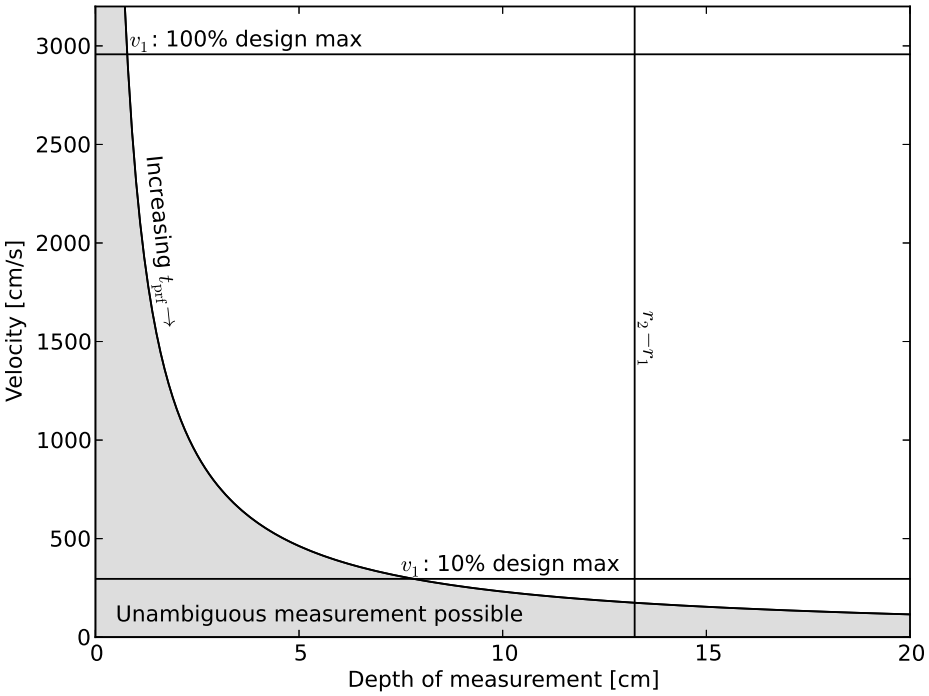

Figure 3.3: Curve of maximum depth of measurement and maximum unambiguously measurable velocity for various values of t_{prf}, assuming $f_e = 4$ MHz and $c = 2.72 \times 10^5$ cm/s. Measurements can be made above this curve, but the t_{prf} required to reach the desired depth will lead to aliasing of the measured velocity. Over-plotted are relevant parameters for the experiment: the inner cylinder velocity at 100% of the design speed (4000 rpm) and at 10% of the design speed (400 rpm), and the distance between the inner and outer cylinders, $r_2 - r_1$.

3.2.4 Transducer arrangement

Two configurations of transducers were used for this work. In both configurations, the primary transducers were mounted on the equator of the experiment, with the beams all lying in the equatorial plane. In experiments with both configurations, additional transducers were sometimes installed in other available ports for specialized measurements. The location of those transducers will be noted when their measurements are presented.

Transducer configuration #1, with a transducer nominally aimed radially toward the inner cylinder and two others passing tangentially to the inner cylinder, was used for optimization of the azimuthal velocity profiles, for much of the measurements of the free shear layer instability, and for initial measurements at MRI-relevant rotation rates.

Transducer Configuration #2 was devised because of the difficulties of obtaining measurements from the radial transducer, both because the beam divergence tended to pick up contributions from the azimuthal velocity, and because at high rotation rates fluid elements did not reside in the beam long enough to make good measurements. In this configuration, the transducers were installed with all centerlines passing tangentially to the inner cylinder. But the sign of the angles varied, with some beams passing ahead of the inner cylinder and some beams passing behind it. This configuration was used for verification of the measurements of the free shear layer instability, and for additional measurements at MRI-relevant rotation rates. Both transducer arrangements are shown in Figure 3.4.

3.2.5 Hardware installation

The transducers were mounted in Delrin port plugs which were then bolted to the outer cylinder. A hole allowing a slip fit to the transducer body was drilled through each port plug at the desired transducer angle. An o-ring in an internal gland provided a seal between the transducer body and the port plug. An example schematic is shown in Figure 3.5

The transducers were mounted on the experiment with an additional backing plate to protect against the ejection of the transducers by the high fluid pressures generated when the experiment is running. Pictures of the port plug, backing plate, and installed assembly

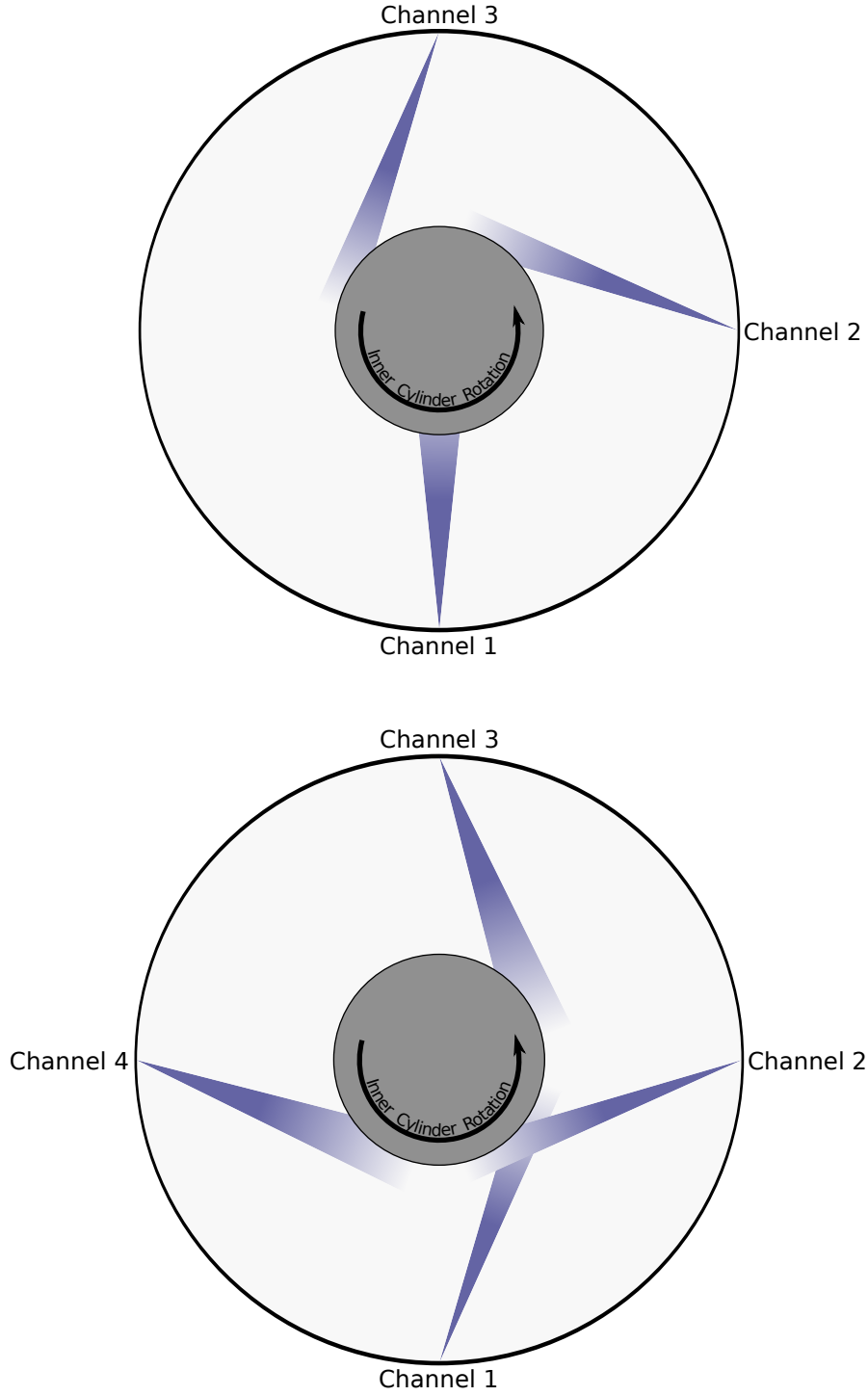

Figure 3.4: *Top:* Transducer configuration #1. *Bottom:* Transducer configuration #2. The diagrams show the transducers installed at the midplane of the experiment. The divergence of the beams in the diagram corresponds to the full width of the primary peak in the directivity function of the acoustic field in the far-field limit.

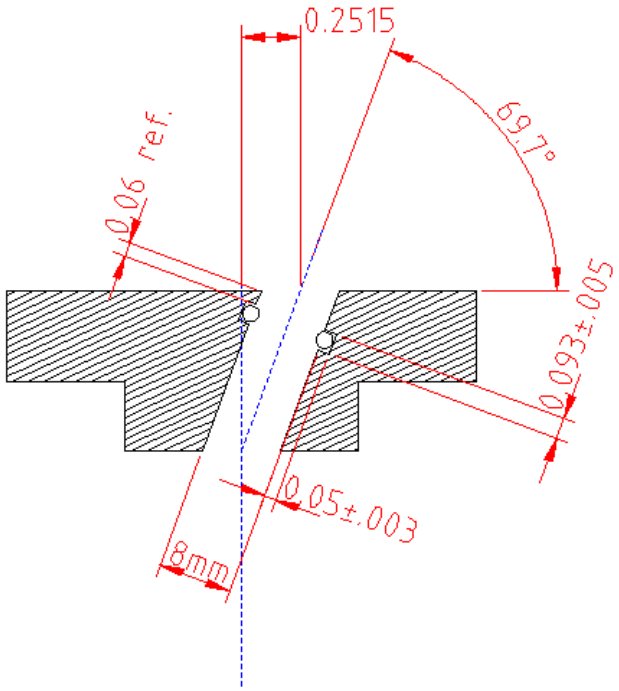

Figure 3.5: An example drawing of a port plug for a 8 mm diameter UDV transducer. A hole is drilled through the Delrin port plug with an 8 mm drill bit, providing a close fit to the body of the transducer. An 8 mm ID x 1.5 mm thick o-ring provides the seal between the body of the transducer and the port plug.

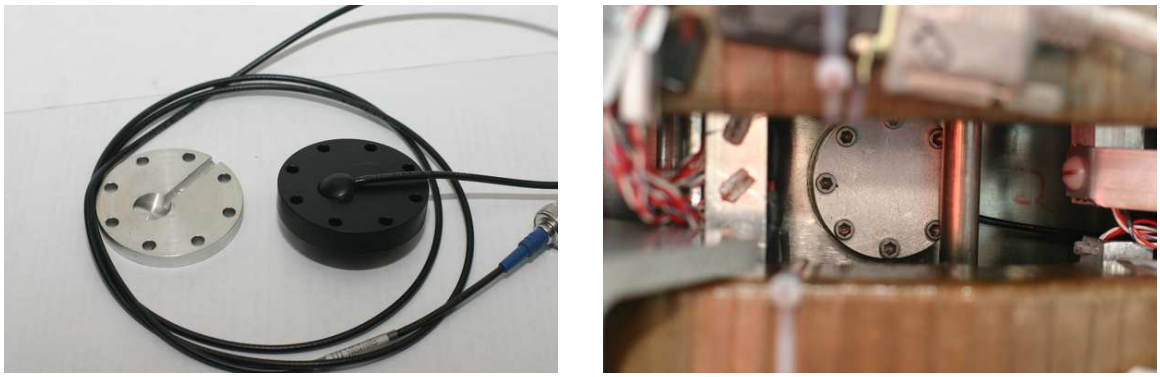

Figure 3.6: *Left:* Port plug and backing plate for UDV mounting. *Right:* Port plug installed in a port on the outer cylinder. The brown objects in the foreground are two of the magnetic field coils.

are shown in Figure 3.6.

Standard RG-174/U coaxial cables terminated with BNC connectors came out of the transducers and passed around the bottom endcap of the experiment, where they were plugged into a patch panel. Any extra cable length was wrapped and secured with zipties to prevent the cables from rubbing against the magnetic field coils when they were forced outward by rotation.

From the patch panel, wires ran to slip rings that transmitted the signals from the rotating experiment to the stationary laboratory environment, shown in Figure 3.7. Coaxial cables connected the laboratory side of the slip ring to the UDV appliance.

Because the UDV appliance used multiplexed channels, only one transducer was being used for a measurement at any given time. We took advantage of this fact to more economically use the limited number of available slip rings by passing the grounds for all of the signals over a single slip ring. The grounds from each coaxial cable in the lab frame were soldered together inside the slip ring assembly housing and passed over one ring. In the rotating frame, this single ground was connected to the ground terminal of each panel-mount BNC connector.

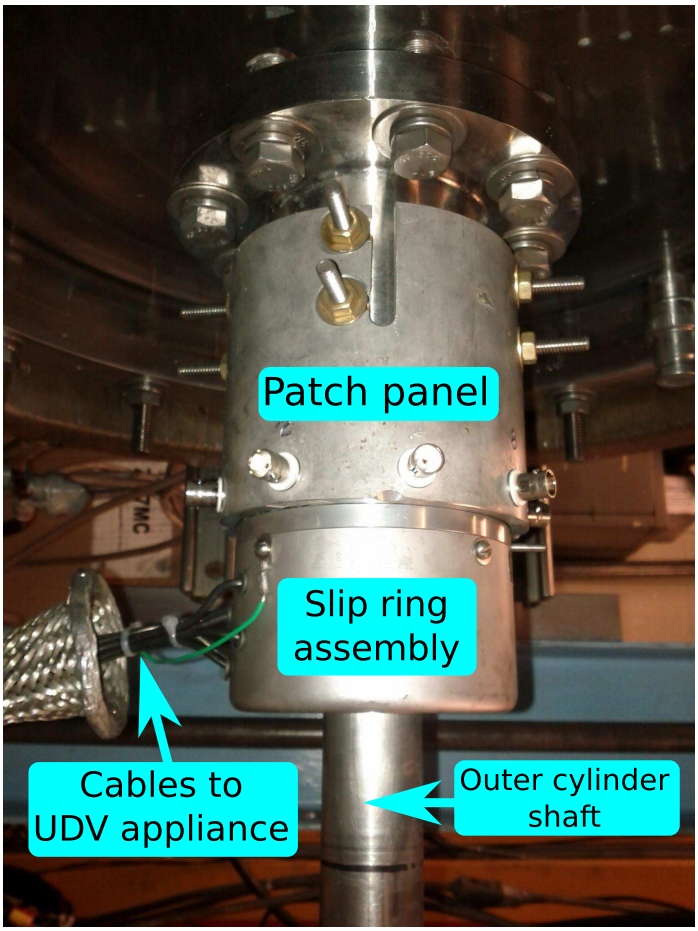

Figure 3.7: Picture of the hardware for transmitting signals between the rotating experiment and the stationary laboratory. The inside of the slip ring assembly and the patch panel rotate on the outer cylinder shaft, while the outside of the slip ring assembly and the incoming cables are stationary.

3.3 Data processing

The UDV diagnostic produces a timeseries of measurements of the velocity component in the direction of the beam at multiple distances from the transducer face along the beam. But for our experiment we wish to know the location of these measurements in cylindrical coordinates, as well as the velocity components not in the direction of the beam, but in the cylindrical coordinate directions.

There are four principle steps in the processing of the UDV data:

1. De-alias raw velocity measurements.
2. Determine position of each measurement in cylindrical coordinates.
3. Combine information from channels to find velocity components in cylindrical coordinates.
4. Transform v_θ to laboratory frame.

Each of these steps is described in its own subsection below.

3.3.1 De-alias raw velocity measurements

The first step in the data processing routine is to unwrap any 2π phase jumps in each measured velocity profile caused by aliasing. A phase jump is typically identified by a jump from more than 75% of the maximum velocity to less than -75%, or vice versa for a reverse phase jump, although this threshold may be adjusted. A tally of these phase jumps is kept along the depth of the measurement, and the velocity is corrected by adding twice the maximum measurable velocity for each jump that has been recorded up to each depth. An example of this is shown in Figure 3.8.

There can be challenges in implementing this technique when there are large gradients in the velocity, for example in the case of a strong boundary layer near the outer cylinder, as is often seen in `split-unstable` configurations. It can be difficult to get an accurate count of the number of 2π phase jumps when passing through such a boundary layer. In

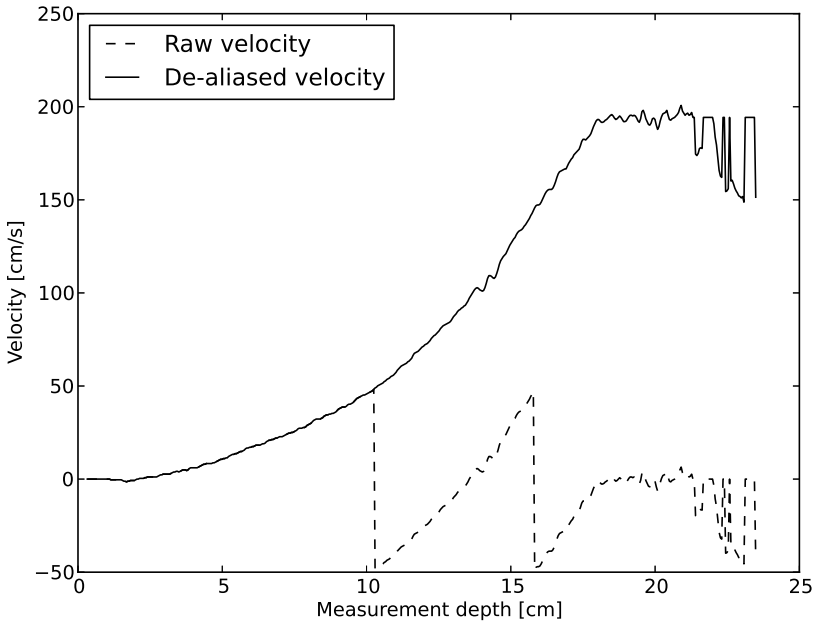

Figure 3.8: An example timesample from the UDV diagnostic with samples suffering from aliasing, as compared to the same data after the 2π phase jumps have been unwrapped.

such cases, it is best to send UDV pulses rapidly enough to ensure that there will be no aliasing when steep velocity gradients are encountered.

3.3.2 Convert measurement depth to location in cylindrical coordinates

The transducer geometry is determined by the radius, height, and azimuthal location of the transducer, and the beam trajectory. The beam trajectory is characterized by two angles: A, the half-opening angle of a cone centered on the radial unit vector; and B, an angle describing the trajectory of the beam on the surface of that cone, with $B = 0$ at the top, $B = 90°$ to the right, and $B = -90°$ to the left when looking from the outer cylinder.

A position in cylindrical coordinates can be found for each measurement depth along the UDV beam, as shown in Appendix B. For illustration, the position of the centerline of the beam as a function of depth-of-measurement is shown in Figure 3.9 for $A = 20.3°$, and $B = 90°$.

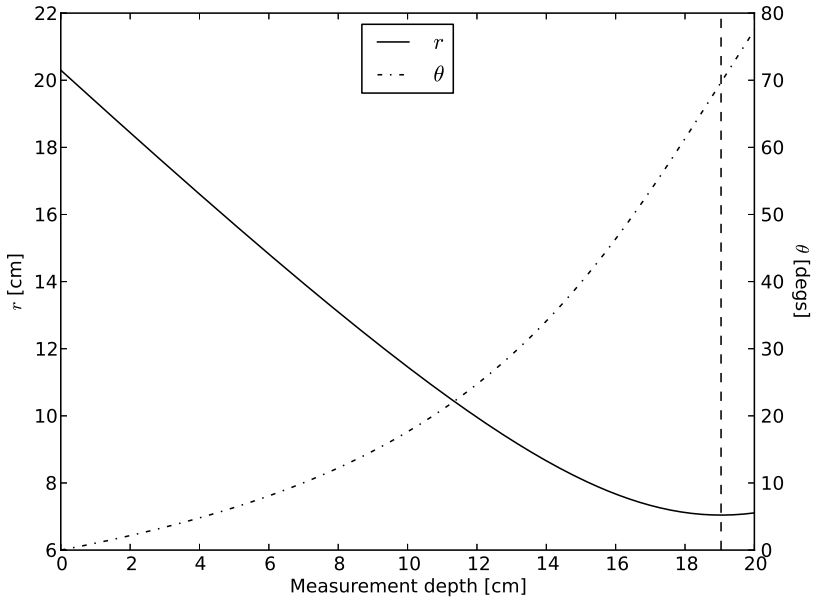

Figure 3.9: Radial position and azimuthal position of measurements for $A = 20.3°$, $B = 90°$. The dashed vertical line shows the point with the minimum radius.

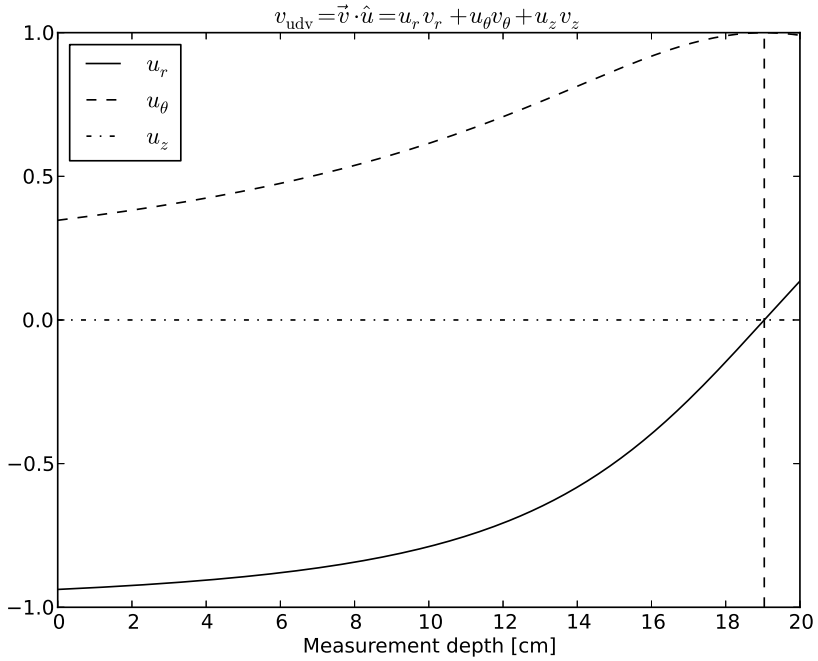

Figure 3.10: Contributions of the components of the velocity vector in cylindrical coordinates to the velocity measured by the UDV diagnostic for $A = 20.3°$, $B = 90°$. The dashed vertical line shows the position with the smallest radius.

3.3.3 Determine velocity components in cylindrical coordinates

The UDV technique measures velocity in the direction of the beam, but we are interested in the velocity components in cylindrical coordinates. At each measurement depth, the UDV-measured velocity will be a mixture of the cylindrical coordinate velocities:

$$v_{\text{udv}} = \vec{v} \cdot \hat{u} = u_r v_r + u_\theta v_\theta + u_z v_z \tag{3.6}$$

where $\hat{u}$ is the unit vector along the beam centerline, as defined in Appendix B. The contributions to the measured velocity as a function of measurement depth are shown in Figure 3.10 for a beam angle with $A = 20.3°$, $B = 90°$.

Once the coefficients are known, it becomes an inversion problem to determine the cylindrical coordinate velocities from measurements by multiple UDV transducers at different angles. Solutions to the inversion problem for several common scenarios are discussed below.

Single transducer measuring v_r or v_z

In principle it is possible to aim a transducer so that it points purely along a radial chord or purely axially. Then the measured velocity is simply v_r or v_z. In practice, these measurements are never that simple. Because the background poloidal flow is typically 1 to 2 orders of magnitude smaller than the azimuthal flow, small deviations from perfect alignment or the divergence of the ultrasound beam can lead to contamination of the signal by v_θ, making measurements of residual v_r and v_z in the background flow almost impossible. However, fluctuations in v_r and v_z can be of the same order of fluctuations in v_θ, making it possible to distinguish these velocity components for unstable modes. This is discussed in more detail in Section 3.4.

Single transducer measuring v_θ

A single transducer is sometimes used to make a measurement of v_θ. Typically this transducer's beam lies in the $r - \theta$ plane, so it measures a mix of radial and azimuthal velocities. But because the background v_r is typically only a few percent of v_θ, it is possible to de-

termine the background v_θ with the assumption that $v_r = 0$ with only a small error as a penalty. In this case, the inversion is trivial:

$$v_\theta = v_{\text{udv}}/u_\theta. \tag{3.7}$$

Two transducers in the $r-\theta$ plane, assuming axisymmetry

A typical arrangement uses two transducers aimed with different angles in the $r-\theta$ plane. Each channel measures a combination of v_r and v_θ. In general, these measurements will not be made at the same azimuthal location. But if we assume axisymmetry, that is we assume that the transducers are measuring the same v_r and v_θ at a given time, these two components of the velocity can be found by the two independent UDV measurements.

First, the data sets must be sampled on a common radial grid. The data from one of the channels is interpolated onto the radial coordinate vector for the other channel using a cubic spline representation with 30 explicit knots evenly spaced in r.

Next, the coefficients u_r and u_θ are found for each channel at each radial location. Now there is a system of equations at each radial location

$$\begin{bmatrix} v_{\text{udv},1} \\ v_{\text{udv},2} \end{bmatrix} = \begin{bmatrix} u_{r,1} & u_{\theta,1} \\ u_{r,2} & u_{\theta,2} \end{bmatrix} \begin{bmatrix} v_r \\ v_\theta \end{bmatrix} \tag{3.8}$$

where the measurements $v_{\text{udv},1}$ and $v_{\text{udv},2}$ are known, as well as the coefficients $u_{r,1}$, $u_{\theta,1}$, $u_{r,2}$, and $u_{\theta,2}$. It is simply a matter of inverting this 2x2 matrix to find the velocity components in cylindrical coordinates at this radius.

Transducers in the $r-\theta$ plane with a known nonaxisymmetric structure

If we have a steady-state nonaxisymmetric velocity structure with a known azimuthal mode number, m, (which can often be verified by examining the signals from transducers at two azimuthal locations) and a known rotation frequency ω, information can still be combined from measurements at different azimuthal locations to accurately determine the contributing velocity components. To properly do the velocity inversion, we would like to have a dataset that is as if all measurements had been made at the same azimuthal location. To do this,

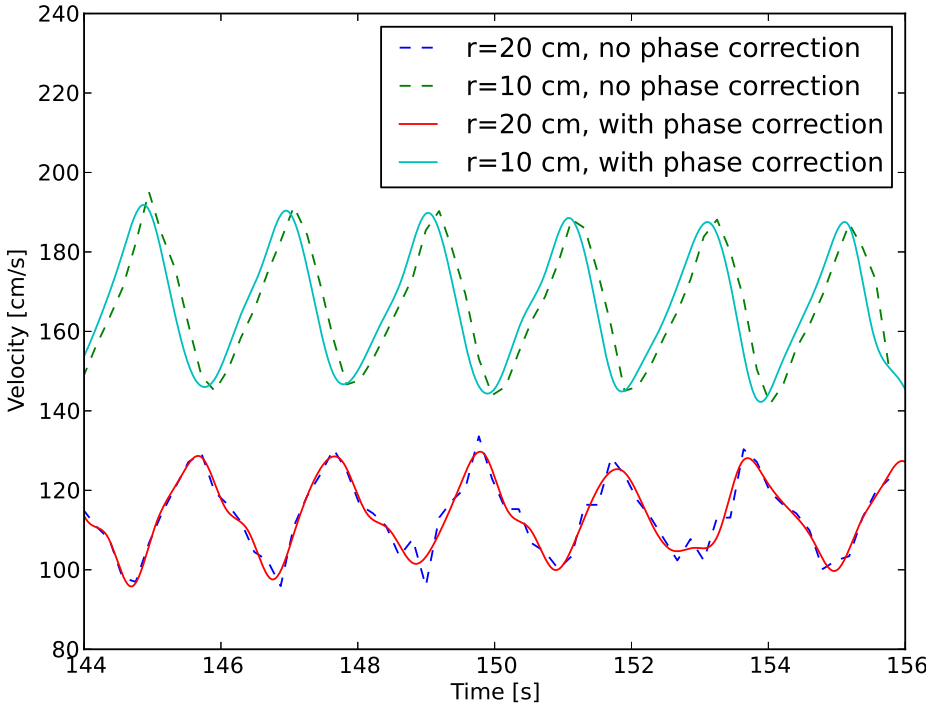

Figure 3.11: Illustration of the offset in the timeseries required to correct for the azimuthal transit of a single ultrasound beam with $A = 20.3°$ and $B = 90°$ when measuring a velocity fluctuation with $m = 1$ and $\omega = 3.1$ rad/sec.

we note that the phase of the velocity at a given radius varies as $m\theta - \omega t$. We wish to combine measurements taken at the same phase of this varying velocity. A measurement made at an azimuthal location shifted by $\delta\theta$ is equivalent to a measurement made at the original location but shifted by a time δt:

$$m(\theta + \delta\theta) - \omega t = m\theta - \omega(t + \delta t), \tag{3.9}$$

if $\delta t = -m\delta\theta/\omega$. So, we shift the timeseries backwards in time according to the azimuthal location of each measurement and use cubic splines with 6 explicit knots per period to interpolate the measurements onto a common time basis. We can then perform the velocity inversion as for an axisymmetric velocity structure. The proper phase shift due to the azimuthal transit of an individual UDV beam is shown in Figure 3.11. The time shifts required to transform measurements from two beams so that each have effective azimuthal measurement locations of $\theta = 0$ are shown in Figure 3.12.

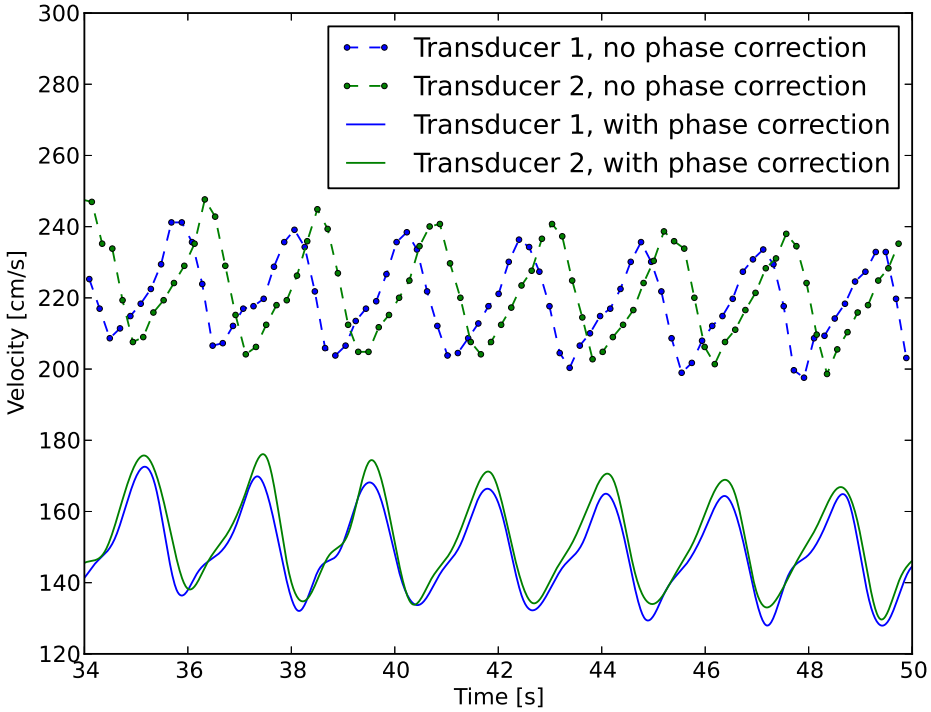

Figure 3.12: Illustration of the offset in the timeseries required to correct for the azimuthal transit of two ultrasound beams with $A = 20.3°$ and $B = 90°$, at azimuthal locations $\theta_1 = \pi/2$ and $\theta_2 = \pi$, when measuring a velocity fluctuation with $m = 1$ and $\omega = 2.7$ rad/sec. The measurements are made at $r = 11$ cm, and both signals are offset to an effective measurement location of $\theta = 0$. The "no phase correction" timeseries have been offset by 70 cm/s for clarity. The "with phase correction" timeseries have been upsampled significantly during the interpolation step of the phase correction process.

3.3.4 Transformation of azimuthal velocity to laboratory frame

All of the measurements are made with the UDV transducers fixed to the rotating outer cylinder. Thus, all velocities are measured in a moving frame of reference. We note the relationship between coordinates in the rotating (prime) frame and those in the lab frame,

$$r' = r, \quad \theta' = \theta - \Omega_2 t, \quad z' = z, \quad t' = t. \tag{3.10}$$

The radial and axial velocities are the same in the rotating and laboratory frames. But we must make a Galilean transformation for the azimuthal velocity

$$v'_\theta = \frac{d}{dt'}(r\theta') = \frac{d}{dt} r(\theta - \Omega_2 t) = v_\theta - r\Omega_2. \tag{3.11}$$

So to find the azimuthal velocity in the lab frame, we simply add a solid-body rotation component to the velocity measured in the rotating frame,

$$v_\theta = v'_\theta + r\Omega_2. \tag{3.12}$$

3.4 Calibration

To properly determine the velocities in cylindrical coordinates in the experiment, two factors need to be calibrated: the speed of sound c in the fluid, and the geometry of each measurement chord. The determination of each of these factors is discussed below.

3.4.1 Speed of sound

The speed of sound was calibrated by measuring the time of flight between the ultrasonic transducer and a hard object which produced a strong echo, with the distance between the two objects capable of being precisely controlled.

A bolt was threaded into a piece of steel and sunk in the GaInSn, with the head of the bolt about 2 cm above the bottom of the container. A UDV transducer was placed in the fluid, with the beam pointing down toward the head of the bolt. The transducer-mounting apparatus was attached to a micrometer-driven optics stage which could precisely raise the transducer up to 1 cm from its starting position.

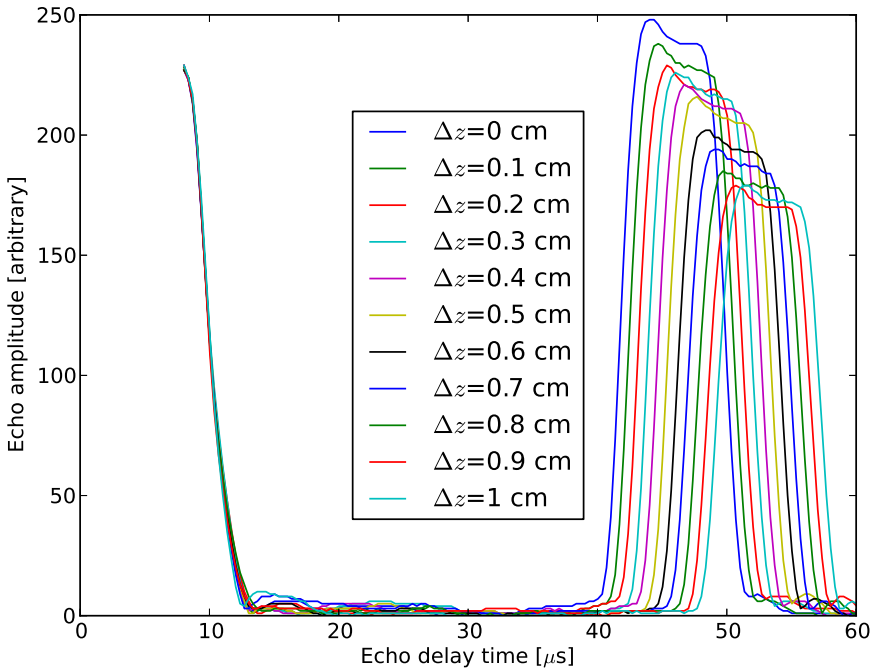

Figure 3.13: One data set showing measurements of the echo off the head of a bolt sunk in GaInSn for a set of additional displacements of the transducer in 0.1 cm increments.

Three independent sets of measurements were taken with the transducer and the bolt head initially separated by ≈5.5 cm. The transducer was raised in 0.1 cm increments and a measurement of the echo amplitude versus time was taken at each step, up to the maximum of 1 cm. An example of one data set is shown in Figure 3.13. The echo time for each measurement was defined to be the time at which the echo signal reached one half of the peak echo signal. For each set of measurements, a linear regression was performed on the set of displacements Δz from the starting position, versus Δt, the change in the echo time from the $\Delta z = 0$ measurement, to yield the speed of sound, as shown in Figure 3.14.

The average of the measurements is 2.72×10^5 cm/s with a standard deviation of 0.05×10^5 cm/s (1.8 %). This result is in reasonable agreement with the previously reported $c = 2.73 \times 10^5$ cm/s for a GaInSn alloy [Morley et al., 2008], and $c = 2.86 \times 10^5$ cm/s for pure gallium [Brito et al., 2001].

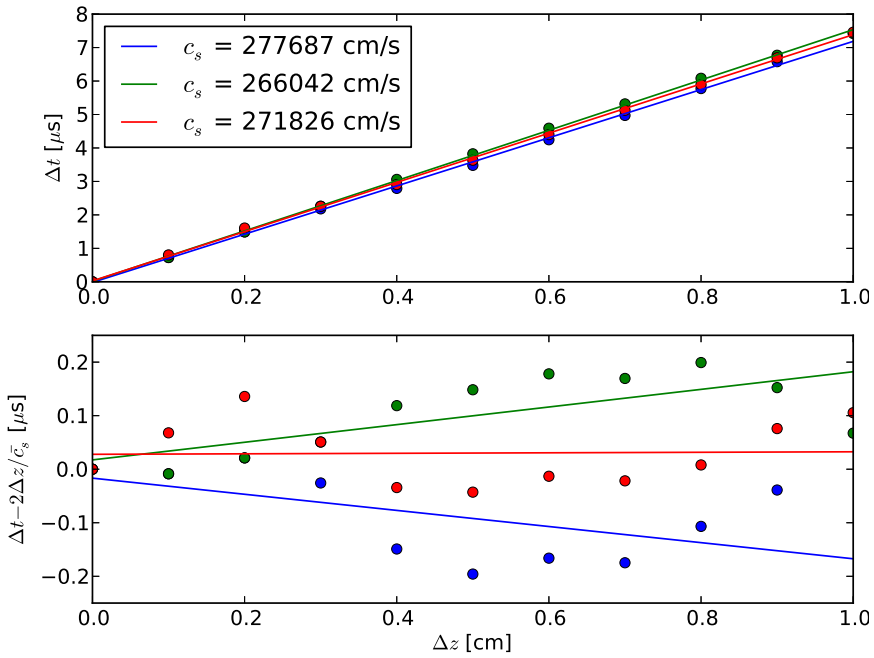

Figure 3.14: Results of the linear regressions of displacement from the initial position Δz versus the change in the echo time Δt for three data sets. The bottom plot shows the residual of all of the measurements and of the three fits as compared to the change in the echo time expected for the mean speed of sound determined by these fits, $\bar{c} = 2.72 \times 10^5$ cm/s.

3.4.2 Transducer position

In Taylor-Couette experiments with velocity diagnostics mounted in the laboratory frame, such as with LDV in experiments with optically transparent fluids, it is common to use solid-body rotation to calibrate the diagnostic. All of the rotating components are rotated at the same frequency. After the flow has had time to settle, the azimuthal velocity has a known functional form, $v_\theta(r) = r\Omega$, and the poloidal velocity components v_r and v_z are known to be zero. The angle of the measured velocity component relative to the azimuthal flow is then relatively easy to determine.

But because the UDV diagnostic is mounted in the rotating frame of the experiment, solid body rotation results in no movement of the measuring transducer relative to the fluid and so it cannot be used for calibration. So we must find a way to calibrate the coordinates of the transducer beam using unknown fluid flows.

A scheme was devised to measure identical differential rotation configurations with the components rotating forwards (with $\hat{\Omega}$ up) and backwards (with $\hat{\Omega}$ down). The assumption is then made that the forward and backward azimuthal velocities are simply inverses of each other, $v_{\theta,\mathrm{f}}(r) = -v_{\theta,\mathrm{b}}(r)$, and that the radial velocities are equal, $v_{r,\mathrm{f}}(r) = v_{r,\mathrm{b}}(r)$. A set of transducer geometrical factors (offsets, and beam angles), can then be chosen so that the velocities inferred from the measurements satisfy these relations.

The calibration presented here was performed for transducer Configuration #2 in the split configuration, with $\Omega_1 = 400$ rpm and Ω_2=53 rpm. The calibration was then tested against forward and backward shots with the forward component speeds (400, 270, 53, 53 rpm) and (800, 106, 106, 106 rpm).

Transducer offset

All transducers were installed with the transducer face recessed at least slightly in the hole drilled through its port plug. Because the velocity profiles are highly sheared, it is important to account for these offsets.

Figure 3.15 shows averaged raw data from each of the channels if we were to assume

that each transducer is flush with the outer cylinder. Channels 1 and 4 should nominally measure the same velocity profile, since they are aimed in approximately the same direction, as should Channels 2 and 3. Additionally, the separation in measured velocity due to the influence of v_r between the forward- and backward-facing transducers should be equal in magnitude for the forward and backward rotation shots. These requirements are not met for the uncorrected raw data.

Figure 3.16 shows these same averaged raw data profiles, with the offset value chosen so that the plots with the adjusted depth scale meet the above requirements. The conditions above actually constrain the *relative* offset of all of the transducers. The absolute offset is chosen so that the relative offsets relations are satisfied, and so that the chosen offsets closely match the distance from the face of the transducer to the front of the port plug as measured before installation.

Transducer angles

With the transducer offsets accounted for, the angles A of the transducers are now determined. The angles were found by a brute-force method of minimizing an error function for each pair of forward- and backward-facing transducers. For a range of angles around the nominal installed angle of $A = 20.3°$, the velocity transformation was done for the forward and backward shots with the new choices of A. An error function was then calculated for this pair of shots,

$$\text{Error} = \frac{\int_{11\,\text{cm}}^{19\,\text{cm}} dr(10|v_{r,\text{f}} - v_{r,\text{b}}| + |v_{\theta,\text{f}} + v_{\theta,\text{b}}|)}{(19\,\text{cm} - 11\,\text{cm})}, \tag{3.13}$$

where the part due to the difference in v_r has been given extra weight since v_r is at least an order of magnitude smaller than v_θ. The error functions for each pair of forward- and backward-facing transducers are shown in Figure 3.17. As can be seen, the error function is very insensitive to equal changes to each transducer angle and so we are getting information about the relative angles of the transducers. The angles were therefore chosen so that the relative angles minimize the error function, and the average of the angles is near the nominal installation angle of $A = 20.3°$.

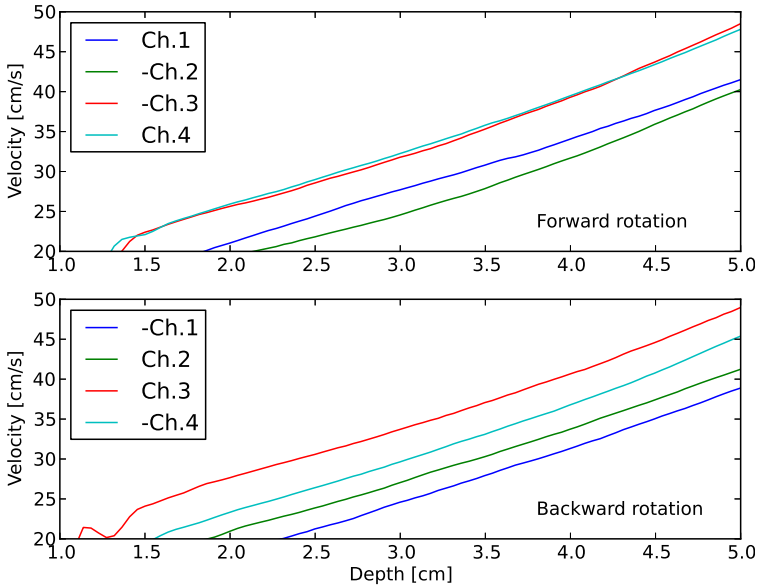

Figure 3.15: Raw transducer signals from forward and backward shots before offset calibration. Negative signs multiply the signals to put the signals from forward and backward shots and transducers with $B = 90°$ and $B = -90°$ on the same scale.

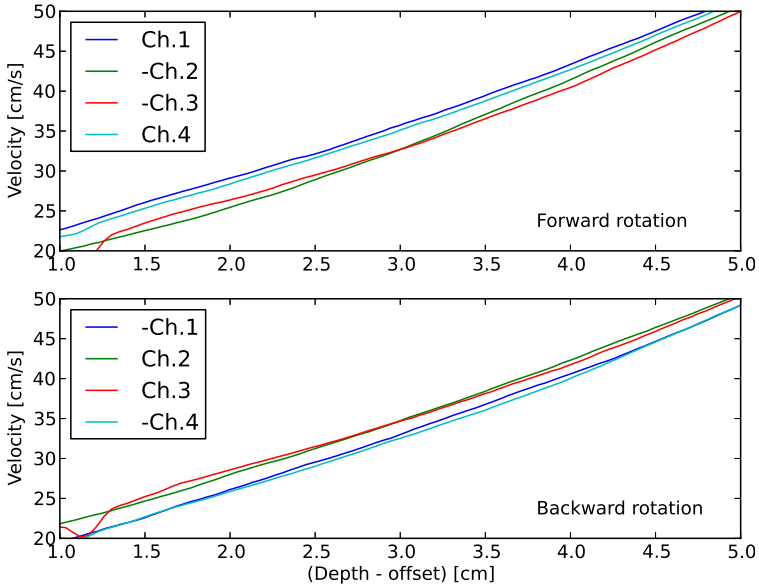

Figure 3.16: Raw transducer signals from forward and backward shots with offset-corrected depth scales. Transducers nominally aimed in the same direction now measure the same velocity. The difference between the transducers with $B = 90°$ and $B = -90°$ is now consistent between forward and backward shots, as it should be if that difference is due to the influence of v_r.

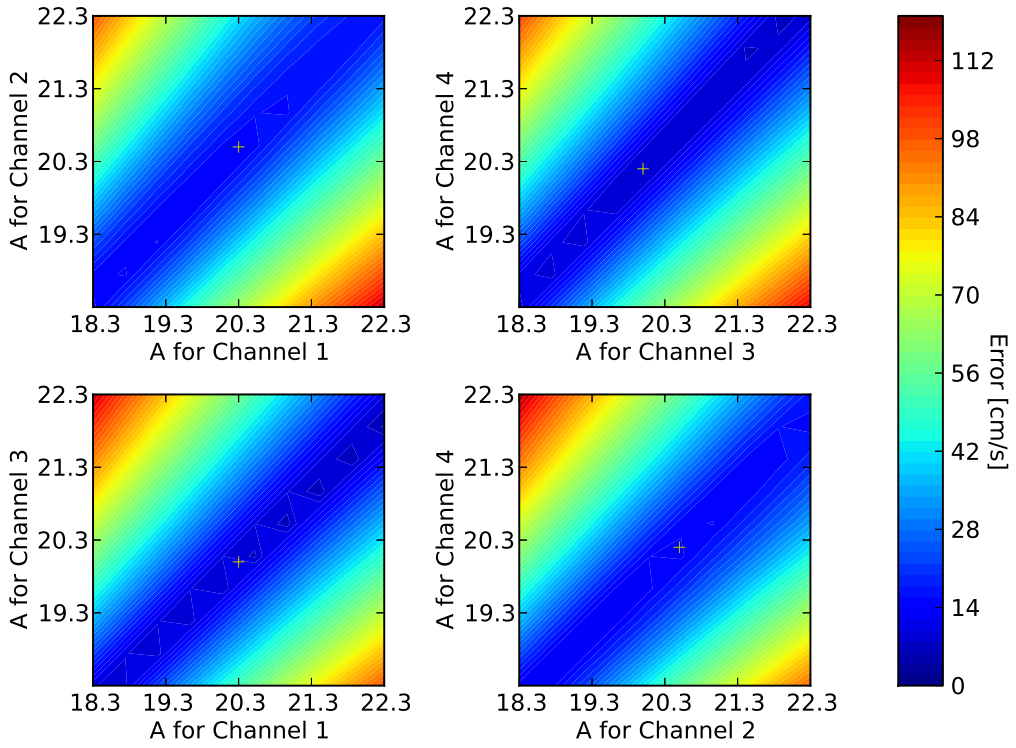

Figure 3.17: Contours of the error function defined in Equation 3.13 for varying angles A of pairs of forward- and backward-facing transducers. The chosen angles are indicated by the yellow '+'s. The error function is invariant for equal shifts of both transducer angles, so these error functions were used to choose the relative angles, with the mean of all angles close to the nominal installation angle of 20.3°.

Check of calibration

To test the calibration, forward and backward shots were taken for several different ring ratios. The measured velocity profiles for the forward and backward shots as calculated from an 80-second time average measured with transducers 1 and 2 are shown in Figure 3.18. There is a good reproduction of the v_θ profile for the forward and backward shots, although there is some deviation in the (400, 270, 53, 53 rpm) case. The measurements in all cases agree that v_r is small, although more detailed information about v_r, such as its sign, is not reliable.

A more-clear picture of the internal inconsistency of finding the velocity components can be seen in Figure 3.19. There, v_r and v_θ (or $-v_\theta$ for the backward rotating shots) were found at several different radii from measurements by each of the 4 pairs of transducers of opposites signs of B: 1 and 2; 3 and 4; 1 and 3; 2 and 4. For each pair of forward and backward shots, there are thus 8 estimates of the velocity components, all of which would be the same assuming a perfect measurement, a perfect calibration, and a perfectly recreated, axisymmetric flow state. The spread of these points is indicative of imperfection in the measurement and calibration, or an incorrect assumption about the flow state.

Good information is obtained about v_θ, where the spread is typically on the order of 5%. The measurement of v_r, however, is more problematic. For the small radial velocities generated by the Ekman circulation in these configurations, the spread is typically 100% or more of the velocity. The situation gets worse for smaller radii, where the combination of a diverging beam geometry and less sensitivity to v_r because of the changing beam unit vector $\hat{u}$ leads to increasingly large errors.

It is difficult to separate the spread in these points due to errors in the measurement and calibration from the spread due to a failure to recreate exactly the same axisymmetric flow state with the forward and backward shots. The configuration that we used for the calibration, (400, 400, 53, 53 rpm), has a relatively small spread in the radial velocities. Attempts were made to perform the same calibration using the measurements of the other two profiles, but it was not possible to obtain the same level of internal consistency as with

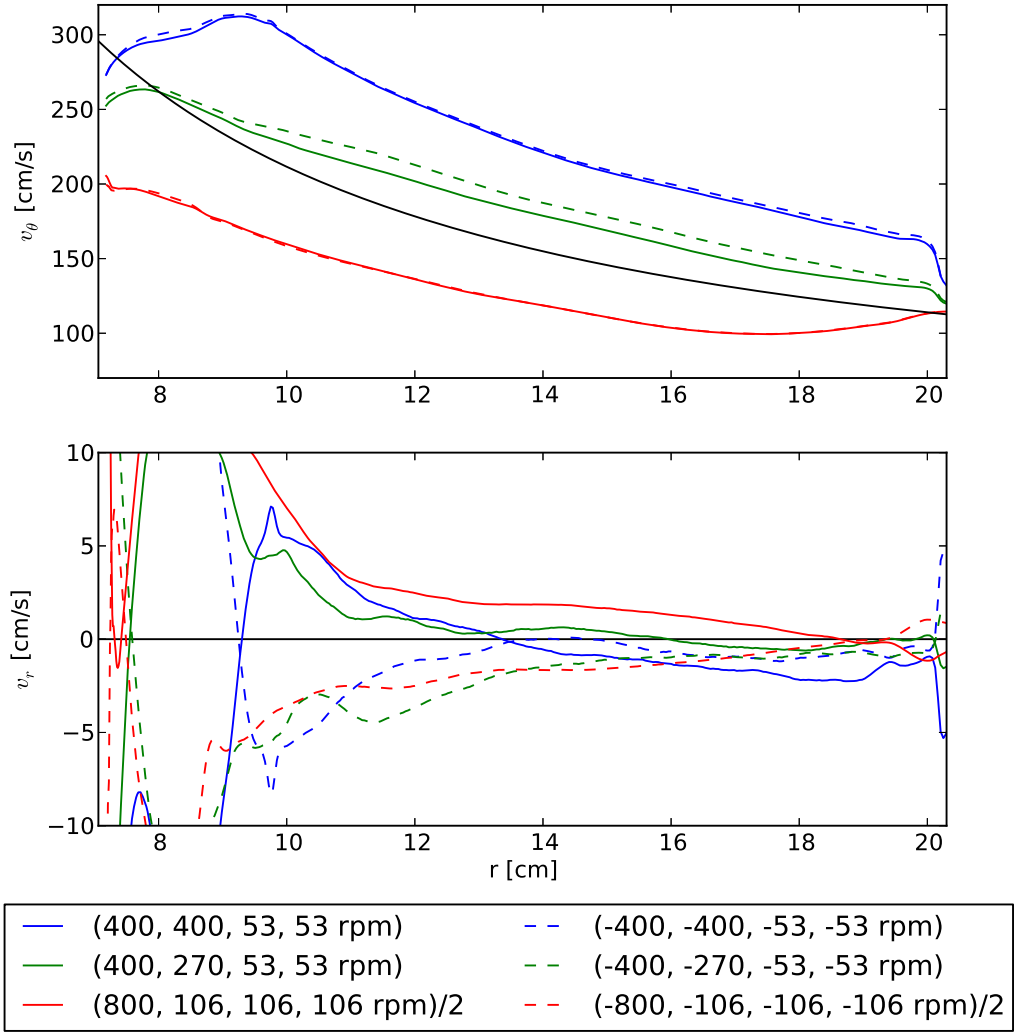

Figure 3.18: Velocity profiles calculated from measurements from transducers 1 and 2, averaged over an 80 second window. The azimuthal velocities from the backward shots have been multiplied by -1 for a direct comparison with the forward shots. The velocities from the (800, 106, 106, 106 rpm) shots have been divided by two to place them on the same scale as the other shots. The black line in the top figure is the ideal Couette profile for the Ω_1 and Ω_2 used.

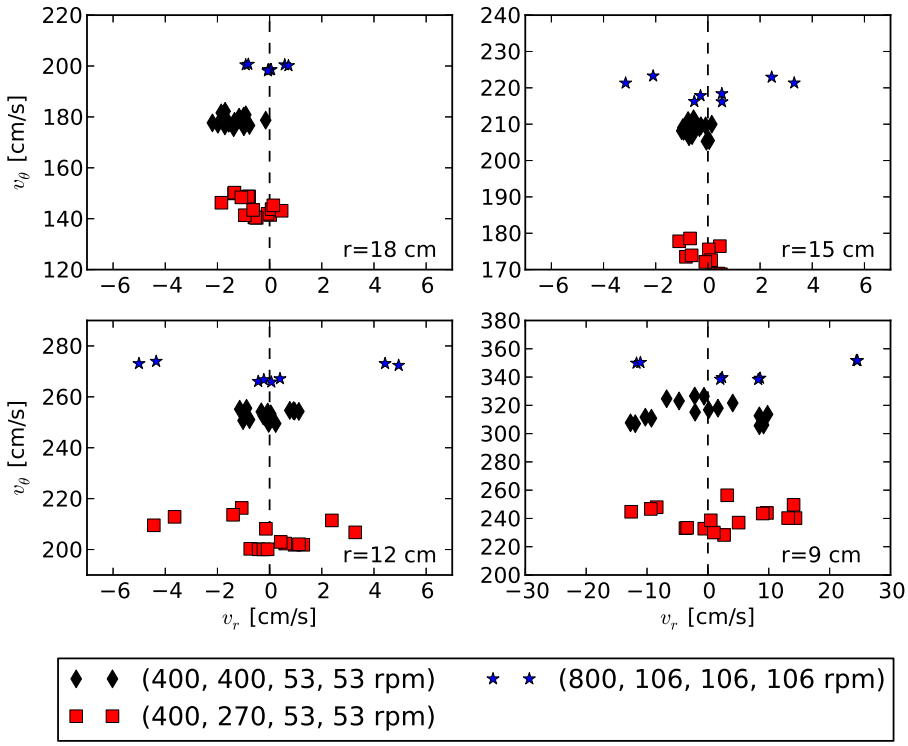

Figure 3.19: Test of calibration with various rotation profiles. Points show the measured v_r and v_θ (or $-v_\theta$) for the forward and backward rotation configurations, with each pair of different-facing transducers (1 and 2; 3 and 4; 1 and 3; 2 and 4). The (400, 400, 53, 53 rpm) and (400, 270, 53, 53 rpm) cases each had two sets of forward and backward shots, yielding 16 total points.

the (400, 400, 53, 53 rpm) case. This indicates that the other profiles may be violating our assumptions about the flow state to some degree.

Reliability of v_r measurement

As shown above, this technique does not produce reliable measurements of the v_r that arises from residual boundary-driven poloidal flow in the experiment. This is because v_r is typically only a few percent of v_θ. Small errors arising in the v_θ contribution can easily swamp the measurement of v_r. Even for configurations with a transducer aimed directly in the radial direction, the divergence of the ultrasound beam allows pickup of v_θ components that can still cause large errors in v_r. Thus, the measurement of a small v_r in the presence

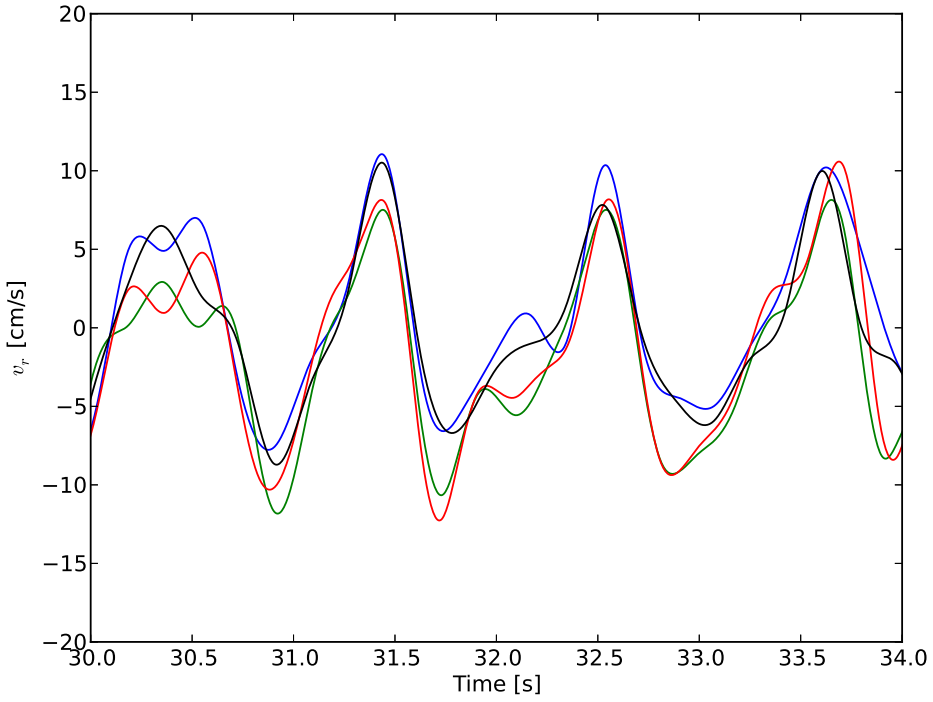

Figure 3.20: Consistency of reconstructions of v_r fluctuations associated with a nonaxisymmetric instability, reconstructed from the four possible pairs of forward- and backward-facing ultrasound transducers.

of a large v_θ is unreliable.

However, for instabilities present in the system, it is often the case that there are fluctuating quantities where v_θ and v_r are of the same order. In this case, even though the mean background v_r is uncertain, the fluctuating quantity can be measured with much greater certainty. An example of this for the Kelvin-Helmholtz instability of a free shear layer discussed later is shown in Figure 3.20. While the four reconstructions of v_r differ in the measured mean, the basic structure and magnitude of the fluctuations on top of that mean are consistent.

Chapter 4

Mean velocity profiles

In this chapter we describe measurements of the mean azimuthal velocity profiles in the experiment, and the effect of an applied axial magnetic field on those flows. We first describe the hydrodynamic state. Then we give a basic explanation of how the application of a magnetic field affects the flows through the induction of Hartmann currents. The flow is then described in the weakly magnetized ($\Lambda \sim O(1)$) and strongly magnetized ($\Lambda \gg 1$) regimes. The measurements in the weakly magnetized regime are used as motivation for a possible technique for identifying the MRI in this experiment.

The flow in the experiment can be described by the equations of nonideal, incompressible MHD, derived in Appendix C, and reproduced here for convenience:

$$\dot{\vec{B}} + \vec{v} \cdot \nabla \vec{B} - \vec{B} \cdot \nabla \vec{v} = \eta \nabla^2 \vec{B}, \tag{4.1}$$

$$\dot{\vec{v}} + \vec{v} \cdot \nabla \vec{v} + \frac{1}{\rho} \nabla P - \frac{\vec{B} \cdot \nabla \vec{B}}{4\pi\rho} = \nu \nabla^2 \vec{v}, \tag{4.2}$$

$$\nabla \cdot \vec{B} = 0, \tag{4.3}$$

$$\nabla \cdot \vec{v} = 0. \tag{4.4}$$

The first equation is the magnetic field evolution equation. The second is the momentum equation describing the flow evolution. The last two equations are constraints on the magnetic field and flow imposed by the absence of magnetic monopoles and the fluid

incompressibility.

4.1 Hydrodynamic flow state

We begin first with the hydrodynamic problem, where there are no currents and no magnetic field. In this case, the problem is described by two equations: the momentum equation with the magnetic field term removed, and the incompressibility constraint.

4.1.1 Ideal Couette flow

The ideal Couette solution is a steady-state solution to the hydrodynamic equations assuming axisymmetry and no axial dependence (implying an infinitely long device) [Couette, 1890, Taylor, 1923]. In this limit, the momentum equation describing the azimuthal flow is simply

$$(\nu\nabla^2\vec{v})_\theta = 0. \tag{4.5}$$

If the viscosity is spatially constant, the azimuthal velocity must satisfy the differential equation

$$\left[r\frac{\partial^2}{\partial r^2} + \frac{\partial}{\partial r} - \frac{1}{r}\right] v_\theta = 0. \tag{4.6}$$

If we posit a solution $v_\theta = \sum_n a_n r^n$, we find

$$\sum_n a_n \left[n(n-1) + n - 1\right] r^{n-1} = 0, \tag{4.7}$$

which can be satisfied for nonzero a_n and r only if $n = \pm 1$. So the ideal Couette solution for the azimuthal velocity is

$$v_\theta(r) = ar + \frac{b}{r}, \tag{4.8}$$

where the constants a and b are found by matching the solution to the rotation speeds of the cylinders at the radial boundaries:

$$a = \frac{\Omega_2 r_2^2 - \Omega_1 r_1^2}{r_2^2 - r_1^2}, \quad b = \frac{(\Omega_1 - \Omega_2) r_1^2 r_2^2}{r_2^2 - r_1^2}. \tag{4.9}$$

Measured azimuthal velocities matching this profile would suggest that the effects due to axial endcaps that might distort the velocity distribution are minimized, so that the fluid is behaving as if it were in an infinitely long device.

4.1.2 Effects of axial boundaries

When there is only azimuthal velocity, the radial force balance is satisfied by a pressure gradient balancing the centrifugal force of the fluid,

$$\frac{v_\theta^2}{r} = \frac{1}{\rho}\nabla P, \tag{4.10}$$

leading to a radial distribution of the pressure

$$P(r) = \rho \int_{r_1}^{r} dr \frac{v_\theta^2}{r}. \tag{4.11}$$

When axial boundaries are added, the fluid at the endcaps is forced by the no-slip boundary condition to corotate with the bounding element. The difference between the rotation speed of the fluid at the endcaps and in the bulk of the fluid leads to an axial gradient in the balancing pressure. This pressure gradient can then drive poloidal secondary circulation, leading to additional axial and radial angular momentum transport, and driving the fluid rotation profile away from the ideal Couette solution. This secondary circulation is known as Ekman circulation.

A solution to this problem is to divide the endcaps into differentially rotatable rings, allowing the speed of the fluid at the boundaries to more-closely match the speed of the fluid in the bulk [Kageyama et al., 2004]. This approach was found to successfully minimize the axial boundary effects in the water phase of this experiment [Burin et al., 2006, Schartman et al., 2009], allowing measurements of the Reynolds stress in the absence of significant secondary circulation [Ji et al., 2006, Schartman et al., 2012].

4.1.3 Measurement of hydrodynamic flow profiles

The hydrodynamic azimuthal velocity profiles were measured in the `Ekman 10%` configuration, the `MRI-Z 10%` configuration, and the `split` configuration with $\Omega_1 = 400$ rpm and

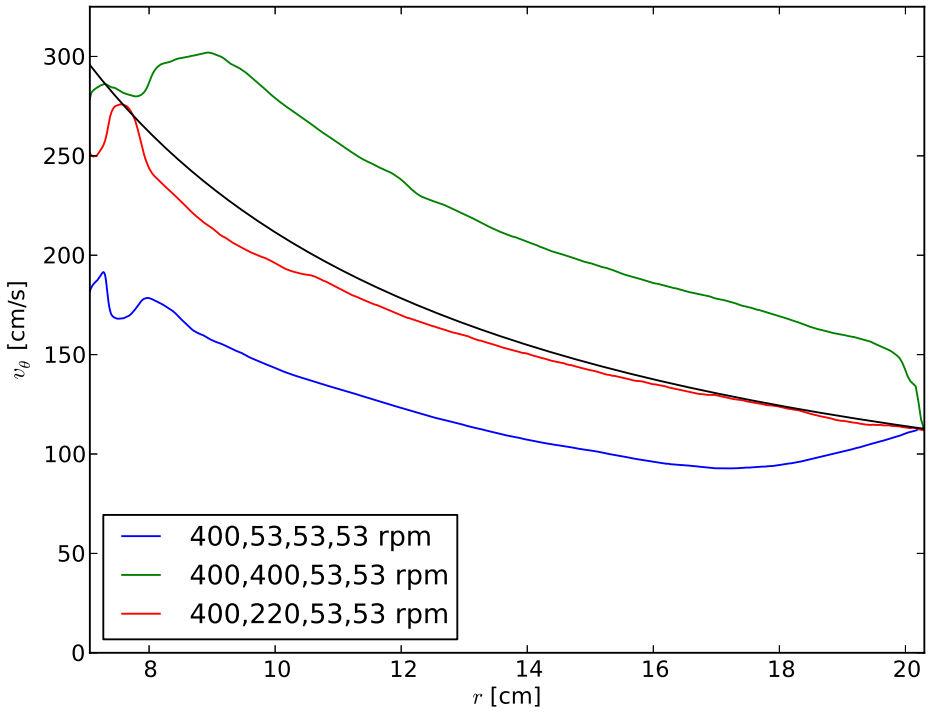

Figure 4.1: Profile of v_θ measured by the UDV diagnostic at the midplane for several different ring speed configurations, all with $\Omega_1 = 400$ rpm and $\Omega_2 = 53$ rpm. The black line shows the ideal Couette solution for these inner cylinder and outer cylinder speeds.

$\Omega_2 = 53$ rpm. The measured profiles are shown in Figure 4.1. The `Ekman` and `split` configurations feature axial boundary configurations that are frequently used in Taylor-Couette devices, though the geometrical aspect ratios of this experiment are quite different from typical Taylor-Couette devices. These configurations yield v_θ profiles that are far from the ideal solution. The optimized `MRI-Z` configuration comes much closer to reproducing the ideal solution. Note in all cases that the azimuthal velocity measurement becomes much less reliable for $r < 9$ cm as the ultrasound beam widens, and all feature an obvious artifact with $r < 8$ cm produced by the interaction of the sound waves with the inner cylinder wall.

Optimization of inner ring speed for MRI-Z profile

As mentioned in Chapter 2, for operational reasons the outer ring and outer cylinder were forced to corotate. So in optimizing the boundary configuration there was only one free parameter: the inner ring speed. Figure 4.2 shows the hydrodynamic v_θ profiles for the

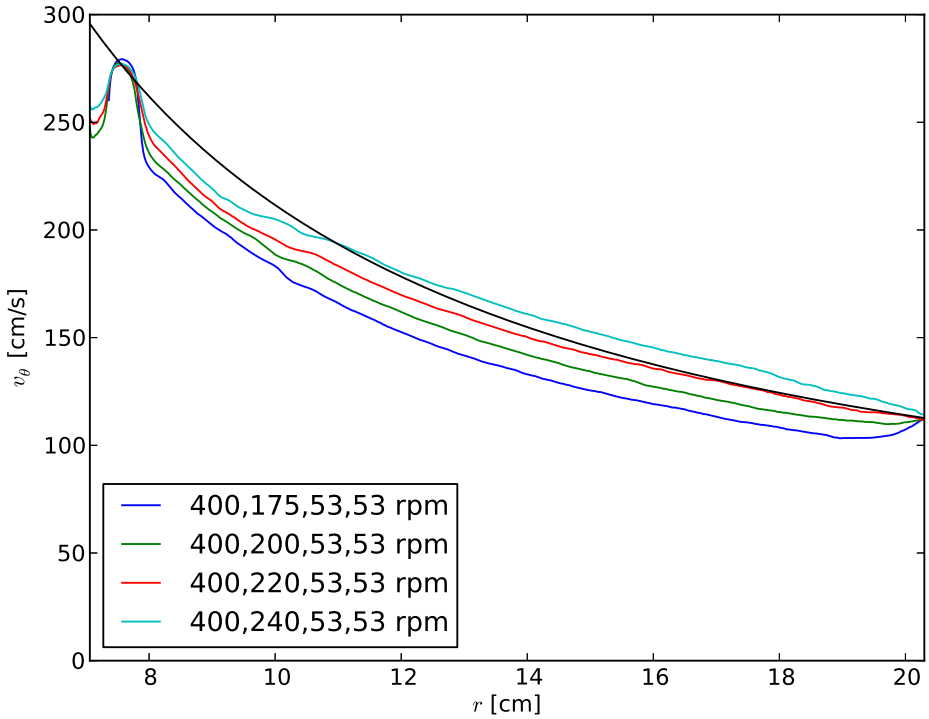

Figure 4.2: Profiles of v_θ at the midplane for several candidate inner ring speeds for the `MRI-Z 10%` configuration. The black line shows the ideal Couette solution for this Ω_1 and Ω_2.

`MRI-Z 10%` configuration with several choices of Ω_3. Note as before the decreasing accuracy of the measurement for $r < 9$ cm and the artifacts at $r < 8$ cm. The (400, 220, 53, 53 rpm) configuration was chosen since it minimizes the error with respect to the ideal Couette solution in the bulk of the fluid volume.

4.2 Modification of flow state by applied magnetic field

For the hydrodynamic problem, v_θ at the midplane is determined by a balance of viscous and inertial forces, the inertial forces arising from the boundary-driven Ekman circulation. The addition of a magnetic field adds magnetic stresses to the v_θ force balance [Loper and Benton, 1970, Benton, 1973, Khalzov et al., 2010], as well as modifying the inertial forces through magnetic braking of the Ekman circulation [Gilman and Benton, 1968, Szklarski and Rüdiger, 2007, Liu, 2008b].

4.2.1 Hartmann currents

The Hartmann current is an electrical current that is driven by the interaction of the axial magnetic field with the axial gradient of the azimuthal velocity arising from the no-slip boundary condition.

The current density in the fluid can be described by Ohm's law,

$$\frac{4\pi\eta}{c^2}\vec{j} = \vec{E} + \frac{1}{c}\vec{v} \times \vec{B}. \tag{4.12}$$

In the absence of fluid flow, currents are just driven by potential gradients. The rotation in the experiment gives rise to an additional $(1/c)v_\theta B_0 \hat{r}$ contribution to Ohm's law. In an infinitely long system, this contribution could be perfectly balanced by an electric field arising from a potential

$$\phi(r) = \frac{B_0}{c}\int_{r_1}^{r} dr v_\theta(r). \tag{4.13}$$

In the same way that the Ekman circulation could be viewed as being driven by an axial pressure gradient arising from the azimuthal velocity difference between the bulk fluid flow and the fluid viscously coupled to the boundary, the Hartmann current can be seen as being driven by an axial electrical potential gradient that arises for the same reason.

Balancing of Ohm's law in a channel: a toy model

We can gain some intuition concerning the effect of the Hartmann current on the flow by considering a simplified problem: that of an infinitely long channel, open at the top, with width w and fluid depth d, shown in Figure 4.3. The bottom boundary is insulating. The flow consists of a boundary layer of thickness δ at the bottom, in which the fluid velocity is everywhere zero, and a bulk flow region in the rest of the channel with velocity v_0. Currents are allowed to pass between the boundary layer and the bulk of the fluid only at the side boundaries, and the potential is uniform along the sides. (One could imagine the boundary layer and fluid being separated by a thin insulating sheet, and the side walls being made of a superconducting material.) A uniform axial magnetic field of magnitude B_0 penetrates the entire fluid.

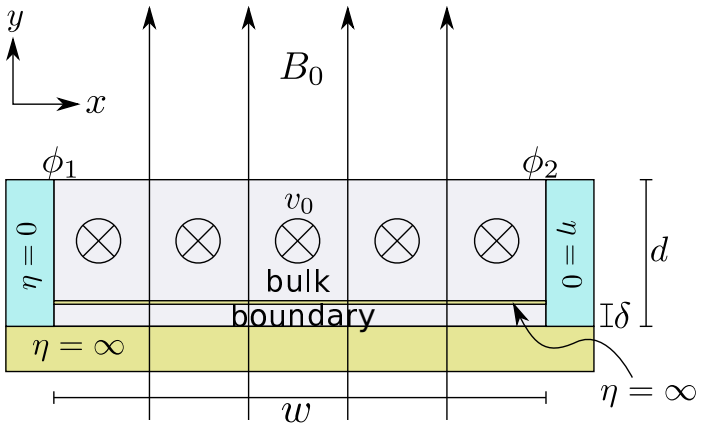

Figure 4.3: Schematic of setup for toy model of Hartmann currents in a channel.

In the bulk of the fluid, Ohm's law takes the form

$$\frac{4\pi\eta}{c^2} j_{\text{bulk}} = -(\phi_2 - \phi_1)/w + \frac{1}{c} v_0 B_0, \tag{4.14}$$

where ϕ_1 is the electrical potential at the left wall, ϕ_2 is the electrical potential at the right wall, and j_{bulk} is the constant current density in the $\hat{x}$-direction in the moving part of the fluid.

In the stationary boundary layer there is no fluid motion, so the balance of Ohm's law is entirely between the current and the potential,

$$\frac{4\pi\eta}{c^2} j_{\text{boundary}} = -(\phi_2 - \phi_1)/w. \tag{4.15}$$

We know that the total current must be conserved, so

$$j_{\text{boundary}}\delta = -j_{\text{bulk}}(d - \delta). \tag{4.16}$$

Now we can substitute to find the relative contribution of the $\nabla\phi$ terms and the $\vec{v} \times \vec{B}$ terms in Ohm's law in the bulk,

$$\frac{\nabla\phi}{(1/c)v_0 B_0} = 1 - \frac{\delta}{d}. \tag{4.17}$$

In the limit where the boundary layer is infinitely thin, $\delta \to 0$, the potential gradient entirely balances $\vec{v} \times \vec{B}$. And in the limit $\delta \to d$, where the boundary layer is infinitely thicker than the bulk flow, the current density term entirely balances $\vec{v} \times \vec{B}$ in the bulk.

In reality, the boundary layer thickness is not a free parameter. It follows the width scaling for a Hartmann layer, $\delta \sim Ha^{-1}$ [Hartmann, 1937, Liu, 2008b], where the Hartmann number describes the square root of the ratio of the Lorentz force to the viscous force in the momentum equation, $Ha = B_0 L/\sqrt{4\pi\rho\eta\nu}$, with L a characteristic length. If we consider the situation for $Ha = 400$ (a reasonable Ha for the parameters of GaInSn, with $L \sim 10$ cm, and $B \sim 1000$ G) and with $d = 1$ cm, we note that the boundary layer is very thin, a few hundredths of a millimeter, and Ohm's law in the bulk of the fluid is balanced by the $\nabla\phi$ and $\vec{v} \times \vec{B}$ terms to within one part in 400. But the forcing of the fluid due to the Hartmann current is still significant. We see that if we compare the $\vec{j} \times \vec{B}$ terms and the viscous term in the momentum equation, the $\vec{j} \times \vec{B}$ forces exceed the viscous force by $Ha^2 = 1.6 \times 10^5$, producing a strong decelerating force in the bulk of the fluid. Thus, while Ohm's law is nearly balanced by $\nabla\phi$, the residual current can still play a very important part in the force balance of the fluid.

We note that the analysis in this toy model was for an insulating bottom boundary, like the axial boundaries in our experiment. If the bottom boundary were conducting, the very thin Ha^{-1} boundary layer would be replaced by a macroscopic conductor, leading to a much larger contribution of $\vec{j}$ to the balance of Ohm's law, and an even larger decelerating force due to $\vec{j} \times \vec{B}$ in the bulk.

Alternative picture for generating Hartmann currents: bending field lines

An alternative way to understand the generation of Hartmann currents dispenses with the admittedly contrived model of the previous section, making use of the induction equation directly. If for now we neglect the diffusive term of the induction equation, and consider magnetic fields generated in a cylindrical system by the spatially uniform $\vec{B} = B_0\hat{z}$ and by a velocity field which is entirely in the azimuthal direction, $\vec{v} = v_\theta\hat{\theta}$, we see that

$$\frac{\partial \vec{B}}{\partial t} = (\vec{B} \cdot \nabla)\vec{v} = B_0 \frac{\partial}{\partial z} v_\theta. \tag{4.18}$$

So the axial shear of the velocity combined with an axial magnetic field generates an azimuthal magnetic field. This new magnetic field is associated with a radial current,

$$\vec{j} = \frac{c}{4\pi}\nabla \times \vec{B} \Rightarrow \frac{\partial}{\partial t} j_r = -\frac{c}{4\pi} B_0 \frac{\partial^2}{\partial z^2} v_\theta. \tag{4.19}$$

So we see that the radial current density is produced as field lines are bent by the axial shear of the flow velocity, producing a force which acts to eliminate the axial velocity shear.

In both models, we see that the effect of the $\vec{j} \times \vec{B}$ force due to the Hartmann current when the fluid in the bulk is rotating faster than the fluid at the boundary is to decelerate the fluid in the bulk, and to attempt to accelerate the fluid at the boundary. (Since the boundary layer is forced to rotate at the boundary component speed by the no-slip boundary condition, this accelerating force leads to a narrowing of the boundary layer, so that the Hartmann number $Ha = B_0 \delta_l / \sqrt{4\pi\rho\eta\nu}$, with δ_l the boundary layer thickness, is always of order one.) The opposite is true if the fluid in the bulk is rotating slower than the boundary: the $\vec{j} \times \vec{B}$ force from the Hartmann current accelerates the fluid in the bulk and attempts to decelerate the fluid in the boundary layer.

Hartmann currents in nonlinear MHD simulations

For the purpose of illustrating the Hartmann current, we show here the Hartmann currents generated from a simulation performed by Wei Liu in the experimental geometry using the ZEUS-2D code [Stone and Norman, 1992a,b], modified to include finite viscosity and resistivity [Liu, 2007]. The simulations were run with $\Omega_1 = 945$ rpm, $\Omega_2 = 160$ rpm, $\Omega_3 = 396$ rpm and $\Omega_4 = 177$ rpm, with $B_0 = 5000$ Gauss, $Re = 6400$ and $Rm = 20$. The axial boundaries were insulating, and the radial boundaries were partially conducting.

A contour plot of the azimuthal velocity is shown in Figure 4.4. The velocity in the bulk of the fluid is mostly uniform axially, with the axial shear concentrated near the axial boundaries. This velocity shear and the induced j_r can be seen for several different radii in Figure 4.5. As the intuition built from our simple model suggested, the force due to the induced j_r attempts to eliminate the axial shear. Contours of j_r and the associated B_θ are shown in Figure 4.6, showing that j_r is largest near the boundary, but there remains a

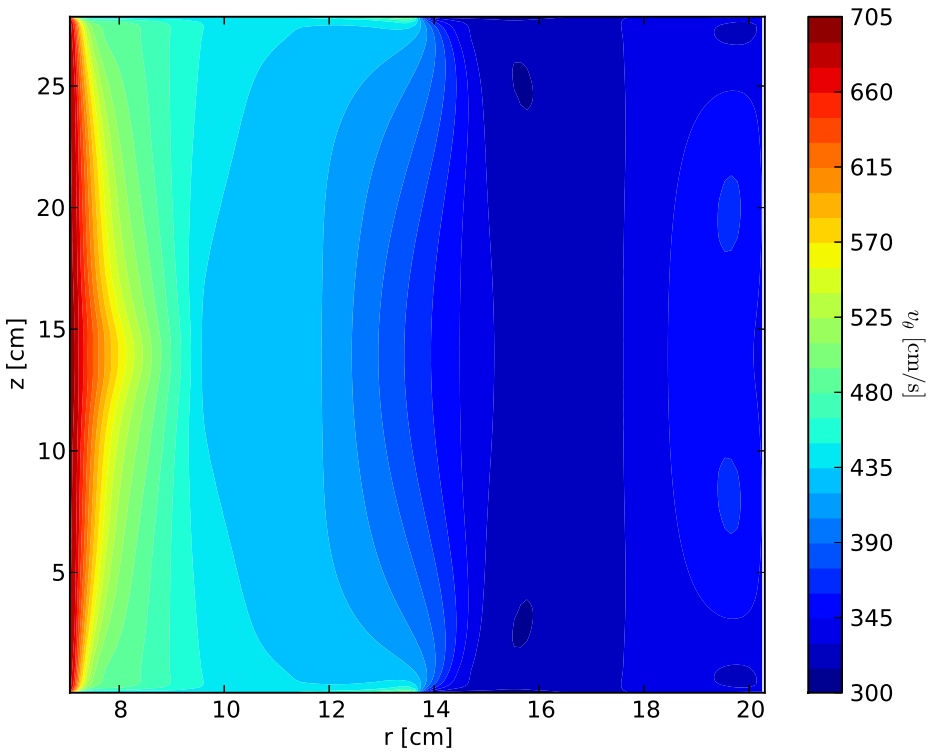

Figure 4.4: Contour plot of v_θ from a ZEUS-2D simulation.

relatively small current density in the bulk of the fluid. But, as illustrated by our toy models, even a relatively small current can have an important effect on flow dynamics because the viscous force in the bulk flow in our experiment tends to be very small.

4.3 Experimental measurements of mean velocity profiles with a magnetic field

The effect of a magnetic field on the hydrodynamically optimized MRI-Z configuration has been investigated for many values of Re and B_0. The application of the magnetic field results in a shift of the mean velocity profile from the hydrodynamic state when the magnetic field is applied. As shown in Figure 4.7, the azimuthal velocity at a given spatial point evolves smoothly in time to a new equilibrium value. The azimuthal velocity profiles at the new equilibrium are shown in Figure 4.8. Note that the applied magnetic field results in a

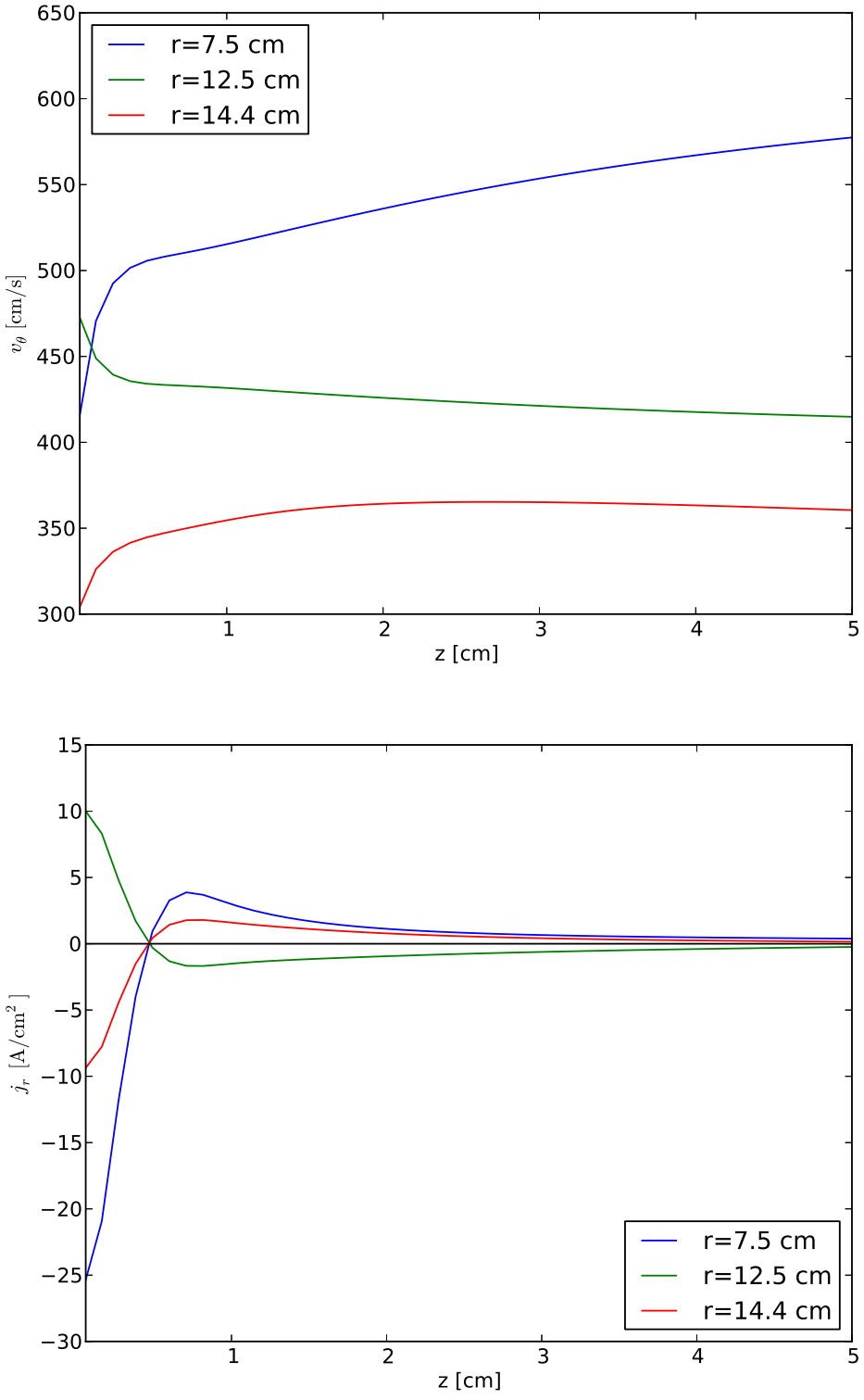

Figure 4.5: Plot of v_θ (*top*) and j_r (*bottom*) as a function of z near the axial boundary for several different radii from a `ZEUS-2D` simulation.

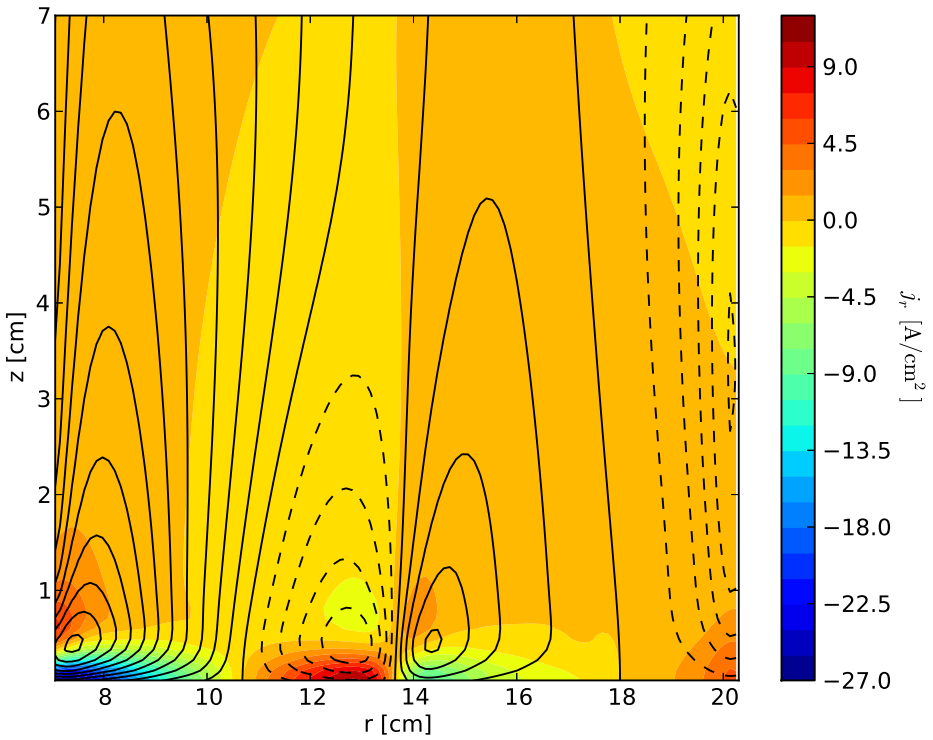

Figure 4.6: Contour plot of j_r and B_θ from a `ZEUS-2D` simulation. Color contours are contours of j_r. Solid black lines are positive contours of B_θ, indicating clockwise current flow, and dashed black lines are negative contours of B_θ, indicating counterclockwise current flow.

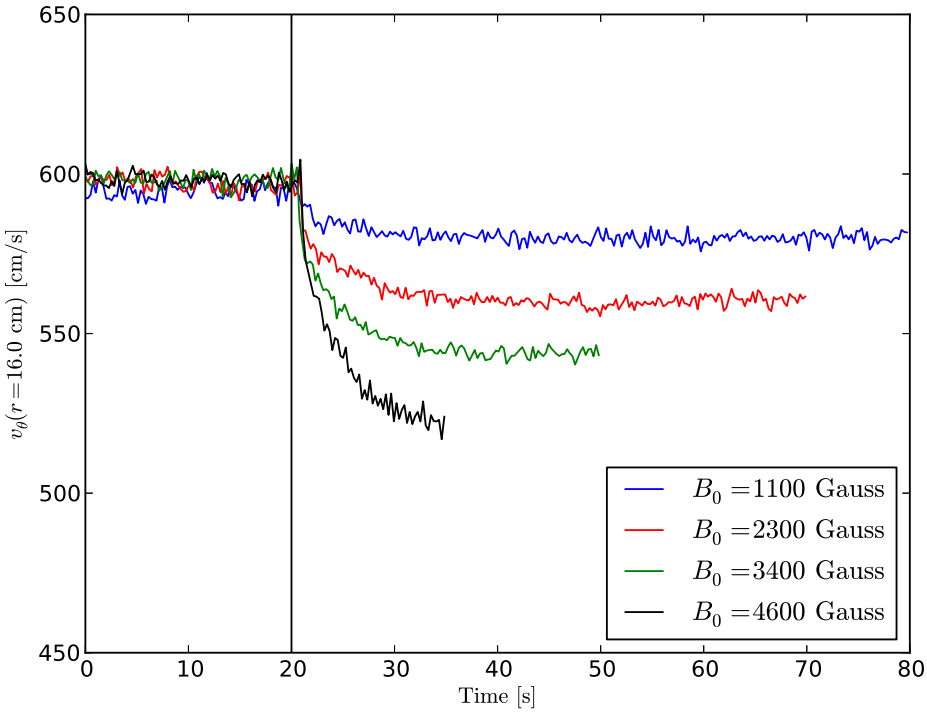

Figure 4.7: Timeseries of azimuthal velocity at the midplane at $r = 16$ cm with several different applied magnetic field strengths for the `MRI-Z 40%` configuration. The black vertical line indicates the beginning of the application of the magnetic field. Each timeseries is cut off at the time that the magnetic field is turned off.

suppression of the azimuthal velocity across the entire gap at the midplane. Our toy model would have suggested that the flow should be accelerated where the boundary speed exceeds the fluid speed with no applied field. But this far from the boundary such effects might be smoothed over, yielding a decrease in v_θ everywhere since the radially averaged boundary speed is slower than the fluid velocity.

4.3.1 Azimuthal velocity scaling

The azimuthal velocity measured at a single point is plotted in Figure 4.9 for various rotation speeds and applied field strengths. Note that the data for each rotation speed all have the same slope, so that applying a magnetic field of a given strength results in the same change of velocity, regardless of what that azimuthal velocity initially was. This fact motivates plotting the measured velocities as scaled quantities, with the measured v_θ normalized by

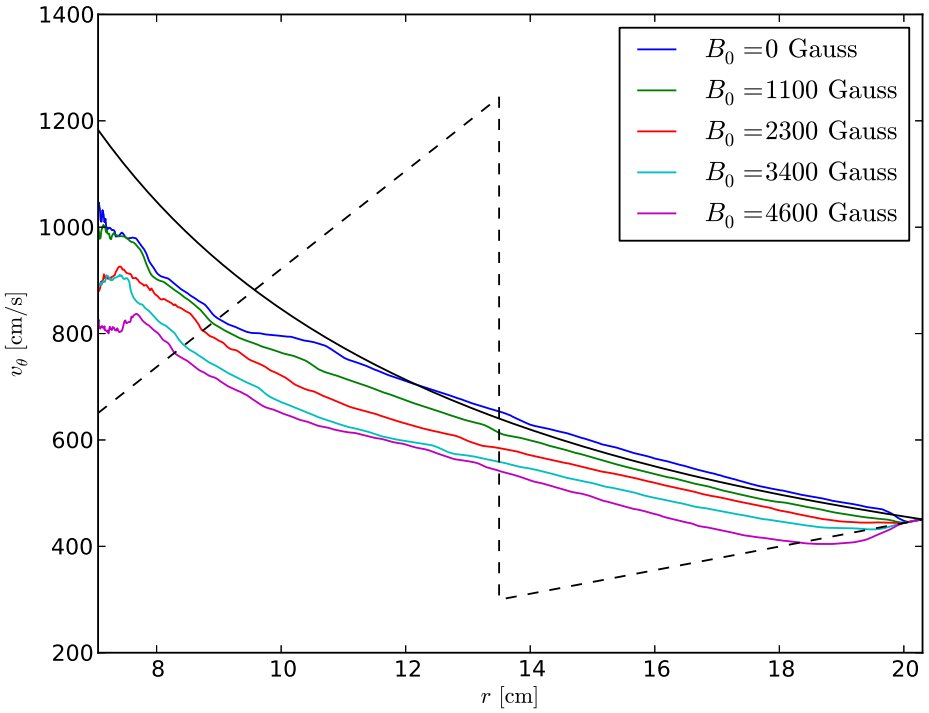

Figure 4.8: Azimuthal velocity profiles in the `MRI-Z 40%` configuration with various applied magnetic field strengths. The solid black line indicates the ideal Couette profile for this configuration. The dashed black line indicates the azimuthal velocity of the axial boundary components.

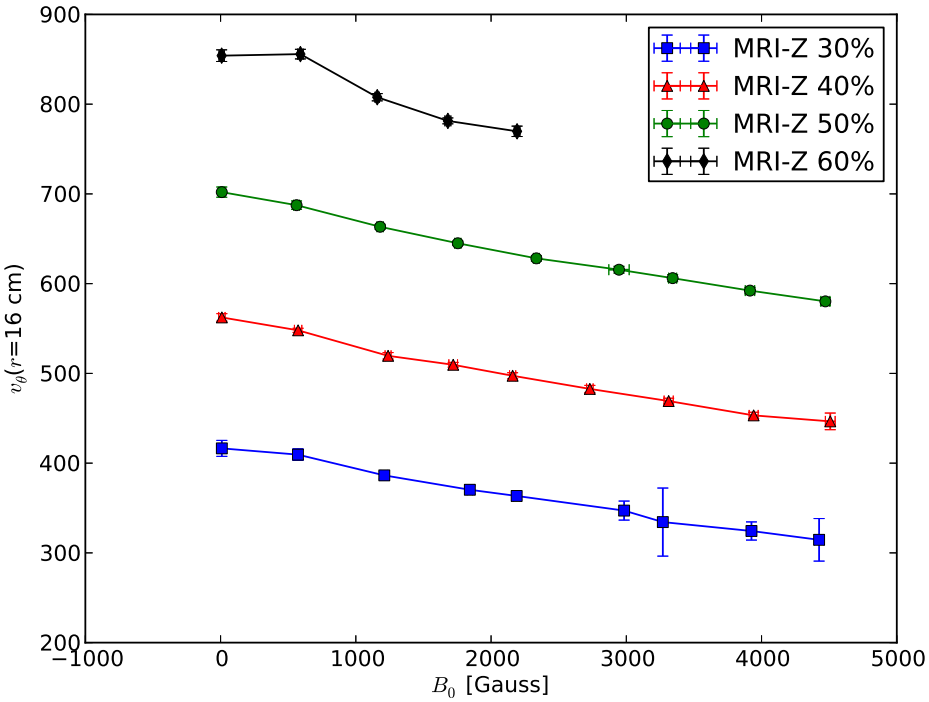

Figure 4.9: v_θ measurements at $r = 16$ cm for several rotation speeds and B_0.

the measured inner cylinder velocity v_1, and the magnetic field B_0, represented by the Alfvén speed, *also* scaled by v_1, as shown in Figure 4.10, where the Alfvén speed $v_A = B_0/\sqrt{4\pi\rho}$. The vertical error bars in this plot come from a combination of the standard deviations of the measured velocity, the measured inner cylinder speed, and the measured outer cylinder speed. They do not include the uncertainty in the speed of sound or the uncertainty due to geometrical errors of the UDV measurement, including averaging of the velocity over the beam width, which should result only in equal shifts of all measurements of similar azimuthal velocity profiles. The horizontal error bars come from a combination of the standard deviations of the measured current to the coils and of the measured inner cylinder speed.

4.3.2 Effect of changes to boundary conditions

Maintenance on the experiment between experimental runs leads to changes to the axial location of boundary components on the order 1-2 mm. As shown in Figure 4.11, this

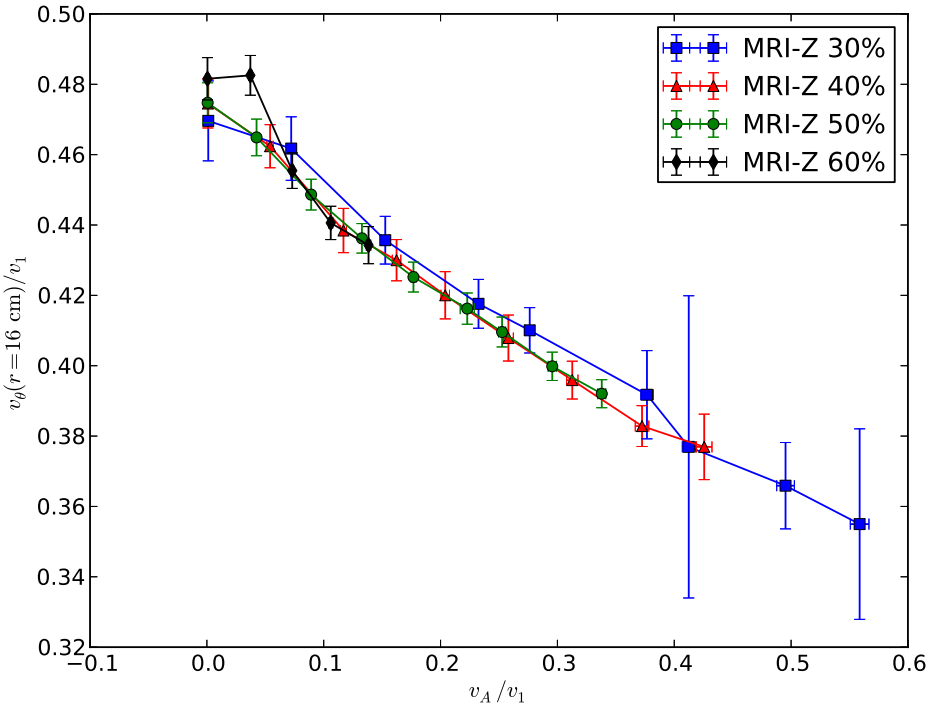

Figure 4.10: Scaled v_θ measurements at $r = 16$ cm for several rotation speeds and B_0. The v_θ for each measurement has been scaled by the inner cylinder speed, and the field B_0 has also been scaled by the inner cylinder speed, with the result plotted in units of a normalized Alfvén speed.

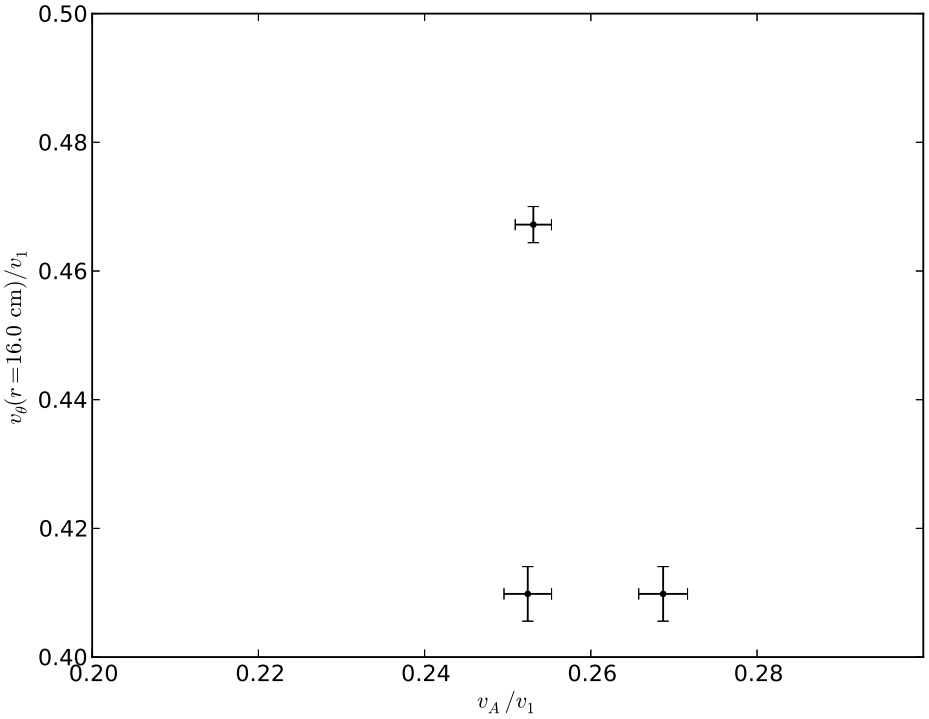

Figure 4.11: Several independent measurements of the scaled v_θ with nearly the same magnetic field, without perfect replication of the relative height of the boundary components

results in significant changes to the (scaled) azimuthal velocity. For appropriate comparisons between shots, it is therefore necessary to compare only within a series of shots in which the positions of the boundary components could not have been altered. When that is done, the scaled velocities for constant v_A/v_1 are quite reproducible over a range of rotation speeds, as shown in Figure 4.12.

4.3.3 Relevance to the MRI

The observed scaling has no clear basis in terms of a force balance between two components of the momentum equation. Instead, it seems to be a result of the global dynamics of the experiment, including viscous shear forces, inertial forces from the residual effects of the Ekman circulation, and $\vec{j} \times \vec{B}$ forces. Attempts have been made with nonlinear MHD codes to reproduce this scaling in simulation, though none have been successful. But it is worth noting that all of the nonlinear simulations use Re smaller than the experiment by one

to three orders of magnitude, and none feature all of the peculiarities of the experiment, including possible gaps or bumps in boundaries, and holes in the bounding components allowing circulation through the boundary.

Still, the experimental robustness of this scaling suggests that a deviation from the scaling with increasing rotation rate could be a sign of the MRI. As shown in Figure 4.12, the normalized velocities are nearly independent of rotation rate for fixed v_A/v_1. It may be possible to identify the MRI from a deviation from this scaling, since the additional Reynolds and Maxwell stresses produced by the MRI will likely act in addition to the inductionless processes that determine the flow dynamics below the critical Rm, leading to an additional suppression of the saturated azimuthal velocity profile.

Unfortunately, simulations have shown that the fully saturated MRI eigenmode will result in changes to the azimuthal velocity of only $\approx 2\%$ [Gissinger et al., 2012]. This is comparable to the drift in experimentally measured velocities below the threshold for the MRI, so the identification of the MRI on top of this drift would be challenging.

4.4 Mean velocity profiles with $\Lambda \gg 1$

The Elsasser number $\Lambda = B_0^2/4\pi\rho\eta\Omega$ describes the ratio of the Lorentz force to the Coriolis force, and as such is a measure of the relative importance to the flow dynamics of the magnetic field compared to rotation. Experiments were undertaken in the `split-unstable` configuration with very small rotation rates (< 1 rpm) yielding Elsasser numbers of 10s to 100s, allowing study of situations where the magnetic field has a very large effect on the flow profiles.

One consequence of such large Elsasser numbers is the appearance of a shear layer at the midplane of the experiment, as the magnetic field attempts to force the flow everywhere to match the step in the boundary velocity at the radial location of the gap between the rings. Example profiles with various magnetic field strengths are shown in Figure 4.13.

A systematic evaluation of the shear layer was performed by fitting a hyperbolic tangent

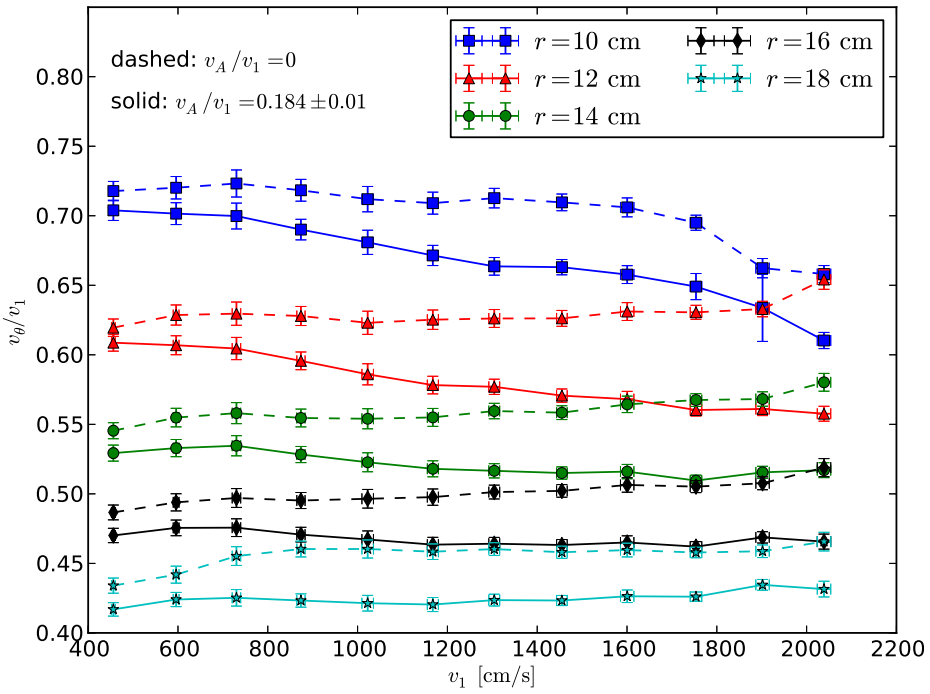

Figure 4.12: v_θ/v_1 for constant v_A/v_1 with several rotation speeds and measurement radii. The slowest rotation speed is for the `MRI-Z 15%` configuration, and the fastest rotation speed is for the `MRI-Z 70%` configuration, with a step taken every 5%.

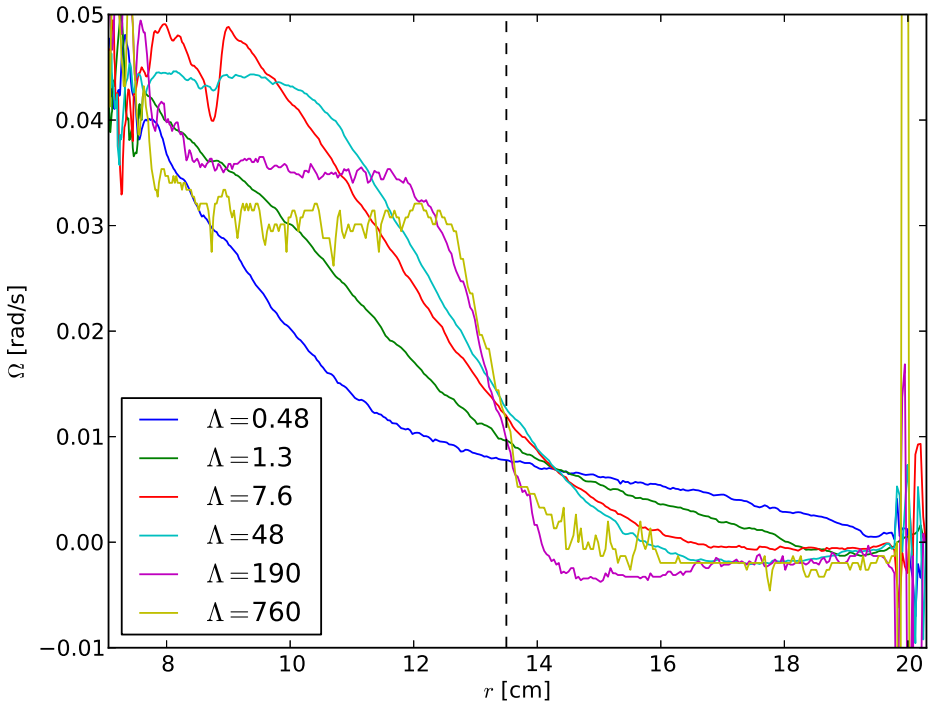

Figure 4.13: Profiles of Ω showing shear layer at midplane of experiment. Profiles are measured before onset of instability with $\Omega_1 = 0.5$ rpm and $\Omega_2 = 0$ rpm.

angular velocity profile to the measured angular velocity at each time point,

$$\Omega(r) = a_1 \tanh\left(\frac{r - r_l}{w_l}\right) + a_2, \tag{4.20}$$

where the free parameters a_1 and a_2 describe the amplitude and offset in Ω of the rotation profile, r_l is the radial location of the center of the shear layer, and w_l is a characteristic width, about one-half the total width of the shear layer. The angular velocity profiles were determined using the measurements only from a single tangential transducer. Two transducers, which would take into account the effects of v_r, were not used because the noise inherent in combining measurements of such slow speeds made a clean determination of the width very difficult. There were several shots whose noise characteristics did permit full reconstructions of v_r and v_θ and a determination of the shear layer width. The results verified that the error in neglecting v_r before the onset of the instability was negligible, and the error in the average determined shear layer width during saturation of the instability was always less than 10%, and normally only a few percent.

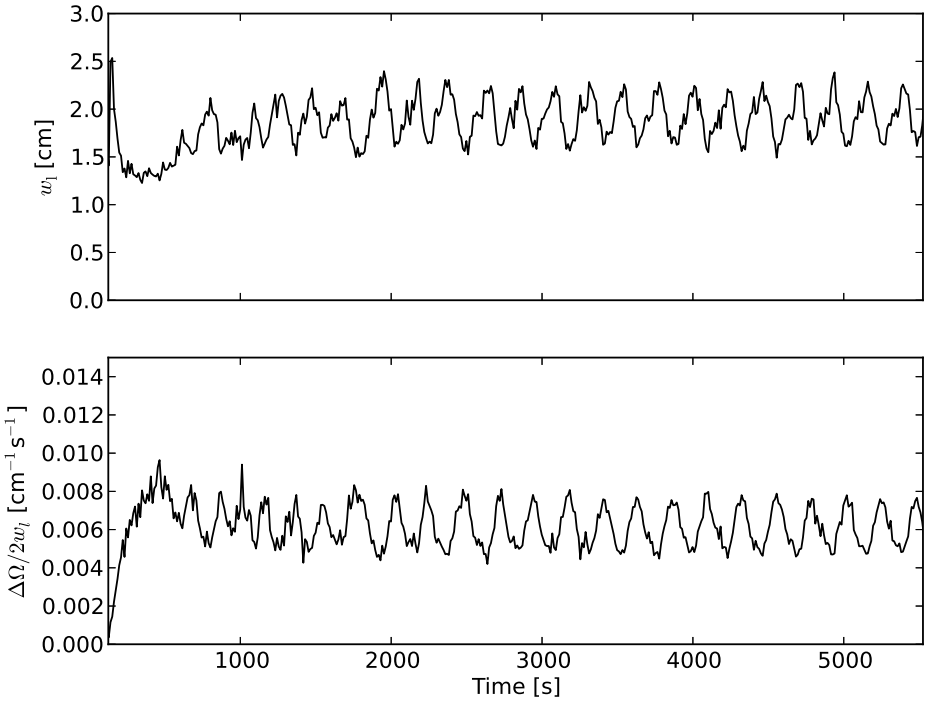

Figure 4.14: Evolution of shear layer width over the course of a shot in the `split-unstable` configuration with $\Omega_1 = 0.25$ rpm and $B_0 = 570$ Gauss ($\Lambda = 61$). The beginning and end of the plotted timeseries are at the turn-on and turn-off of the magnetic field. *Top*: shear layer half-width w_l in cm. *Bottom*: measure of total shear associated with the layer, found by dividing the change in Ω across the shear layer by the full width, $2w_l$.

An example of the evolution of the shear layer as a function of time can be seen in Figure 4.14. After the magnetic field is applied, the shear layer width approaches a steady-state value between $t = 200$ s and $t = 400$ s. Note that even as the shear layer width saturates, the associated shear continues to rise because the angular velocity jump $\Delta\Omega$ across the shear layer continues to increase. All of these shots are subject to the magnetic-field-initiated instability discussed later, evidenced here by oscillations in the layer width and shear. When the instability sets in, there is an average increase in the shear layer width and a decrease in the amount of shear associated with the layer.

Since the growth time for the instability is long compared to the time to establish the shear layer, the shear layer can be examined in a regime where the layer width is mediated by the molecular viscosity rather than the Reynolds stress associated with the instability. The width of a free shear layer in cylindrical geometry in the large-Λ limit has been found

to scale as $Ha^{-0.5}$ [Vempaty and Loper, 1978] in the small Ro limit, just as it does for free shear layers in spherical geometry [Hollerbach, 2000] and in the boundary layer of pipes [Shercliff, 1953, Roberts, 1967]. We show the measured scaling of the shear layer width as a function of Hartmann number in Figure 4.15. Note that results are presented for fields that could not be run in steady state since the measurements of the shear layer width only require that the field be on for tens to hundreds of seconds, rather than the thousands of seconds required for measurements of the instability.

We find that the shear layers here scale as $Ha^{-0.63\pm0.15}$ and $Ha^{-0.62\pm0.14}$ for the measurements at $z = 14.5$ cm and $z = 3$ cm. The scaling $Ha^{-0.5}$ is contained within one standard deviation of both measurements, but just barely, suggesting that an adjustment to this scaling may be necessary for cases such as this with $Ro \sim O(1)$.

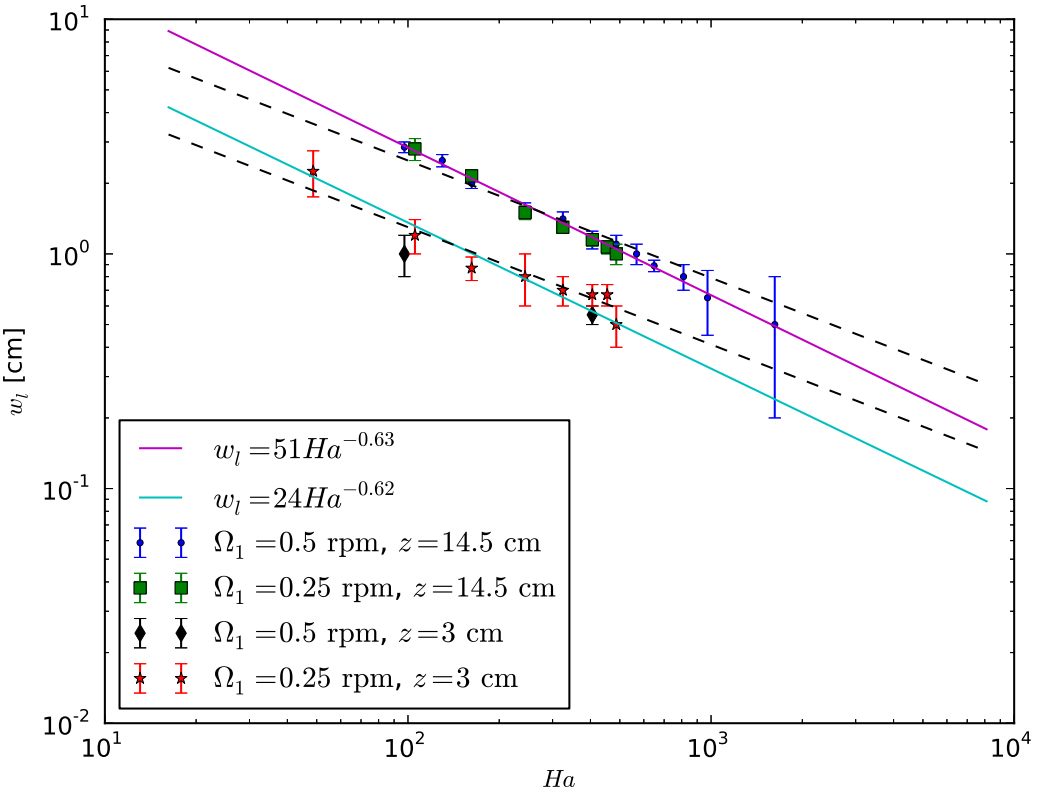

Figure 4.15: Scaling of shear layer width w_l with Hartmann number Ha for large Λ. Measured saturated widths are shown in the `split-unstable` configuration for two rotation speeds, $\Omega_1 = 0.5$ rpm and $\Omega_1 = 0.25$ rpm, from measurements at the midplane, $z = 14.5$ cm and $z = 3$ cm. Power law fits for the data at $z = 14.5$ cm and $z = 3$ cm show a scaling of $Ha^{-0.63\pm0.15}$ and $Ha^{-0.62\pm0.14}$, respectively. The dashed lines show the scaling $Ha^{-0.5}$ for reference.

Chapter 5

Kelvin-Helmholtz instability of free shear layers: experiments

Under the right conditions, the flow in the experiment is unstable to a Kelvin-Helmholtz instability of a free shear layer. The eigenmodes are nonaxisymmetric and rotate with respect to the outer cylinder, producing measurable velocity fluctuations with a dominant frequency determined by the rotation rate. These results were first published in a limited form in Roach et al. [2012].

The first section of this chapter describes the conditions under which the Kelvin-Helmholtz instability is observed. The second section describes the characteristics of the unstable mode near marginal stability, and the third section describes the instability far from marginal stability in the magnetized case, with $\Lambda \gg 1$. A comparison of the measurements to the linear instability analysis of a free shear layer is deferred to Chapter 6.

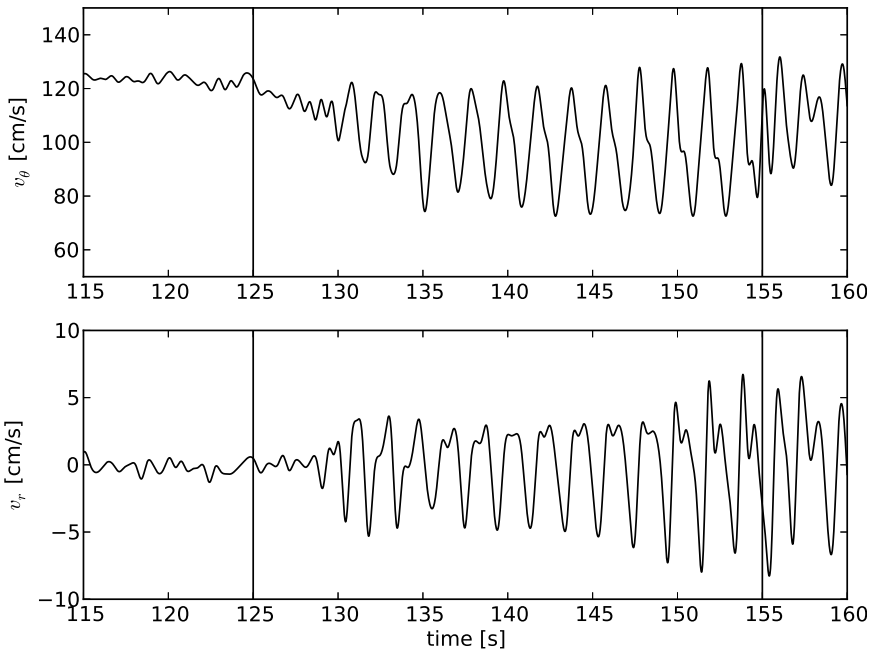

Figure 5.1: Example timeseries of velocity fluctuations during flow destabilization with applied magnetic field, measured at $r = 18$ cm for `MRI-Z 10%` configuration with $B = 3440$ Gauss. The vertical lines indicate the start and the end of the application of the magnetic field.

5.1 Destabilization criteria for the Kelvin-Helmholtz instability

5.1.1 Destabilization with magnetic field

Starting with both hydrodynamically stable and hydrodynamically unstable background rotation states, application of a sufficiently strong background magnetic field results in the appearance of the Kelvin-Helmholtz instability. In the case of the hydrodynamically unstable background, the application of the magnetic field results initially in the damping of the broadband fluctuations characteristic of the hydrodynamically unstable state, with the single-frequency Kelvin-Helmholtz instability growing up some time later. Figure 5.1 shows an example of these velocity fluctuations.

The amount of field required for the instability with the hydrodynamically stable `MRI-Z` background is shown in Figure 5.2. The Kelvin-Helmholtz unstable points are shown by

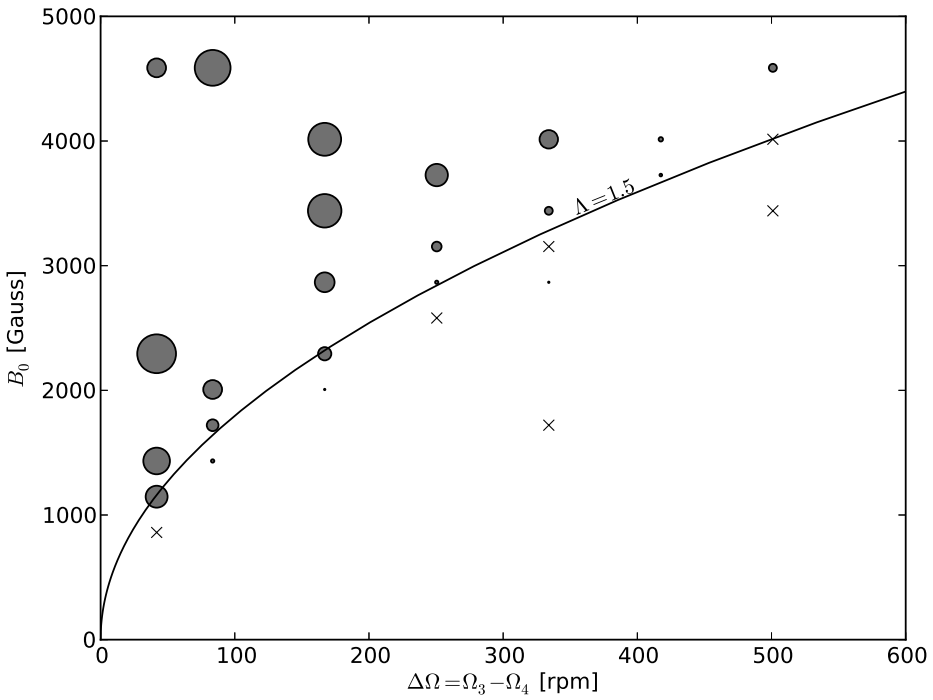

Figure 5.2: Measured Kelvin-Helmholtz instability space with an `MRI-Z` background. Area of circles are proportional to the power in the primary frequency band at saturation of the instability, normalized to the square of velocity jump at the inner-ring/outer-ring junction. 'X's indicate stability.

plotting a circle with area proportional to the power in a narrow band around the dominant frequency peak normalized to the square of the velocity jump between the inner and outer endcap rings, as is done for all such plots in this chapter. These calculations were made in all cases from the raw timeseries of velocity fluctuations measured by a tangential transducer at $r = 19$ cm, and thus represent a combination of v_θ and v_r velocity fluctuations. The boundary between the stable and unstable regions occurs at a constant Elsasser number defined using the difference between the inner ring and outer ring rotation rates, $\Lambda = B_0^2/4\pi\rho\eta(\Omega_3 - \Omega_4)$. Note that the transition region is gradual, with the saturated amplitude tending to grow with increasing B_0 above the stability boundary.

For the `split-unstable` configuration, the instability region was measured over a much broader range of rotation rates, spanning more than 3 orders of magnitude from $\Omega_1 = \Omega_3 = 0.25$ rpm at the low end, up to $\Omega_1 = \Omega_3 = 800$ rpm at the high end. This represents a range

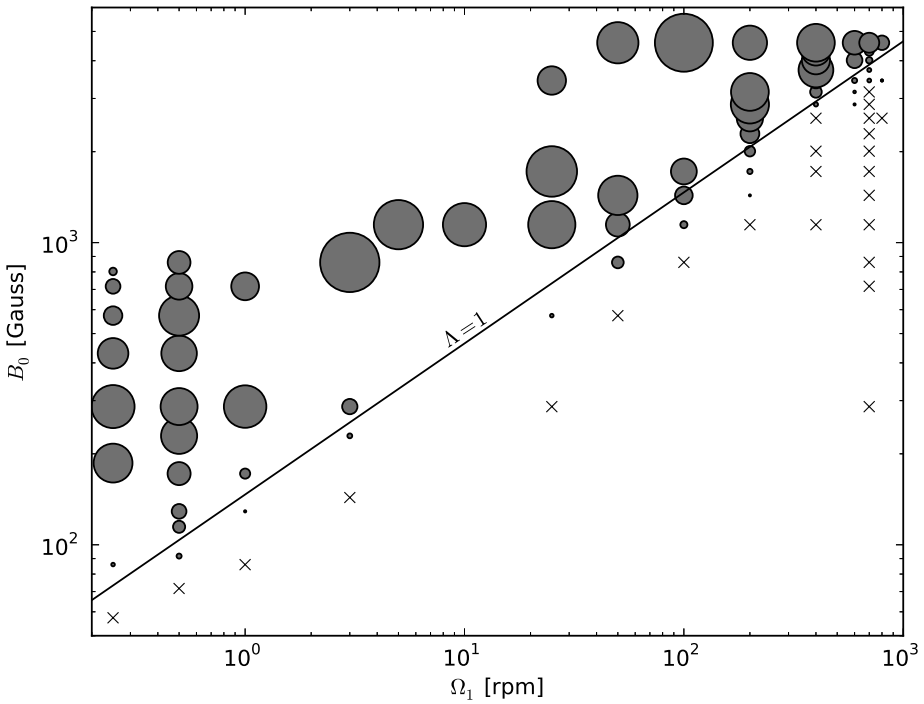

Figure 5.3: Measured Kelvin-Helmholtz instability space with a `split-unstable` background. Area of circles are proportional to the power in the primary frequency band at saturation of the instability, normalized to the square of the velocity jump at the inner-ring/outer-ring junction. 'X's indicate stability.

of Reynolds numbers from 820 to 2.6×10^6. The condition for instability again requires a minimum critical Elsasser number, as shown in Figure 5.3. Note that the absence of data points in the upper left of that plot is not in itself an indication of stability there. For each rotation rate there is a maximum magnetic field with which the instability can be studied because of the time limits caused by resistive heating of the magnet coils. But the decrease in saturated mode amplitudes with increasing field is a suggestion of a move toward stability, a topic that will be discussed further in Section 5.3.5.

5.1.2 Requirement of shear at axial boundary for instability

The effect of the shear at the inner-ring/outer-ring interface was investigated by starting with the `MRI-Z 10%` configuration and varying the inner ring speed Ω_3 from matching Ω_1 at the high end, to matching Ω_4 at the low end. The result on the stability threshold are

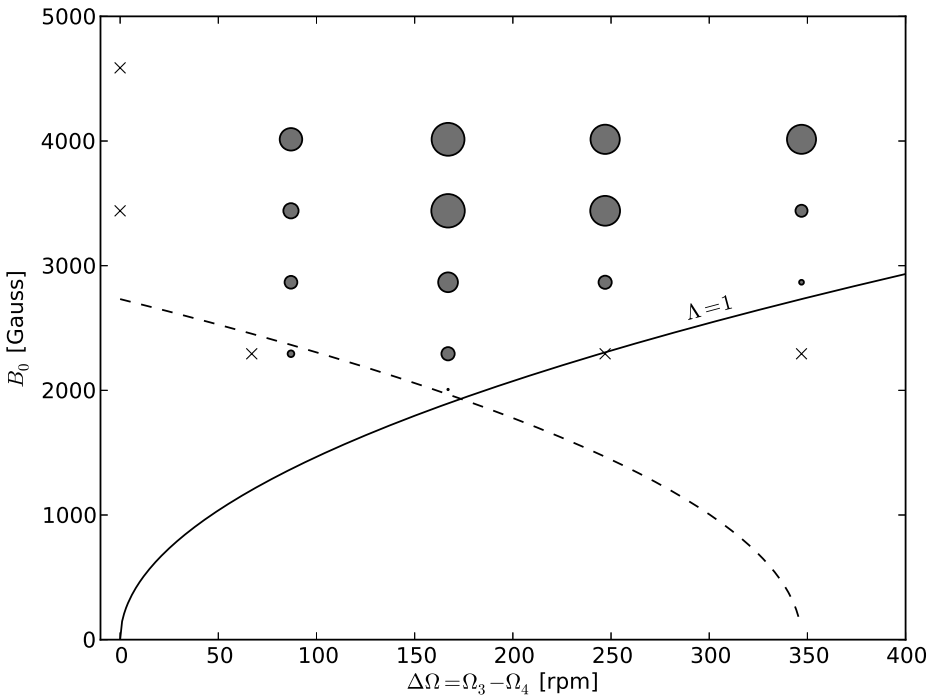

Figure 5.4: Effect of shear at the inner-ring/outer-ring interface on the Kelvin-Helmholtz instability. The base state is the `MRI-Z 10%` configuration, with the inner ring speed Ω_3 varied. The solid black line shows the constant Elsasser number $\Lambda = 1$ boundary. The dashed line shows a boundary for a modified Elsasser number $\Lambda = B_0^2/4\pi\rho\eta(\Omega_1 - \Omega_3) = 1$, defined by the difference between the inner cylinder and inner ring speeds, rather than the inner ring and outer ring speeds.

shown in Figure 5.4.

There is no instability for any magnetic field strength when the differential rotation between the endcaps is eliminated. When the differential rotation between the endcap components is small, the transition threshold does not follow the line of constant Elsasser number $\Lambda = B_0^2/4\pi\rho\eta(\Omega_3 - \Omega_4)$. Instead, it seems to follow a constant modified Elsasser number, written in terms of the differential rotation between the inner cylinder and inner ring $\Lambda = B_0^2/4\pi\rho\eta(\Omega_1 - \Omega_3)$. Although the data suggesting this are rather sparse, this does suggest a different mechanism for the development of the instability in these cases.

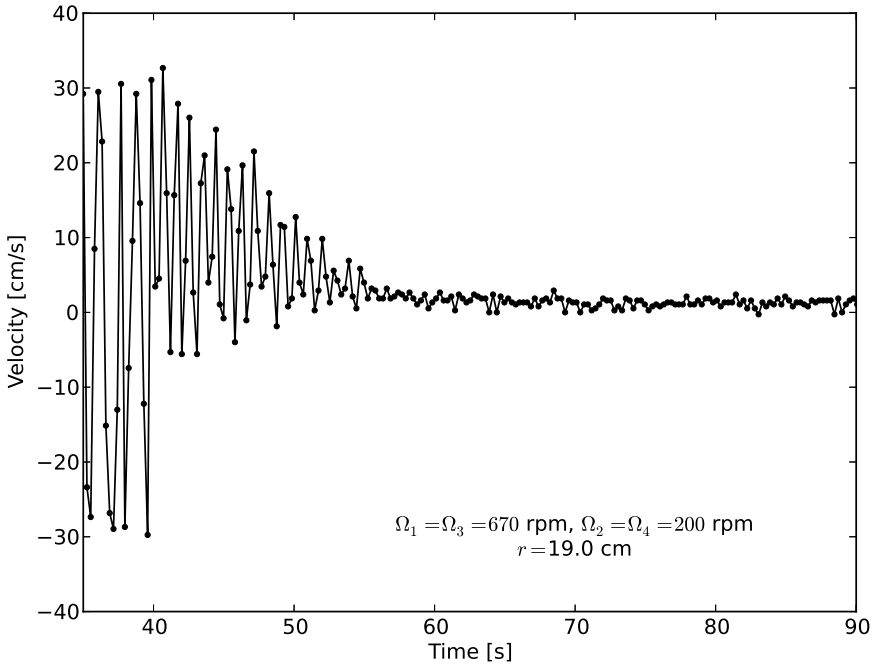

Figure 5.5: Timeseries of raw velocity measurement from a tangential transducer with $Ro = 2.35$.

5.1.3 Destabilization of `split` configuration with background rotation

The effects of background rotation were examined with component speeds rotating in the `split` configuration, with nonzero $\Omega_2 = \Omega_4$. With this configuration, the instability is observed when the outer cylinder rotation is sufficiently large compared to the differential rotation. The marginally stable state is characterized by a Kelvin-Helmholtz instability that is driven in the spin-up phase of the experiment, but is damped as the flow reaches full speed, as shown in Figure 5.5. The scaling of $\Delta\Omega$ with Ω_2 for this marginal state is shown in Figure 5.6, showing a critical Rossby number $Ro = \Delta\Omega/\Omega_2 = 2.35$.

5.1.4 Destabilization of `split` configuration with background rotation and magnetic field

Further experiments were conducted in the `split` configuration with $\Omega_2 \neq 0$ and with $B_0 \neq 0$. When adding a strong enough magnetic field to the marginally stable state with $Ro = 2.35$, the Kelvin-Helmholtz instability reappears. An example timeseries is shown in

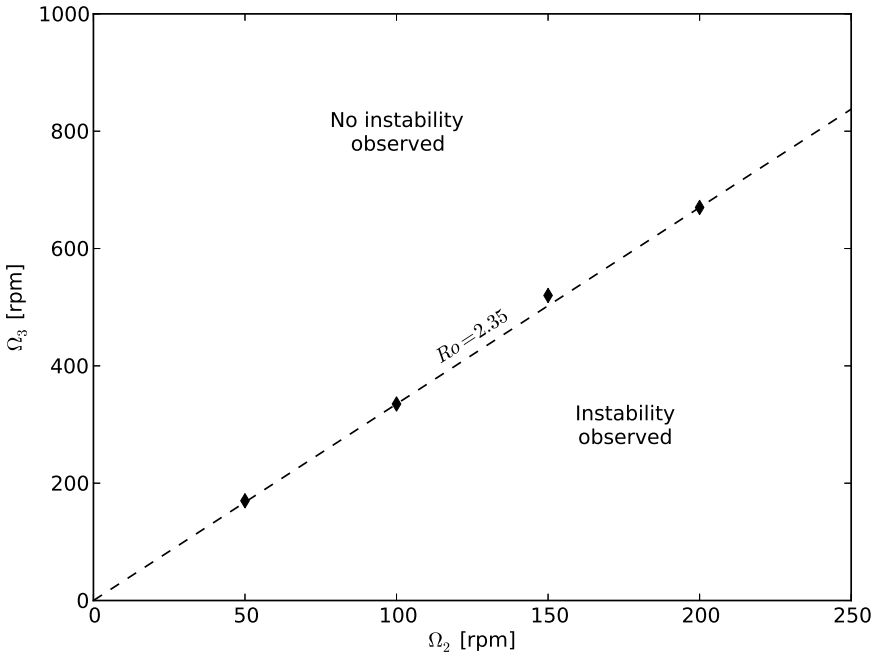

Figure 5.6: Kelvin-Helmholtz instability space in `split` configuration with $\Omega_2 \neq 0$. Experimentally determined marginal stability points are shown, with the line $Ro = \Delta\Omega/\Omega_2 = 2.35$ overplotted.

Figure 5.7.

The critical magnetic field for the cases with $Ro = 2.35$ is shown in Figure 5.8, following a line of constant Λ as in the magnetized cases with larger Ro shown at the beginning of this section.

There is some interesting behavior in the stability plot with constant Ω_2 and varying $\Delta\Omega$, shown in Figure 5.9. When $\Delta\Omega$ is small and the instability is present in the absence of a magnetic field, the addition of the magnetic field has no effect on the instability. The magnetic field can provoke the instability for the marginal case with $Ro = 2.35$, but it doesn't require a small amount of magnetic field to do so. It requires just as much field as if Ω_2 were zero.

5.1.5 Destabilization in cyclonic flow

The `cyclonic` configuration is an analog of the `split-unstable` configuration, but with the inner components at rest, $\Omega_1 = \Omega_3 = 0$, and the outer components rotating with $\Omega_4 = \Omega_2$. It

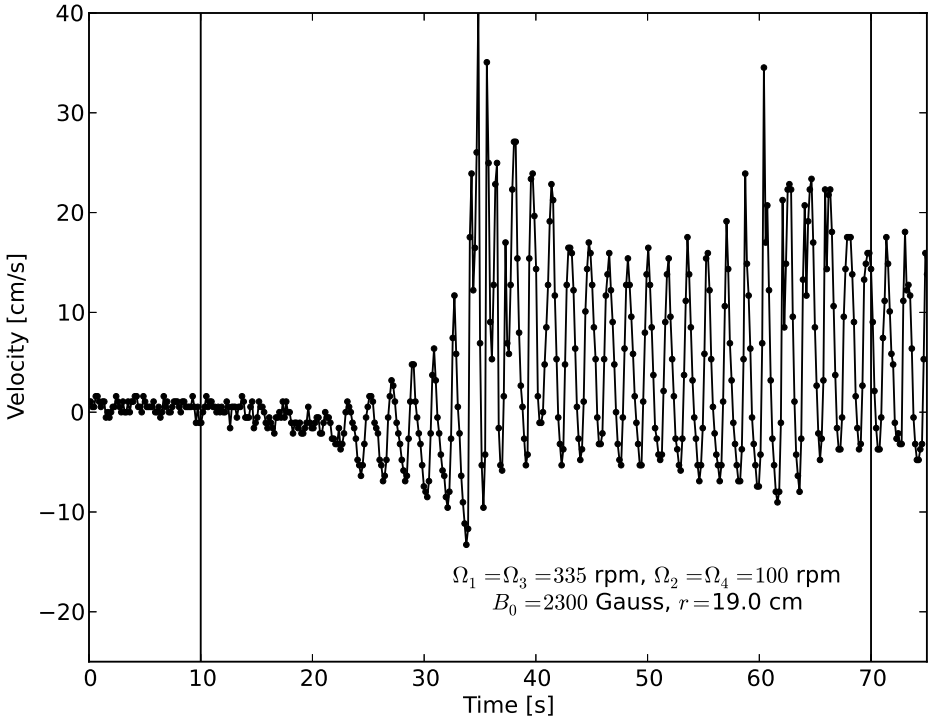

Figure 5.7: Timeseries of velocity fluctuations in the `split` configuration with $Ro = 2.35$ and $\Lambda > 1$. Measurements are the raw velocity measured by a tangential transducer at $r = 19$cm. The magnetic field is applied in the region between the two vertical lines.

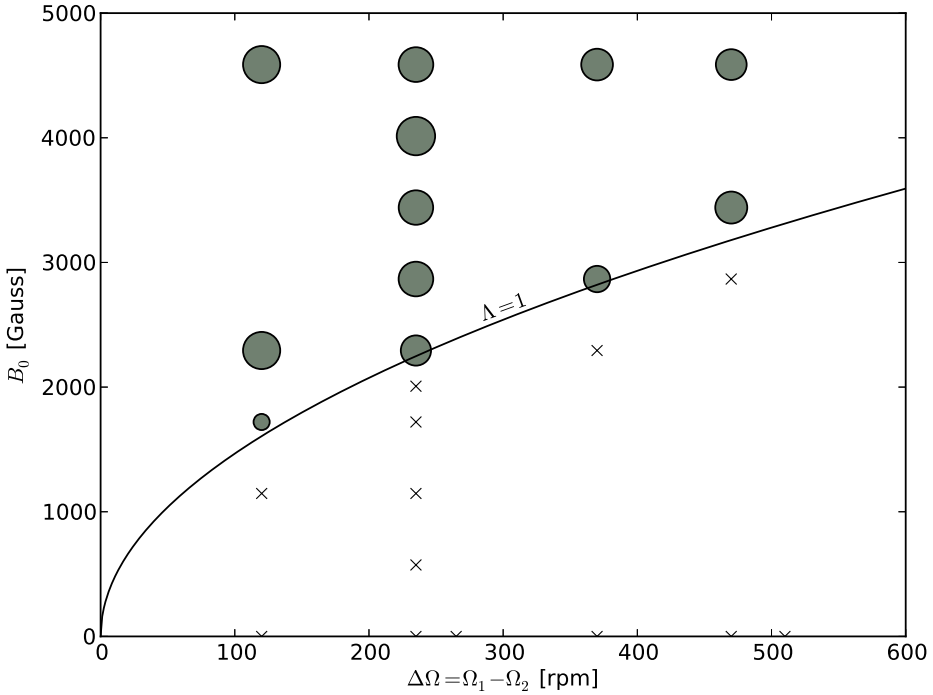

Figure 5.8: Kelvin-Helmholtz instability space in `split` configuration with fixed $Ro = 2.35$.

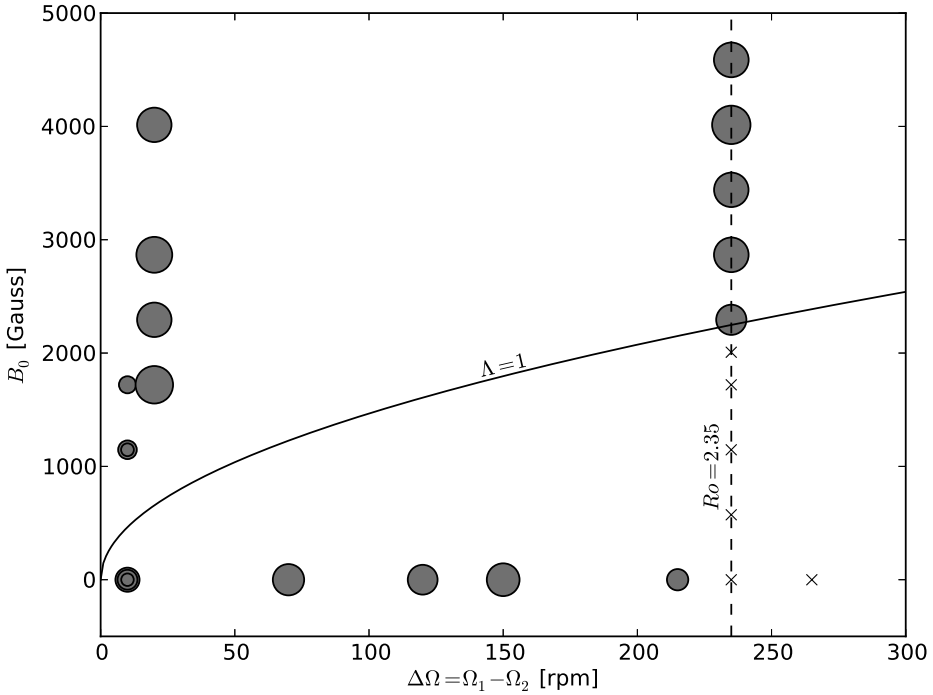

Figure 5.9: Kelvin-Helmholtz instability space in `split` configuration with fixed $\Omega_2 = 100$ rpm and varying B and $\Delta\Omega$. The Kelvin-Helmholtz instability is seen if $Ro < 2.35$ or $\Lambda > 1$.

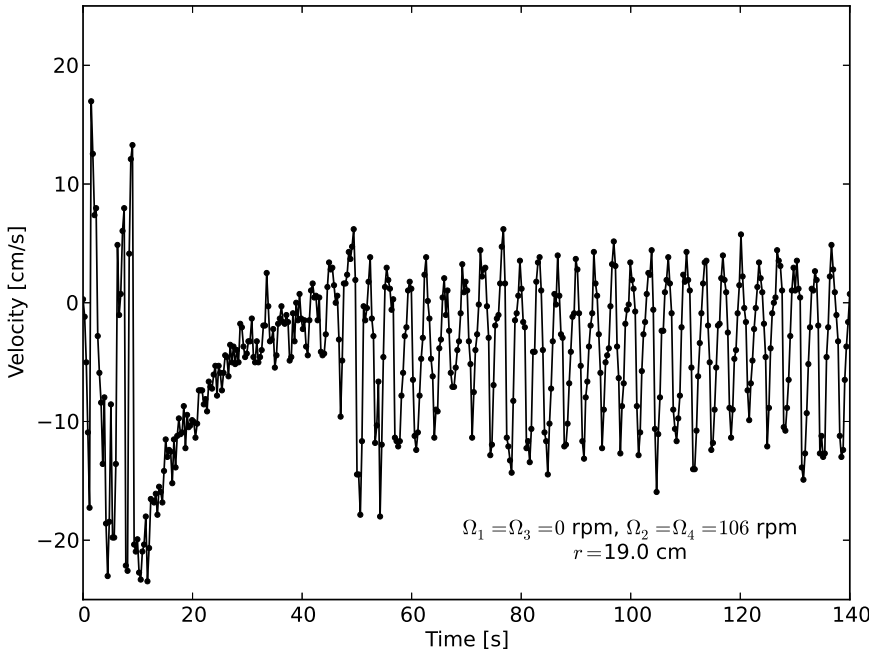

Figure 5.10: Timeseries of raw velocity measurements from a tangential transducer at $r = 19$ cm in the `cyclonic` configuration with $\Omega_1 = \Omega_3 = 0$ rpm and $\Omega_4 = \Omega_2 = 106$ rpm.

has the same amount of shear at the split between the axial endrings as the `split-unstable` configuration, but the angular momentum gradient is reversed. Experiments were carried out with $\Omega_4 = \Omega_2 = 106$ rpm and $\Omega_4 = \Omega_2 = 26.5$ rpm. In the `cyclonic` configuration, the instability is observed with *no* magnetic field applied, with an example timeseries shown in Figure 5.10. The instability appears as the flow is spinning up, and continues to be vigorously unstable when the flow reaches full speed. Application of a magnetic field up to 4000 Gauss, the maximum examined, had no effect on the instability in these cases.

5.2 Instability characteristics near marginal stability

As we have seen, the onset of the instability is characterized by large-amplitude velocity fluctuations. Figure 5.11 shows the effect on the azimuthal and radial velocity profiles.

The power spectrum of the fluctuations measured by a transducer show a single dominant frequency at saturation as shown in Figure 5.12. The square root of the power at this frequency in each of the velocity components v_r and v_θ can be plotted as a function of

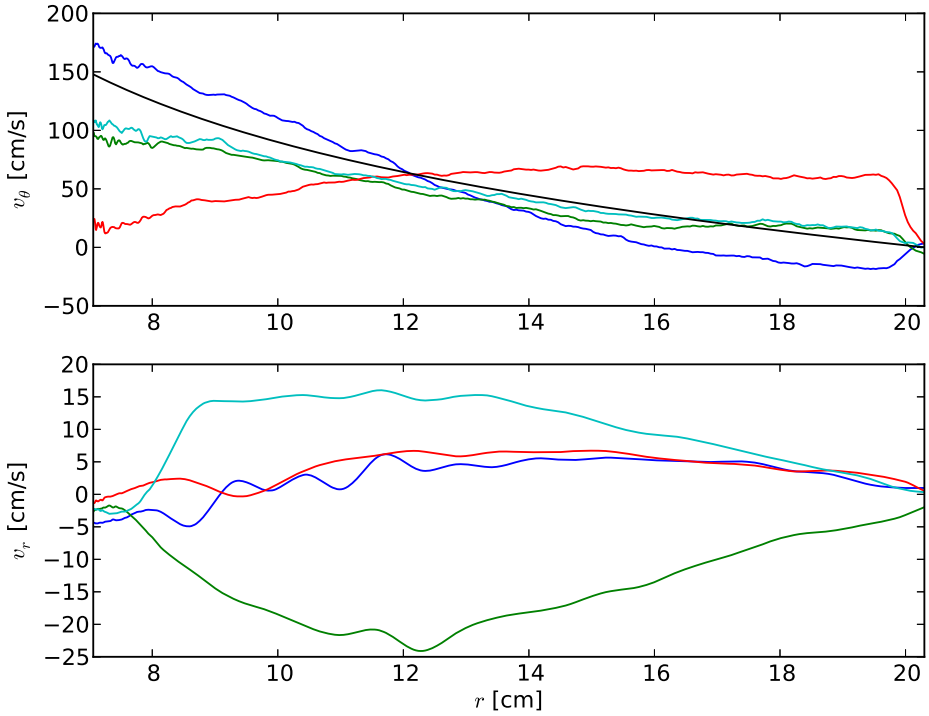

Figure 5.11: Effect of instability on v_θ and v_r profiles in the `Split-unstable` configuration with $\Omega_1 = 200$ rpm, and $B_0 = 3440$ Gauss.. Curves represent four independent measurement, each separated by 1/4 of an oscillation period in time. The black line in the v_θ plot indicates the ideal Couette rotation profile for these inner and outer cylinder speeds.

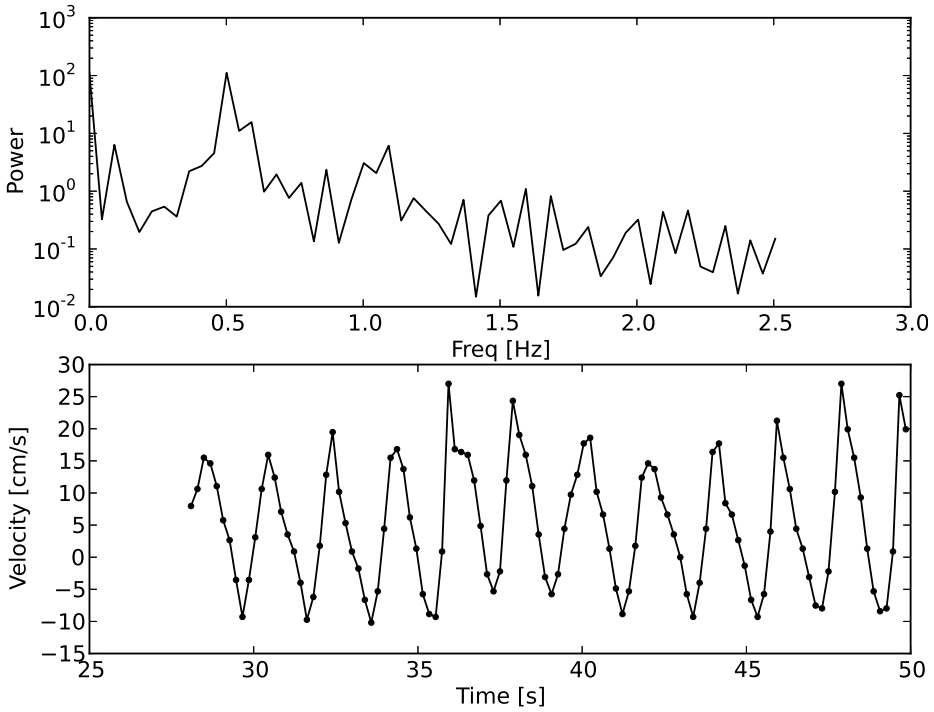

Figure 5.12: Power spectrum of velocity fluctuations during saturation of the instability for the `split-unstable` configuration with $\Omega_1 = 200$ rpm and $B = 3440$ Gauss. A single frequency is dominant, with a hint of a second harmonic with less power.

radius to give information about the radial structure of the velocity fluctuations, as shown in Figure 5.13. The fluctuation in v_θ is peaked near the inner and outer cylinders, going nearly to zero in the middle of the experiment. The opposite is true for the fluctuation of v_r, which peaks in the middle.

Using two transducers aimed identically but separated by $\pi/2$ in azimuth, azimuthal phase information about the fluctuations can be obtained. As shown in Figure 5.14, the two transducers record the fluctuation with a $\pi/2$ phase difference at saturation, suggesting an $m = 1$ mode structure, although it appears that a larger azimuthal mode number is dominant before saturation.

5.2.1 Mode structure

Once the azimuthal mode number, and therefore the time for the mode structure to complete one rotation, is known, it is possible to use the measurements by the UDV diagnostic to

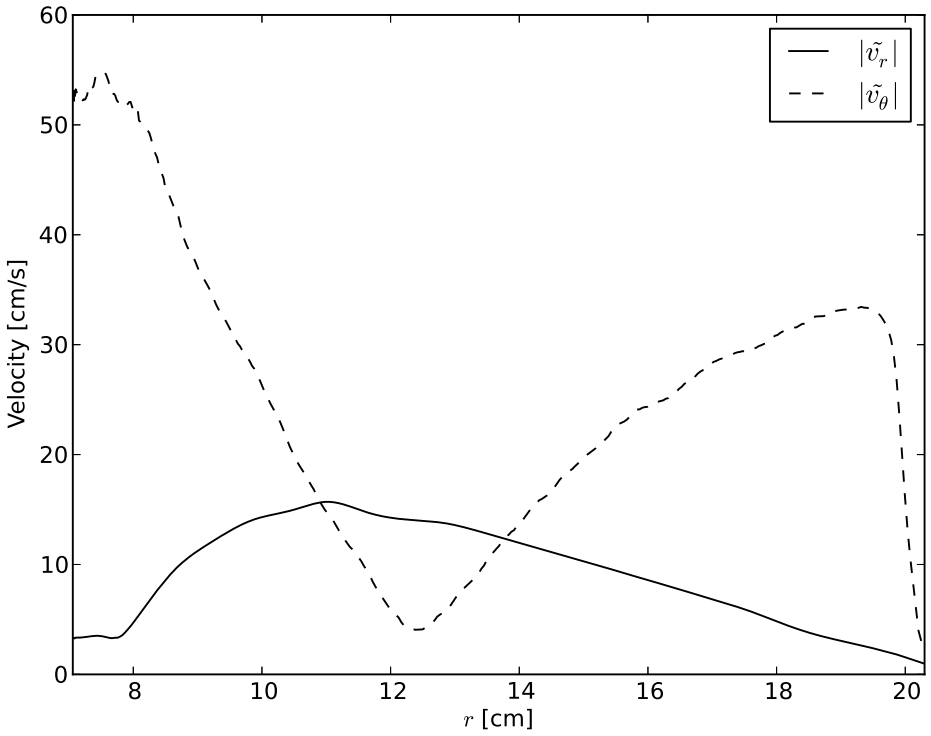

Figure 5.13: Velocity fluctuation amplitude as a function of radius for the `split-unstable` configuration with $\Omega_1 = 200$ rpm and $B_0 = 3440$ Gauss. The amplitude is calculated from the square root of the measured power for each velocity component at each radius, appropriately normalized to correspond to the actual velocity fluctuation amplitude in cm/s.

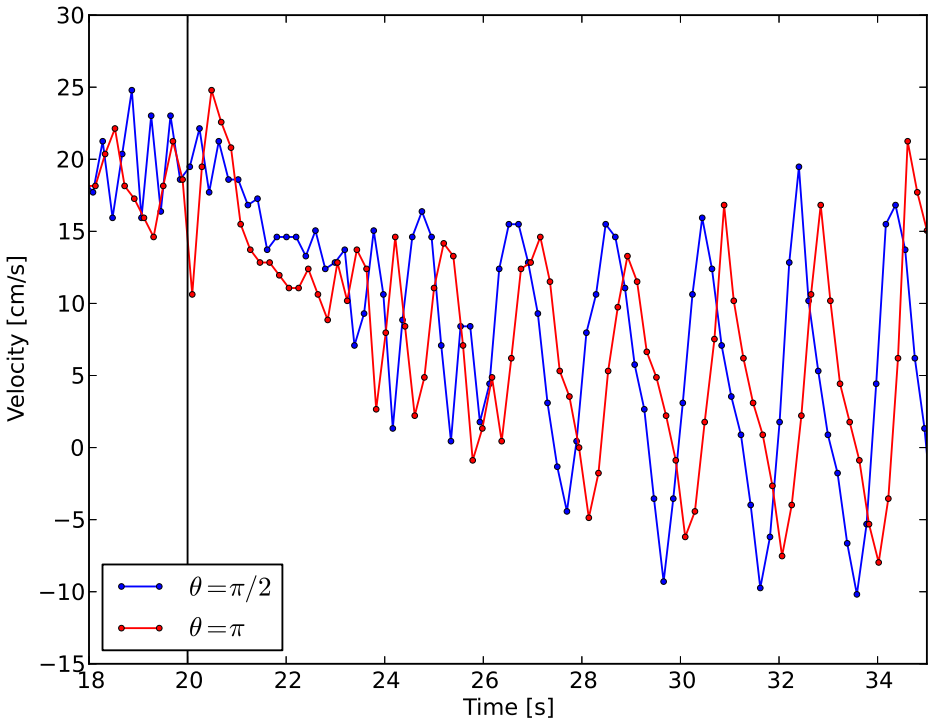

Figure 5.14: Example timeseries of raw velocity measurements during flow destabilization in the `Split-unstable` configuration with $\Omega_1 = 200$ rpm and $B_0 = 3440$ Gauss. Time traces show measurements from two tangential transducers at the midplane with $\theta = \pi/2$ (*blue*), and $\theta = \pi$ (*red*). The black vertical line indicates the turn on of the magnetic field.

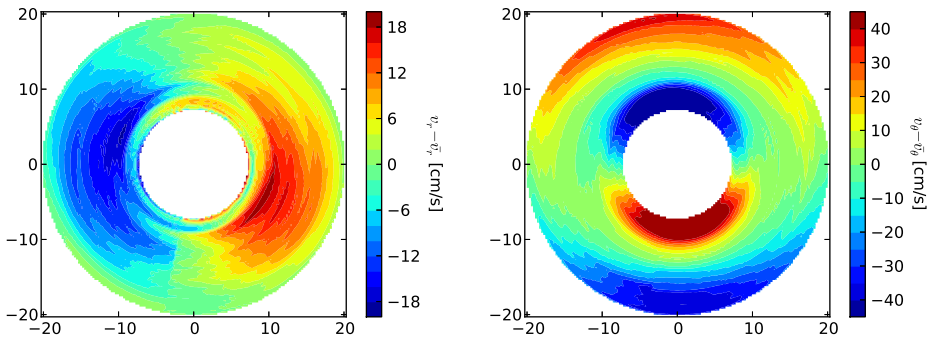

Figure 5.15: Typical $m = 1$ mode structure near $\Lambda = 1$ stability boundary. The mode was reconstructed by measurements from two UDV transducers during the saturated phase of the instability, with the mean $m = 0$ contribution at each radius subtracted off, leaving only the fluctuating velocity contribution. `Split-unstable` configuration with $\Omega_1 = 400$ rpm and $B_0 = 4000$ Gauss, for $\Lambda = 1.9$.

reconstruct the mode structure. As the mode rotates by, a measurement at some time corresponds to a particular point in the mode phase. By projecting the timeseries of velocity measurements onto the $r - \theta$ plane, the mode structure can be visualized, taking care to account for the different azimuthal locations of the transducers used to perform the reconstruction as discussed in Chapter 3. In all of the plots of the mode structures that follow, the $m = 0$ component (determined from the mean of the velocity timeseries) at each radius is subtracted, leaving only the fluctuating part of each velocity component.

The mode structure near the $\Lambda = 1$ stability threshold is typified by Figure 5.15. The mode is m=1, and consists of two large circulation cells that fill the gap between the two cylinders.

5.2.2 Axial structure

Two identically aimed transducers mounted at the same azimuthal location at $z = 14.5$ cm (the midplane) and $z = 3$ cm were used to investigate the axial structure of the unstable mode. As shown in Figure 5.16, measurements at the two axial locations are almost identical, having the same magnitude and phase of oscillations, even replicating the features caused by higher-order azimuthal mode numbers quite well. This suggests that there is almost no axial dependence on the unstable mode structure in the bulk of the fluid, although

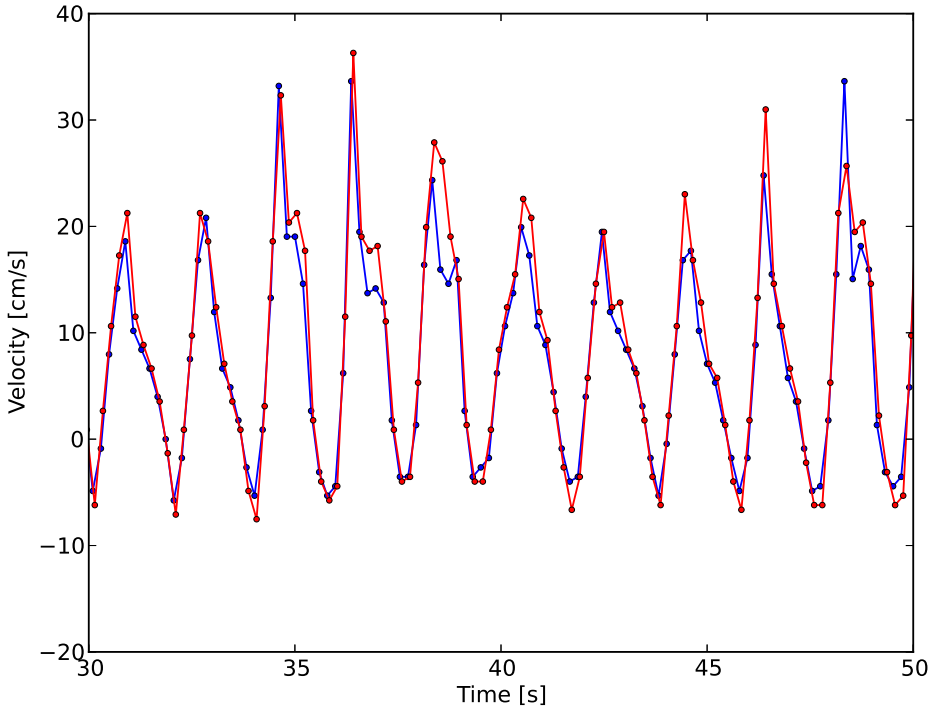

Figure 5.16: Comparison of raw velocity timeseries during the instability from two identically aimed transducers mounted at the same azimuthal location but different axial positions. *Blue:* Raw velocity measurement at $z = 14.5$ cm (midplane). *Red:* Raw transducer signal at $z = 3$ cm.

there must certainly be axial structure near the boundary as the velocity transitions to that required by the no-slip boundary condition.

5.2.3 Correlated fluctuations in v_z

Using the normal transducer arrangement, only fluctuations in v_θ and v_r can be measured. To determine the amount of correlated fluctuation in v_z, an ultrasound transducer was mounted on the end of a rod with its projected beam extending perpendicular to the rod. The rod passed through a port plug at the midplane of the experiment, where it was sealed with an o-ring. The o-ring seal permitted the rod to be rotated and to be translated radially. Measurements were made at radii of 11, 12, 13, 14, and 15 cm, all with the outer cylinder fixed. Before each measurement of the unstable mode, the probe rotation angle was adjusted until a pair of shots with forward and backward rotation indicated no bias in

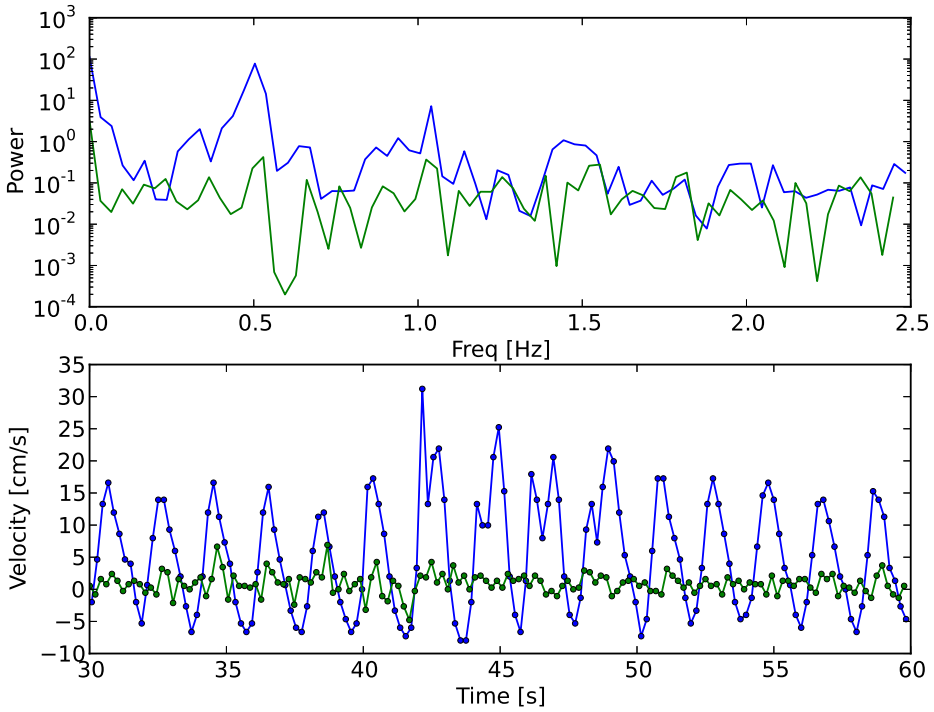

Figure 5.17: Measurement of the amount of correlated v_z fluctuation of the unstable mode. *Top*: power spectra, and *bottom*: timeseries of raw measurements from a tangentially-aimed transducer (*blue*), and a transducer mounted on a rod and aimed axially at $r = 15$ cm (*green*). Measurements are 2 cm from the face of the transducer in both cases.

the beam orientation that would cause the transducer to pick up a contribution from v_θ.

No correlated fluctuations were evident by examination of the timeseries or examination of the power spectra at any of the measured radii or at any distance from the transducer. An example power spectrum and timeseries are shown in Figure 5.17. The noise floor of the measurements limits the constraint that can be placed on the fluctuating axial velocity to $\tilde{v_z} < 0.05\tilde{v_\theta}$.

The addition of the stationary rod resulted in a reduction in the mean azimuthal velocity because of the additional drag on the fluid. The instability as measured by the permanent transducers seemed to be unfazed by this change, but it is worth noting nonetheless. If anything, we expect that the addition of the rod would mix some of the azimuthal flow into the axial direction, leading to an overestimate of the contribution of the fluctuating v_z. So we retain confidence in our bound on $\tilde{v_z}$ even though the act of measuring it perturbed the

flow.

5.2.4 Frequency of fluctuations

The frequencies of the unstable modes during the saturation phase were found by fitting the timeseries to a single frequency sinusoid, using the peak in the power spectrum as a starting value. Frequencies found by this method could be found more precisely than examining the power spectrum directly.

The frequency of one full rotation of the unstable mode is typically 10-20% of the difference between Ω_3 and Ω_4 as measured in the frame of the outer cylinder. Rotation rates for all of the unstable modes in the `MRI-Z` and `split-unstable` configurations are shown in Figure 5.18. There seems to be a general trend from lower rotation frequency near the stability boundary, increasing with magnetic field, although that is not universally true.

It must be noted that the frequency is not entirely reproducible even with the component rotation speeds and magnetic field reproduced as accurately as they can be. Frequencies can vary by up to 30% under seemingly identical conditions. The frequency during the saturated phase can also drift over the course of a shot by a slightly smaller amount. Since the modes seem to be advected by the flow, the frequency will depend on the precise character of that flow state, which is dependent on component rotation speeds, magnetic field, and to some extent the history of the development of that flow.

5.3 Instability in high-Λ regime

The high-Λ regime was explored using very slow rotation in the `split-unstable` configuration. Significant changes from the behavior near the marginal stability curve were found for $\Omega_1 = 0.5$ and $\Omega_1 = 0.25$ rpm. Because of the extremely long timescales with such slow rotation, full exploration of the instability could only be performed for magnetic fields below 800 Gauss, which could be sustained in the steady state. But even this relatively modest field allowed experiments up to $\Lambda = 120$.

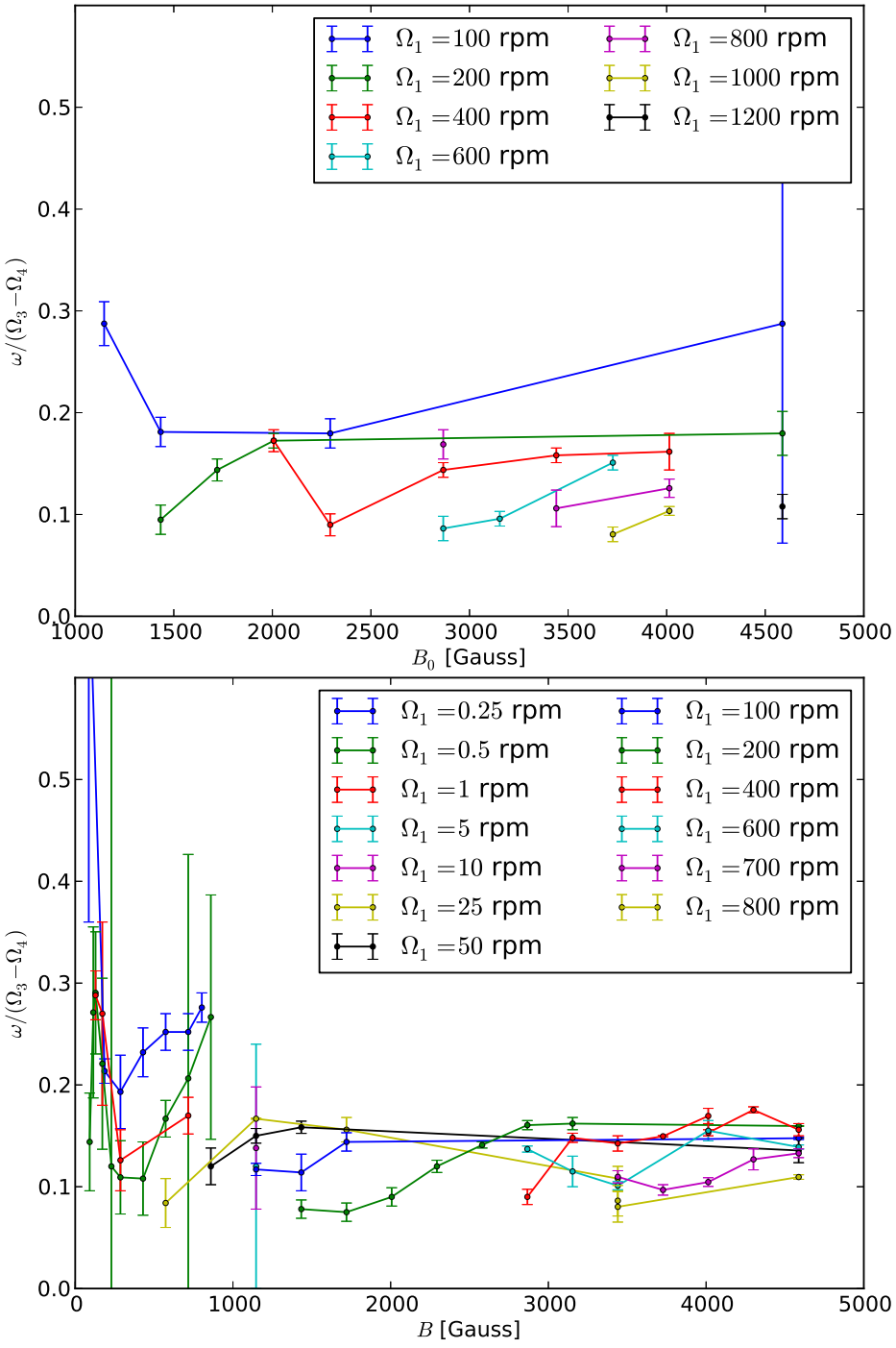

Figure 5.18: Unstable mode frequencies in the `MRI-Z` configuration (*top*) and `split-unstable` configuration (*bottom*). Frequencies are normalized by the difference between the inner ring and outer ring speeds, and are reported in the frame of the outer cylinder.

5.3.1 Saturated shear layer width

As shown in Chapter 4, the azimuthal velocity profiles for $\Lambda \gg 1$ are those of free shear layers penetrating throughout the experiment. The scaling of the shear layer width was investigated there by fitting a hyperbolic tangent shear layer model to the measured angular velocity profiles, with the time evolution of the shear layer half width w_l for one shot shown in Figure 4.14. It was noted that the average shear layer width decreased with the onset and saturation of the instability.

The initial (before onset of the instability) and final (at instability saturation) shear layer widths are plotted in Figure 5.19 for the range of B_0 for which there was sufficient time to observe the instability. The values are also tabulated in Table 5.1. The saturation of the instability is associated with the broadening of the shear layer in all cases. While the initial shear layer width is independent of Ω_1, the saturated state exhibits larger w_l for larger Ω_1. Before the onset of the instability, the shear layer width is mediated by the viscous stress [Hunt and Shercliff, 1971], leading to a scaling in Hartmann number, $w_l \sim Ha^{-0.5}$, which has no dependence on the rotation rate. In other words, $\sqrt{B_0 L} w_l/(4\pi\rho\eta\nu)^{1/4}$ is constant. We could consider writing this relation in terms of the Reynolds stress rather than the viscous stress, balancing the $\vec{j} \times \vec{B}$ force with the inertial force due to the instability. We can replace $\nu r \Delta\Omega / w_l^2$, the viscous force associated with the shear layer, with the characteristic inertial force $r^2 \Delta\Omega^2 / w_l$ to find that $\sqrt{B_0 L} w_l^{3/4}/(4\pi\rho\eta r \Delta\Omega)^{1/4}$ is constant for the shear layer mediated by Reynolds stress. We note the appearance of the Elsasser number in this expression instead of the Hartmann number, suggesting that $w_l \sim \Lambda^{-1/3}$ in the presence of the Kelvin-Helmholtz instability. The shear layer width versus $\Lambda^{-1/3}$ is plotted in Figure 5.20. This scaling eliminates the differences between the 0.25 rpm and 0.5 rpm measurements at the midplane, and the measurements lie roughly along a line, suggesting that this scaling is capturing some of the physics. But this is a simplistic model and leaves out several potentially very important effects, including the changing Reynolds stress with changing mode structure, and the influence of viscous stress for small shear layer widths.

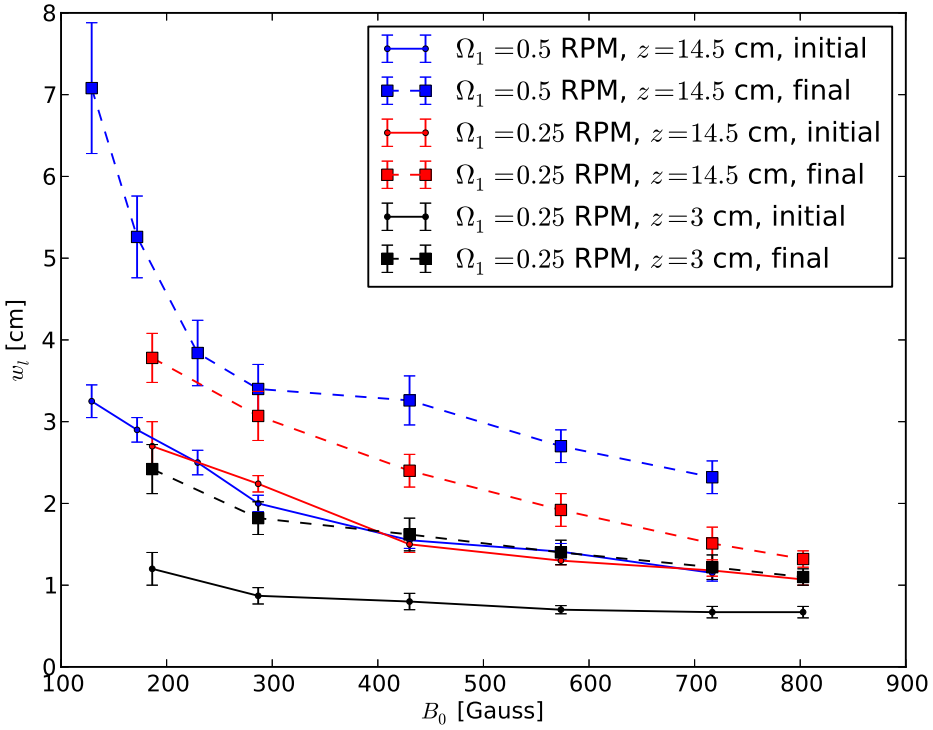

Figure 5.19: w_l versus B_0 in the $\Lambda \gg 1$ regime. "Initial" values are the values before the onset of instability, and "final" values are the values at saturation of the instability.

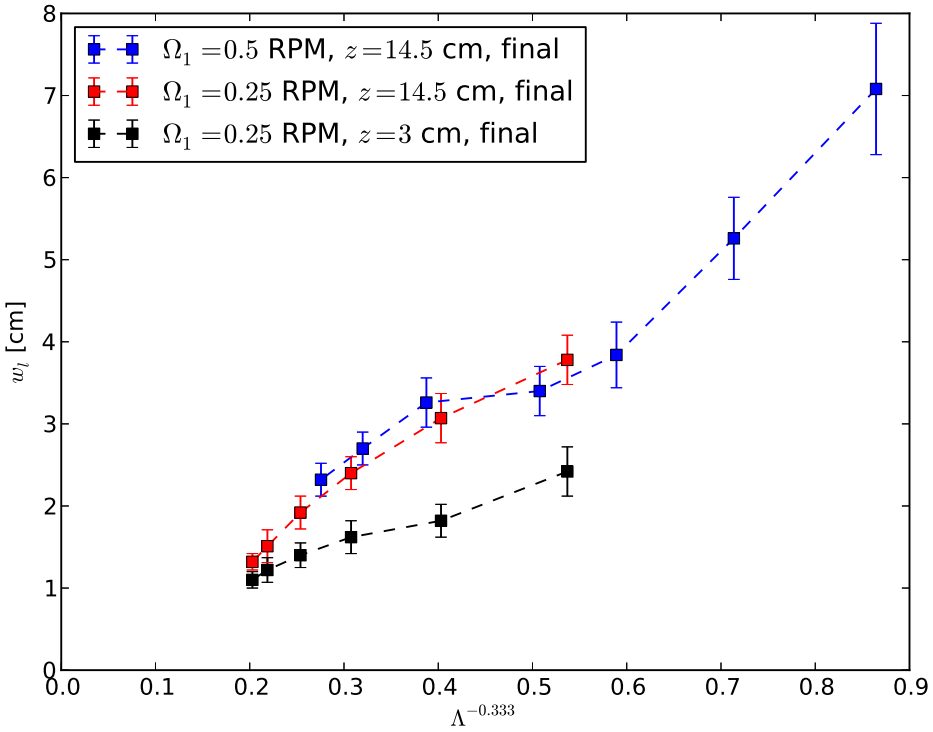

Figure 5.20: w_l versus $\Lambda^{-1/3}$ in the presence of the Kelvin-Helmholtz instability in the $\Lambda \gg 1$ regime.

5.3.2 Azimuthal mode number

The azimuthal mode number m is determined by the phase of the oscillating velocity measured by two identically aimed tangential transducers located at $\theta = \pi/2$ and $\theta = \pi$ at the midplane of the experiment. Because the mode structures tend to be dominated by a single azimuthal mode number, the mode number can often be determined rather easily by inspection of the timeseries, as in Figures 5.21 and 5.22.

A more formal approach to determining the azimuthal mode number uses the auto-correlation of one of the channels, $v_1 \star v_1$ or $v_2 \star v_2$, and the cross-correlation between the two channels, $v_2 \star v_1$, where v_1 is the velocity from the transducer with $\theta = \pi/2$, and v_2 from the transducer with $\theta = \pi$. For a mode with a single dominant azimuthal mode number, the auto-correlation time $\tau_{\rm ac}$ is the time for the mode to rotate by $2\pi/m$ radians, so the phase speed $d\Theta/dt = 2\pi/m\tau_{\rm ac}$. The cross-correlation time $\tau_{\rm cc}$ is the time for the mode rotate by $\pi/2$ radians, so the phase speed $d\Theta/dt = \pi/2\tau_{\rm cc}$. Equating the phase speeds, we find m in terms of $\tau_{\rm ac}$ and $\tau_{\rm cc}$,

$$m = \frac{4\tau_{\rm cc}}{\tau_{\rm ac}} \tag{5.1}$$

An example of the auto-correlation and cross-correlation functions for these measurements in shown in Figure 5.23. The measured correlation times and the associated azimuthal mode numbers for several rotation rates and magnetic fields are in Table 5.1.

It is important to note that since the cross correlation function is periodic with period $\tau_{\rm ac}$, it is not possible to distinguish $m = 4\tau_{\rm cc}/\tau_{\rm ac}$ from $m = 4(\tau_{\rm cc} + n\tau_{\rm ac})/\tau_{\rm ac} = 4\tau_{\rm cc}/\tau_{\rm ac} + 4n$, where n is any integer. We can only determine the azimuthal mode number modulo 4, so, for example, the same phase differences that would arise from a signal with $m = 2$ could also arise from a signal with $m = 6$.

But we have faith in the reported azimuthal mode numbers. As will be shown later, simulations and theory suggest strongly that the saturated mode number near $\Lambda = 1$ is $m = 1$. And the increase in mode number with increasing Λ at a single rotation rate can be tracked with increasing B_0, showing an increase in rotation frequency roughly proportional to the increase in m.

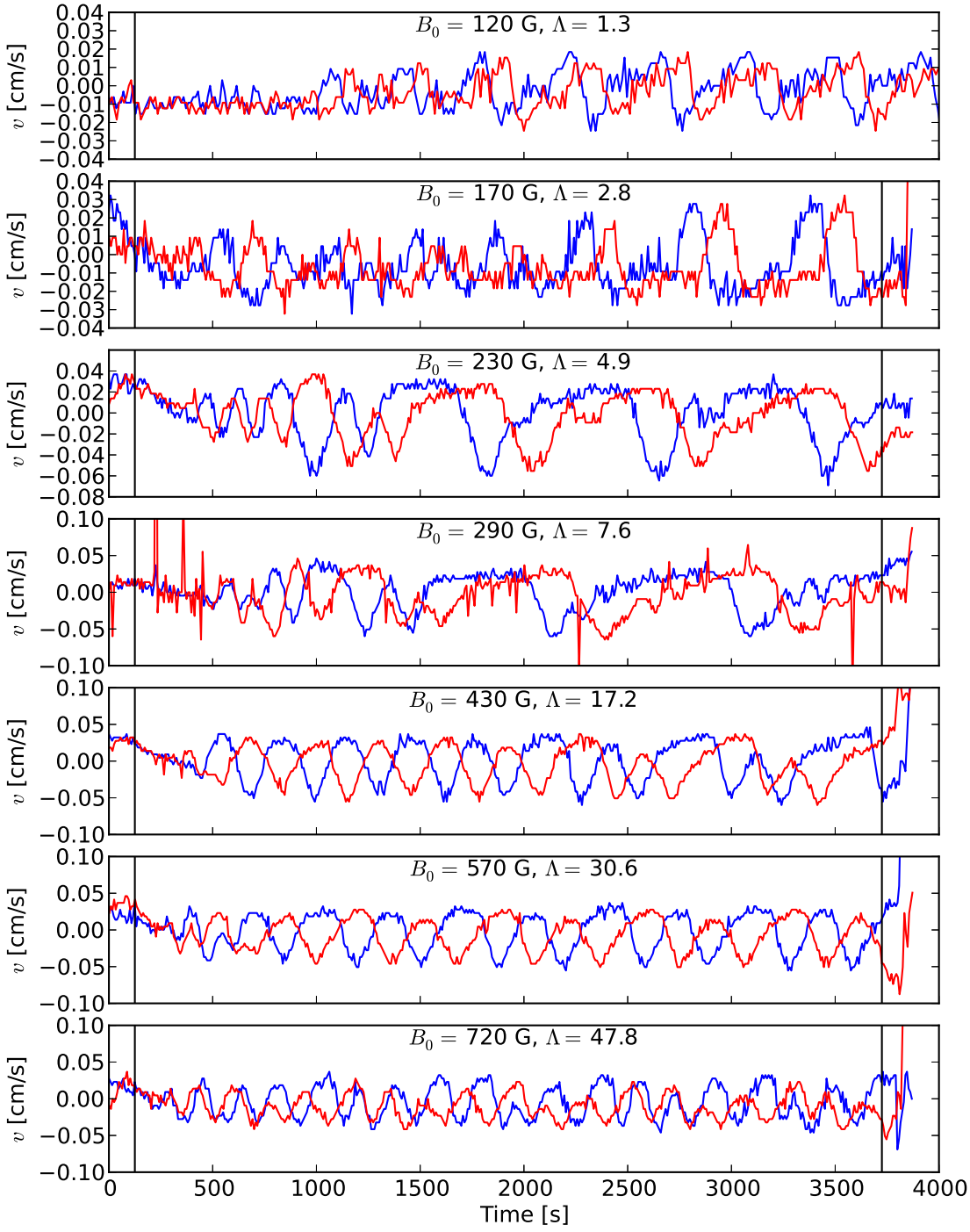

Figure 5.21: Raw velocity timeseries for `split-unstable` configuration with $\Omega_1 = 0.5$ rpm. Velocities are measured at $r = 17$ cm by two tangential transducers located at the midplane at $\theta = \pi/2$ (*blue*) and $\theta = \pi$ (*red*). The phase of the two signals is an indication of the azimuthal mode number.

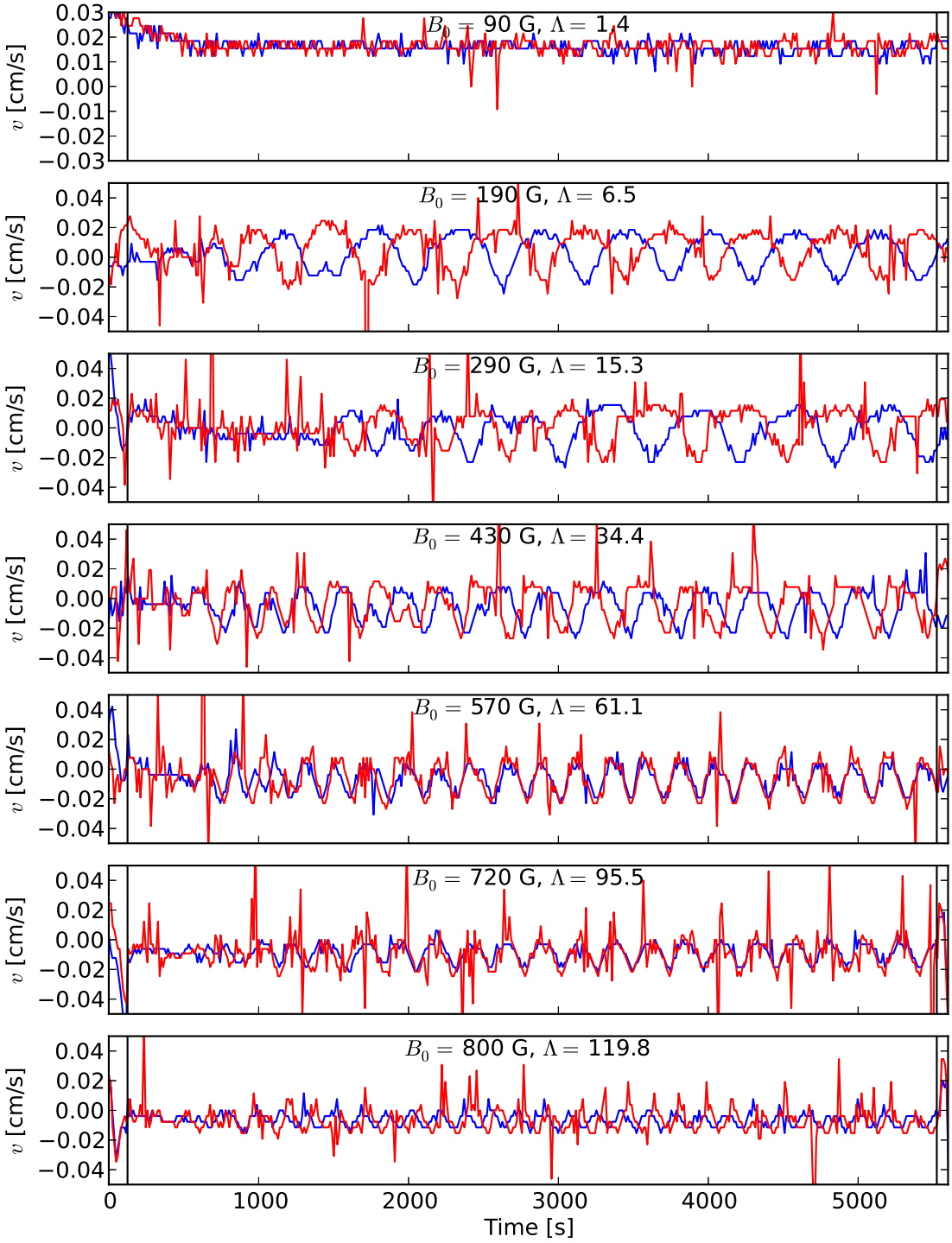

Figure 5.22: Raw velocity timeseries for `split-unstable` configuration with $\Omega_1 = 0.25$ rpm. Velocities are measured at $r = 17$ cm by two tangential transducers located at the midplane at $\theta = \pi/2$ (*blue*) and $\theta = \pi$ (*red*). The phase of the two signals is an indication of the azimuthal mode number.

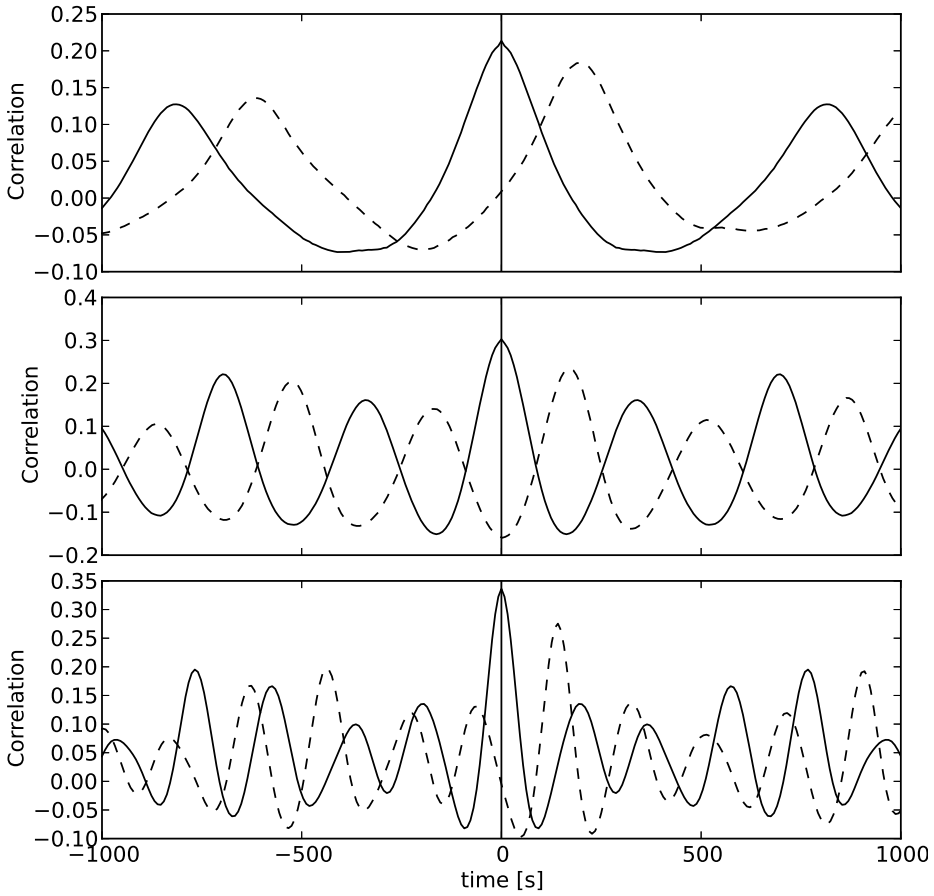

Figure 5.23: Example auto-correlation (*solid*) and cross-correlation (*dashed*) functions for raw velocity measurements at $r = 17$ cm by two tangential UDV transducers mounted at the midplane at $\theta = \pi$ and $\theta = \pi/2$. Examples show several different azimuthal mode numbers: *top*: $m = 1$, *middle*: $m = 2$, and *bottom*: $m = 3$.

Shot number	Ω_1 [rpm]	B_0 [G]	Λ	τ_{ac} [s]	τ_{cc} [s]	m	w_l [cm] $z = 14.5$ cm initial	$z = 14.5$ cm final	$z = 3$ cm initial	$z = 3$ cm final
1221	1	130	0.77	N/A	N/A	1	N/A	N/A	N/A	N/A
1193	1	290	3.8	428	99	1	N/A	N/A	N/A	N/A
1215	1	720	24	331	81	1	N/A	N/A	N/A	N/A
1198	0.5	120	1.3	418	98	1	3.3	7.1	N/A	N/A
1207	0.5	170	2.8	540	125	1	2.9	5.3	N/A	N/A
1208	0.5	230	4.9	817	197	1	2.5	3.8	N/A	N/A
1206	0.5	290	7.6	920	225	1	2.0	3.4	N/A	N/A
1209	0.5	430	17	660/300	160	1/2	1.5	3.2	N/A	N/A
1210	0.5	570	31	339	170	2	1.4	2.7	N/A	N/A
1200	0.5	720	48	198	141	3	1.3	2.3	N/A	N/A
1227	0.25	86	1.4	N/A	N/A	1	N/A	N/A	N/A	N/A
1228	0.25	190	6.5	558	270	2	2.7	3.8	1.2	2.4
1233	0.25	290	15	605	293	2	2.2	3.1	0.9	1.8
1231	0.25	430	34	348	252	3	1.5	2.4	0.8	1.6
1232	0.25	570	61	233	228	4	1.3	1.9	0.7	1.4
1229	0.25	720	96	235	238	4	1.2	1.5	0.7	1.2
1235	0.25	800	120	172	41	5	1.1	1.3	0.7	1.1

Table 5.1: Characteristics of the Kelvin-Helmholtz instability in the $\Lambda \gg 1$ regime for several different rotation speeds in the `split-unstable` configuration. τ_{ac} is the auto-correlation time for a velocity measurement at $r = 17$ cm from a single tangential transducer, and τ_{cc} represents the peak in the cross correlation between the measured velocity at $r = 17$ cm for two tangential transducers located at $\theta = \pi$ and $\theta = \pi/2$ at the midplane. Correlation times marked 'N/A' correspond to marginally unstable shots in which the signals were too weak for a proper correlation analysis. Shot 1209 featured two mode numbers of nearly equal amplitude. The underlined quantities indicate the dominant τ_{ac} and m.

5.3.3 Mode structure

The mode structures for the high-Λ scenarios accessed at the slowest rotation speeds, shown in Figures 5.24 and 5.25, are much richer than the mode structures at higher speeds. The progression to larger azimuthal mode number with increasing Λ is evident. The presence of additional harmonics is also clear, particularly for the cases with $\Omega_1 = 0.5$ rpm.

The mode structures for $\Omega_1 = 0.25$ rpm are shown at the midplane, $z = 14.5$ cm, but also closer to the endcaps, at $z = 3$ cm, where those measurements are available. Even though the shear layer widths differ significantly at these different axial locations, the mode structures remain unchanged, with the exception that the measurements near the endcaps suffer from a bit less measurement noise. This is a further testament to the elongated and invariant nature of the unstable modes in the axial direction, and suggests that the effective shear layer width that dictates the dynamics of the instability may be an axial average.

5.3.4 Reynolds stress

In contrast to the mode structure at marginal stability where the v_r and v_θ components of the unstable mode are $\pi/2$ radians out of phase with each other, the mode structures in the $\Lambda \gg 1$ regime have significant in-phase components or v_r and v_θ, producing a measurable contribution to the Reynolds stress. The Reynolds stress component $\langle \tilde{v}_r \tilde{v}_\theta \rangle$ in this regime are plotted in Figure 5.26. All show a positive Reynolds stress, indicating positive radial angular momentum transport. For the $\Omega_1 = 0.5$ rpm case, there is a clear trend toward an increase in the magnitude and a decrease in the width of the peak of the Reynolds stress, except for the anomalous case with $\Lambda = 7.6$. The $\Omega_1 = 0.25$ rpm case seems to show an increase in the Reynolds stress from the smallest Λ case to the higher Λ cases, with a hint of a decrease in the Reynolds stress for the highest Λ. While the noise in the measurement makes this drop uncertain, such a drop may not be entirely unexpected as the viscous stress becomes more important with decreasing layer width at large Λ.

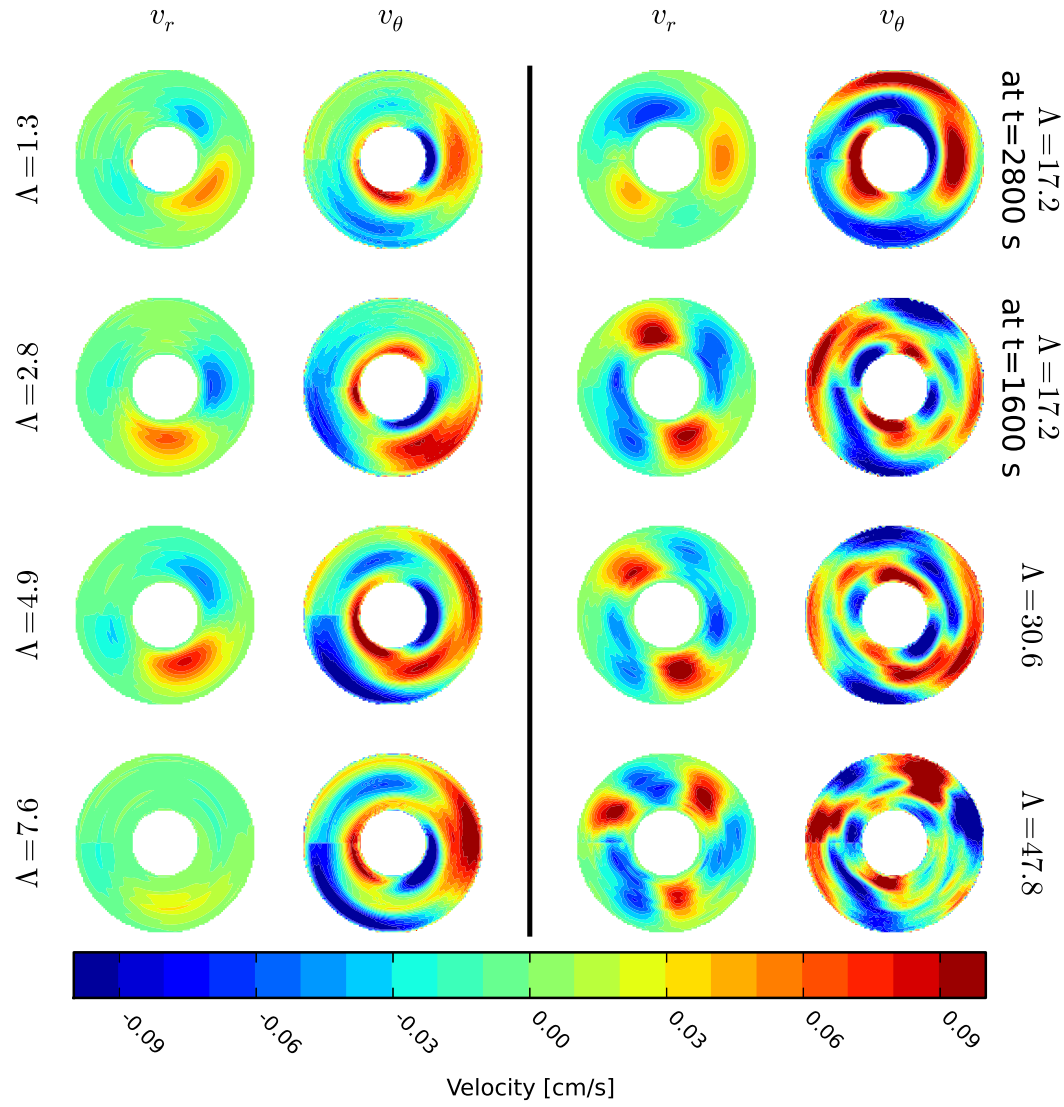

Figure 5.24: Measured mode structures for `split-unstable` configuration with $\Omega_1 = 0.5$ rpm and various B_0. All contour plots of velocity share a common color scale.

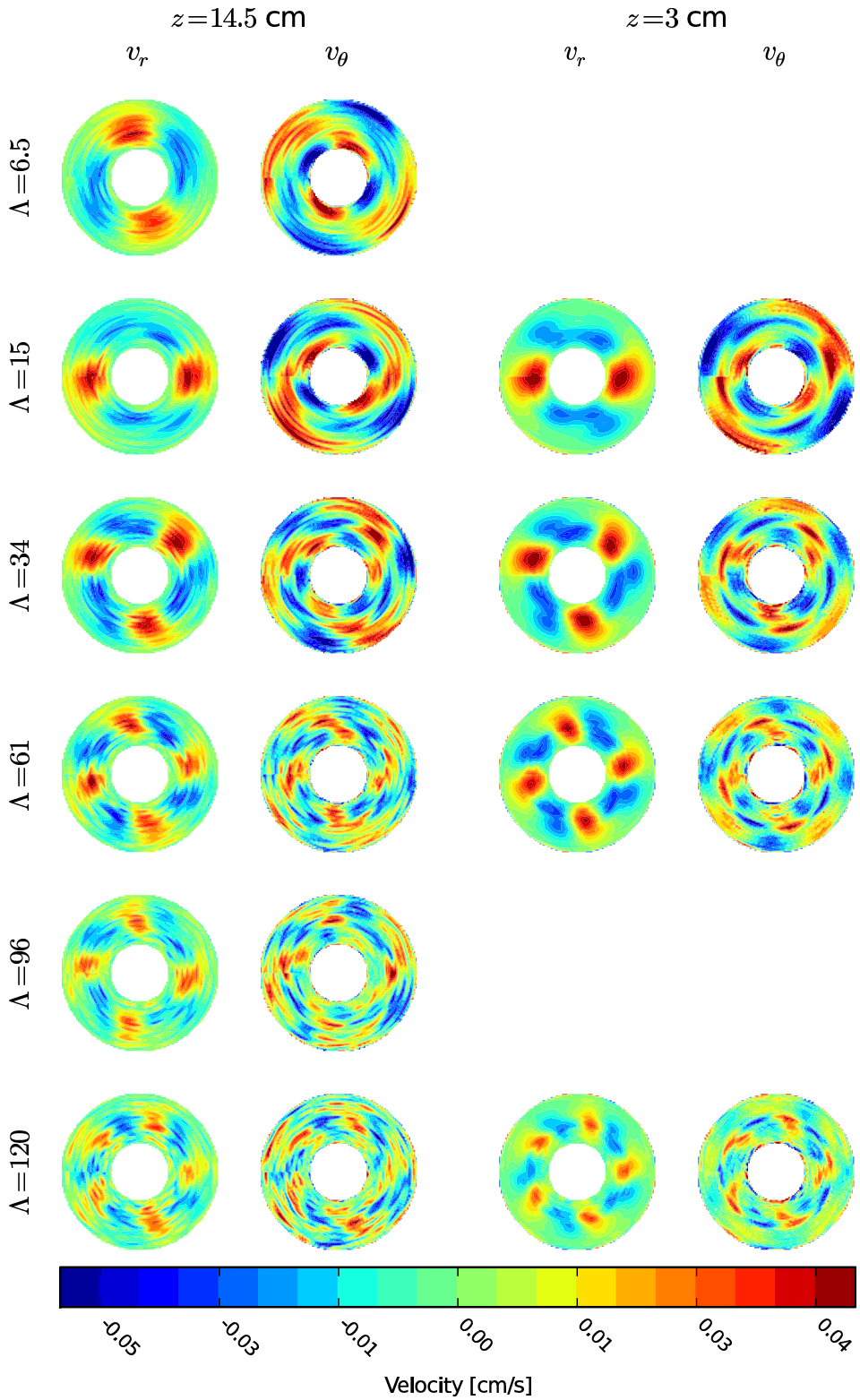

Figure 5.25: Measured mode structures for `split-unstable` configuration with $\Omega_1 = 0.25$ rpm and various B_0. All contour plots of velocity share a common color scale.

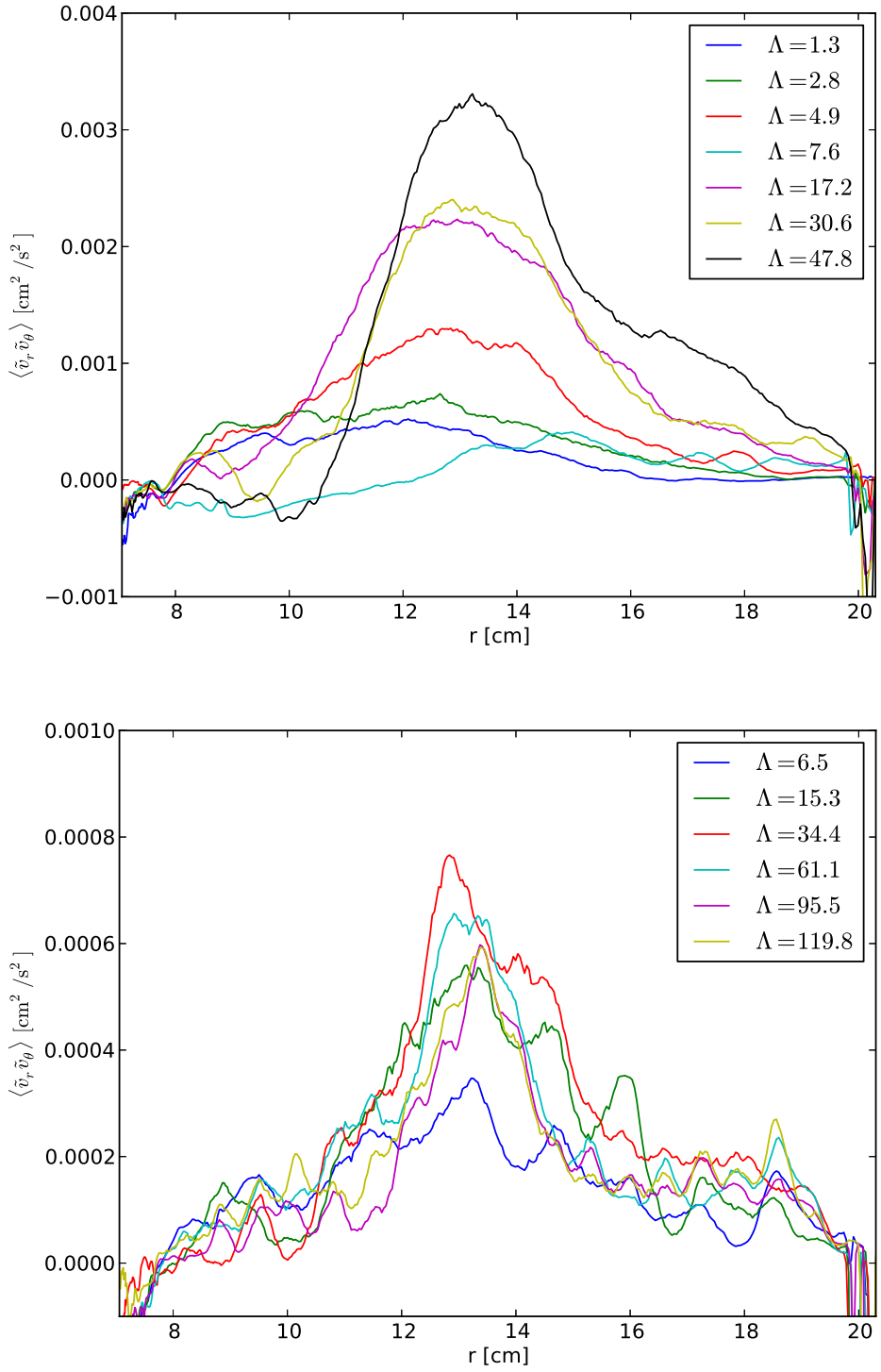

Figure 5.26: Average Reynolds stress component $\langle \tilde{v}_r \tilde{v}_\theta \rangle$ due to nonaxisymmetric velocity fluctuations in the $\Lambda \gg 1$ regime as measured at the midplane. *Top:* `split-unstable` configuration with $\Omega_1 = 0.5$ rpm. *Bottom:* `split-unstable` configuration with $\Omega_1 = 0.25$ rpm. Measurements are $\pm 20\%$ of the peak $\langle \tilde{v}_r \tilde{v}_\theta \rangle$ for each curve.

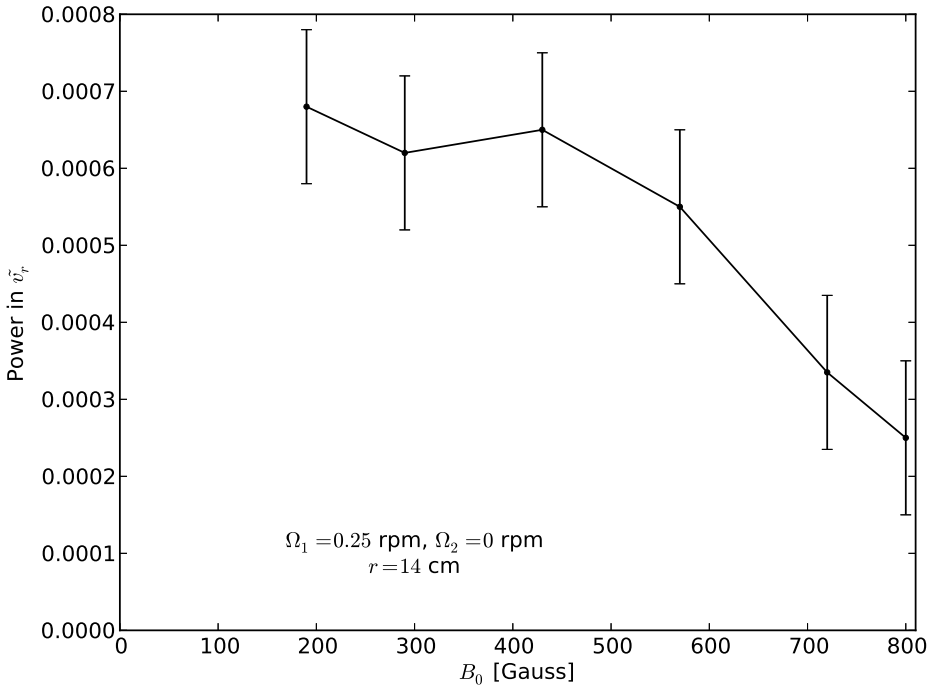

Figure 5.27: Power in the dominant frequency band of the v_r fluctuation at $r = 14$ cm versus applied magnetic field for the `split-unstable` configuration with $\Omega_1 = 0.25$ rpm.

5.3.5 Trend toward restabilization

The lower left corner of Figure 5.3 seems to show a trend toward lower power in the unstable mode with increasing magnetic field in the high-Λ regime. Those results may be somewhat suspect, as the measurements are of a mixture of the v_r and v_θ components less than 1.5 cm from the outer cylinder and more than 5 cm from the radial location of the shear layer. To gain a better picture of the potential restabilization, the power in the dominant v_r frequency band at $r = 14$ cm is plotted for the `split-unstable` configuration with $\Omega_1 = 0.25$ rpm in Figure 5.27. Here again there is a trend toward decreasing fluctuation amplitude with larger applied magnetic field, indicative of a restabilization with strong magnetic field, although the measurement is complicated by changing mode structure with increasing B_0.

Chapter 6

Linear stability of a free shear layer

This chapter examines calculations of the linear stability of a free shear layer in the geometry of the experiment. The global linear stability code described in Appendix D is used for these calculations. The code assumes an infinitely long device, and finds eigenmodes of the linearized, nonideal, incompressible MHD equations with a fixed azimuthal mode number m and axial wavenumber k, but with arbitrary variation of the eigenmode in r. It allows an axisymmetric, axially independent background azimuthal flow with arbitrary variation in r, and a spatially uniform background axial magnetic field B_0.

The background rotation profile for these studies is of the form

$$\Omega(r) = a_1 \tanh\left(\frac{r - r_l}{w_l}\right) + a_2, \tag{6.1}$$

where r_l is the radius of the center of the shear layer, w_l is the characteristic width, approximately half the width of the shear layer, and a_1 and a_2 are normalized such that $\Omega(r_1) = \Omega_1$ and $\Omega(r_2) = \Omega_2$:

$$\begin{aligned} a_1 &= \frac{\Omega_1 - \Omega_2}{\tanh\left[(r_1 - r_l)/w_l\right] - \tanh\left[(r_2 - r_l)/w_l\right]}, \\ a_2 &= \Omega_2 - a_1 \tanh\left[(r_2 - r_l)/w_l\right]. \end{aligned} \tag{6.2}$$

Example rotation profiles for various shear layer half widths are shown in Figure 6.1.

This chapter will examine two hydrodynamic instabilities as competitors for the free energy in the shear layer. The first section discusses the Kelvin-Helmholtz instability, driven

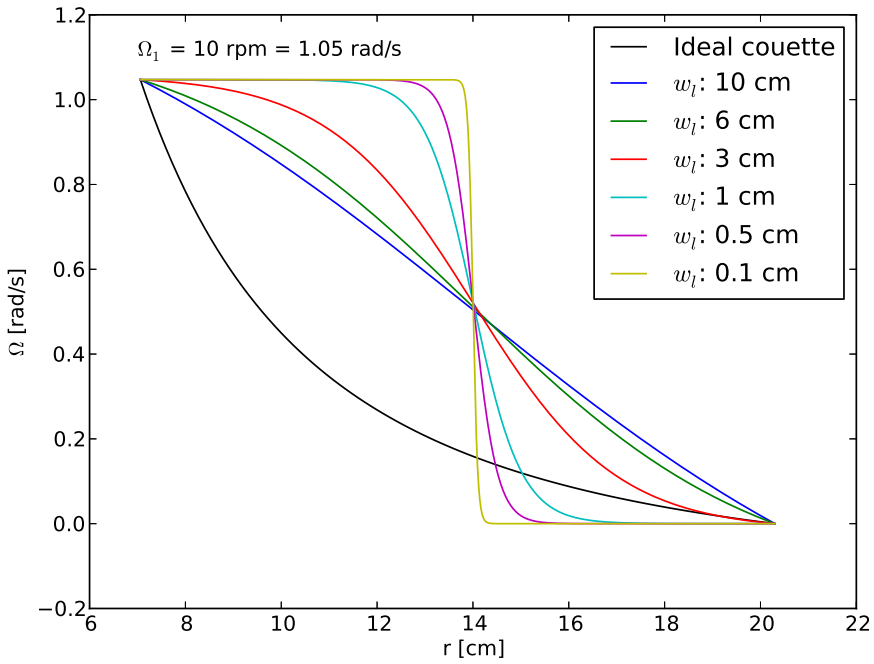

Figure 6.1: Example background rotation profiles for various values of the shear layer half width, w_l, with $\Omega_1 = 10\,\text{rpm}$, $\Omega_2 = 0$, $r_1 = 7.06\,\text{cm}$, $r_2 = 20.3\,\text{cm}$, and $r_l = 14\,\text{cm}$. The ideal Couette profile for this configuration is shown for comparison.

by the flow shear. The Kelvin-Helmholtz instability is a very common instability, and there has been considerable effort devoted to understanding it. Drazin and Reid [1981] gives a good summary of the instability in the 2-D planar geometry, with references to more detailed studies in specific geometries, including one to an early numerical study with a hyperbolic tangent shear layer [Betchov and Szewczyk, 1963]. It is useful to summarize some of the characteristics of the Kelvin-Helmholtz instability in 2-D planar flow, as our results in cylindrical geometry will share many features. Free shear layers are inviscidly unstable for wavenumbers smaller than some critical wavenumber, with the critical wavenumber scaling as $1/w_l$. The most unstable wavenumber also scales as $1/w_l$, and the growthrate scales as $\Delta v/w_l$, where Δv is the velocity change across the layer. The constants of proportionality depend on the geometry in which the shear layer is contained and the specific shape of the shear layer. The addition of viscosity to the problem limits the range of unstable wavenumbers for small $Re = \Delta v w_l/\nu$. In this section, the linearly unstable Kelvin-Helmholtz modes of the free shear layer are examined in the limit that $k = 0$ and $m \neq 0$. Comparisons of the

linearly unstable modes to the mode structures observed in the experiment provide strong evidence that it is a Kelvin-Helmholtz instability that drives the large velocity fluctuations observed at the midplane of the experiment.

The second section examines the centrifugal instability as a competitor to the Kelvin-Helmholtz instability for the free energy of the shear layer. The centrifugal instability is driven by a negative specific angular momentum gradient rather than by the velocity shear itself. The centrifugal instability may be stabilized by eliminating the negative specific angular momentum gradient. It has long been known that an axial applied magnetic field of sufficient strength may also stabilize the centrifugal instability [Chandrasekhar, 1961, Donnelly and Ozima, 1960, 1962, Donnelly and Caldwell, 1964]. The second section examines the linearly unstable eigenmodes of the centrifugal instability in the limit that $k \neq 0$ and $m = 0$. It is shown that the expected stabilization of the centrifugal instability scales with the observed appearance of the Kelvin-Helmholtz instability, suggesting that it is a competition between these two instabilities that determines the threshold for the appearance of the unstable Kelvin-Helmholtz modes in the experiment.

6.1 Kelvin-Helmholtz instability

Calculations of the Kelvin-Helmholtz instability were performed with the following parameters:

$\Omega_1 = 0.05 - 800$ rpm $= 5.24 \times 10^{-3} - 83.8$ rad/s,	$\nu = 2.98 \times 10^{-3}$ cm^2/s,
$\Omega_2 = 0$ rpm $= 0$ rad/s,	$\eta = 2.57 \times 10^{3}$ cm^2/s,
$r_1 = 7.06$ cm,	$\rho = 6.36$ g/cm^3,
$r_2 = 20.3$ cm,	$B_0 = 0$ Gauss,
$r_l = 14$ cm,	$w_l = 0.05 - 14$ cm,
$k = 0$ cm^{-1},	$m = 0 - 8$,
$N = 8000$ grid cells,	Conducting boundaries.

Setting $k = 0$ in these calculations guarantees that the centrifugal instability will have no influence on the results. Note that when $k = 0$, v_r and v_θ satisfy the incompressibility equation, so there is no perturbed v_z. Also, although we set B_0 explicitly to 0, the velocity is coupled to the magnetic field only through a term that goes as kv_A, so the magnetic field has no effect on the evolution of the velocity when $k = 0$.

6.1.1 Growth rates

As shown in Figure 6.2, the Kelvin-Helmholtz modes become unstable below a critical shear layer width. Starting from the right of the figure, as the shear layer width is decreased, the $m = 1$ mode is the first to be destabilized at $w_l = 6$ cm. The $m = 2$ mode is destabilized next at $w_l = 5$ cm, and with decreasing layer width its growth rate surpasses that of the $m = 1$. The $m = 3$ mode is next to be destabilized at $w_l = 4$ cm, eventually reaching an even larger growth rate. This pattern continues for increasing azimuthal mode number.

The critical shear layer width is consistent over a broad range of rotation speeds. The growth rate of the modes scales linearly with the rotation rate in the region of experimental interest, as shown in Figure 6.3. The Kelvin-Helmholtz instability is viscously stabilized for slower rotation rates than those investigated experimentally, $\Omega_1 = 0.05 - 0.10$ rpm.

6.1.2 Eigenmodes

The unstable eigenmodes are shown in Figure 6.4. Each marginally stable eigenmode exhibits a high degree of symmetry, but the modes take on more of a spiral structure as the shear layer width is decreased. Some of these modes bear a striking similarity to the mode structures observed in the experiment. Direct comparisons are made in Figure 6.5.

Stream functions

Because there is no axial velocity, it is possible to define a stream function in the $r-\theta$ plane for the eigenmodes of this instability,

$$\vec{v} = \nabla \times \vec{\psi}, \quad \text{where} \quad \vec{\psi} = \psi_z \hat{z}. \tag{6.3}$$

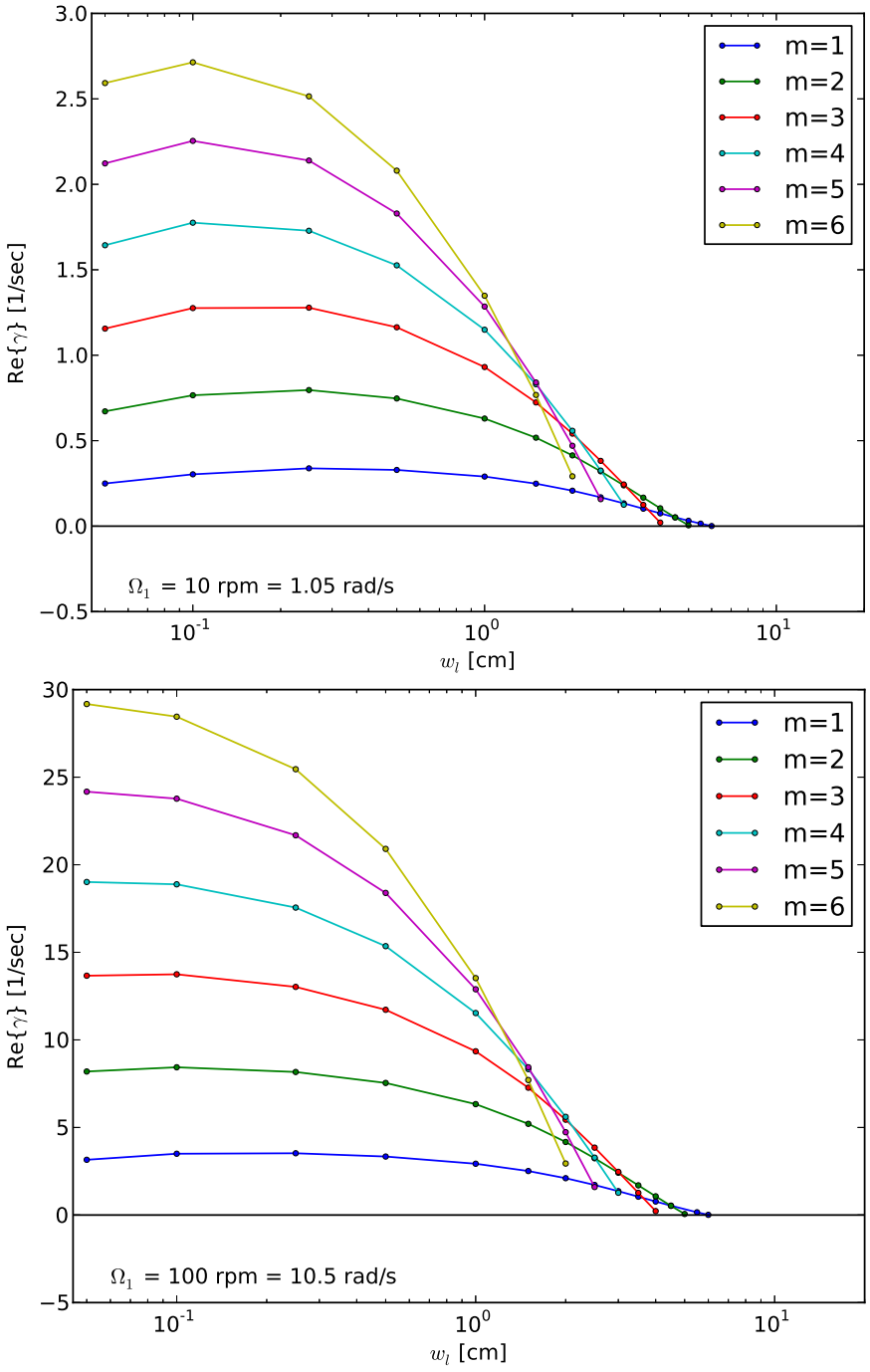

Figure 6.2: Growth rates for the Kelvin-Helmholtz instability as a function of shear layer width for various azimuthal mode numbers m. Only cases with a positive $Re\{\gamma\}$ are plotted. The top shows the results for $\Omega_1 = 10$ rpm, and the bottom for $\Omega_1 = 100$ rpm. The plots are almost identical, except that the growth rates in the faster rotation case are larger by a factor of 10. The critical shear layer width is independent of rotation rate.

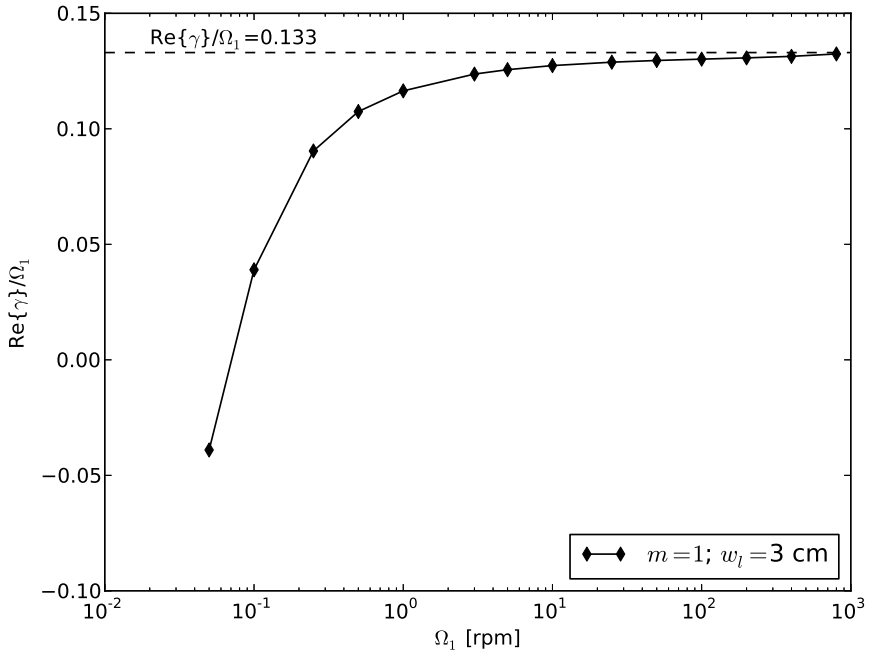

Figure 6.3: Growth rate for the Kelvin-Helmholtz instability, $\mathrm{Re}\{\gamma\}$, normalized to the inner cylinder rotation rate Ω_1 in rad/s for $m = 1$ and shear layer half width $w_l = 3$ cm. For rotation rates typically seen in the experiment, $\Omega_1 \sim 1 - 1000$ rpm, the growth rate is approximately linear in the rotation rate, $\mathrm{Re}\{\gamma\} \approx 0.13\Omega_1$.

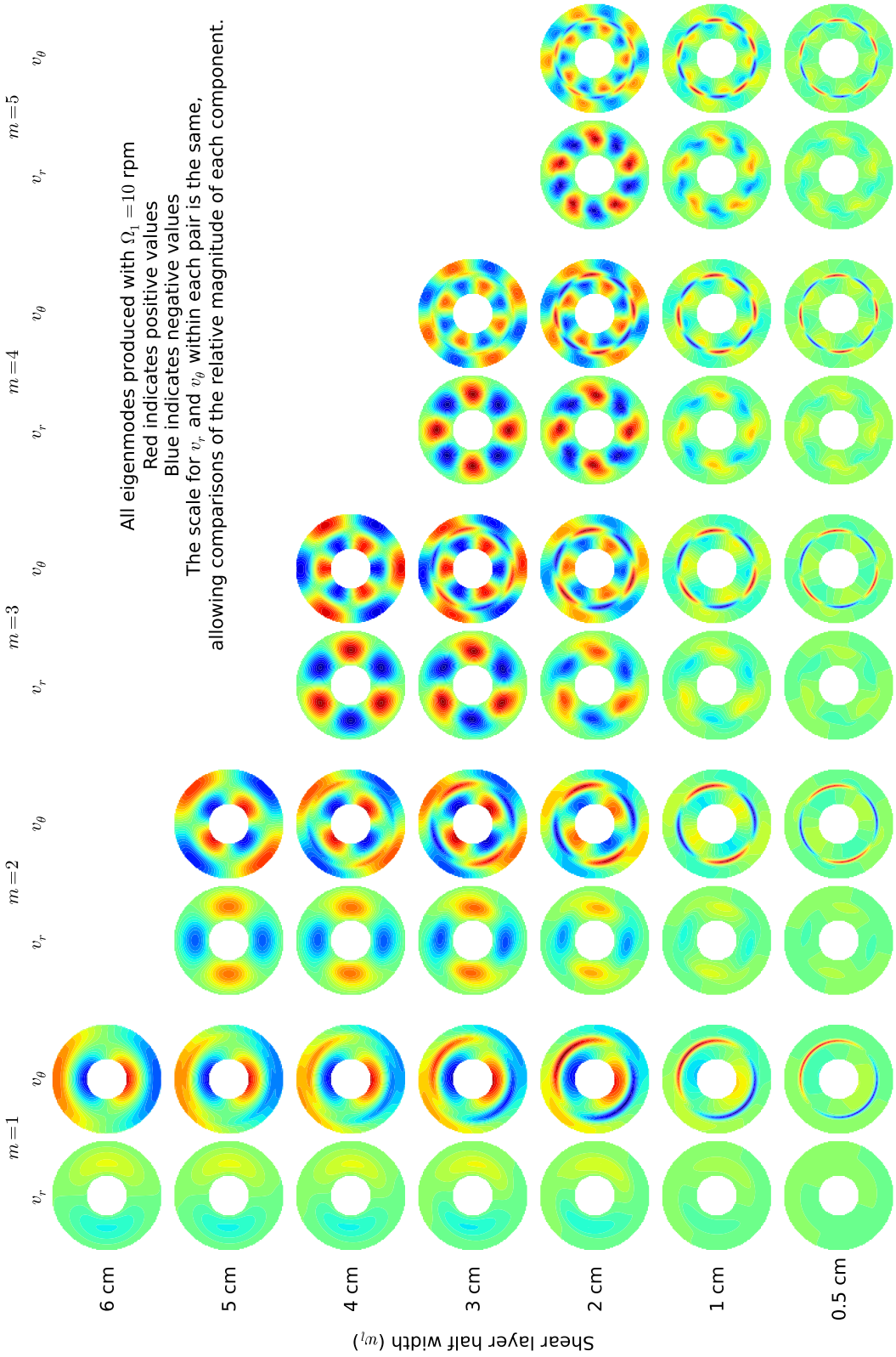

Figure 6.4: Linear eigenmodes of the Kelvin-Helmholtz instability.

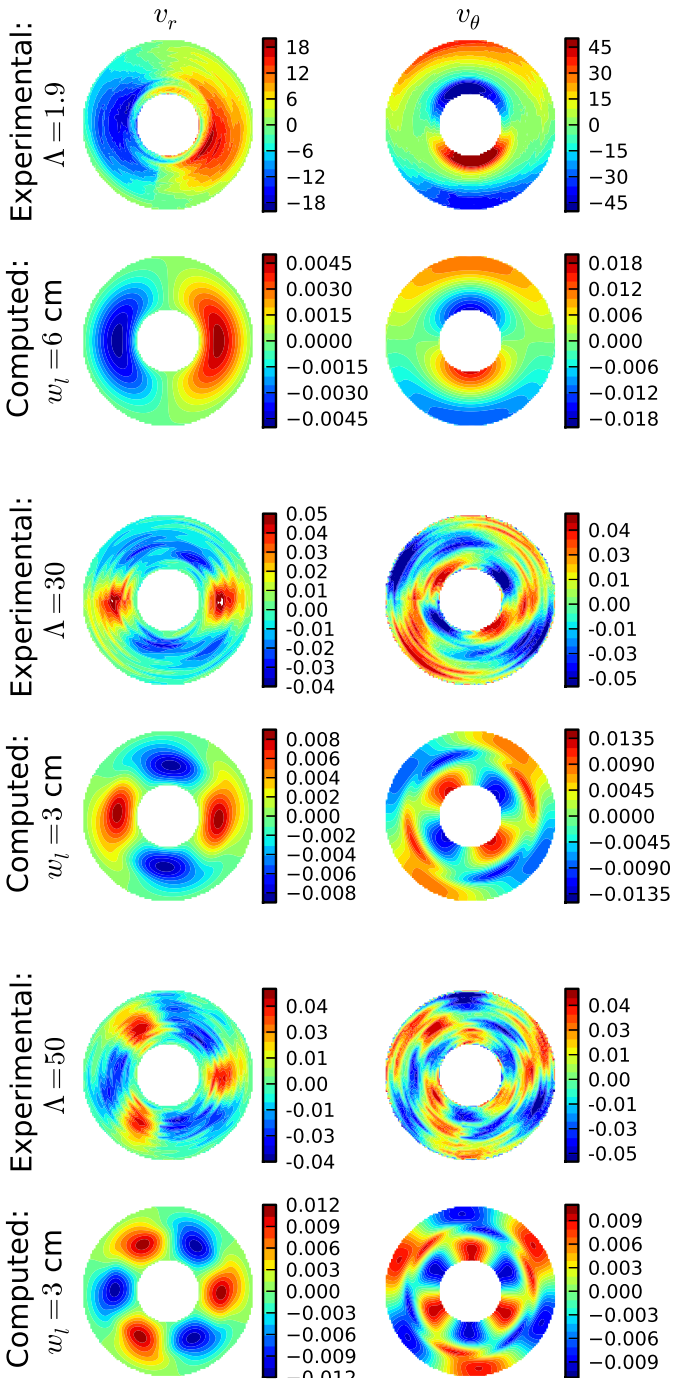

Figure 6.5: Comparison of experimentally measured saturated mode structures and Kelvin-Helmholtz linear eigenmodes. All computed eigenmodes have arbitrary amplitudes and were computed with $\Omega_1 = 10$ rpm. All experimental measurements were measured in the `split-unstable` configuration, and are in units of cm/s. *Top*: $m = 1$. Experimental measurement with $\Omega_1 = 400$ rpm, $B_0 = 4000$ Gauss, and $\Lambda = 1.9$. *Middle*: $m = 2$. Experimental measurement with $\Omega_1 = 0.25$ rpm, $B_0 = 290$ Gauss, and $\Lambda = 15$. *Bottom*: $m = 3$. Experimental measurement with $\Omega_1 = 0.25$ rpm, $B_0 = 430$ Gauss, and $\Lambda = 34$.

From the definition, we see that

$$v_r = \frac{1}{r}\frac{\partial}{\partial\theta}\psi_z, \quad \text{and} \quad v_\theta = -\frac{\partial}{\partial r}\psi_z, \tag{6.4}$$

so we can calculate ψ_z one of two ways:

$$\psi_z = -\frac{ir}{m}v_r, \quad \text{or} \quad \psi_z = -\int_{r_1}^{r_2} dr v_\theta, \tag{6.5}$$

where the calculation by the first method is simplified since the eigenmodes have a single azimuthal mode number.

The stream functions for the modes shown in Figure 6.4 are plotted in Figure 6.6. Note that the stream lines become more skewed as the shear layer thickness decreases.

Reynolds stress

The skewed stream lines for narrow shear layer widths represent correlations between the v_r and v_θ velocity components, which give a positive contribution to the Reynolds stress component associated with radial angular momentum transport: $\tilde{v}_r\tilde{v}_\theta$. The correlation can be better examined by considering the phase difference between the two components as a function of radius, as demonstrated below.

The azimuthally averaged Reynolds stress at a given radius is

$$\langle\tilde{v}_r\tilde{v}_\theta\rangle = \frac{1}{2\pi}\int_0^{2\pi} d\theta \tilde{v}_r\tilde{v}_\theta. \tag{6.6}$$

For the complex-valued v_r and v_θ produced by the global stability code,

$$\tilde{v}_r = \mathrm{Re}\{v_r\} = |v_r|\cos(m\theta + \phi_{v_r}), \quad \tilde{v}_\theta = \mathrm{Re}\{v_\theta\} = |v_\theta|\cos(m\theta + \phi_{v_\theta}), \tag{6.7}$$

where ϕ_{v_r} and ϕ_{v_θ} are the arguments of v_r and v_θ, respectively. Substituting these into the expression for the Reynolds stress,

$$\begin{aligned}\langle\tilde{v}_r\tilde{v}_\theta\rangle &= \frac{1}{2\pi}\int_0^{2\pi} d\theta \left[|v_r|\cos(m\theta + \phi_{v_r})|v_\theta|\cos(m\theta + \phi_{v_\theta})\right], \\ &= \frac{1}{4\pi}|v_r||v_\theta|\int_0^{2\pi} d\theta \left[\cos(\phi_{v_r} - \phi_{v_\theta}) + \cos(2m\theta + \phi_{v_r} + \phi_{v_\theta})\right].\end{aligned} \tag{6.8}$$

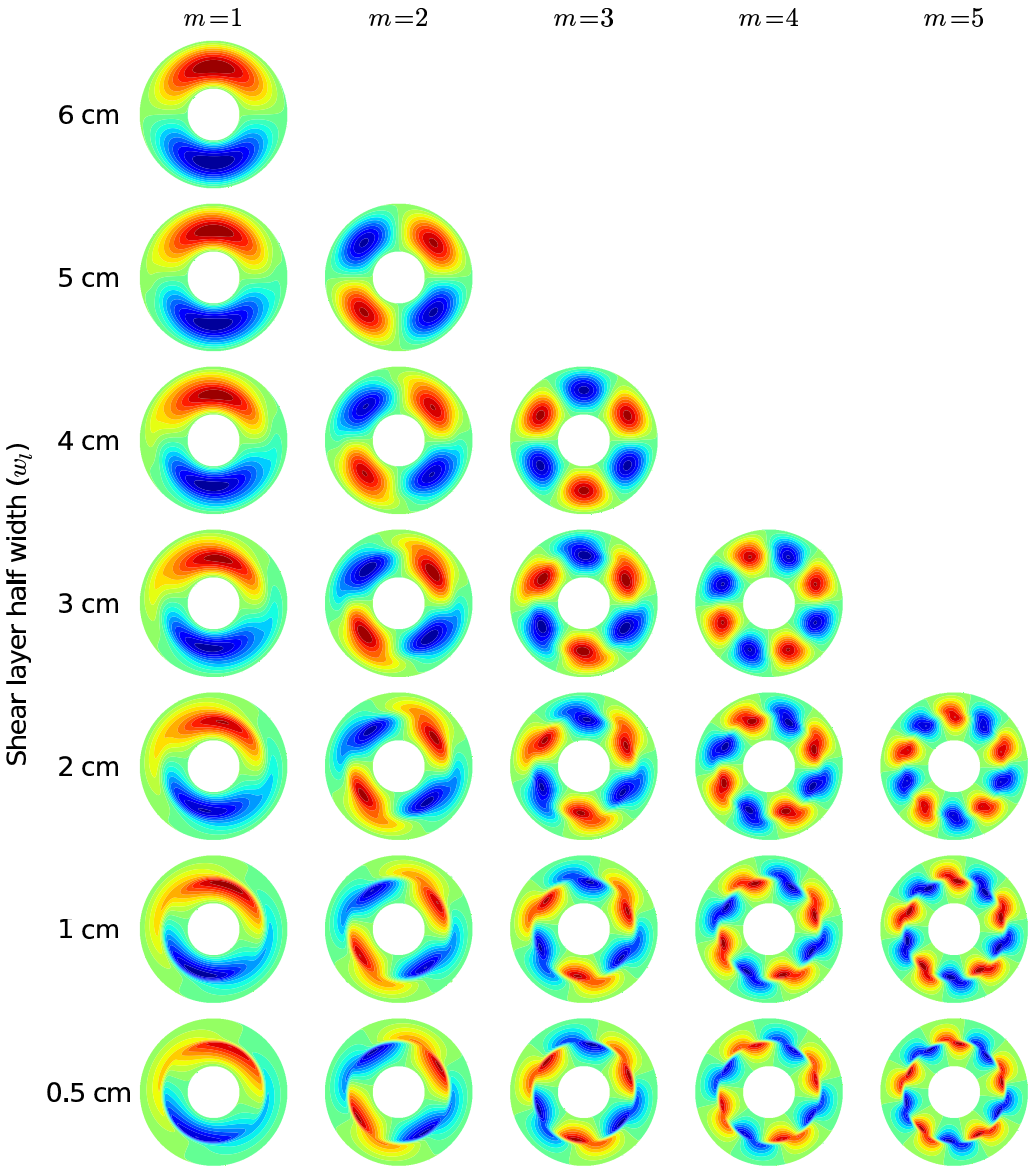

Figure 6.6: Contour plot of the stream function for the Kelvin-Helmholtz eigenmodes of a free shear layer shown in Figure 6.4. Red indicates positive values (counterclockwise flow), and blue indicates negative values (clockwise flow).

The second cosine term integrates to zero over a full period in θ, leaving

$$\langle \tilde{v}_r \tilde{v}_\theta \rangle = \frac{1}{2} |v_r||v_\theta| \cos(\phi_{v_r} - \phi_{v_\theta}). \tag{6.9}$$

The average contribution to the Reynolds stress at a given radius therefore depends on the phase difference between the v_r and v_θ components. When the components are $\pi/2$ out of phase, there is no net contribution to the Reynolds stress. And when they are perfectly in phase (or perfectly out of phase), there is the maximal possible contribution for fixed $|v_r|$ and $|v_\theta|$.

Plots of the velocity magnitudes, velocity phase differences, and the azimuthally averaged Reynolds stress component $\langle \tilde{v}_r \tilde{v}_\theta \rangle$ are shown in Figure 6.7, where the velocities have been normalized so that $\sum_{j=0}^{N} |v_{r,j}|^2 + \sum_{j=0}^{N} |v_{\theta,j}|^2 = 2N^2$, where N is the number of grid cells. In the case of large w_l, the phase difference nearly everywhere is $\pm\pi/2$ except at the center, where $|v_\theta|$ goes to zero. So there is a negligible contribution to the Reynolds stress. In contrast, in the case of smaller w_l, the Reynolds stress is peaked at middle of the shear layer where v_r and v_θ are nearly in phase, and where the magnitude of each velocity component is also significant. The peak value of the Reynolds stress for the unstable Kelvin-Helmholtz eigenmodes with various w_l and m is shown in Figure 6.8. There is an increase for all m with decreasing w_l below the w_l required for instability.

The forcing of the azimuthal velocity due to this component of the Reynolds stress is

$$\frac{\partial}{\partial t} v_\theta = -\frac{1}{r} \frac{\partial}{\partial r} (r \langle \tilde{v}_r \tilde{v}_\theta \rangle). \tag{6.10}$$

A positive radial gradient leads to local deceleration of the fluid, while a negative radial gradient leads to local acceleration. So the effect of the Reynolds stress for the eigenmodes in Figure 6.7 with $w_l = 3$ cm and $w_l = 1$ cm would be to decelerate the faster-rotating fluid on the inside of the shear layer, and to accelerate the slower-rotating fluid on the outside of the shear layer, leading to a decrease in the shear with an increase in the layer width.

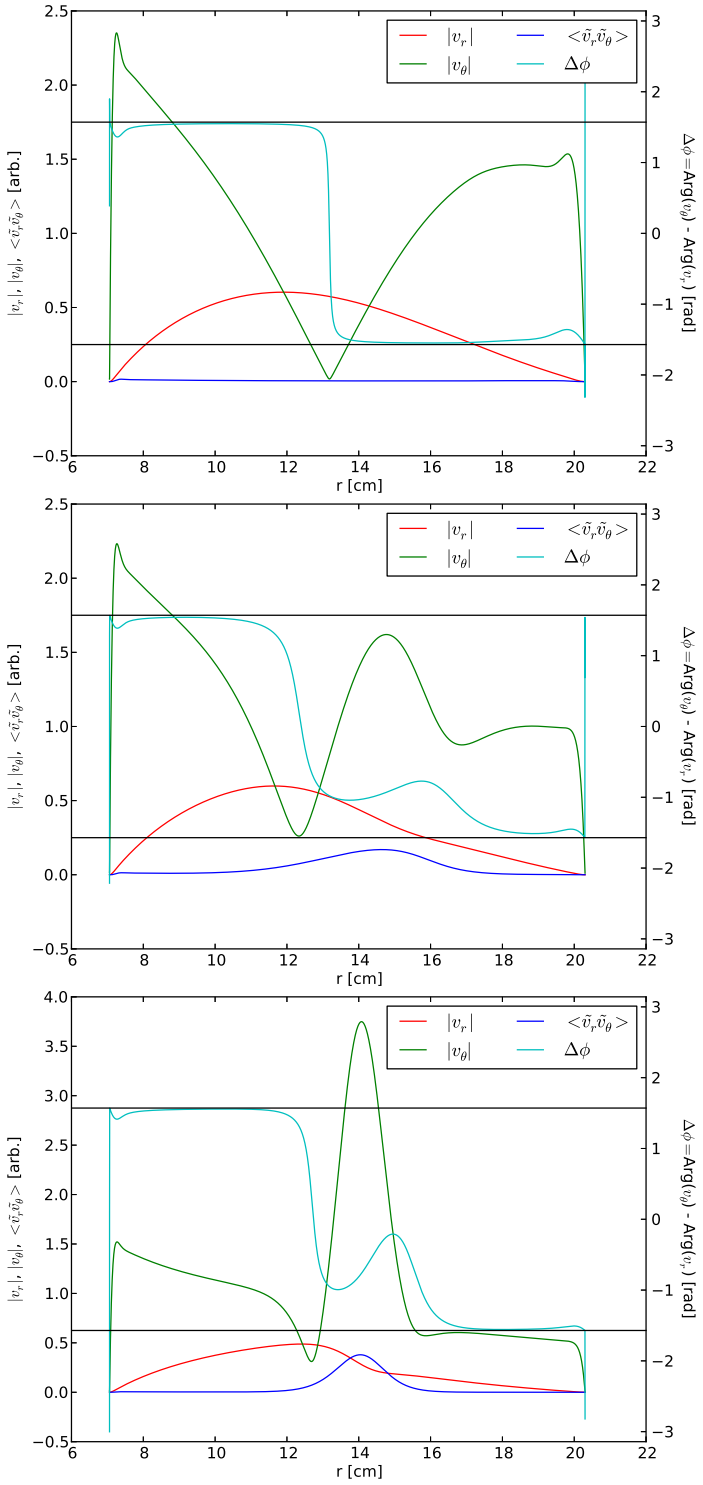

Figure 6.7: Magnitude and phase differences of v_r and v_θ and the associated azimuthally averaged Reynolds stress component $\langle\tilde{v}_r\tilde{v}_\theta\rangle$ for three values of w_l with $\Omega_1 = 10$ rpm and $m = 1$. *Top*: $w_l = 6$ cm, *middle*: $w_l = 3$ cm, *bottom*: $w_l = 1$ cm. The black horizontal lines indicate a phase difference of $\pi/2$, where there is no net contribution to the Reynolds stress.

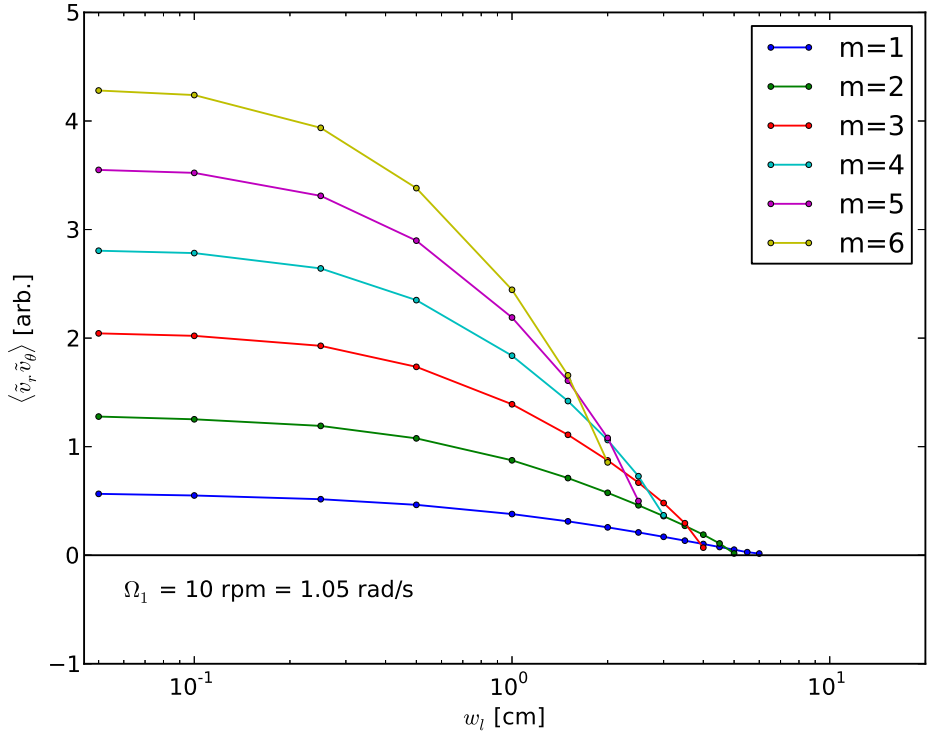

Figure 6.8: Peak of the azimuthally averaged Reynolds stress component $\langle \tilde{v}_r \tilde{v}_\theta \rangle$ for the Kelvin-Helmholtz eigenmodes with $\Omega_1 = 10$ rpm and various m and w_l. All eigenvectors have been normalized so that $\sum_{j=0}^{N} |v_{r,j}|^2 + \sum_{j=0}^{N} |v_{\theta,j}|^2 = 2N^2$, where N is the number of grid cells.

.

6.1.3 Effect of geometry on Kelvin-Helmholtz instability

The progression of maximally unstable azimuthal mode numbers m with decreasing w_l is a global effect and is dependent on the geometry of the experiment. As shown in Figure 6.9, in the large gap limit, where $r_1 \gg r_2 - r_1$, small azimuthal mode numbers are destabilized for nearly the same critical w_l. Because the wavenumber goes as m/r_l, it is only for much larger mode numbers that the azimuthal wavenumber is comparable to the shear layer width. The separation of the critical r_l for destabilization of any azimuthal mode therefor occurs for $m \sim O(10)$.

In contrast, increasing the gap width $r_2 - r_1$ compared to the experimental geometry still results in separation of the critical w_l for the small azimuthal mode numbers, but in this case the $m = 1$ is not the first to be destabilized with decreasing w_l. Instead, $m = 2$ is the first to be destabilized, followed by increasing larger azimuthal mode numbers. Nowhere is $m = 1$ the most unstable mode.

6.1.4 Summary of Kelvin-Helmholtz instability

- Shear layers of sufficiently narrow width are destabilized by Kelvin-Helmholtz modes:
  - Critical shear layer width is independent of Ω_1 for speeds of interest.
  - $m = 1$ destabilized first, at $w_l = 6$ cm; higher mode numbers require more shear.
  - Growth rates scale linearly with Ω_1 for speeds of interest: $\mathrm{Re}\{\gamma\} \approx 0.13\Omega_1$ for $m = 1$ and $w_l = 3$ cm.
- Eigenmodes are strikingly similar to those observed in the experiment.
- Increasing shear layer width associated with increasingly skewed stream functions, larger contributions to the Reynolds stress.
- Reynolds stress associated with eigenmodes would act to smooth out the shear layer.

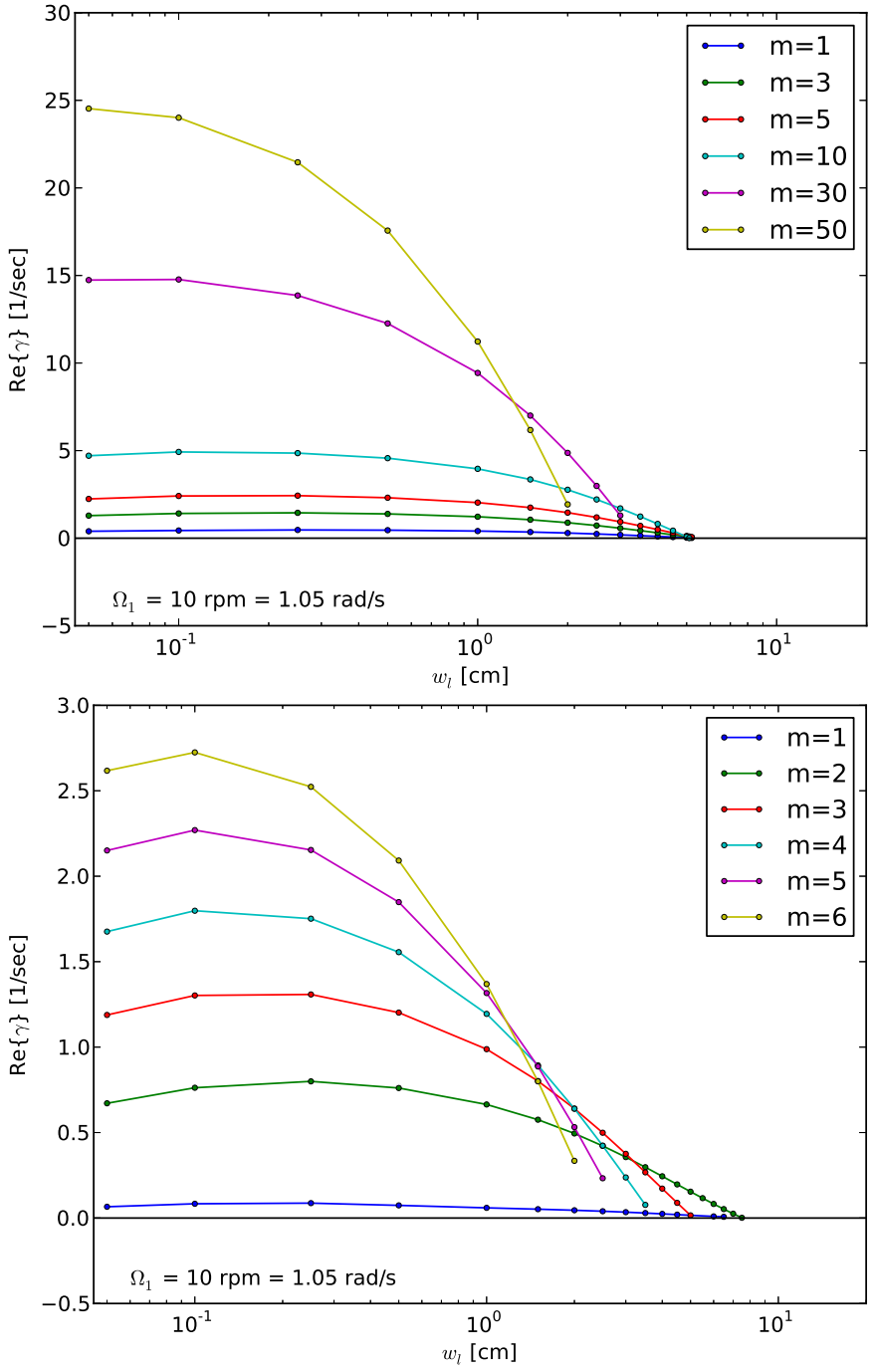

Figure 6.9: Effect of geometry on Kelvin-Helmholtz instability. Only the cases with positive growth rates $\mathrm{Re}\{\gamma\}$ are plotted. Both figures are produced with $\Omega_1 = 10$ rpm and $\Omega_2 = 0$ rpm. *Top:* $r_1 = 107.06$ cm, $r_2 = 120.30$ cm, and $r_l = 114.0$ cm. *Bottom:* $r_1 = 1.06$ cm, $r_2 = 26.30$ cm, and $r_l = 14.0$ cm.

6.2 Centrifugal instability

Calculations of the centrifugal instability in the shear layer background rotation profile were performed with the following parameters:

$\Omega_1 = 0.05 - 2000$ rpm $= 5.24 \times 10^{-3} - 209.4$ rad/s,	$\nu = 2.98 \times 10^{-3}$ cm^2/s,
$\Omega_2 = 0 - 1200$ rpm $= 0 - 125.7$ rad/s,	$\eta = 2.57 \times 10^{3}$ cm^2/s,
$r_1 = 7.06$ cm,	$\rho = 6.36$ g/cm^3,
$r_2 = 20.3$ cm,	$B_0 = 0 - 20000$ Gauss,
$r_l = 14$ cm,	$w_l = 1$, 3, 6 cm,
$k = 0.001 - 1000$ cm^{-1},	$m = 0$,
$N = 8000$ grid cells,	Conducting boundaries.

6.2.1 Unstable modes

In contrast to the Kelvin-Helmholtz modes, the modes of the centrifugal instability have $m = 0$ but finite k. As shown in Appendix D, v_r and v_θ are in phase in $\hat{z}$. So the average value of the Reynolds stress term is

$$\langle \tilde{v}_r \tilde{v}_\theta \rangle = \frac{k}{2\pi} \int_0^{2\pi} dz \mathrm{Re}\{v_r\}\mathrm{Re}\{v_\theta\} \sin^2(kz) = \frac{\mathrm{Re}\{v_r\}\mathrm{Re}\{v_\theta\}}{2}. \tag{6.11}$$

The velocity components and average Reynolds stress term are plotted for a linear eigenmode of the centrifugal instability in Figure 6.10, with the normalization as for the Kelvin-Helmholtz eigenmodes satisfying $\sum_{j=0}^{N} |v_{r,j}|^2 + \sum_{j=0}^{N} |v_{\theta,j}|^2 = 2N^2$, where N is the number of grid cells.

Note that the velocity components for the centrifugal eigenmode are much more tightly confined to the shear layer than they were for the Kelvin-Helmholtz eigenmode. But the effect on the Reynolds stress is similar. The Reynolds stress is peaked in the middle of the shear layer, and the gradients of the Reynolds stress indicate that this linear eigenmode would act to smooth out the shear and broaden the layer.

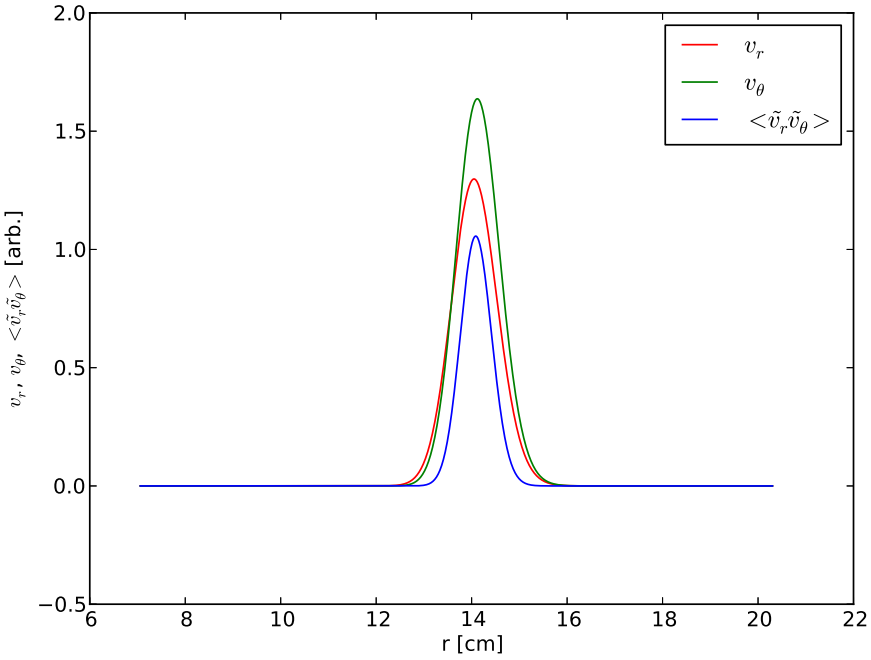

Figure 6.10: Velocity components v_r and v_θ and average contribution to the Reynolds stress component $\langle\tilde{v}_r\tilde{v}_\theta\rangle$ versus radius for the most unstable centrifugal instability eigenmode with $\Omega_1 = 100$ rpm, $\Omega_2 = 0$ rpm, $w_l = 3$ cm, and $B_0 = 0$.

6.2.2 Stabilizing effect of magnetic field

Calculations were made with fixed $\Omega_2 = 0$ and varying Ω_1, k, and B_0, with some of the results shown in Figure 6.11. The centrifugal instability can be stabilized by a sufficiently strong magnetic field, with a stronger magnetic field required for larger values of Ω_1.

Critical magnetic field

To gain a more systematic understanding of the magnetic field required to stabilize the centrifugal instability, each of the curves in Figure 6.11 is parametrized by 3 values: k_{peak}, the most unstable k; k_{max}, the maximum unstable k defined as the k where the curve crosses the $\text{Re}\{\gamma\} = 0$ axis; and the peak growth rate, the value of $\text{Re}\{\gamma\}$ at $k = k_{\text{peak}}$.

These values were determined by using the peak growth rate computed by the eigenvalue solver for a given k as an input to two function optimization routines, one to find the peak of the spectrum in k and another to find the zero-crossing. The peak-finder searched over

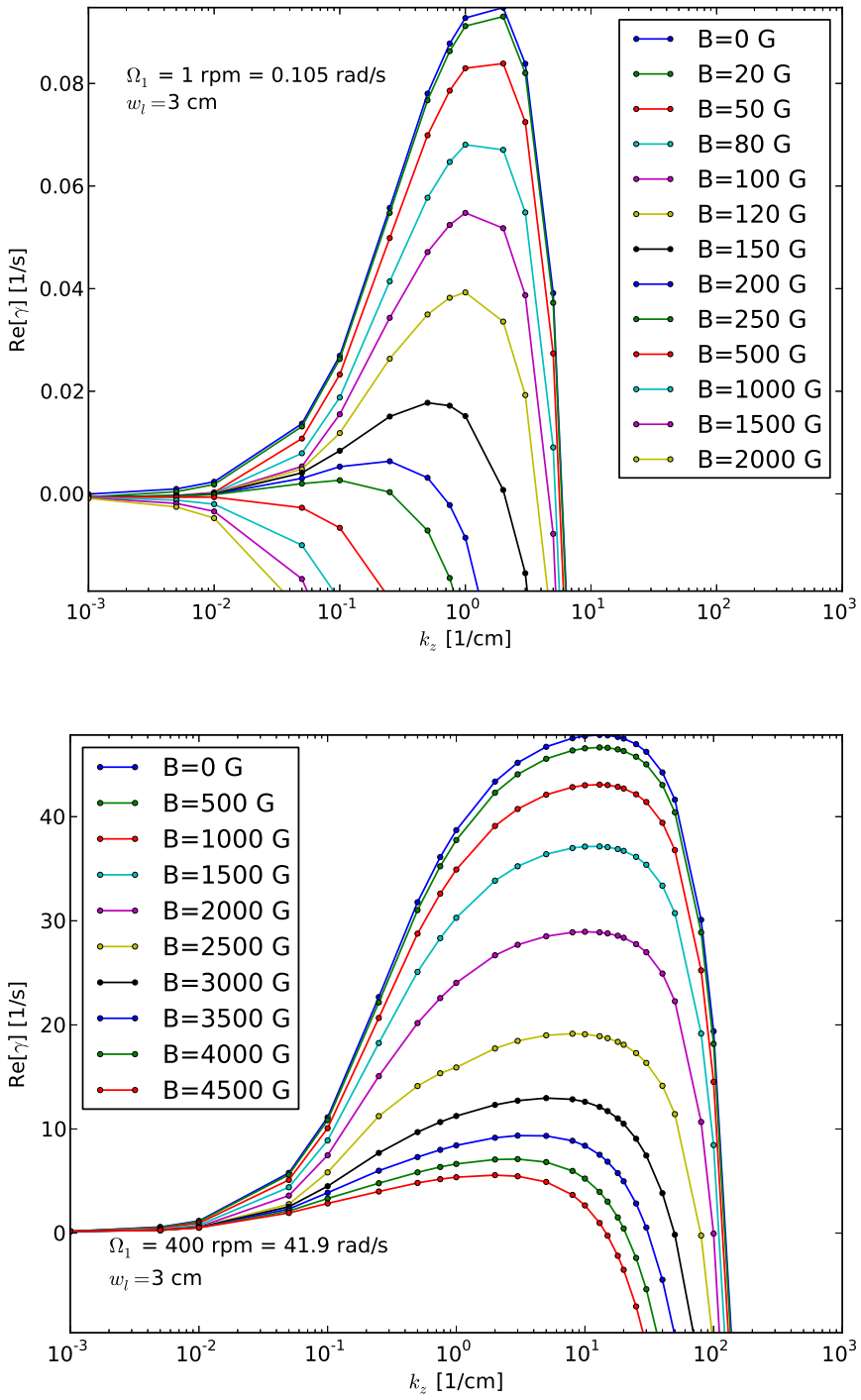

Figure 6.11: Effect of a magnetic field on centrifugal instability of a free shear layer. The plots are of the peak growth rate for several values of k and B_0, for $w_l = 3$ cm and $\Omega_2 = 0$. *Top:* $\Omega_1 = 1$ rpm. *Bottom:* $\Omega_1 = 400$ rpm. A stronger magnetic field is required to stabilize more-highly-sheared rotation profiles. In later analysis, k_{peak} and the peak growth rate refer to k and $\text{Re}\{\gamma\}$ at the peak of these curves, and k_{max} refers to the k at which the function crosses the $Re\{\gamma\} = 0$ axis on the right of the figure.

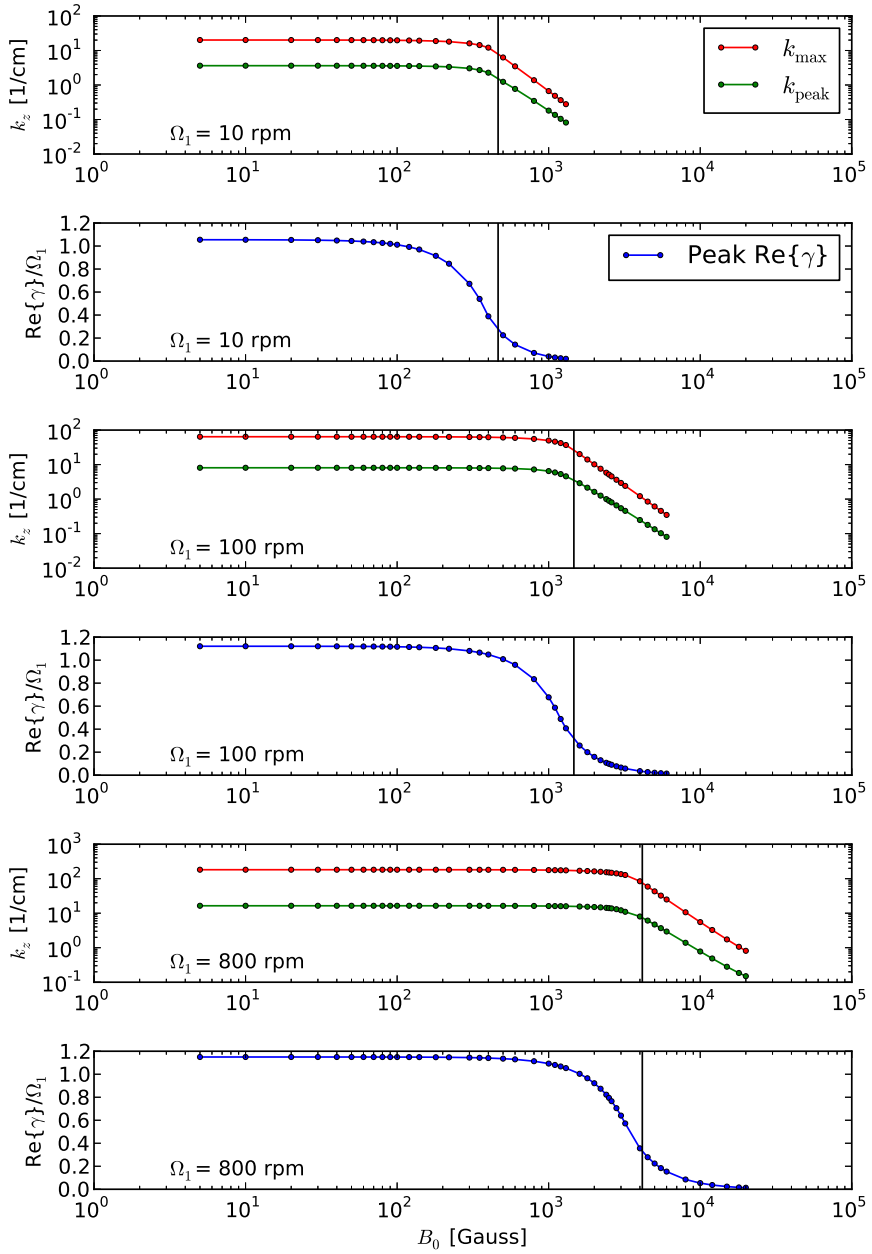

Figure 6.12: Plots of k_{peak}, $k_{\max}$, and peak Re$\{\gamma\}$ versus B_0 for various values of Ω_1. Plots are arranged in pairs, with the first plot at each speed showing the critical k values, and the second plot showing the growth rate. The vertical lines are drawn at $\Lambda = 1$.

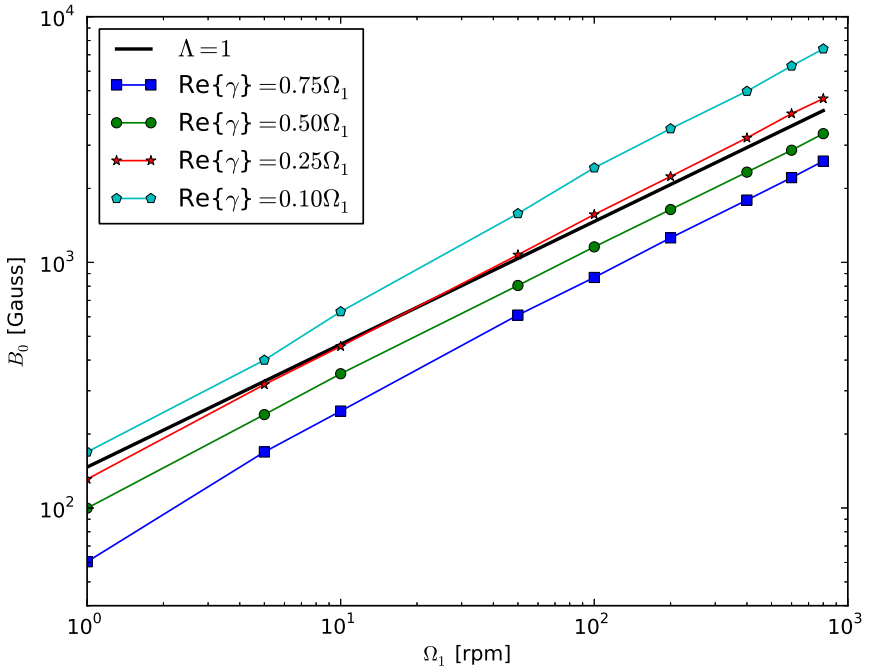

Figure 6.13: Magnetic field required to reduce the centrifugal instability growth rate to values of 0.75, 0.5, 0.25, and 0.1 of Ω_1, versus Ω_1. The solid black line shows the experimentally determined value of the onset of the Kelvin-Helmholtz instability, $\Lambda = 1$.

a wide range of wavenumbers, $k = 0.01 - 1000$ cm^{-1}, with the initial guess of k provided in the input file, typically 0.1 cm^{-1}. The root finder used to find $k_{\max}$ operated over the range $k = k_{\text{peak}} - 1000$ cm^{-1}. Convergence with these values was normally acceptable, although values near marginal stability sometimes failed to converge correctly and required manually-adjusted initial values in the search for k_{peak} for correct convergence.

The quantities are plotted versus B_0 for several values of Ω_1 in Figure 6.12. While there is a rather broad transition in B_0 from maximal instability to stability, the required B_0 for this transition scales as $\sqrt{\Omega_1}$.

This can be seen more clearly by looking at the scaling of several characteristic values of Re$\{\gamma\}/\Omega_1$ as a function of B_0, shown in Figure 6.13. The value of B_0 for each of these values scales as $\sqrt{\Omega}$, with larger B_0 causing more complete stabilization.

6.2.3 Stabilizing effect of background rotation

Background rotation can also have a stabilizing effect on the centrifugal instability. To examine this effect, calculations were made with varying amounts of $\Delta\Omega = \Omega_1 - \Omega_2$, Ω_2, and k. Some of the results for fixed $\Delta\Omega$ are shown in Figure 6.14. The background rotation has an effect similar to the effect of the magnetic field, stabilizing the centrifugal instability, with more background rotation required to stabilize more strongly sheared rotation profiles.

Critical background rotation

An analysis similar to the magnetic field case was performed to determine k_{peak}, k_{max}, and the peak $\text{Re}\{\gamma\}$ for varying values of $\Delta\Omega$ and Ω_2. The results for a few values of $\Delta\Omega$ are shown in Figure 6.15.

The background rotation acts to stabilize the instability, like the magnetic field does, but the transition region is sharper than it was for the magnetic field stabilization. Also, in this case the critical value for the stabilizing quantity, $\Omega_{2,\text{crit}}$, scales linearly with the shear $\Delta\Omega$.

This scaling can be seen by examining the trend of the characteristic values of $Re\{\gamma\}/\Delta\Omega$ as a function of Ω_2, shown in Figure 6.16, where the scaling $\Omega_2 \sim \Delta\Omega$ is clear.

6.2.4 Mixed magnetic field and background rotation

The effect of combined background rotation and magnetic field was examined for a fixed $\Omega_2 = 100$ rpm, with varying $\Delta\Omega$ and B_0. The results are most easily visualized as a contour of the normalized peak growth rate $\text{Re}\{\gamma\}/\Delta\Omega$, shown in Figure 6.17.

For the case with background rotation, a certain amount of shear is required to generate the instability, $\Delta\Omega_{\text{crit}} = 130$rpm for Ω_2 as shown in the figure. There is a sharp transition above $\Delta\Omega_{\text{crit}}$ to a region where $B_{0,\text{crit}} \sim \sqrt{\Delta\Omega}$, as if there were no background rotation at all, likely due to the sharp cutoff from stability to instability seen earlier with just background rotation. By $\Delta\Omega \sim 220$ rpm, the stability curves of the case with $\Omega_2 = 0$ and with $\Omega_2 = 100$ rpm are nearly indistinguishable.

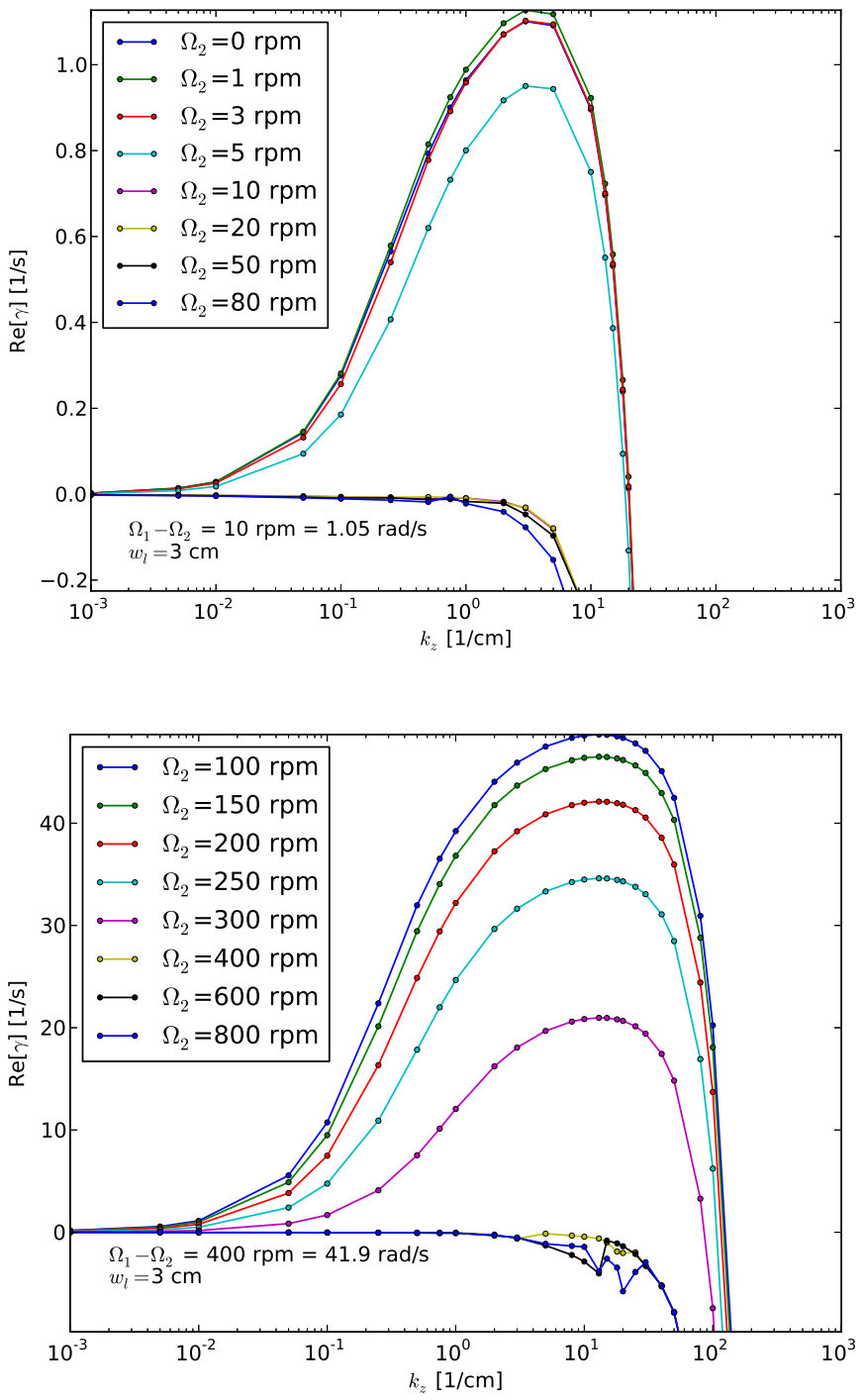

Figure 6.14: Effect of background rotation on centrifugal instability of a free shear layer. The plots are of the peak growth rate for several values of k and Ω_2 for $w_l = 3$ cm and $B_0 = 0$. *Top:* $\Delta\Omega = 10$ rpm. *Bottom:* $\Delta\Omega = 400$ rpm. More background rotation is required to stabilized more-highly-sheared rotation profiles.

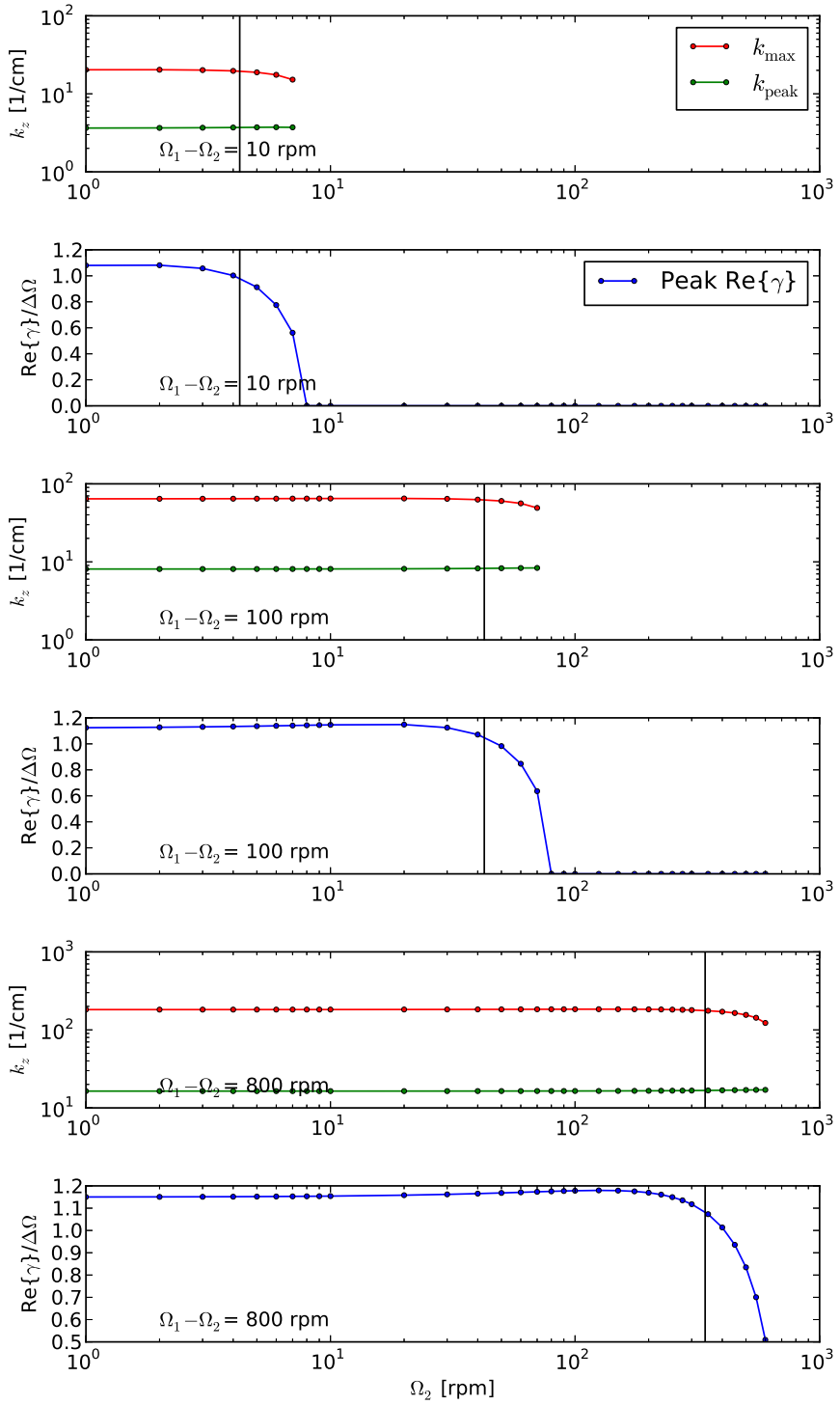

Figure 6.15: Plots of k_{peak}, $k_{\max}$, and peak Re$\{\gamma\}$ versus Ω_2 for various values of $\Delta\Omega$. Plots are arranged in pairs, with the first plot at each speed showing the critical k values, and the second plot showing the growth rate. The vertical lines are drawn at $Ro = 2.35$.

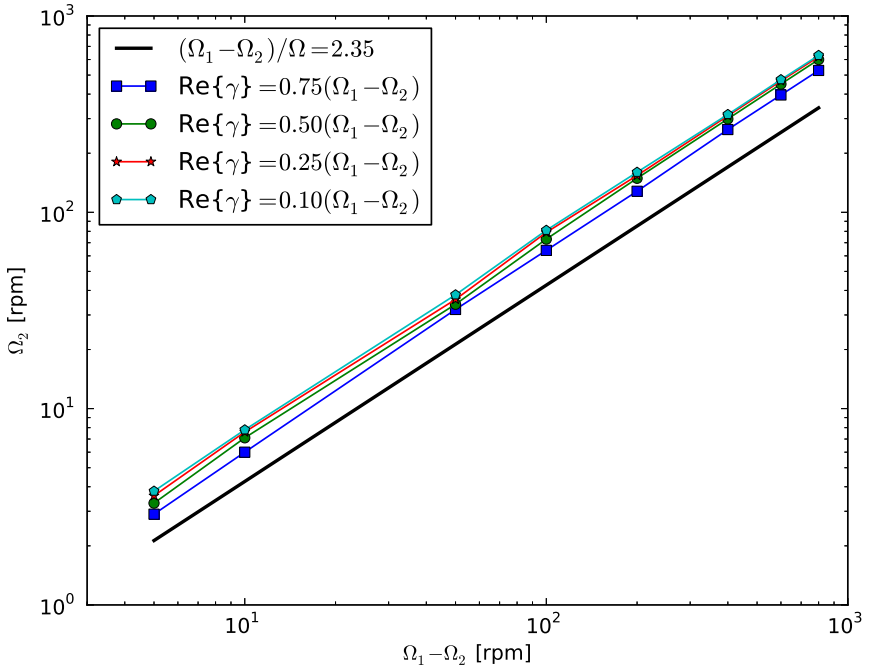

Figure 6.16: Background rotation required to reduce the centrifugal instability growth rate to values of 0.75, 0.5, 0.25, and 0.1 of $\Delta\Omega$, versus $\Delta\Omega$. The solid black line shows the experimentally determined value of the onset of the Kelvin-Helmholtz instability with no magnetic field, $Ro = 2.35$.

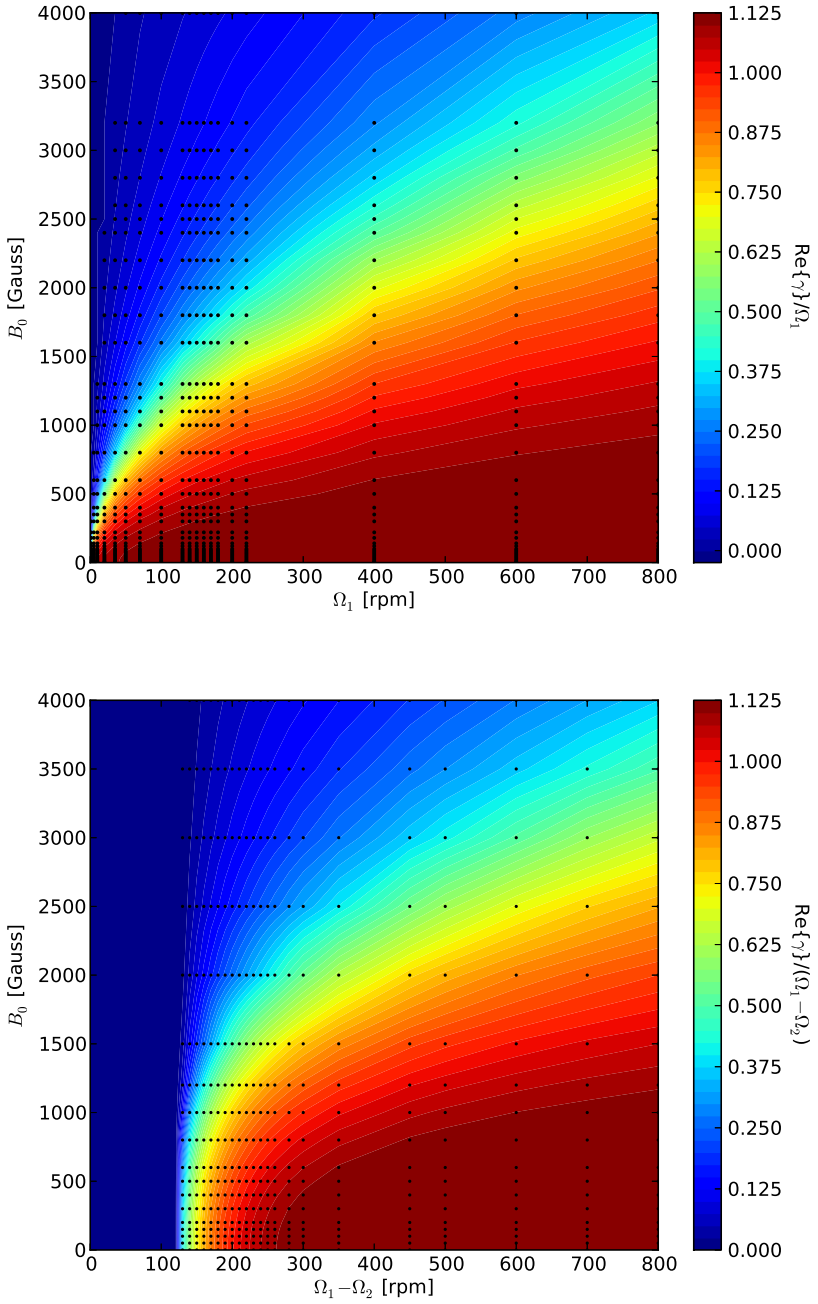

Figure 6.17: Contours of normalized growth rate for varying $\Delta\Omega$ and B_0. *Top:* $\Omega_2 = 0$. *Bottom:* $\Omega_2 = 100$ rpm. The black dots indicate the points where calculations were made.

6.2.5 Nonaxisymmetric centrifugal instability

Up until now, the Kelvin-Helmholtz instability was investigated with $k = 0$, and the centrifugal instability was investigated with $m = 0$. With both nonzero k and nonzero m, effects of both instabilities may be present. Figure 6.18 compares the stabilizing effects of B_0 and Ω_2 with various values of k and with a fixed $\Delta\Omega$ for $m = 0$ and $m = 1$. At large k, the behavior of the centrifugal instability remains mostly unchanged, with only a marginal decrease in the growth rate of the mode. But at small k, the behavior is very different. In the axisymmetric case, the growth rates in all cases go to zero. In the nonaxisymmetric case, the growth rates converge to a constant nonzero value as the Kelvin-Helmholtz instability dominates in this region.

The transition from centrifugal instability to Kelvin-Helmholtz instability with decreasing k can be visualized by considering the contributions of each of the velocity components to the incompressibility equation,

$$\nabla \cdot \vec{v} = \frac{1}{r}\frac{\partial}{\partial r}(rv_r) + \frac{1}{r}\frac{\partial v_\theta}{\partial \theta} + \frac{\partial v_z}{\partial z} = 0. \tag{6.12}$$

For the pure Kelvin-Helmholtz instability, the flow associated with the mode is entirely in the $r - \theta$ plane, so the v_z contribution to the incompressibility equation is zero. But for Taylor vortices characteristic of the the centrifugal instability, the contribution of the v_z term in the incompressibility equation is comparable to the v_r term [Taylor, 1923]. By summing the magnitude of each of the terms of the incompressibility equation across all grid cells and comparing them to each other, we have a measure of the relative contribution of the centrifugal instability and the Kelvin-Helmholtz instability for each unstable mode. Results of this procedure are shown in Figure 6.19, showing a transition from the centrifugal instability to the Kelvin-Helmholtz instability for $k \sim 0.1 - 0.01$ cm^{-1} for all values of the applied field.

The transition may also be visualized by comparing the unstable mode structures, shown in Figure 6.20. With decreasing k, the mode transitions from the nonaxisymmetric centrifugal instability, localized in the region the shear layer, to a mode that is indistinguishable

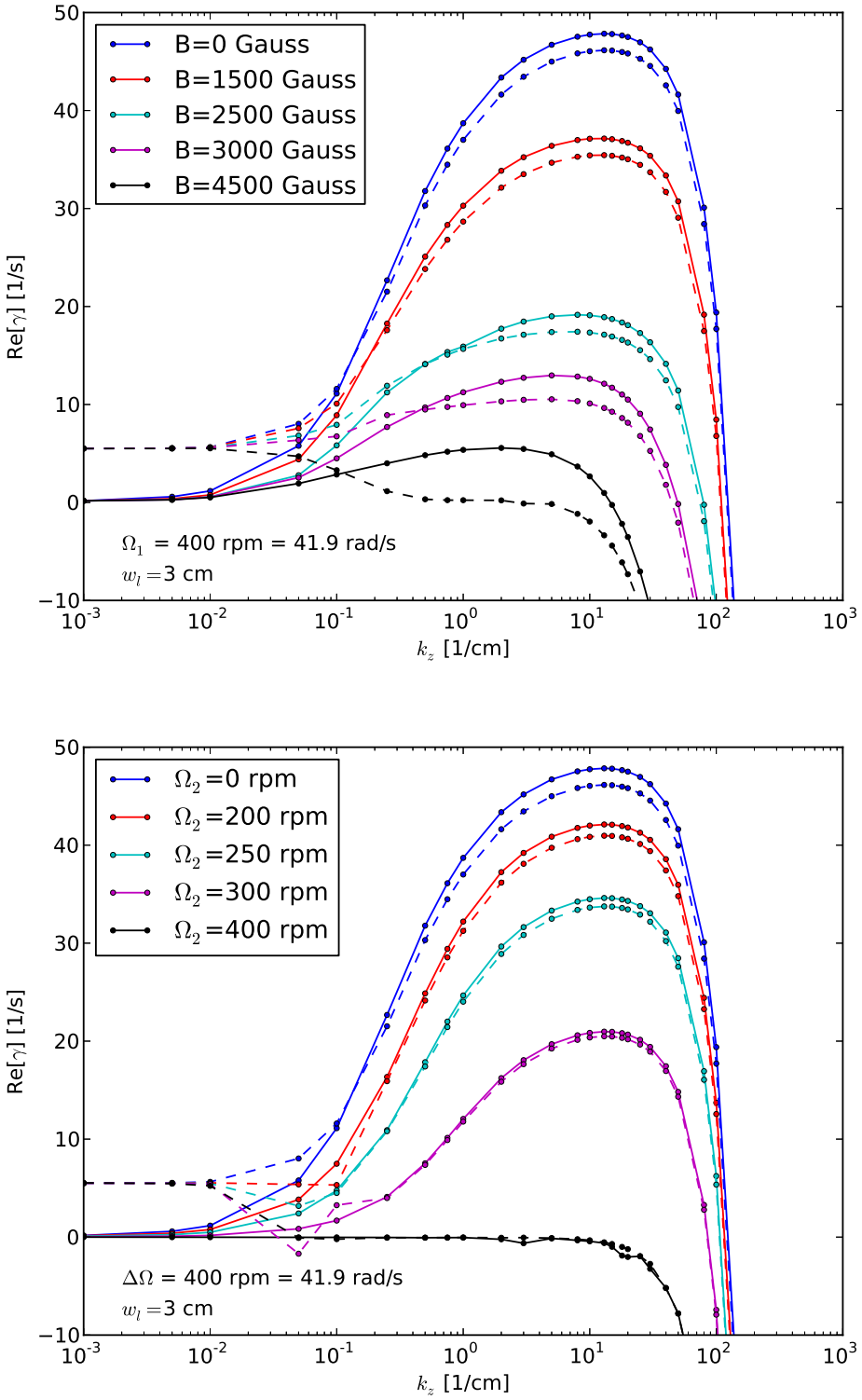

Figure 6.18: Effect of stabilizing forces on nonaxisymmetric centrifugal instability. *T*op: $\Omega_1 = 400$ rpm and $\Omega_2 = 0$, for various values of B_0. *B*ottom: $\Omega_1 - \Omega_2 = 400$ rpm and $B_0 = 0$, for various values of Ω_2. In both plots, solid lines indicate computations with $m = 0$, and dashed lines indicate computations with $m = 1$.

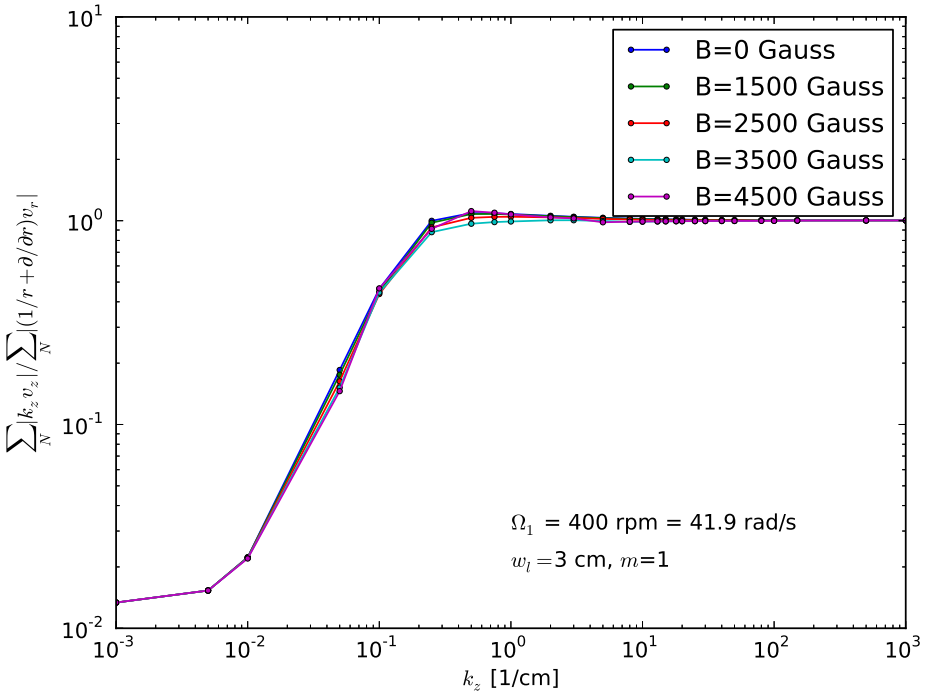

Figure 6.19: Relative contribution of the v_z and v_r terms to the incompressibility equation with $m = 1$, $\Omega_1 = 400$ rpm, and $\Omega_2 = 0$. The absolute value of the contribution of each term is summed across all grid cells, and the relative contributions of the two terms are compared.

from the pure Kelvin-Helmholtz instability with $k = 0$.

6.2.6 Effect of geometry and layer width

All of the centrifugal instability results thus far have been for $w_l = 3$ cm. More limited calculations have been carried out for $w_l = 1$ cm and $w_l = 6$ cm with $m = 0$. In both cases $B_{0,\mathrm{crit}}$ and $\Omega_{2,\mathrm{crit}}$ for restabilization follow the constant Λ and constant Ro scaling, as for $w_l = 3$ cm, although the magnitude of each quantity required for stabilization changes with w_l. Calculations have also been performed in the PROMISE-2 geometry (see Appendix E for more details), showing the effect of a different radial shear layer position r_l. For the case with background rotation, $\Omega_{2,\mathrm{crit}} \sim r_l \Delta\Omega / w_l$. The scaling with magnetic field is less certain because of the combination of the gradual stabilization with increasing B_0 and the small range of w_l and r_l investigated. The scaling seems to be $B_{0,\mathrm{crit}} \sim r_l^{3/4} \sqrt{\Delta\Omega} / w_l^{1/3}$. The exponent on w_l is particularly uncertain, lying somewhere between 1/4 and 1/2 with a slight residual dependence on $\Delta\Omega$, suggesting that this functional form may be an over-simplification.

Local dispersion relation with $B_0 = 0$

The scalings listed above can be compared in some limits to the local, axisymmetric dispersion relation, derived in Ji et al. [2001],

$$\left[(\gamma + \nu k^2)(\gamma + \eta k^2) + (k_z v_A)^2\right]^2 \frac{k^2}{k_z^2} + \kappa^2 (\gamma + \eta k^2)^2 + \frac{\partial \Omega^2}{\partial \ln r} (k_z v_A)^2 = 0, \tag{6.13}$$

where the epicyclic frequency κ is defined by $\kappa^2 = (1/r^3)\partial(r^4\Omega^2)/\partial r = 4\Omega^2 + \partial\Omega^2/\partial \ln r$ and k is the total wavenumber, $k^2 = k_z^2 + k_r^2$. (Note that this definition of k in the local dispersion relation is different from that used elsewhere throughout this chapter, where $k = k_z$ and the modes have arbitrary radial dependence.)

In the absence of a magnetic field, Equation 6.13 reduces to

$$(\gamma + \nu k^2)^2 \frac{k^2}{k_z^2} + \kappa^2 = 0. \tag{6.14}$$

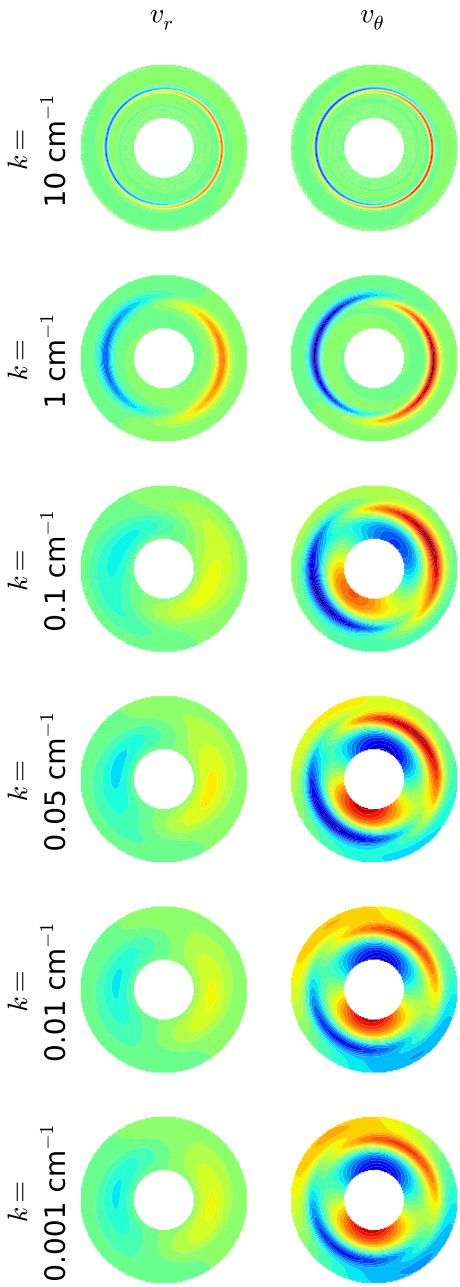

Figure 6.20: Mode structures for the transition from the nonaxisymmetric centrifugal instability to the Kelvin-Helmholtz instability with decreasing k, with $m = 1$, $\Omega_1 = 400$ rpm, $\Omega_2 = 0$, $w_l = 3$ cm, and $B_0 = 0$. Each pair of v_r and v_θ share a common colorscale, allowing comparison of the relative magnitudes of the two velocities.

We can rewrite κ in terms of Ω_2 and $\Delta\Omega$, using $\Omega = \Omega_2 + \Delta\Omega/2$ and $\partial\Omega/\partial r = -\Delta\Omega/2w_l$,

$$\kappa^2 = 4\left[\Omega_2 + \frac{\Delta\Omega}{2}\right]^2 - \frac{r_l}{w_l}\left[\Omega_2 + \frac{\Delta\Omega}{2}\right]\Delta\Omega. \tag{6.15}$$

This leads to the dispersion relation

$$\gamma = -\nu k^2 + \frac{k_z}{k}\sqrt{-4\left[\Omega_2 + \frac{\Delta\Omega}{2}\right]^2 + \frac{r_l}{w_l}\Delta\Omega\left[\Omega_2 + \frac{\Delta\Omega}{2}\right]}. \tag{6.16}$$

If we neglect the νk^2 term, which will be small for the rotation rates that we consider, this dispersion relation has roots for

$$-4\Omega_2^2 + \left(\frac{r_l}{w_l} - 4\right)\Delta\Omega\Omega_2 + \left(\frac{r_l}{2w_l} - 1\right)\Delta\Omega^2 = 0. \tag{6.17}$$

With the additional assumption that $w_l \ll r_l$, the solution to this equation suggests that

$$\Omega_{2,\mathrm{crit}} \sim r_l\Delta\Omega/w_l, \tag{6.18}$$

which is consistent with the results observed over a narrow range in the global analysis.

It is interesting that Equation 6.16 suggests that there are some situations in which the addition of a small Ω_2 results in an *increase* in the growth rate, with additional Ω_2 again resulting in stabilization. Since k_r and k_z tend to remain unchanged by Ω_2, the trend in the growth rate is determined entirely by the expression under the square root. In the limit of small Ω_2 relative to $\Delta\Omega$, again neglecting the viscous damping, the change in the growth rate is

$$\frac{\gamma}{\gamma_{\Omega_2=0}} = 1 + \frac{\Omega_2}{\Delta\Omega}\frac{r_l - 4w_l}{r_l - 2w_l}. \tag{6.19}$$

So for small shear layer widths satisfying $w_l < r_l/4$, the addition of a small Ω_2 results in further destabilization of the centrifugal instability. This effect can be seen to a limited extent for $w_l = 3$ cm in Figure 6.15, and can be seen more clearly for $w_l = 1$ cm in Figure 6.21.

Local dispersion relation with $\Omega_2 = 0$

The local dispersion is more complicated and somewhat less useful with $B_0 \neq 0$ and $\Omega_2 = 0$ because both k_z and k_r are functions of B_0, as shown in Figure 6.12. But, we will make an attempt to glean some useful information from it anyway.

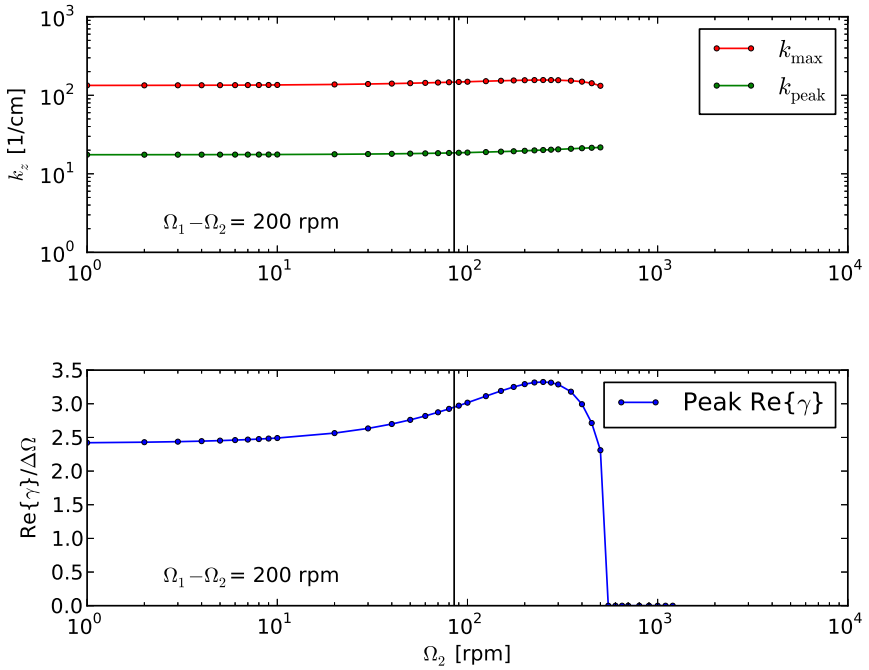

Figure 6.21: Plots of k_{peak}, $k_{\max}$, and peak Re$\{\gamma\}$ versus Ω_2 for $\Delta\Omega = 200$ rpm and $w_l = 1$ cm. The vertical line is drawn at $Ro = 2.35$.

Starting with Equation 6.13, we will neglect the $4\Omega^2$ contribution to κ^2, keeping only the $\partial\Omega^2/\partial \ln r = -(r_l/2w_l)\Delta\Omega^2$ contribution. This is justifiable in the limit that $w_l \ll r_l/2$. We can separate the $\Delta\Omega$ terms and the B_0 terms on opposite sides of the dispersion relation,

$$\frac{r_l}{2w_l}\Delta\Omega^2 = \frac{\left[(\gamma+\nu k^2)(\gamma+\eta k^2)+(k_z v_A)^2\right]^2}{(\gamma+\eta k^2)^2+(k_z v_A)^2}\frac{k^2}{k_z^2}. \tag{6.20}$$

We now choose to investigate the condition for marginal stability, $\gamma = 0$, further simplifying the equation to

$$\frac{r_l}{2w_l}\Delta\Omega^2 = \frac{\left[\nu\eta k^4+(k_z v_A)^2\right]^2}{\eta^2 k^4+(k_z v_A)^2}\frac{k^2}{k_z^2}. \tag{6.21}$$

We can invoke the ordering $\eta^2 k^2 \gg v_A^2 \gg \nu\eta k^2$, noting that k and k_z are of the same order, to eliminate the $\nu\eta k^4$ term from the numerator of the right hand side, and the $(k_z v_A)^2$ term from the denominator. This ordering is at least marginally satisfied even for the strongest fields and smallest wavelengths relevant to our problem. The resulting equation is

$$\frac{r_l}{2w_l}\Delta\Omega^2 = \frac{k_z^4 v_A^4}{\eta^2 k^4}\frac{k^2}{k_z^2}, \tag{6.22}$$

which gives the relation between B_0 and $\Delta\Omega$ at marginal stability,

$$\frac{B_0^2}{4\pi\rho\eta\sqrt{r_l/2w_l}\Delta\Omega}\frac{k_z}{k} = 1. \tag{6.23}$$

So the critical B_0 for marginal stability scales as

$$B_{0,\mathrm{crit}} \sim \sqrt{\eta}\sqrt{\frac{k}{k_z}}\left(\frac{r_l}{w_l}\right)^{1/4}\sqrt{\Delta\Omega}. \tag{6.24}$$

The scaling with $\Delta\Omega$ matches that found from the global calculations. The different scaling with r_l and w_l compared to the global calculations must be explained by a changing eigenmode structure which would lead to a dependence of k/k_z on r_l and w_l.

6.2.7 Summary of centrifugal instability

- Shear layer rotation profiles are vigorously unstable to the centrifugal instability.
- Like the Kelvin-Helmholtz eigenmodes, eigenmodes of the centrifugal instability act to flatten the shear layer.
- Instability can be suppressed by a magnetic field, with the magnetic field required for stabilization $B_{0,\mathrm{crit}} \sim \sqrt{\Delta\Omega}$.
- Instability can also be suppressed by background rotation, with the critical background rotation $\Omega_{2,\mathrm{crit}} \sim \Delta\Omega$.
- With both background rotation and magnetic field, $\Delta\Omega$ must be greater than a certain value for a given Ω_2 for instability. But for $\Delta\Omega$ above that value, stabilization by the magnetic field occurs as if $\Omega_2 = 0$, with $B_{0,\mathrm{crit}} \sim \sqrt{\Delta\Omega}$.

6.3 Comparison to experimental results

To explain the observations of the Kelvin-Helmholtz instability in the experiment, I propose a model of competition between the Kelvin-Helmholtz and centrifugal instabilities for the free energy in the shear layer.

For the shear layer widths observed experimentally [1] , in the absence of an applied magnetic field or background rotation, the centrifugal instability has growth rates of order $\Delta\Omega$, but the Kelvin-Helmholtz instability only has a growth rate of order $0.1\Delta\Omega$. The centrifugal instability grows and removes free energy from the shear layer. These relatively high-k_z modes are confined near the endcaps, allowing the flow near the midplane of the experiment to remain quiet.

As magnetic field or background rotation are introduced, the growth rate of the centrifugal instability is suppressed, eventually becoming comparable to the growth rate of the Kelvin-Helmholtz instability. The scalings for the damping of the centrifugal instability, constant Λ with magnetic field and constant Ro with rotation, match the experimental observations for the appearance of the Kelvin-Helmholtz instability.

Also note the similarity of the sharp transition to $B_{0,\mathrm{crit}} \sim \sqrt{\Delta\Omega}$ above $\Delta\Omega_{\mathrm{crit}}$ for the linear calculations in the mixed magnetic field and background rotation case (shown in Figure 6.17) and of the experimental results of the Kelvin-Helmholtz destabilization of a Stewartson layer with $\Delta\Omega < \Delta\Omega_{\mathrm{crit}}$ by an applied magnetic field (shown in Figure 5.9). In both cases, the sharp change in the growth rate of the centrifugal instability near $\Omega_{2,\mathrm{crit}}$ results in the background rotation $\Omega_2 < \Omega_{2,\mathrm{crit}}$ having a negligible effect on the magnitude of the applied magnetic field required to stabilize the centrifugal instability and to allow the growth of the Kelvin-Helmholtz instability.

In the case of cyclonic flow with $\Omega_1 = \Omega_3 = 0$ and $\Omega_2 = \Omega_4 \neq 0$, the centrifugal instability is always suppressed because the gradient in specific angular momentum is positive everywhere. The Kelvin-Helmholtz instability in this case has no competition, and so it would be expected to be generated in the absence of overall background rotation or

[1] Because the peak growth rate for the Kelvin-Helmholtz instability scales as $r_l\Delta\Omega/w_l$ whereas the peak growth rate for the centrifugal instability scales only as $\sqrt{r_l/w_l}\Delta\Omega$, the Kelvin-Helmholtz instability will grow faster than the centrifugal instability for a sufficiently small w_l. An estimate of the critical w_l by extrapolating the growth rates computed for each instability at larger w_l suggests that the Kelvin-Helmholtz instability will dominate for $w_l < 0.4$ cm. While this is narrower than any w_l observed experimentally, it is not unreasonably small and could exist at large Ha near the endcaps. In this situation, the Kelvin-Helmholtz instability may grow first with a large m. But it is expected that the effect of the instability would be to increase w_l, ultimately producing the competition between the centrifugal instability and the Kelvin-Helmholtz instability described here.

applied magnetic field. This is consistent with the experimental observation of vigorous Kelvin-Helmholtz instability in the cyclonic regime.

During the initial growth of the Kelvin-Helmholtz instability, the shear layer may be quite thin, encouraging the growth of higher-m modes that are more unstable for small values of w_l. As the instability smooths out the shear layer and decreases the free energy, low-m modes are more unstable, leading to the observation of the $m = 1$ mode in the experiment with $\Lambda \sim O(1)$. Because the Kelvin-Helmholtz mode has a small k ($k = 0$ in the computations), the mode can extend to fill the volume of the experiment, driving strong fluctuations at the midplane even though the rotation profiles there are locally stable to this instability.

For $\Lambda \gg 1$, the reinforcement due to Hartmann currents can be very strong so that the shear layer stays relatively narrow even when there are velocity fluctuations of order the background velocity due to the Kelvin-Helmholtz instability. In this case, the shear layer remains most unstable to larger-m modes even at saturation.

This theory of competition between the Kelvin-Helmholtz and centrifugal instabilities is consistent with most of the experimental observations. It should be noted, though, that in the case of MRI-like runs with varying inner ring speed, there did seem to be a region with Ω_3 near Ω_4 and Ω_2 where $B_{0,\mathrm{crit}} \sim \sqrt{\Omega_1 - \Omega_3}$ rather than $B_{0,\mathrm{crit}} \sim \sqrt{\Omega_3 - \Omega_4}$. In cases with particularly strong Ekman flow relative to the shear between the endcap rings, the effect of the Ekman flow on the shear layer may be more important than the effect of the centrifugal instability.

Chapter 7

Conclusion

The implementation and operation of the UDV diagnostic has provided measurements of fluid velocities in the Princeton MRI experiment, allowing experiments related to the behavior of mean sheared velocity flows in the presence of a magnetic field and their relationship to the search for the MRI, and of the stability of free shear layers generated by shear at the axial boundaries of the experiment. Each of these topics is summarized separately below.

7.1 Magnetorotational instability

Mechanical improvements to the experiment have allowed operation in the region of the critical Rm expected for generation of the MRI, yielding measurements up to 70% of the maximum experimental design speed. It was found that the normalized saturated azimuthal velocity v_θ/v_1 at a point is constant for a given v_A/v_1 below the critical Rm for MRI. It is expected that the growth and saturation of the MRI would lead to deviations from this scaling, although no such deviations beyond the drifts that occur below the critical Rm have been detected. If the most recent MHD simulations of the experiment are to be believed, the change in the azimuthal velocity due to the MRI may be too small to distinguish from the otherwise gradual drifts with changes in rotation rate [Gissinger et al., 2012].

7.1.1 Future work

Determine mechanism controlling behavior of v_θ in the absence of the MRI

The experimentally determined behavior of the saturated azimuthal velocity with applied magnetic field in the absence of the MRI has so far not been explained. An identification of the mechanism producing that scaling would be both interesting and necessary to interpret any deviations from that scaling that may be caused by the MRI.

In the $\Lambda \sim O(1)$ regime where these measurements are made, inertial forces arising from the rotation and $\vec{j} \times \vec{B}$ forces are comparable. So the azimuthal velocity in the bulk of the flow will be determined by a combination of viscous, inertial, and Lorentz forces. Simulations have shown that the application of a magnetic field in this limit acts directly on the flow via the Lorentz force, but also indirectly via magnetic braking of the rotation-induced Ekman flow [Liu, 2008b, Szklarski and Rüdiger, 2007, Khalzov et al., 2010]. The exact balance of these effects is likely to be dependent on geometry and boundary conditions.

There is experimental evidence that modifying the boundary by altering the flow path through the holes in the endcaps or by perturbing the relative height of the endcaps may have an effect on the azimuthal velocity measured at a point. But the measured scaling of the effect of the magnetic field remains consistent for each boundary situation. So although these quirks of the experimental boundary condition do affect the flow, the behavior that v_θ/v_1 is constant for constant v_A/v_1 is relatively robust.

Attempts to recreate the experimentally determined threshold through simulation have so far been unsuccessful, though the reason is unclear. The scaling has been observed experimentally only over a relatively small range of Reynolds number in the experiment, down to $Re \approx 2 \times 10^6$. This is substantially larger than the simulations, which are limited to $Re \sim O(10^4)$. So the discrepancy may be due to a difference in Reynolds number, which is not unreasonable since viscosity plays an important role in the force balance of the boundary layers through which the rotating components communicate with the fluid.

This is an area that would best be explored through further nonlinear MHD simulations. Simulations with larger Re, while computationally expensive, may be necessary to more

closely match the operational regime of the experiment. The velocities measured in the bulk of the fluid are very quiet at saturation and do not seem to have significant 3-D features, so 2-D simulations may be sufficient to recreate the dynamics observed in the experiment. But the experimental measurements do not rule out 3-D effects at the boundaries, such as turbulence in the boundary layers, that may affect the coupling between the bulk of the fluid and the boundaries. If 2-D simulations at large Re fail to reproduce the experimental observations, this might be an indication that 3-D effects in some part of the flow play an important role.

Find robust, experimentally measurable signature of MRI

It may be helpful to find a more sensitive indicator of the MRI than measurement of the fluid velocities. Simulations have predicted a small change, $\sim 2\%$, of the azimuthal velocity due to the MRI [Gissinger et al., 2012]. This change would be at the limit of what is currently measurable with the UDV diagnostic. And, in general, the imperfect bifurcation from Ekman circulation observed in simulations is problematic because it suggests that the change in almost any measurable quantity will be a gradual one, making a thorough understanding of the global behavior of the fluid in the absence of the MRI of the utmost importance.

Some have suggested supplementing the viscous drive of the fluid with additional body forcing, such as through $\vec{j} \times \vec{B}$ forcing from an externally imposed radial current. This could result in a larger saturated amplitude of the MRI eigenmode, potentially leading to a larger v_r that may be measurable. But this would be a fundamental change to the design of the experiment, and would require the expected behavior of the MRI to be entirely reanalyzed.

Other options include direct measurements of the torque at the outer cylinder to detect the enhanced angular momentum transport due to the MRI, or internal magnetic diagnostics to measure the associated Maxwell stress. But again, for the small saturated amplitudes of the instability that are expected, an understanding of the behavior of these quantities in the absence of the MRI is necessary in order to claim that any change from that behavior

is a sign of the MRI.

Here, again, simulations can play an important role. Not only could they be useful to understand the expected effect of the MRI on measurable quantities in the experiment. But they may also be useful to direct efforts to maximize the saturated amplitude of the MRI eigenmode. Different configurations of endcap ring speeds, for example, could lead to a larger saturated amplitude or a sharper transition from the residual Ekman flow.

Mechanical improvements to allow higher Rm operation

Improvements in the mechanical apparatus up to this point have produced useful measurements at 65% of the maximum design speed, with brief runs up to 75% of the maximum design speed. These speeds produce an Rm slightly larger than the computationally determined threshold for the MRI at $\sim 60\%$ of the maximum design speed.

Further improvements in the mechanical apparatus are necessary to generate Rm significantly greater than the critical Rm. The mechanical complexity of the experiment makes for slow progress in this area. Mechanisms for reducing the complexity have been proposed, including electromagnetic coupling of drives to the rotating components to eliminate the shaft seals, but such deviations from the current approach would be a major undertaking.

The easiest mechanical improvements that could be made to the experiment concern the interface between the lip seals and the shafts. The lip seals ride on a chromed surface on the shafts. The surface in many places has worn at the contact point with the lip seal, leading to irregularities in the shaft diameter. This makes the behavior of the seals particularly dependent on their precise axial location along the shaft. It might be beneficial to machine down these sealing surfaces, re-chrome them, grind them to the precise specified diameter, and polish them to minimize seal friction.

It is likely that further weaknesses in the design of the experiment will be exposed at higher rotation speeds. One of the biggest challenges of high speed operation is the increased fluid pressure, which may reach up to 350 psi at the outer cylinder at full speed operation. Problems related to these high pressures, including difficultly maintaining the

relative axial position of rotating components and damage to seal assemblies, have already been uncovered and addressed. But more problems may arise with increasing speed. Future experimenters should be aware of the potential problems presented by these high pressures.

7.2 Kelvin-Helmholtz instability of free shear layers

We have presented results showing a minimum $\Lambda = B_0^2/4\pi\rho\eta\Delta\Omega$ and a maximum finite $Ro = \Delta\Omega/\Omega_2$ for the observation of the Kelvin-Helmholtz instability of a free Shercliff layer and Stewartson layer, respectively. We have explained these observations in terms of a competition for the free energy of the shear layer between the centrifugal instability and the Kelvin-Helmholtz instability. This result is interesting first since the vast majority of the work on the Kelvin-Helmholtz destabilization of free shear layers has been done at the threshold of viscous stabilization, with small Ro or small Re, and, perhaps more interestingly, because the Kelvin-Helmholtz instability is observed throughout the fluid volume even when there is no evidence of the shear layer only a few centimeters from the boundary. In contrast to the eigenmodes of the centrifugal instability, which remain confined to the shear layer, the small radial wavenumbers and even smaller axial wavenumbers for the Kelvin-Helmholtz eigenmodes allow them to fill the volume of the experiment. The eigenmodes of the Kelvin-Helmholtz instability produce a positive contribution to the radial angular momentum transport through their associated Reynolds stress, leading to the measured broadening of the free shear layers observed when $\Lambda \gg 1$.

It is interesting to compare our observations to axisymmetric simulations of the experiment [Hollerbach and Fournier, 2004, Liu, 2008b]. They predicted that the free shear layers generated at the axial boundaries would be Kelvin-Helmholtz unstable. The Kelvin-Helmholtz instability, it was thought, would limit the extension of the shear layer. This is likely correct, although it was not predicted that the unstable Kelvin-Helmholtz modes would still be present throughout the fluid volume even as the shear layers were limited to a region near the boundary.

The generation of the Kelvin-Helmholtz instability by 3-D MHD simulations [Gissinger et al.,

2012] should be viewed as a great success of the agreement between simulation and experiment. The threshold and eigenmode structures for the instability match very well with the experimental observations. The largest discrepancy between experiment and simulation is that the simulations predicted that the free shear layer would penetrate much more deeply than the experimental observations show. Perhaps this is because the numerical simulations are typically limited to Reynolds numbers several orders of magnitude smaller than in the experiment. Indeed, the shear layer was observed to penetrate deeply into the fluid during very slow rotation giving $Re \sim 10^3$, in the range of the computations.

The success of simulations in this case lends confidence to the results from 3-D MHD simulations that explained the observations of unstable nonaxisymmetric modes in a spherical Couette experiment as Kelvin-Helmholtz instability of free shear layers at the tangent cylinder[Hollerbach, 2009, Gissinger et al., 2011], even though the experimental results were initially presented as evidence of the MRI [Sisan et al., 2004].

7.2.1 Future work

Effects of axial variation

The linear stability analysis assumed that the background flow was axially uniform and that the unstable modes were also axially uniform ($k = 0$). The real experiment is bounded axially, leading to an axial variation of the shear layer width as well as axial variation of the unstable mode structure, since the mode amplitude is forced to zero at the boundaries by the no-slip boundary condition.

Details of the effect of axial variation are currently unknown, and would probably be best explored through further 3-D nonlinear MHD simulations. Topics of particular interest are the additional damping of the instability due to magnetic coupling with the no-slip axial boundary layer, as well as the selection of a dominant azimuthal mode number in a shear layer with axially varying width, and hence axial variation in the locally most-unstable azimuthal mode number.

Effect of large-scale poloidal circulation

There is experimental evidence that the large-scale poloidal flow associated with Ekman circulation can be an additional factor in disrupting the shear layer, inhibiting the appearance of the Kelvin-Helmholtz instability. 2-D nonlinear MHD simulations have shown that this flow can indeed have an effect on the shear layer [Spence et al., 2012], though these simulations could not generate the Kelvin-Helmholtz instability because they were axisymmetric.

Since there is a small base of experimental measurements relevant to this subject, it would be useful to carry out further experiments in the regime where large-scale poloidal circulation is expected to be most important, with Ω_3 near Ω_4, but $\Omega_1 \gg \Omega_3$. It might also be interesting to investigate the role of poloidal circulation in the `cyclonic` configuration, where there will be no effect of the centrifugal instability and where poloidal circulation would be the principle mechanism for disruption of the free shear layer.

Further simulations would also be helpful here. While 2-D simulations have shown effects on the shear layer, 3-D simulations would be capable of generating the Kelvin-Helmholtz instability and would provide a better comparison for the experimental measurements.

Stabilization of instability with very large magnetic field

Experimental measurements have hinted at a stabilization of the Kelvin-Helmholtz instability with vary large applied magnetic field strengths ($\Lambda \gg 1$). Such an effect might be expected, both because the magnetic field will act to damp axial variations in the motion that occur between the unstable eigenmode and the no-slip axial boundary condition, and because the Kelvin-Helmholtz instability will be viscously stabilized for very narrow shear layer widths.

At the slowest rotation rates studied, $\Omega_1 = 0.25$ rpm, the steady state magnetic fields applied were not large enough to stabilize the instability. It is possible that at even slower rotation rates it could be restabilized, although this would also be entering a regime where viscous effects become important even in the absence of a magnetic field. Measurements

using the UDV system would be challenging because of the very small fluid velocities, but it is possible that meaningful measurements could be made.

Again, this is an area where 3-D nonlinear MHD simulations could provide interesting information. Most of the work so far has focused on reproducing the minimum B_0 for appearance of the Kelvin-Helmholtz instability because of the relevance to the experimental measurements, but simulations addressing a maximum B_0 should also be possible.

Measurement of instability in PROMISE-2 geometry

It would be very interesting to attempt to generate this Kelvin-Helmholtz instability in the PROMISE-2 experiment, a cylindrical Taylor-Couette MHD experiment with split endcaps similar to our own but with a slightly different geometry. The brief calculations presented in Appendix E indicate the experimental parameters that we would expect to generate the instability in that device. In particular, the effect of the larger relative height of that experiment might shed some light on some of the open questions concerning axial variation of the instability.

Appendix A

Parameters and dimensionless numbers used in this thesis

Table A.1: Symbols used in this thesis

Symbol	Description
r_1	Inner cylinder radius
r_2	Outer cylinder radius
h	Experiment height
Ω_1	Inner cylinder rotation rate
Ω_2	Outer cylinder rotation rate
Ω_3	Inner ring rotation rate
Ω_4	Outer ring rotation rate
$\Delta\Omega$	Change in angular velocity across ring gap, $\Delta\Omega = \Omega_3 - \Omega_4$
v_1	Azimuthal velocity at inner cylinder
v_2	Azimuthal velocity of outer cylinder
B_0	Applied magnetic field strength
v_A	Alfvén speed, $v_A = B_0/\sqrt{4\pi\rho}$
ρ	Density of fluid
ν	Kinematic viscosity of fluid
η	Magnetic diffusivity of fluid
r_l	Radial location of a free shear layer
w_l	Half-width of a free shear layer
m	Azimuthal mode number
k	Axial wavenumber

Table A.2: Dimensionless numbers used in this thesis

Symbol	Definition	Description
Re	$\frac{\Omega_1 r_1 (r_2 - r_1)}{\nu}$	Reynolds number: ratio of inertial force to viscous force in the momentum equation
Rm	$\frac{\Omega_1 r_1 (r_2 - r_1)}{\eta}$	Magnetic Reynolds number: ratio of induction to resistive dissipation
Pm	$\frac{\nu}{\eta}$	Magnetic Prandtl number: ratio of viscous to resistive dissipation
Λ	$\frac{B_0^2}{4\pi\rho\eta(\Omega_3 - \Omega_4)}$	Elsasser number: ratio of $\vec{j} \times \vec{B}$ force to inertial force in the momentum equation
Ha	$\frac{B_0 (r_2 - r_1)}{\sqrt{4\pi\rho\eta\nu}}$	Hartmann number: square root of the ratio of $\vec{j} \times \vec{B}$ force to viscous force in the momentum equation
Ro	$\frac{\Omega_3 - \Omega_4}{\Omega_2}$	Rossby number: ratio of the inertial force to the Coriolis force in the momentum equation

Appendix B

UDV beam geometry transformations

Two principle angles are used to describe the direction of the centerline of an ultrasound beam emitted by a UDV transducer. The first angle, A, describes the opening half-angle of a cone centered on the radial unit vector and with its vertex at the transducer location at the outer cylinder. The second angle, B, describes the angular position of the centerline of the ultrasound beam on the surface of that cone. $B = 0$ for the beam traveling on the top-most trajectory on the cone, $B = 90^\circ$ for the right-most trajectory, and $B = -90^\circ$ for the left-most trajectory.

As illustrated in Figure B.1, at a distance d along the beam, the beam will have traveled the following distances in each of the Cartesian coordinate directions:

$$\begin{aligned} \Delta x &= d \cos A, \\ \Delta y &= d \sin A \sin B, \\ \Delta z &= d \sin A \cos B. \end{aligned} \tag{B.1}$$

The transformation of this point to cylindrical coordinates can be accomplished by noting that $r^2 = (\Delta y)^2 + (r_2 - \Delta x)^2$, where r_2 is the radius of the transducer face (typically the outer cylinder radius), and that $\sin\theta = \Delta y / r$:

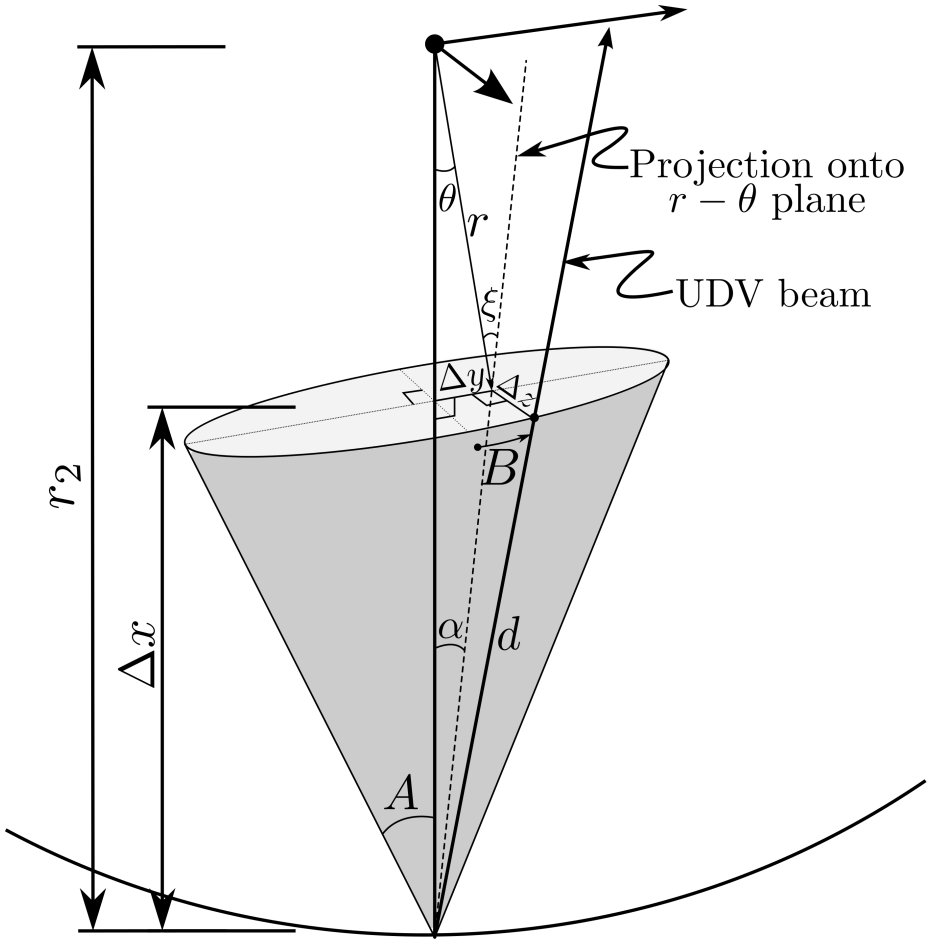

Figure B.1: Geometry for transformation of UDV signals into cylindrical coordinates. The centerline of the ultrasound beam lies on a cone centered on a purely radial vector with an opening half-angle A and with its apex at the transducer location at the outer cylinder. The angle B describes the beam's angular location on the surface of the cone, with $B = 0$ corresponding to the trajectory confined in the $r - z$ plane with increasing z along the length of the beam, and B increasing as the beam moves clockwise from the perspective of an observer at the outer cylinder, facing inward.

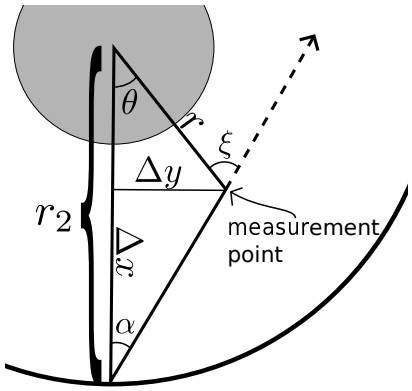

Figure B.2: Geometry of the projection of the centerline of the transducer beam onto the $r-\theta$ plane.

$$
\begin{aligned}
r &= \sqrt{d^2 \sin^2 A \sin^2 B + (r_2 - d\cos A)^2}, \\
\theta &= \arcsin\left[\frac{d \sin A \sin B}{r}\right] = \arcsin\left[\frac{d \sin A \sin B}{\sqrt{d^2 \sin^2 A \sin^2 B + (r_2 - d\cos A)^2|}}\right], \\
z &= d \sin A \cos B.
\end{aligned}
\tag{B.2}
$$

We now know the location of each measurement in cylindrical coordinates. But we also wish to determine the unit vector $\hat{u}$ in the direction of the beam in cylindrical coordinates at an arbitrary point along its path. We need to know this so that we can correctly determine the contribution from each of the velocity components on the measured velocity, $v_{\text{udv}} = \vec{v} \cdot \hat{u}$. We can express $\hat{u}$ in the form

$$\hat{u} = \frac{a\hat{r} + b\hat{\theta} + c\hat{z}}{\sqrt{a^2 + b^2 + c^2}}. \tag{B.3}$$

We will find a, b, and c by considering a movement of an infinitesimal distance l along the ultrasound beam at a distance d. The distance moved in the $\hat{z}$ direction gives $c = l \sin A \cos B$. The length of the projection of this movement into the $r-\theta$ plane, $l' = \sqrt{a^2 + b^2}$, can be found by solving $l^2 = a^2 + b^2 + c^2 = (l')^2 + (l \sin A \cos B)^2$, yielding $l' = \sqrt{l^2 - l^2 \sin^2 A \sin^2 B}$.

The contributions to l' by the $\hat{r}$ and $\hat{\theta}$ components depend on ξ, the angle between the projection of the beam into $r-\theta$ plane and the radial unit vector at the distance d. An

illustration of the projection of the UDV beam onto the $r-\theta$ plane is shown in Figure B.2. The geometry shows us that

$$\xi = \pi - (\pi/2 - \theta) - (\pi/2 - \alpha) = \theta + \alpha, \tag{B.4}$$

where α is the angle between the projection of the beam in the $r-\theta$ plane and the radial vector pointing at the UDV transducer:

$$\tan\alpha = \Delta y/\Delta x \quad \Rightarrow \quad \alpha = \arctan(\tan A \sin B). \tag{B.5}$$

Once we know ξ, we can find a and b by noting that $a = -l'\cos\xi$ and $b = l'\sin\xi$. Since the sum $a^2 + b^2 + c^2 = l^2$, we divide each component by our original infinitesimal distance to yield the normalized components of the unit vector,

$$\hat{u} = -\left[\sqrt{(1-\sin^2 A\cos^2 B)}\cos\xi\right]\hat{r} + \left[\sqrt{(1-\sin^2 A\cos^2 B)}\sin\xi\right]\hat{\theta} + [\sin A\cos B]\,\hat{z}. \tag{B.6}$$

Two other useful quantities that are readily found by algebra are the distance d that must be traveled along the beam to reach a radius r,

$$d = \frac{r_2\cos A - \sqrt{r^2(\sin^2 A\sin^2 B + \cos^2 A) - r_2^2\sin^2 A\sin^2 B}}{\sin^2 A\sin^2 B + \cos^2 A}, \tag{B.7}$$

and the minimum radius through which the beam passes

$$r_{\min} = \left|\frac{r_2\sin A\sin B}{\sqrt{\sin^2 A\sin^2 B + \cos^2 A}}\right|. \tag{B.8}$$

Appendix C

Equations of incompressible, nonideal MHD

We wish to find the equations of nonideal, incompressible MHD. We start with three of Maxwell's equations plus Ohm's law in CGS units:

$$\nabla \times \vec{E} = -\frac{1}{c}\frac{\partial \vec{B}}{\partial t} \qquad \text{Faraday's law,} \tag{C.1}$$

$$\nabla \times \vec{B} = \frac{1}{c}\frac{\partial \vec{E}}{\partial t} + \frac{4\pi}{c}\vec{j} \qquad \text{Ampère's law,} \tag{C.2}$$

$$\nabla \cdot \vec{B} = 0 \qquad \text{No monopoles,} \tag{C.3}$$

$$\frac{4\pi\eta}{c^2}\vec{j} = \vec{E} + \frac{1}{c}\vec{v} \times \vec{B} \qquad \text{Ohm's law,} \tag{C.4}$$

where η is the magnetic diffusivity in units of cm^2/s. We make the normal MHD assumption that the displacement current is zero, leading to a simplified version of Ampère's law

$$\nabla \times \vec{B} = \frac{4\pi}{c}\vec{j}. \tag{C.5}$$

Induction equation

If we take the curl of Equation C.4, substitute for $\nabla \times \vec{E}$ in Equation C.1, and then substitute for $\vec{j}$ from Equation C.5, we find

$$-\frac{1}{c}\frac{\partial \vec{B}}{\partial t} = \nabla \times \left[\frac{4\pi\eta}{c^2}\vec{j} - \frac{1}{c}\vec{v} \times \vec{B}\right] = \nabla \times \left[\frac{\eta}{c}\nabla \times \vec{B} - \frac{1}{c}\vec{v} \times \vec{B}\right]. \tag{C.6}$$

We can now rearrange the equation and make use of the vector identity $\nabla\times(\nabla\times\vec{B}) = -\nabla^2\vec{B}$, when $\nabla \cdot \vec{B} = 0$,

$$\frac{\partial \vec{B}}{\partial t} - \nabla \times \left(\vec{v} \times \vec{B}\right) = \eta\nabla^2\vec{B}. \tag{C.7}$$

This is the magnetic field induction equation in nonideal MHD. In the incompressible limit, where

$$\nabla \cdot \vec{v} = 0, \tag{C.8}$$

the induction equation can be rewritten

$$\frac{\partial \vec{B}}{\partial t} + (\vec{v} \cdot \nabla)\vec{B} - (\vec{B} \cdot \nabla)\vec{v} = \eta\nabla^2\vec{B}. \tag{C.9}$$

Momentum equation

The momentum equation is found by considering Newton's second law, $m\vec{a} = \vec{F}$, for a fluid element, including pressure forces, electromagnetic $\vec{j} \times \vec{B}$ forces, and forces due to the divergence of the viscous stress,

$$\rho\left(\frac{d\vec{v}}{dt}\right) = -\nabla p + \frac{\vec{j} \times \vec{B}}{c} + \mu\nabla^2\vec{v}, \tag{C.10}$$

where ρ is the fluid density, μ is the dynamic viscosity, and p is the hydrodynamic pressure. We now expand the convective derivative $d/dt = \partial/\partial t + \vec{v} \cdot \nabla$ and divide by ρ to find

$$\frac{\partial \vec{v}}{\partial t} + (\vec{v} \cdot \nabla)\,\vec{v} = -\frac{1}{\rho}\nabla p + \frac{1}{\rho c}\vec{j} \times \vec{B} + \nu\nabla^2\vec{v}, \tag{C.11}$$

where $\nu = \mu/\rho$ is the kinematic viscosity in units of cm^2/s.

We can make a substitution for $\vec{j}$ in the $\vec{j} \times \vec{B}$ term using Ampère's law

$$\begin{aligned}\frac{1}{\rho c}\vec{j} \times \vec{B} = \frac{1}{4\pi\rho}\left(\nabla \times \vec{B}\right) \times \vec{B} &= \frac{1}{4\pi\rho}\left[-\left(\nabla\vec{B}\right) \cdot \vec{B} + \left(\vec{B} \cdot \nabla\right)\vec{B}\right] \\ &= \frac{1}{4\pi\rho}\left[-\frac{1}{2}\nabla\vec{B}^2 + \left(\vec{B} \cdot \nabla\right)\vec{B}\right],\end{aligned} \tag{C.12}$$

leading to a new form for the momentum equation

$$\frac{\partial \vec{v}}{\partial t} + (\vec{v} \cdot \nabla)\,\vec{v} = -\frac{1}{\rho}\nabla p - \frac{1}{8\pi\rho}\nabla\vec{B}^2 + \frac{1}{4\pi\rho}\left(\vec{B} \cdot \nabla\right)\vec{B} + \nu\nabla^2\vec{v}. \tag{C.13}$$

Finally, we can rewrite the momentum equation using a combined hydrodynamic and magnetic pressure $P = p + \vec{B}^2/8\pi$.

$$\frac{\partial \vec{v}}{\partial t} + (\vec{v} \cdot \nabla)\, \vec{v} = -\frac{1}{\rho}\nabla P + \frac{1}{4\pi\rho}\left(\vec{B} \cdot \nabla\right) \vec{B} + \nu \nabla^2 \vec{v}. \tag{C.14}$$

Appendix D

Global linear stability code

This chapter describes the development of a computer code to solve the linearized, nonideal, incompressible MHD equations with zeroth-order azimuthal velocity and axial magnetic field in a cylindrical geometry that is periodic in the axial and azimuthal directions. This work follows a similar approach to that used to examine the MRI in Goodman and Ji [2002], though the approach here is more general, allowing nonaxisymmetric modes, arbitrary background azimuthal velocity distributions, and being capable of solving for all eigenmodes of the system, not only the fastest-growing eigenmode.

D.1 Linearized equations

We start with the equations of incompressible, nonideal MHD, summarized here from Equations C.9, C.14, C.3, and C.8, where a dot over a quantity represents a derivative with respect to time, $\partial/\partial t$.

$$\dot{\vec{B}} + \vec{v}\cdot\nabla\vec{B} - \vec{B}\cdot\nabla\vec{v} = \eta\nabla^2\vec{B}, \tag{D.1}$$

$$\dot{\vec{v}} + \vec{v}\cdot\nabla\vec{v} + \frac{1}{\rho}\nabla P - \frac{\vec{B}\cdot\nabla\vec{B}}{4\pi\rho} = \nu\nabla^2\vec{v}, \tag{D.2}$$

$$\nabla\cdot\vec{B} = 0, \tag{D.3}$$

$$\nabla\cdot\vec{v} = 0. \tag{D.4}$$

We assume a background state with zeroth-order $\vec{B} = B_0\hat{z}$ and $\vec{v} = r\Omega(r)\hat{\theta}$. First order quantities will be denoted by a δ.

We define two radial derivative operators, $\partial_r \equiv \frac{\partial}{\partial r}$ and $\partial_r^\dagger \equiv \frac{\partial}{\partial r} + \frac{1}{r}$. The combination $\partial_r\partial_r^\dagger = \frac{\partial^2}{\partial r^2} - \frac{1}{r^2} + \frac{1}{r}\partial_r$.

Radial component of the induction equation

The radial component of the induction equation is

$$\dot{B}_r + v_r\partial_r B_r + \frac{v_\theta}{r}\partial_\theta B_r + v_z\partial_z B_r - B_r\partial_r v_r - \frac{B_\theta}{r}\partial_\theta v_r - B_z\partial_z v_r = \eta\left(\nabla^2 B_r - \frac{2}{r^2}\partial_\theta B_\theta - \frac{1}{r^2}B_r\right). \tag{D.5}$$

After linearization, keeping only 1st-order quantities, this becomes

$$\delta\dot{B}_r + \Omega\partial_\theta\delta B_r - B_0\partial_z\delta v_r = \eta\left[\left(\partial_r\partial_r^\dagger + \frac{1}{r^2}\partial_\theta^2 + \partial_z^2\right)\delta B_r - \frac{2}{r^2}\partial_\theta\delta B_\theta\right]. \tag{D.6}$$

Azimuthal component of the induction equation

The azimuthal component of the induction equation is

$$\dot{B}_\theta + v_r\partial_r B_\theta + \frac{v_\theta}{r}\partial_\theta B_\theta + v_z\partial_z B_\theta + \frac{v_\theta}{r}B_r - B_r\partial_r v_\theta - \frac{1}{r}B_\theta\partial_\theta v_\theta - B_z\partial_z v_\theta - \frac{v_r}{r}B_\theta = \eta\left(\nabla^2 B_\theta + \frac{2}{r^2}\partial_\theta B_r - \frac{1}{r^2}B_\theta\right). \tag{D.7}$$

After linearization, this becomes

$$\delta\dot{B}_\theta + \Omega\partial_\theta\delta B_\theta - B_0\partial_z\delta v_\theta - \delta B_r r\partial_r\Omega = \eta\left[\left(\partial_r\partial_r^\dagger + \frac{1}{r^2}\partial_\theta^2 + \partial_z^2\right)\delta B_\theta + \frac{2}{r^2}\partial_\theta\delta B_r\right]. \tag{D.8}$$

Axial component of the induction equation

The axial component of the induction equation is

$$\dot{B}_z + v_r\partial_r B_z + \frac{v_\theta}{r}\partial_\theta B_z + v_z\partial_z B_z - B_r\partial_r v_z - \frac{1}{r}B_\theta\partial_\theta v_z - B_z\partial_z v_z = \eta\left[\frac{1}{r}\partial_r + \partial_r^2 + \frac{1}{r^2}\partial_\theta^2 + \partial_z^2\right]B_z. \tag{D.9}$$

After linearization this becomes

$$\delta\dot{B}_z + \Omega\partial_\theta\delta B_z - B_0\partial_z\delta v_z = \eta\left[\partial_r^\dagger\partial_r + \frac{1}{r^2}\partial_\theta^2 + \partial_z^2\right]\delta B_z. \tag{D.10}$$

Radial component of the momentum equation

The radial component of the momentum equation is

$$\begin{aligned} &\dot{v_r} + v_r\partial_r v_r + \frac{v_\theta}{r}\partial_\theta v_r + v_z\partial_z v_r - \frac{v_\theta^2}{r} + \frac{1}{\rho}\partial_r P \\ &-\frac{1}{4\pi\rho}\left(B_r\partial_r B_r + \frac{B_\theta}{r}\partial_\theta B_r + B_z\partial_z B_r - \frac{B_\theta^2}{r}\right) \\ &\qquad = \nu\left(\nabla^2 v_r - \frac{2}{r^2}\partial_\theta v_\theta - \frac{1}{r^2}v_r\right). \end{aligned} \tag{D.11}$$

After linearization this becomes

$$\begin{aligned} &\delta\dot{v_r} + \Omega\partial_\theta\delta v_r - 2\Omega\delta v_\theta + \partial_r\frac{\delta P}{\rho} - \frac{B_0}{4\pi\rho}\partial_z\delta B_r \\ &\quad = \nu\left[\left(\partial_r\partial_r^\dagger + \frac{1}{r^2}\partial_\theta^2 + \partial_z^2\right)\delta v_r - \frac{2}{r^2}\partial_\theta\delta v_\theta\right]. \end{aligned} \tag{D.12}$$

Azimuthal component of the momentum equation

The azimuthal component of the momentum equation is

$$\begin{aligned} &\dot{v_\theta} + v_r\partial_r v_\theta + \frac{v_\theta}{r}\partial_\theta v_\theta + v_z\partial_z v_\theta + \frac{v_\theta v_r}{r} + \frac{1}{\rho}\frac{1}{r}\partial_\theta P \\ &-\frac{1}{4\pi\rho}\left[B_r\partial_r B_\theta + \frac{B_\theta}{r}\partial_\theta B_\theta + B_z\partial_z B_\theta + \frac{B_\theta B_r}{r}\right] \\ &\qquad = \nu\left(\nabla^2 v_\theta + \frac{2}{r^2}\partial_\theta v_r - \frac{1}{r^2}v_\theta\right). \end{aligned} \tag{D.13}$$

After linearization this becomes

$$\begin{aligned} &\delta\dot{v_\theta} + \delta v_r\partial_r^\dagger(r\Omega) + \Omega\partial_\theta\delta v_\theta + \frac{1}{r}\partial_\theta\frac{\delta P}{\rho} - \frac{B_0}{4\pi\rho}\partial_z\delta B_\theta \\ &\quad = \nu\left[\left(\partial_r\partial_r^\dagger + \frac{1}{r^2}\partial_\theta^2 + \partial_z^2\right)\delta v_\theta + \frac{2}{r^2}\partial_\theta\delta v_r\right]. \end{aligned} \tag{D.14}$$

Axial component of the momentum equation

The axial component of the momentum equation is

$$\begin{aligned} &\dot{v_z} + v_r\partial_r v_z + \frac{v_\theta}{r}\partial_\theta v_z + v_z\partial_z v_z + \frac{1}{\rho}\partial_z P \\ &-\frac{1}{4\pi\rho}\left[B_r\partial_r B_z + \frac{B_\theta}{r}\partial_\theta B_z + B_z\partial_z B_z\right] \\ &\qquad = \nu\left[\frac{1}{r}\partial_r + \partial_r^2 + \frac{1}{r^2}\partial_\theta^2 + \partial_z^2\right]v_z. \end{aligned} \tag{D.15}$$

After linearization this becomes

$$\delta\dot{v}_z + \Omega\partial_\theta\delta v_z + \partial_z\frac{\delta P}{\rho} - \frac{B_0}{4\pi\rho}\partial_z\delta B_z = \nu\left[\partial_r^\dagger\partial_r + \frac{1}{r^2}\partial_\theta^2 + \partial_z^2\right]\delta v_z. \tag{D.16}$$

Constraint equations

The equation of incompressibility, $\nabla\cdot\vec{v} = 0$ is

$$\partial_r^\dagger\delta v_r + \frac{1}{r}\partial_\theta\delta v_\theta + \partial_z\delta v_z = 0, \tag{D.17}$$

and $\nabla\cdot\vec{B} = 0$ is

$$\partial_r^\dagger\delta B_r + \frac{1}{r}\partial_\theta\delta B_\theta + \partial_z\delta B_z = 0. \tag{D.18}$$

D.2 Forms of perturbations

These linearized equations will be evaluated to find modes with an arbitrary radial dependence that grow exponentially with a growth rate γ, and that vary periodically in $\hat{\theta}$ and $\hat{z}$ with mode numbers m and k, respectively[1] . The equations suggest the phase relation between the various components in $\hat{z}$, leading to the following forms for the first-order perturbations:

$$\begin{aligned}
\delta B_r/\sqrt{4\pi\rho} &= \mathrm{Re}\{\beta_r(r)e^{\gamma t+im\theta}\cos kz\}, & \delta v_r &= \mathrm{Re}\{\phi_r(r)e^{\gamma t+im\theta}\sin kz\},\\
\delta B_\theta/\sqrt{4\pi\rho} &= \mathrm{Re}\{\beta_\theta(r)e^{\gamma t+im\theta}\cos kz\}, & \delta v_\theta &= \mathrm{Re}\{\phi_\theta(r)e^{\gamma t+im\theta}\sin kz\},\\
\delta B_z/\sqrt{4\pi\rho} &= \mathrm{Re}\{\beta_z(r)e^{\gamma t+im\theta}\sin kz\}, & \delta v_z &= \mathrm{Re}\{\phi_z(r)e^{\gamma t+im\theta}\cos kz\},\\
\delta P/\rho &= \mathrm{Re}\{\Pi(r)e^{\gamma t+im\theta}\sin kz\}.
\end{aligned} \tag{D.19}$$

The quantities β, ϕ, and Π are complex, holding information about both the magnitude and phase of these components as functions of r. Following the convention common in harmonic analysis, the real parts of the perturbed forms are evaluated to find physically

[1]The linearized quantities have a time behavior that goes as $e^{\gamma t}$. Comparing to the time behavior for the form of a wave traveling in the positive direction, $e^{i(\vec{k}\cdot\vec{x}-\omega t)}$, we see that $\mathrm{Re}\{\gamma\} = \mathrm{Im}\{\omega\}$, and $\mathrm{Im}\{\gamma\} = -\mathrm{Re}\{\omega\}$. So the growth rate of the mode is given by $\mathrm{Re}\{\gamma\}$, and the oscillation frequency is given by $-\mathrm{Im}\{\gamma\}$.

meaningful quantities. Because the equations are linear, we are justified in dropping the 'Re' when rewriting the equations in terms of these perturbed quantities. Note that we have made use of the Alfvén speed $v_A = B_0/\sqrt{4\pi\rho}$:

$$\gamma\beta_r + im\Omega\beta_r - kv_A\phi_r = \eta\left[\left(\partial_r\partial_r^\dagger - \frac{m^2}{r^2} - k^2\right)\beta_r - \frac{2im}{r^2}\beta_\theta\right], \tag{D.20}$$

$$\gamma\beta_\theta + im\Omega\beta_\theta - kv_A\phi_\theta - r(\partial_r\Omega)\beta_r = \eta\left[\left(\partial_r\partial_r^\dagger - \frac{m^2}{r^2} - k^2\right)\beta_\theta + \frac{2im}{r^2}\beta_r\right], \tag{D.21}$$

$$\gamma\beta_z + im\Omega\beta_z + kv_A\phi_z = \eta\left[\left(\partial_r^\dagger\partial_r - \frac{m^2}{r^2} - k^2\right)\beta_z\right], \tag{D.22}$$

$$\gamma\phi_r + im\Omega\phi_r - 2\Omega\phi_\theta + \partial_r\Pi + kv_A\beta_r = \nu\left[\left(\partial_r\partial_r^\dagger - \frac{m^2}{r^2} - k^2\right)\phi_r - \frac{2im}{r^2}\phi_\theta\right], \tag{D.23}$$

$$\gamma\phi_\theta + im\Omega\phi_\theta + \phi_r\partial_r^\dagger(r\Omega) + \frac{im}{r}\Pi + kv_A\beta_\theta = \nu\left[\left(\partial_r\partial_r^\dagger - \frac{m^2}{r^2} - k^2\right)\phi_\theta + \frac{2im}{r^2}\phi_r\right], \tag{D.24}$$

$$\gamma\phi_z + im\Omega\phi_z + k\Pi - kv_A\beta_z = \nu\left[\left(\partial_r^\dagger\partial_r - \frac{m^2}{r^2} - k^2\right)\phi_z\right], \tag{D.25}$$

$$\partial_r^\dagger\phi_r + \frac{im}{r}\phi_\theta - k\phi_z = 0, \tag{D.26}$$

$$\partial_r^\dagger\beta_r + \frac{im}{r}\beta_\theta + k\beta_z = 0. \tag{D.27}$$

D.3 Reduced set of equations

We can reduce the set of equations by applying the operator $\partial_r^\dagger$ to Equation D.23, (im/r) to Equation D.24, and $-k$ to Equation D.25, and then summing the equations. The following relations are useful in casting some of the terms into the correct form for elimination by the constraint equations:

$$\frac{1}{r}\partial_r\partial_r^\dagger = \partial_r^\dagger\partial_r\frac{1}{r} - \frac{2}{r^3} + \frac{2}{r^2}\partial_r, \tag{D.28}$$

$$\partial_r^\dagger\frac{1}{r^2} = \frac{1}{r^2}\partial_r^\dagger - \frac{2}{r^3}. \tag{D.29}$$

The following constraint equation is then produced:

$$im\left(\frac{2\Omega}{r} + 2\partial_r\Omega\right)\phi_r - \partial_r^\dagger\left(2\Omega\phi_\theta\right) + \left(\partial_r^\dagger\partial_r - \frac{m^2}{r^2} - k^2\right)\Pi = 0. \tag{D.30}$$

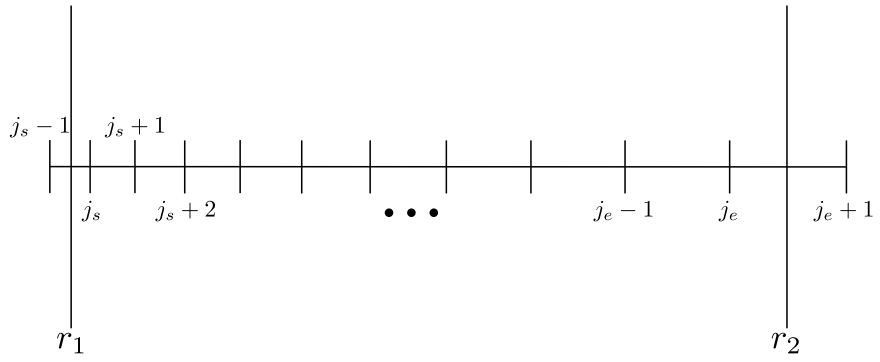

Figure D.1: Radial grid used for the discretization of the linearized MHD equations. There is one ghost zone outside of each boundary, which is used to specify the boundary conditions. The grid is equally spaced in $x = \ln r$.

We will solve the system of equations formed by Equations D.20, D.21, D.23, D.25, and D.30 for the quantities β_r, β_θ, ϕ_r, ϕ_θ, and Π. β_z and ϕ_z can be found from $\nabla \cdot \vec{B} = 0$ and $\nabla \cdot \vec{v} = 0$ if desired.

D.4 Discretization

Again following Goodman and Ji [2002], we use a radial grid that is equally spaced in $x = \ln r$, as shown in Figure D.1. The radial derivatives can be written in terms of the new coordinate x: $\partial_r = (1/r)\partial_x$ and $\partial_r^2 = -(1/r^2)\partial_x + (1/r^2)\partial_x^2$. This means that $\partial_r \partial_r^\dagger = (1/r^2)\partial_x^2 - (1/r^2)$ and $\partial_r^\dagger \partial_r = (1/r^2)\partial_x^2$.

The equations are evaluated with second-order centered differences. The quantity $\beta_{r,j}$ indicates the value of β_r at the jth grid cell. Δx indicates the size of the grid step.

The following finite difference equations are found:

$$\gamma\beta_{r,j} = -\left(\frac{2\eta}{r_j^2\Delta x^2} + \frac{\eta}{r_j^2} + \frac{\eta m^2}{r_j^2} + \eta k^2 + im\Omega_j\right)\beta_{r,j} + \frac{\eta}{r_j^2\Delta x^2}(\beta_{r,j+1} + \beta_{r,j-1}) - \frac{2im\eta}{r_j^2}\beta_{\theta,j} + kv_A\phi_{r,j}, \tag{D.31}$$

$$\gamma\beta_{\theta,j} = -\left(\frac{2\eta}{r_j^2\Delta x^2} + \frac{\eta}{r_j^2} + \frac{\eta m^2}{r_j^2} + \eta k^2 + im\Omega_j\right)\beta_{\theta,j} + \frac{\eta}{r_j^2\Delta x^2}(\beta_{\theta,j+1} + \beta_{\theta,j-1}) + \left[\frac{\Omega_{j+1} - \Omega_{j-1}}{2\Delta x} + \frac{2im\eta}{r_j^2}\right]\beta_{r,j} + kv_A\phi_{\theta,j}, \tag{D.32}$$

$$\gamma\phi_{r,j} = -\left(\frac{2\nu}{r_j^2\Delta x^2} + \frac{\nu}{r_j^2} + \frac{\nu m^2}{r_j^2} + \nu k^2 + im\Omega_j\right)\phi_{r,j} + \frac{\nu}{r_j^2\Delta x^2}(\phi_{r,j+1} + \phi_{r,j-1}) + \left[2\Omega_j - \frac{2im\nu}{r_j^2}\right]\phi_{\theta,j} - kv_A\beta_{r,j} - \frac{1}{2r_j\Delta x}\left(\Pi_{j+1} - \Pi_{j-1}\right), \tag{D.33}$$

$$\gamma\phi_{\theta,j} = -\left(\frac{2\nu}{r_j^2\Delta x^2} + \frac{\nu}{r_j^2} + \frac{\nu m^2}{r_j^2} + \nu k^2 + im\Omega_j\right)\phi_{\theta,j} + \frac{\nu}{r_j^2\Delta x^2}(\phi_{\theta,j+1} + \phi_{\theta,j-1}) + \left[\frac{2im\nu}{r_j^2} - 2\Omega_j - \frac{1}{2\Delta x}\left(\Omega_{j+1} - \Omega_{j-1}\right)\right]\phi_{r,j} - kv_A\beta_{\theta,j} - \frac{im}{r_j}\Pi_j, \tag{D.34}$$

$$0 = \left[\frac{2im\Omega_j}{r_j} + \frac{im}{r_j\Delta x}(\Omega_{j+1} - \Omega_{j-1})\right]\phi_{r,j} - \frac{2\Omega_j}{r_j}\phi_{\theta,j} - \frac{1}{r_j\Delta x}\left(\Omega_{j+1}\phi_{\theta,j+1} - \Omega_{j-1}\phi_{\theta,j-1}\right) - \left[\frac{2}{r_j^2\Delta x^2} + \frac{m^2}{r_j^2} + k^2\right]\Pi_j + \frac{1}{r_j^2\Delta x^2}\left(\Pi_{j+1} + \Pi_{j-1}\right). \tag{D.35}$$

D.5 Boundary conditions

Boundary conditions are implemented by a set of constraint equations at the inner and outer cylinders.

D.5.1 Velocity boundary conditions

The hydrodynamic boundary conditions on ϕ_r and ϕ_θ are satisfied by $\phi_r = 0$ (no inflow) and $\phi_\theta = 0$ (no slip) at the boundary. There is a further no-slip constraint on ϕ_z. Because ϕ_z is not being solved for in the equations, this is satisfied by setting $\partial_r^\dagger\phi_r = 0$ at the boundary, implying $\phi_z = 0$ by the incompressibility constraint. Since we have already specified that $\phi_r = 0$, this means that $\partial_r\phi_r = 0$ as well.

In the code, the constraints on ϕ_r are specified by setting the values in the ghost zones

$$\phi_{r,js-1} = 0, \quad \phi_{r,js} = 0, \tag{D.36}$$

$$\phi_{r,je+1} = 0, \quad \phi_{r,je} = 0, \tag{D.37}$$

$$\phi_{\theta,js-1} + \phi_{\theta,js} = 0, \tag{D.38}$$

$$\phi_{\theta,je+1} + \phi_{\theta,je} = 0. \tag{D.39}$$

D.5.2 Magnetic boundary condition: perfectly conducting

For this boundary condition, we consider the radial boundaries to be perfectly conducting cylinders, rotating at a fixed speed. We make use of the general boundary condition for a fluid with a moving interface [Stix, 1992],

$$\hat{n} \times \left(\vec{E}_f - \vec{E}_c\right) = \frac{\vec{v} \cdot \hat{n}}{c} \left(\vec{B}_f - \vec{B}_c\right) = 0 \quad \text{for } \vec{v} \cdot \hat{n} = 0. \tag{D.40}$$

where $\hat{n}$ is the unit vector normal to the conductor, pointing into the fluid, and 'f' and 'c' indicate fluid and cylinder values. Since the velocity at the boundary is purely azimuthal, where the normal vector is radial, this states that the tangential component of the electric field across the boundary is continuous.

For stationary conductors, the internal electric field is zero. But we are considering a moving conductor, in which an electric field can be generated to balance $\vec{v} \times \vec{B}$ in Ohm's law:

$$\vec{E} + \frac{1}{c}\vec{v} \times \vec{B} = \frac{4\pi\eta}{c^2}\vec{j} = 0 \quad \text{for } \eta = 0. \tag{D.41}$$

We note that $\vec{v} = r\Omega\hat{\theta}$, and $\vec{B} = B_0\hat{z}$, so the electric field in the conductor will be purely in the $\hat{r}$-direction, and $\vec{E} \times \hat{n} = 0$. So, we still find that the tangential electric field is zero at the boundary. To find the implications of this on the magnetic field, we dot Faraday's law with $\hat{n}$:

$$\left(\nabla \times \vec{E}\right) \cdot \hat{n} = -\frac{1}{c}\frac{\partial \vec{B} \cdot \hat{n}}{\partial t}. \tag{D.42}$$

The curl of $\vec{E}$ in the $\hat{n}$ comes purely from the tangential components of $\vec{E}$, which we have shown are zero. We find that $\partial B_r/\partial t = 0$, so B_r is invariant in time. Since our initial condition is $B_r = 0$, we find $\beta_r = 0$ at the boundary.

To find the condition on B_θ, we cross Ohm's law with $\hat{n}$:

$$\frac{4\pi\eta}{c^2}\vec{j}\times\hat{n} = \vec{E}\times\hat{n} + \frac{1}{c}\vec{v}\times\vec{B}\times\hat{n} = 0. \tag{D.43}$$

Both terms on the right hand side are 0 at the boundary. We showed previously that the tangential electric field, $\vec{E}\times\hat{n}$, is zero. The $\vec{v}\times\vec{B}\times\hat{n}$ term is 0 because $\vec{v}$ is purely azimuthal, and $B_r = 0$, so $\vec{v}\times\vec{B}$ can only be in the radial (normal) direction. This means that there is no tangential component of the current density, $\vec{j}\times\hat{n}$, at the boundary. From Ampère's law, this implies that the tangential component of the curl of B is 0:

$$\left(\nabla\times\vec{B}\right)\times\hat{n} = 0. \tag{D.44}$$

Evaluating the axial component of the curl of $\vec{B}$, we see

$$\frac{1}{r}\frac{\partial}{\partial r}\left(rB_\theta\right) - \frac{1}{r}\frac{\partial B_r}{\partial\theta} = 0. \tag{D.45}$$

Since $B_r = 0$ at the boundary, we find the boundary condition on B_θ, $\partial/\partial r(rB_\theta) = B_\theta + r\partial/\partial r B_\theta = 0$. Written in terms of our perturbed quantities and logarithmic coordinate x:

$$\beta_\theta + \frac{\partial}{\partial x}\beta_\theta = 0. \tag{D.46}$$

The equations describing the boundary condition for the magnetic field are therefore

$$\beta_{r,j_s-1} + \beta_{r,j_s} = 0, \tag{D.47}$$

$$\beta_{r,j_e+1} + \beta_{r,j_e} = 0, \tag{D.48}$$

$$\beta_{\theta,j_s-1} - \frac{(1+\Delta x/2)}{(1-\Delta x/2)}\beta_{\theta,j_s} = 0, \tag{D.49}$$

$$\beta_{\theta,j_e+1} - \frac{(1-\Delta x/2)}{(1+\Delta x/2)}\beta_{\theta,j_e} = 0. \tag{D.50}$$

D.5.3 Magnetic boundary condition: perfectly insulating[2]

In the MHD approximation, Ampère's law is

$$\nabla\times\vec{B} = \frac{4\pi}{c}\vec{j}. \tag{D.51}$$

[2]Thanks to Jeremy Goodman for guidance in implementing this boundary condition.

In the insulating region outside the fluid, the current density is zero, so the magnetic field can be written in terms of a scalar potential

$$\vec{B} = \nabla\Phi. \tag{D.52}$$

Since $\nabla \cdot \vec{B} = 0$, we know that $\nabla^2\Phi = 0$. In cylindrical coordinates, this means

$$\left[\frac{1}{r}\frac{\partial}{\partial r}r\frac{\partial}{\partial r} + \frac{1}{r^2}\frac{\partial^2}{\partial\theta^2} + \frac{\partial^2}{\partial z^2}\right]\Phi = 0. \tag{D.53}$$

If we assume a form for Φ that goes as $\Phi(r,\theta,z) = e^{i(m\theta+kz)}\tilde{\Phi}(r)$ this yields a differential equation in $\tilde{\Phi}$

$$\frac{d^2}{dr^2}\tilde{\Phi} + \frac{1}{r}\frac{d}{dr}\tilde{\Phi} - \left(\frac{m^2}{r^2} + k^2\right)\tilde{\Phi} = 0. \tag{D.54}$$

This equation is satisfied by modified Bessel functions

$$\tilde{\Phi}(r) = A_{\text{in}}I_m(kr) + A_{\text{out}}K_m(kr). \tag{D.55}$$

Because $K_m(kr) \to \infty$ as $kr \to 0$ and $I_m(kr) \to \infty$ as $kr \to \infty$, $A_{\text{out}} = 0$ in the inner region, and $A_{\text{in}} = 0$ in the outer region.

$$\tilde{\Phi}(r) = \begin{cases} A_{\text{in}}I_m(kr), & r \le r_1, \\ A_{\text{out}}K_m(kr), & r \ge r_2. \end{cases} \tag{D.56}$$

We evaluate $\nabla\Phi$ to find the components of the field

$$B_r = \frac{\partial\Phi}{\partial r} = e^{i(m\theta+kz)}\begin{cases} kA_{\text{in}}\left[I_{m+1}(kr) + \frac{m}{kr}I_m(kr)\right], & r \le r_1, \\ kA_{\text{out}}\left[-K_{m+1}(kr) + \frac{m}{kr}K_m(kr)\right], & r \ge r_2, \end{cases} \tag{D.57}$$

$$B_\theta = \frac{1}{r}\frac{\partial\Phi}{\partial\theta} = \frac{im}{r}e^{i(m\theta+kz)}\begin{cases} A_{\text{in}}I_m(kr), & r \le r_1, \\ A_{\text{out}}K_m(kr), & r \ge r_2. \end{cases} \tag{D.58}$$

We now match the insulating solution to the magnetic field value just inside the boundary to find A_{in} and A_{out}. Once those constants are known, the value of the magnetic field

in the ghost zone can be calculated. Note also the special case when $m = 0$, where $B_\theta = 0$ at the boundary:

$$\beta_{r,j_s-1} - \beta_{r,j_s} \frac{\left[I_{m+1}(kr_{j_s-1}) + \frac{m}{kr_{j_s-1}} I_m(kr_{j_s-1})\right]}{\left[I_{m+1}(kr_{j_s}) + \frac{m}{kr_{j_s}} I_m(kr_{j_s})\right]} = 0, \tag{D.59}$$

$$\beta_{r,j_e+1} - \beta_{r,j_e} \frac{\left[-K_{m+1}(kr_{j_e+1}) + \frac{m}{kr_{j_e+1}} K_m(kr_{j_e+1})\right]}{\left[-K_{m+1}(kr_{j_e}) + \frac{m}{kr_{j_e}} K_m(kr_{j_e})\right]} = 0. \tag{D.60}$$

For $m \neq 0$:

$$\beta_{\theta,j_s-1} - \beta_{\theta,j_s} \frac{r_{j_s}}{r_{j_s-1}} \frac{I_m(kr_{j_s-1})}{I_m(kr_{j_s})} = 0, \tag{D.61}$$

$$\beta_{\theta,j_e+1} - \beta_{\theta,j_e} \frac{r_{j_e}}{r_{j_e+1}} \frac{K_m(kr_{j_e+1})}{K_m(kr_{j_e})} = 0. \tag{D.62}$$

For $m = 0$:

$$\beta_{\theta,j_s-1} + \beta_{\theta,j_s} = 0, \tag{D.63}$$

$$\beta_{\theta,j_e+1} + \beta_{\theta,j_e} = 0. \tag{D.64}$$

D.6 Solving the equations

The problem is to solve a system of $5N$ equations, where N is the number of grid cells including ghost zones. The equations can be cast in the form of a generalized eigenvalue problem

$$\mathbf{A} \cdot \mathbf{x} = \gamma \mathbf{B} \cdot \mathbf{x}, \tag{D.65}$$

where γ is the eigenvalue; $\mathbf{x}$ is the eigenvector made up of the components β_r, β_θ, ϕ_r, ϕ_θ, and Π at each grid cell; $\mathbf{A}$ is a band-diagonal matrix of bandwidth 15 that is made up of the terms in the linearized equations and constraint equations; and $\mathbf{B}$ is a diagonal matrix with a 1 corresponding to the position of the time evolution equation for each of the quantities β_r, β_θ, ϕ_r, and ϕ_θ in the fluid, and a 0 at the position of each boundary condition equation and each constraint equation on Π.

Two methods are used to solve this generalized eigenvalue problem. The first solves the full problem for all eigenvalues and eigenmodes. Because resolutions of a few thousand grid cells are sometimes necessary to fully resolve boundary layers, the calculation of all the eigenvalues and eigenmodes can take a long time. A second method can be used to solve for a subset of the eigenvalues and eigenmodes, saving time in the calculation. In both cases the eigenvalues and eigenmodes that are found are sorted are stored in a `NetCDF-4` file for later analysis.

D.6.1 Full solution

The full solution method uses a call to the `LAPACK` routine `ZGGEV` [Anderson et al., 1999] The routine does not take advantage of the banded nature of the problem and takes in $(5N)^2$ complex values describing the matrices $\mathbf{A}$ and $\mathbf{B}$, and requires additional memory allocation for its work. This is not a very efficient mechanism, requiring large amounts of both time and memory, as shown in Figure D.2. On the order of 20-30% of the eigenvalues are spurious, with infinite eigenvalues. These eigenvalues are rejected before saving the results.

D.6.2 Subset of eigenvalues with `ARPACK`

The code has the option to use the `ARPACK` routine `ZNAUPD` to find a subset of the eigenvalues [Lehoucq et al., 1998]. This routine supplies a reverse-communication interface for the iteration algorithm, requesting calls to the `BLAS` routine `ZGBMV` [Dongarra et al., 1990] and the `LAPACK` routine `ZGBTRS` to do its work. Both of these routines can operate on compressed banded matrices, requiring less memory than the method for the full solution to the eigenvalue problem. `ARPACK` is a library that can be used to find a number of extremal eigenvalues meeting several different possible criteria: smallest magnitude, largest magnitude, largest real part, smallest real part, largest imaginary part, or smallest imaginary part. We are most often interested in the largest growing modes, so at first glance it should be as easy as using the `ARPACK` routine to find the modes with the largest real

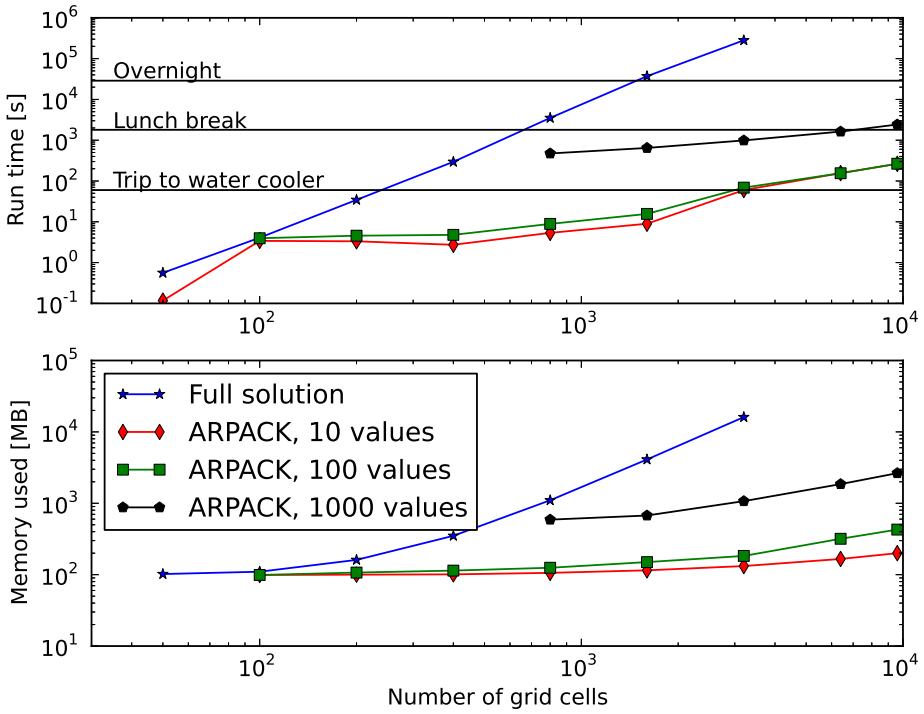

Figure D.2: Execution time and memory scaling for several different modes of operation of the global eigenvalue code. Solving the full problem for all eigenvalues becomes prohibitively difficult for large numbers of grid cells. Using the `ARPACK` subroutines results in dramatically more efficient operation, at the cost of increased complexity in setting up the problem.

part. Unfortunately, the `ZNAUPD` routine can only directly solve for the eigenvalues with largest real part if the matrix $\mathbf{B}$ in the generalized eigenvalue problem is positive definite. In our case, it is positive semi-definite (made up of '1's and '0's on the diagonal), and so we are forced to use the routine in shift-invert mode, where a set of eigenvalues λ are found that are related to the original eigenvalues of the problem by $\lambda = 1/(\gamma - \sigma)$, where σ is a user-specified shift. This can be rewritten

$$\lambda = \frac{1}{\gamma - \sigma} = \frac{\mathrm{Re}\{\gamma - \sigma\} - i\mathrm{Im}\{\gamma - \sigma\}}{|\gamma - \sigma|^2}. \tag{D.66}$$

The choice of σ, the eigenvalue shift, is very important for correct behavior of the `ARPACK` routine, since it determines which part of the eigenvalue spectrum will be returned. We are interested in the eigenvalue with the largest real part of γ. To select the largest-growing eigenvalue γ, we can ask for the eigenvalue λ with the largest magnitude, for a shift σ with a very large real part, much larger than its imaginary part or either part of γ. In other words, $\sigma = \mathrm{Re}\{\sigma\}^{(0)} + \epsilon\mathrm{Im}\{\sigma\}^{(1)}$, and $\gamma = \epsilon\mathrm{Re}\{\gamma\}^{(1)} + \epsilon\mathrm{Im}\{\gamma\}^{(1)}$ where ϵ is a small number, and the superscripts $^{(0)}$ and $^{(1)}$ denote zeroth- and first-order quantities, respectively. In this case, the magnitude of λ, neglecting second-order terms, is

$$|\lambda| = \frac{1}{\sqrt{(\gamma - \sigma)\,(\gamma^* - \sigma^*)}} \approx \frac{1}{\sqrt{(\mathrm{Re}\{\sigma\})^2 - 2\mathrm{Re}\{\sigma\}\mathrm{Re}\{\gamma\}}}, \tag{D.67}$$

which is maximized for the largest $\mathrm{Re}\{\gamma\}$.

We are guaranteed to get the largest growing eigenvalue if we choose a very large, real σ. Unfortunately, as the value σ gets farther from the eigenvalues of interest, the routine becomes much more inefficient, leading to increased computation time and larger errors in the computed eigenvalues. So, σ is chosen by an iterative technique, using a σ with a very large real part at first to make sure we find the fastest-growing eigenvalue, and then adjusting the value closer to the eigenvalue of interest. The initial value $\sigma_0 = 5|\Omega_1| + 5|\Omega_2| - im(\Omega_1/2 + \Omega_2/2)$, since the largest growth rate and frequency of any mode are expected to be of order Ω_1 in the absence of very large Alfvèn frequencies and since a Doppler shift of order $m\bar{\Omega}$ is expected. The problem is solved first with a relatively large tolerance of 10^{-2}. Next, a new value of σ_1 is determined based on the largest-growing

computed eigenvalue γ_0, $\sigma_1 = 0.1\sigma_0 + 0.9\gamma_0$, and the tolerance is halved. This process is repeated four times, and the resulting σ is then used to solve the problem at machine tolerance.

Using the `ARPACK` subroutine results in greatly improved performance, as shown in Figure D.2. But there is a danger of picking eigenvalues from the incorrect part of the spectrum with a bad choice of σ. And even if σ is picked correctly for the fastest growing eigenvalue, asking for n eigenvalues by this technique may not return the fastest-growing n eigenvalues. If, for example, the second-fastest growing eigenvalue has a very different imaginary part from the fastest-growing eigenvalue, the routine may return the fastest-growing eigenvalue followed by a different slower-growing eigenvalue with an imaginary part closer to that of the fastest-growing eigenvalue. Because of this, it is advisable to verify some of the runs with the results of a full eigenvalue calculation to ensure that the relevant parts of the spectrum are being returned.

D.6.3 Convergence

Convergence of computed eigenvalues with increasing grid resolution was tested both in order to validate the `ARPACK` solver and to find the optimum grid resolution for computations. The results of a convergence test using the marginally stable MRI eigenmode from the first part of the "Test problems" section are shown in Figure D.3. Results from the full eigenvalue solution and from the `ARPACK` method are very consistent with each other up to the largest resolution at which it was reasonable to calculate the full solution, with the error in each dropping as $1/N^2$, as should be expected for second-order centered differences. The error for the `ARPACK` solution eventually levels out, suggesting an intrinsic error in the eigenvalue solver. 2000-8000 grid cells are typically used for the computations in this work.

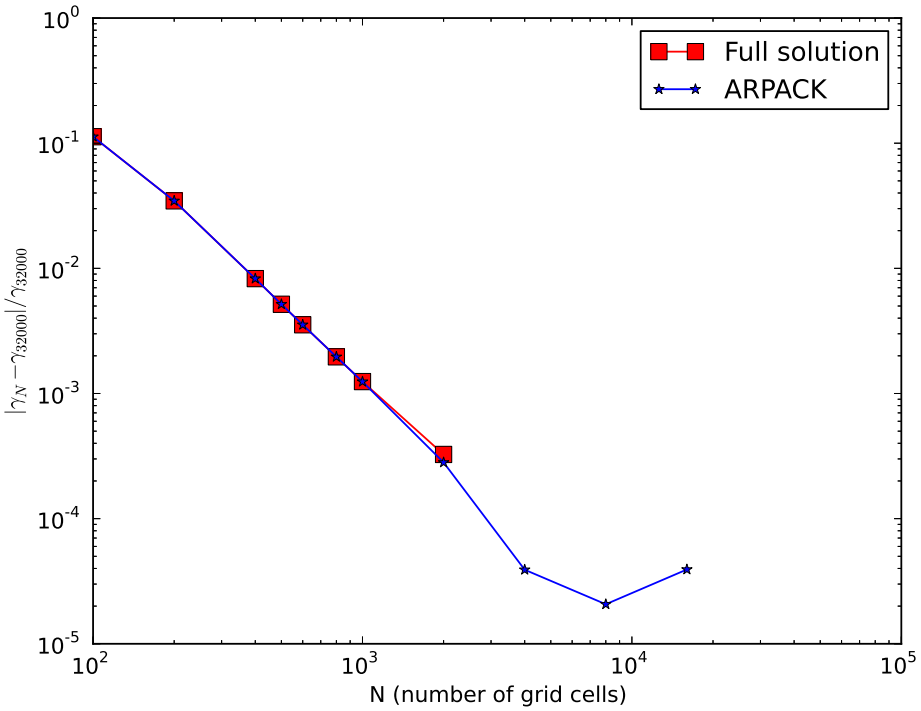

Figure D.3: Convergence of computed global eigenvalues with increasing grid resolution for the `ARPACK` solver and for the full eigenmode solution. The eigenvalue is that of the marginally stable MRI eigenmode described in the first part of the "Test problems" section. The relative error of each computed eigenvalue compared to the `ARPACK` solution with 32000 grid cells is shown.

D.7 Test problems

D.7.1 Magnetorotational instability

The code was used to solve the problem of the marginally unstable eigenmode in an ideal Couette background from Goodman and Ji [2002] with the following parameters:

$\Omega_1 = 2720$ rpm $= 284.84$ rad/s,	$\nu = 3.2 \times 10^{-3}$ cm^2/s,
$\Omega_2 = 328.4$ rpm $= 34.39$ rad/s,	$\eta = 2.0 \times 10^{3}$ cm^2/s,
$r_1 = 5$ cm,	$\rho = 6.0$ g/cm^3,
$r_2 = 15$ cm,	$B_0 = 3000$ Gauss,
$k = 2\pi n/h = 2\pi * 0.5/10$ cm $= 0.314$ cm^{-1},	
$N = 4000$ grid cells,	Insulating boundaries.

Axisymmetric modes

The spectrum of eigenvalues for the axisymmetric case, $m = 0$, is shown in figure D.4. The marginally stable eigenmode is shown in Figure D.5. The mode found here is a match to that shown in Figure 2(b) of Goodman and Ji [2002].

The unstable mode has a k_r such that a half-wavelength of the mode spans the gap between the two cylinders, with boundary layers at the interfaces with the cylinder walls. The other, damped modes of the system are modes with increasing k_r as they are increasingly damped. A few examples of the damped eigenmodes are shown in Figure D.6.

Nonaxisymmetric modes

It is also possible to examine nonaxisymmetric eigenmodes with these parameters. The spectrum of eigenvalues for $m = 1$ is shown in Figure D.7. The nonaxisymmetric modes in this case are all damped. Typical eigenmodes of this problem are shown in Figure D.8. The velocity components of these eigenmodes have a relatively large k_r and are confined in an envelope localized at some radius. The oscillation frequency $-\mathrm{Im}\{\gamma\}$ is Doppler shifted

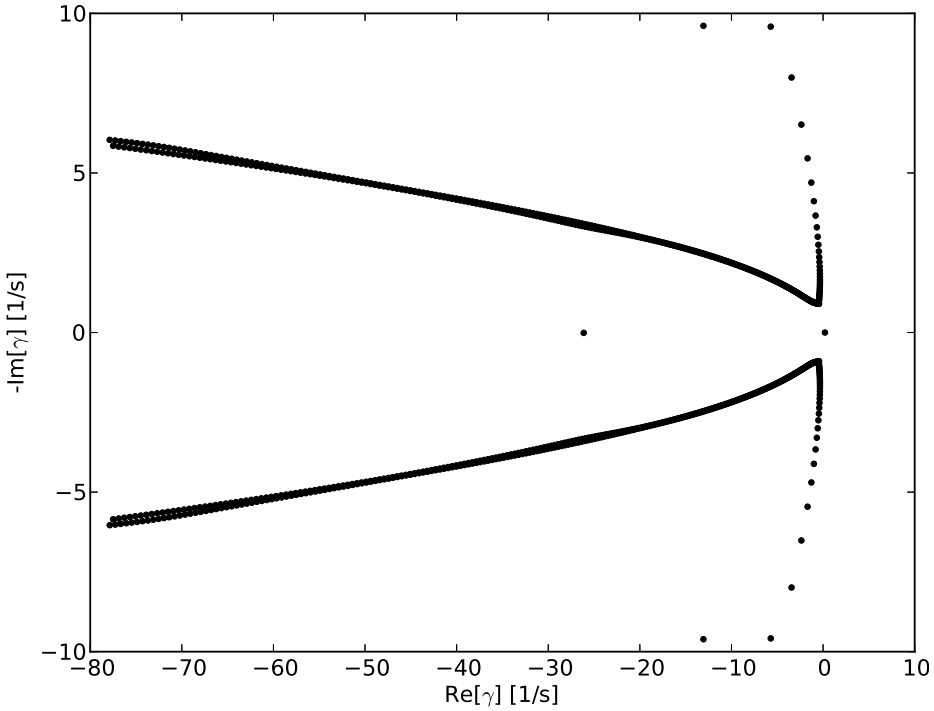

Figure D.4: Spectrum of 1000 eigenvalues for axisymmetric MRI problem. Eigenvalue with a slightly positive growth rate and zero frequency corresponds to the marginally unstable MRI mode.

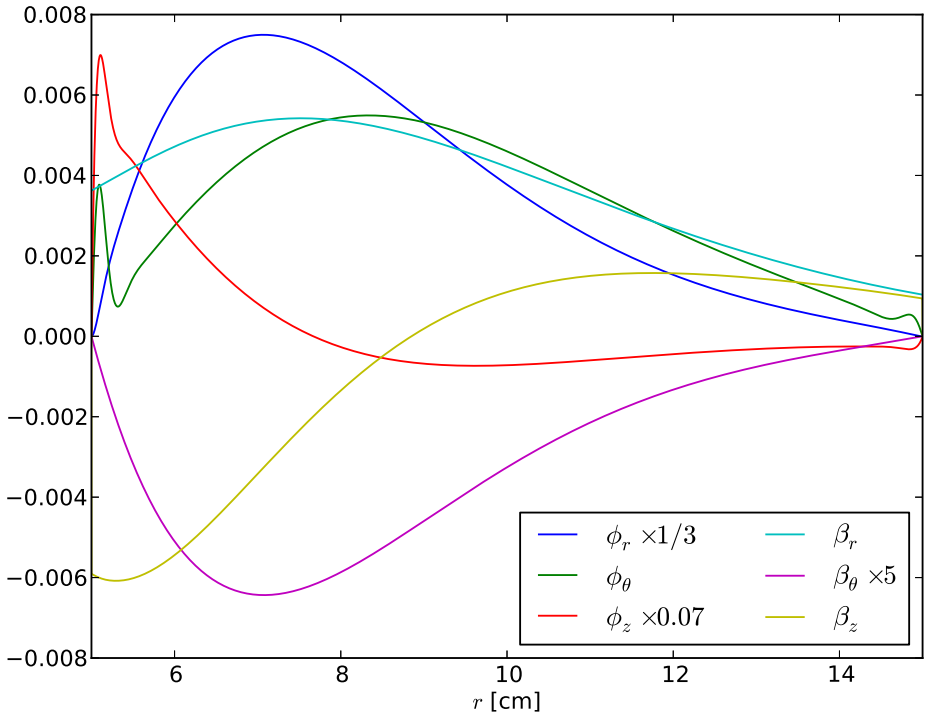

Figure D.5: Marginally unstable axisymmetric MRI mode. Compare to Figure 2(b) from Goodman and Ji [2002].

by the rotation frequency at that radius. The magnetic components have a larger length scale, and often have tails that extend far beyond the localized velocity fluctuations.

D.7.2 Basic waves in narrow-gap limit

With a very narrow gap, such that $r_1 \gg r_2 - r_1$, the effects of the curvature terms in the linearized equations can be neglected ($k_r \gg 1/r$). In this case, a local dispersion relation can be derived, as in the axisymmetric dispersion relation derived in Ji et al. [2001]:

$$\left[(\gamma+\nu k^2)(\gamma+\eta k^2)+(k_z v_A)^2\right]^2 \frac{k^2}{k_z^2}+\kappa^2(\gamma+\eta k^2)^2+\frac{\partial\Omega^2}{\partial \ln r}(k_z v_A)^2=0, \tag{D.68}$$

where the epicyclic frequency κ is defined by $\kappa^2 = (1/r^3)\partial(r^4\Omega^2)/\partial r = 4\Omega^2 + \partial\Omega^2/\partial \ln r$ and k is the total wavenumber, $k^2 = k_z^2 + k_r^2$. (Note that this definition of k in the local dispersion relation is different from that used elsewhere throughout this chapter, where $k = k_z$ and the modes have arbitrary radial dependence.)

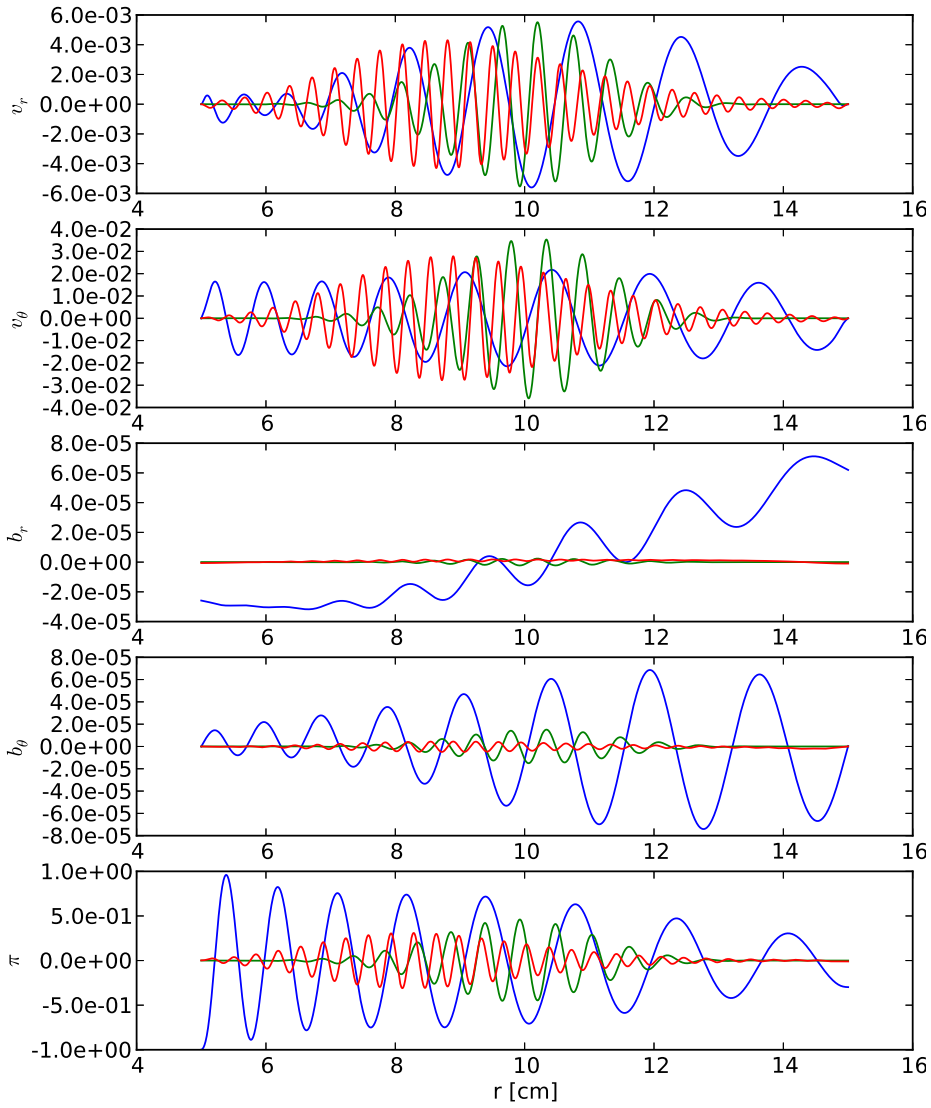

Figure D.6: Typical damped modes of the axisymmetric MRI problem. The modes fill the space between the two cylinders with different values of k_r.

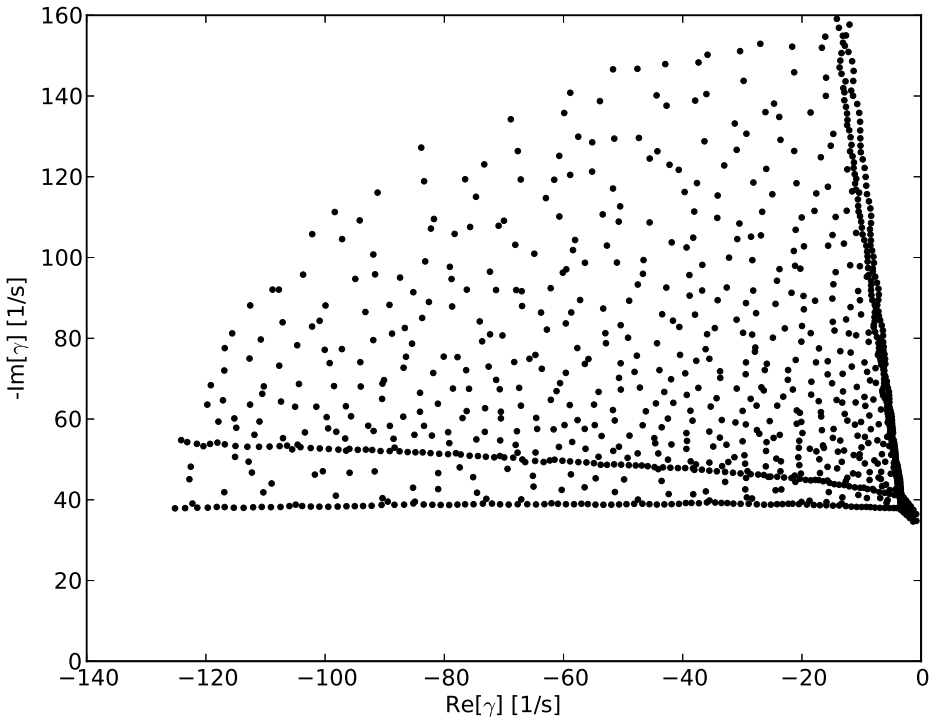

Figure D.7: Spectrum of 1000 nonaxisymmetric eigenvalues for the MRI problem with $m = 1$ and with all other parameters the same as the axisymmetric case. There are no growing modes, and the average $-\mathrm{Im}\{\gamma\}$ is shifted from the axisymmetric case because of the Doppler shift of the frequencies.

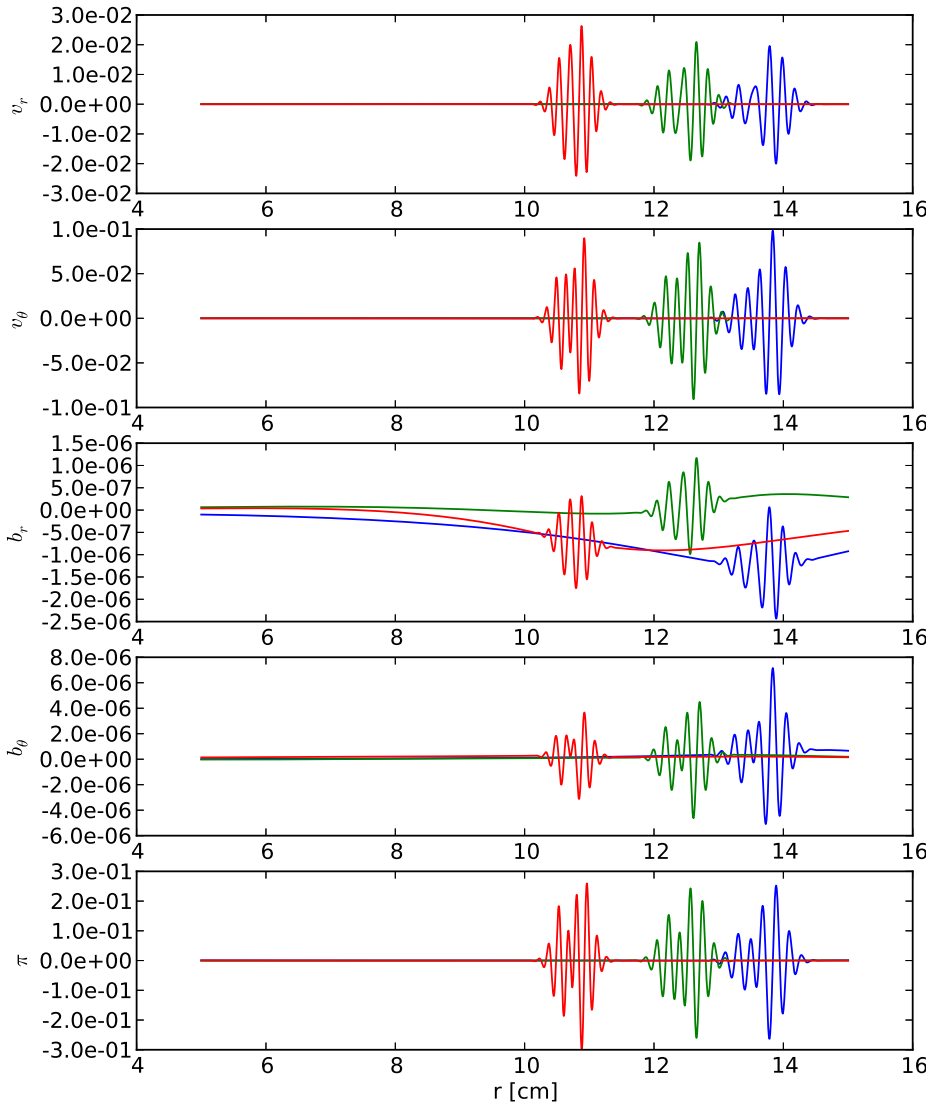

Figure D.8: Typical damped nonaxisymmetric modes for the MRI problem. Modes have a relatively large k_r and are confined to an envelope localized to a particular radius.

The lowest-order effects of a nonaxisymmetric correction to this dispersion relation are a Doppler shift to the frequency ($\gamma \rightarrow \gamma - im\Omega$) and an additional contribution to the wavenumber $k^2 \rightarrow k_r^2 + k_z^2 + m^2/r^2$. We can compare the behavior of eigenmodes in this narrow-gap limit to the local dispersion relation. We do this below for two of the basic waves of rotating MHD systems: Alvén waves and inertial waves.

Alfvén waves with $Pm = 1$

Eigenvalues and eigenmodes were calculated in the narrow-gap limit for the case with an applied magnetic field but no rotation with the following parameters:

$\Omega_1 = 0$ rpm $= 0$ rad/s,	$\nu = 1.0 \times 10^{-4}$ cm^2/s,
$\Omega_2 = 0$ rpm $= 0$ rad/s,	$\eta = 1.0 \times 10^{-4}$ cm^2/s,
$r_1 = 20.2$ cm,	$\rho = 6.36$ g/cm^3,
$r_2 = 20.3$ cm,	$B_0 = 1000$ Gauss,
$k = 2\pi n/h = 2\pi * 500/100$ cm $= 31.4$ cm^{-1},	$m = 1$,
$N = 2000$ grid cells,	Conducting boundaries.

The eigenmodes of this system are Alfvén waves with varying values of k_r are shown in Figure D.9.

The dispersion relation with no rotation in the narrow gap limit reduces to

$$\gamma = -(\nu k^2 + \eta k^2) \pm i\sqrt{\frac{k_z^2 B_0^2}{4\pi\rho} - \frac{1}{4}(\nu k^2 - \eta k^2)^2}. \tag{D.69}$$

Because $Pm = \nu/\eta = 1$ here, the second term under the square root is zero. To compare the calculated eigenvalues to this dispersion relation, the value of k_r must be determined, with all other parameters having already been specified as inputs to the calculation. k_r is found by finding the peak in the spatial Fourier spectrum of the eigenmode between the two cylindrical walls. The dispersion relation of the computed eigenvalues and eigenmodes is compared to the local dispersion relation in Figure D.10.

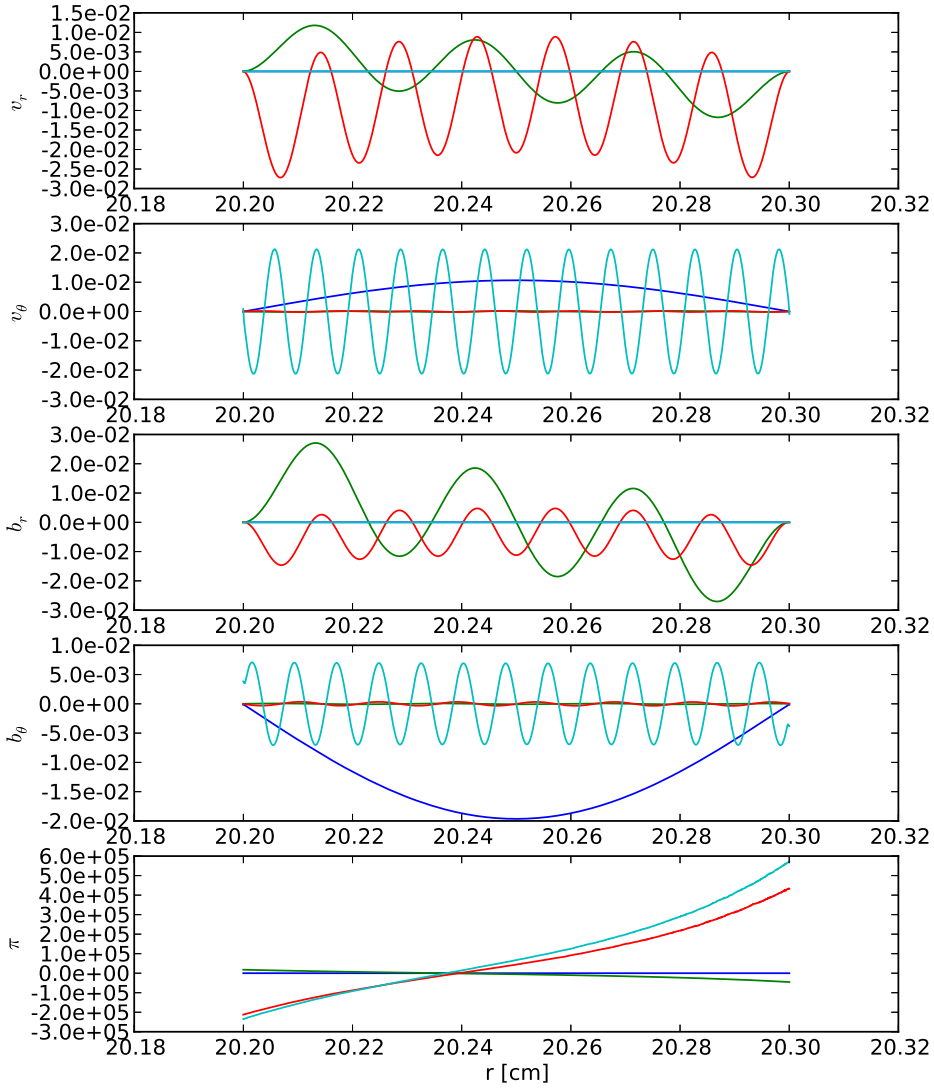

Figure D.9: Alfvén wave eigenmodes with $Pm = 1$ in a narrow gap. Modes with several different values of k_r are shown. Note the two primary polarizations of the wave: one with perturbations primarily in v_r and b_r, and the other with perturbations primarily in v_z and b_z.

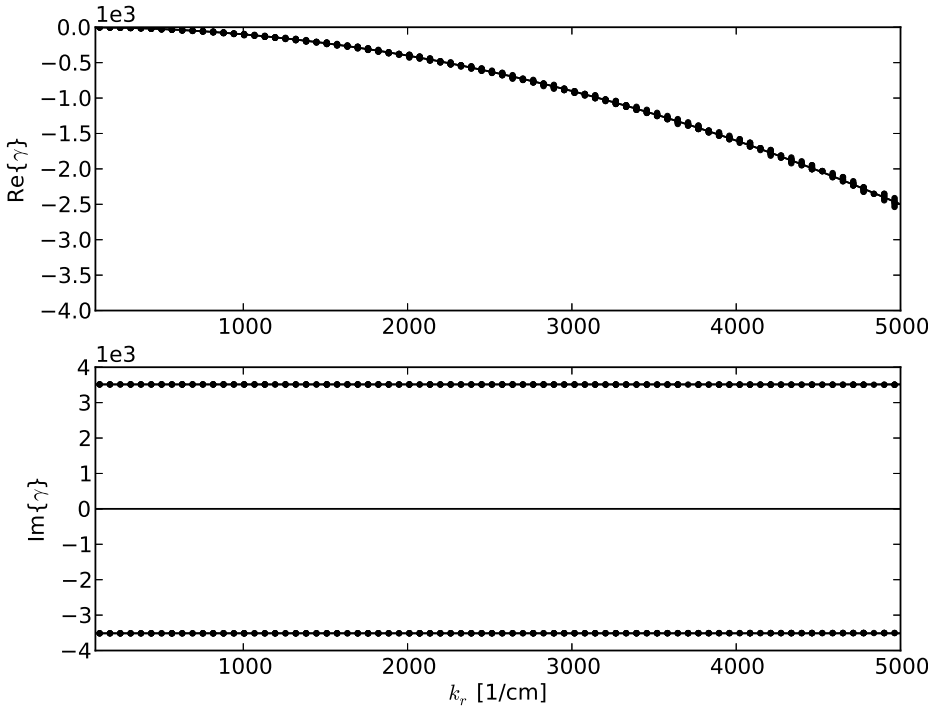

Figure D.10: Dispersion relation of Alfvén waves with $Pm = 1$ in a narrow gap. The dots indicate the calculated eigenvalues, with k_r determined from finding the peak in the spatial Fourier spectrum for each eigenmode. The black lines indicate the solution to the local dispersion relation.

Alfvén waves with $Pm = 0.1$

The same problem in the previous case was evaluated with all parameters the same except for different values of ν and η to yield $Pm = \nu/\eta = 0.1$:

$\Omega_1 = 0$ rpm $= 0$ rad/s,	$\nu = 3.4 \times 10^{-2}$ cm^2/s,
$\Omega_2 = 0$ rpm $= 0$ rad/s,	$\eta = 3.4 \times 10^{-3}$ cm^2/s,
$r_1 = 20.2$ cm,	$\rho = 6.36$ g/cm^3,
$r_2 = 20.3$ cm,	$B_0 = 1000$ Gauss,
$k = 2\pi n/h = 2\pi * 500/100$ cm $= 31.4$ cm^{-1},	$m = 1$,
$N = 2000$ grid cells,	Conducting boundaries.

Because the second term under the square root of Equation D.69 is no longer zero, Im$\{\gamma\}$ goes to zero for a sufficiently large k_r. The dispersion relation of the computed eigenmodes was calculated as before, and is shown in Figure D.11.

Inertial waves

Eigenvalues and eigenmodes were calculated in the narrow-gap limit for the case with background solid body rotation but no background magnetic field with the following parameters:

$\Omega_1 = 400$ rpm $= 41.9$ rad/s,	$\nu = 1.0 \times 10^{-5}$ cm^2/s,
$\Omega_2 = 400$ rpm $= 41.9$ rad/s,	$\eta = 1.0 \times 10^{-5}$ cm^2/s,
$r_1 = 20.2$ cm,	$\rho = 6.36$ g/cm^3,
$r_2 = 20.3$ cm,	$B_0 = 0$ Gauss,
$k = 2\pi n/h = 2\pi * 50000/100$ cm $= 3141.6$ cm^{-1},	$m = 1$,
$N = 2000$ grid cells,	Conducting boundaries.

The eigenmodes of this system are inertial waves with varying values of k_r and are shown in Figure D.12.

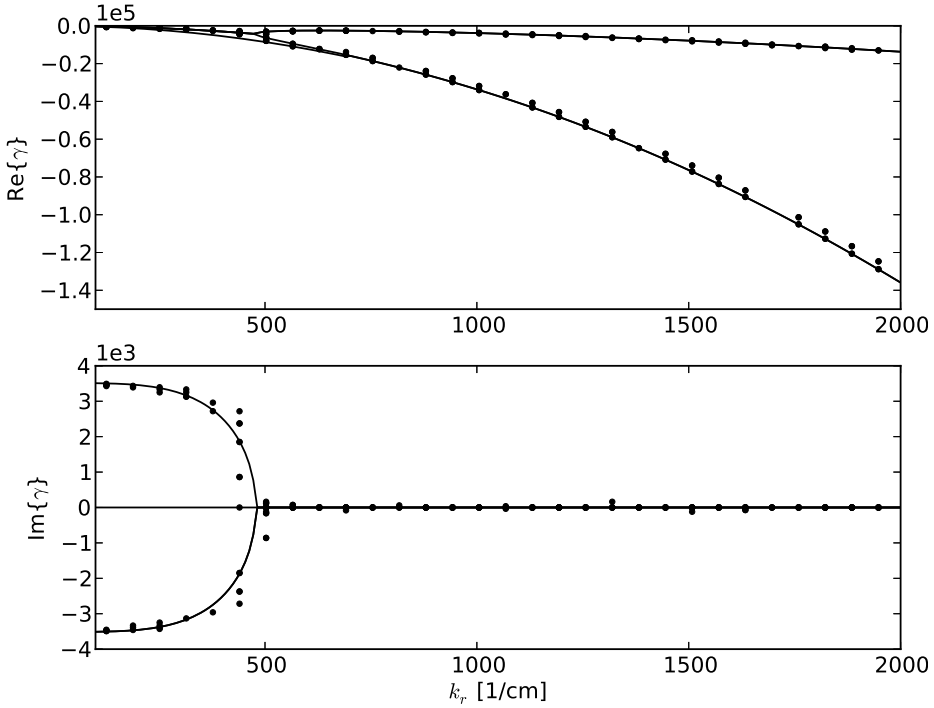

Figure D.11: Dispersion relation of Alfvén waves with $Pm = 0.1$ in a narrow gap. The dots indicate the calculated eigenvalues, with k_r determined from finding the peak in the spatial Fourier spectrum for each eigenmode. The lines indicate the solution to the local dispersion relation. Note that there is some deviation of the calculated eigenvalues from the local dispersion relation, most likely due to errors in determining k_r.

The dispersion relation with no applied field in the narrow gap limit reduces to

$$\gamma = \nu k^2 - im\Omega \pm i\frac{2\Omega k_z}{k}, \tag{D.70}$$

where the $-im\Omega$ term represents the Doppler shift of nonaxisymmetric modes.

As before, k_r for each mode was found from the peak in the spatial Fourier transform so that the calculated eigenvalues could be compared to the local dispersion relation. The result is shown in Figure D.13.

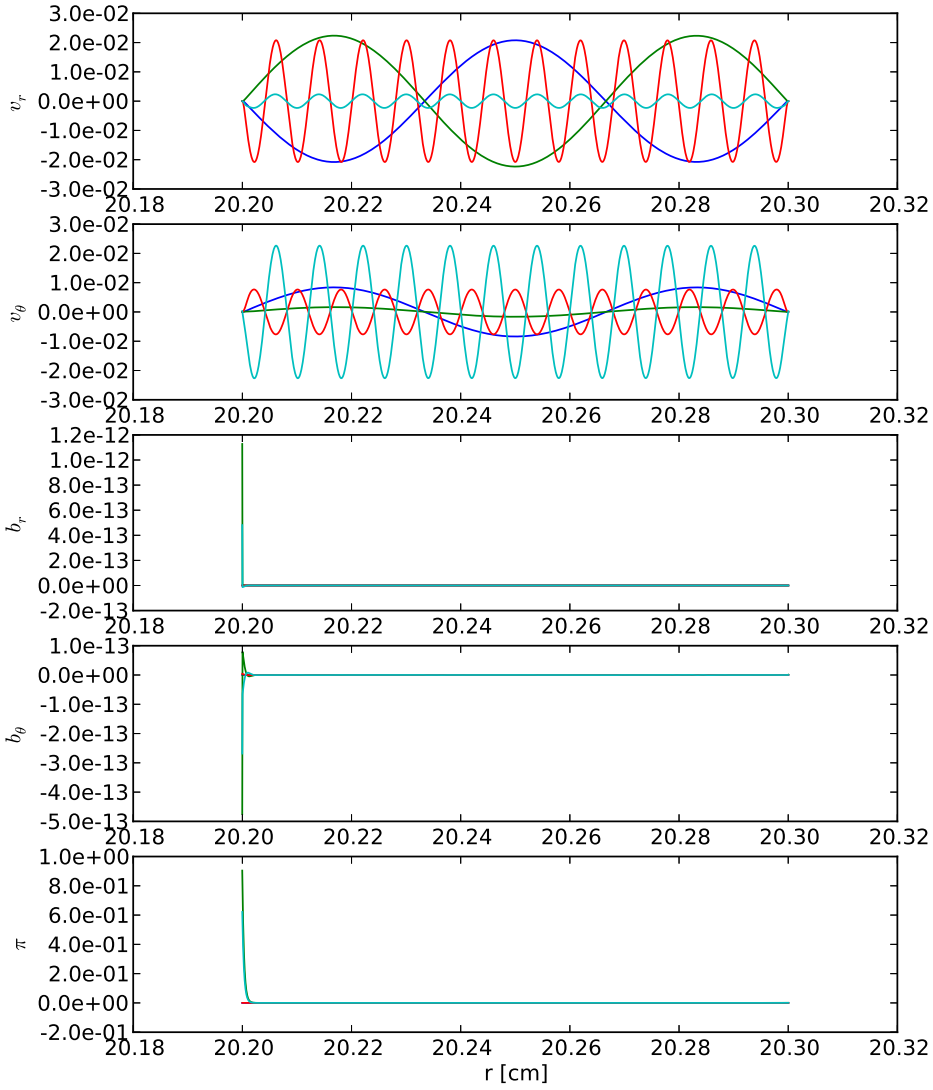

Figure D.12: Inertial wave eigenmodes in a narrow gap with several different values of k_r.

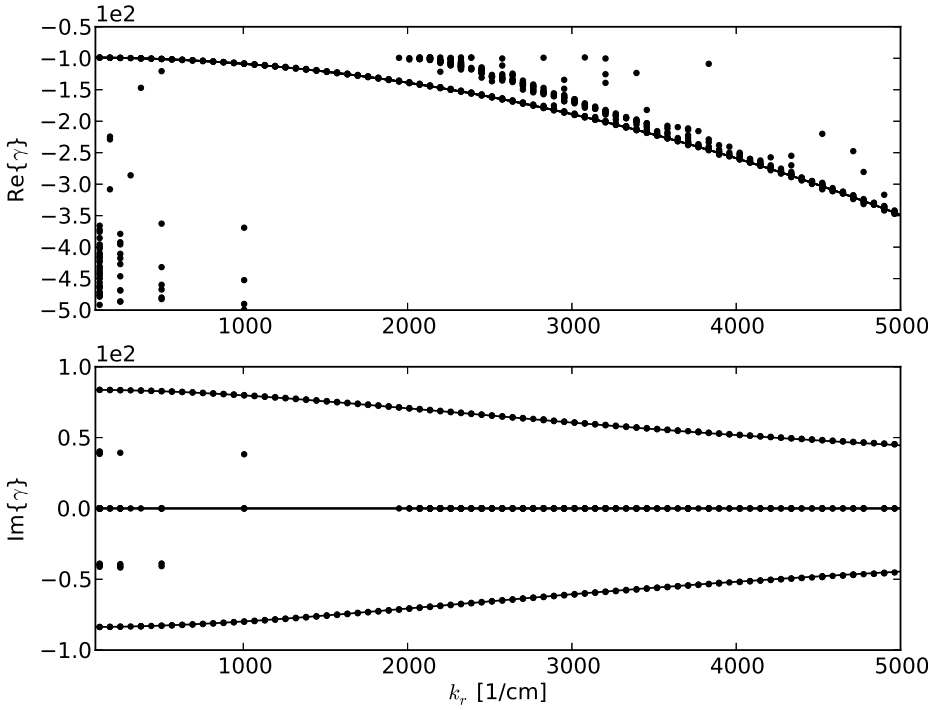

Figure D.13: Dispersion relation of inertial waves in a narrow gap. The dots indicate the calculated eigenvalues, with k_r determined from finding the peak in the spatial Fourier spectrum for each eigenmode. The black lines indicate the solution to the local dispersion relation. Note that there is some deviation of the calculated eigenvalues from the local dispersion relation because of errors in calculating k_r. Note also the branch at $\mathrm{Im}\{\gamma\} = 0$, which are zero-frequency Alfvén waves that are completely decoupled from the inertial waves since $B_0 = 0$.

Appendix E

Free shear layer instabilities in the PROMISE-2 geometry

In this appendix, we give a shortened treatment of linear stability of a free shear layer in the geometry of the PROMISE-2 experiment Stefani et al. [2009], with $r_1 = 4.0$ cm, $r_2 = 8.0$ cm, and $r_l = 5.6$ cm. The model shear layer rotation profiles in this geometry are shown in Figure E.1. The PROMISE-2 experiment was designed for much lower speed operation than the MRI experiment, with a maximum $\Omega_1 = 10$ rpm. Calculations will be performed assuming that only an axial field is applied, even though PROMISE has the capability of applying an azimuthal field, as well. These calculations are identical to those performed in Chapter 6, so we will not reproduce much of the discussion of the physics, and will instead show the results and provide some commentary on the comparison between the two geometries.

E.1 Kelvin-Helmholtz instability

The calculations of the Kelvin-Helmholtz instability were performed with the following parameters:

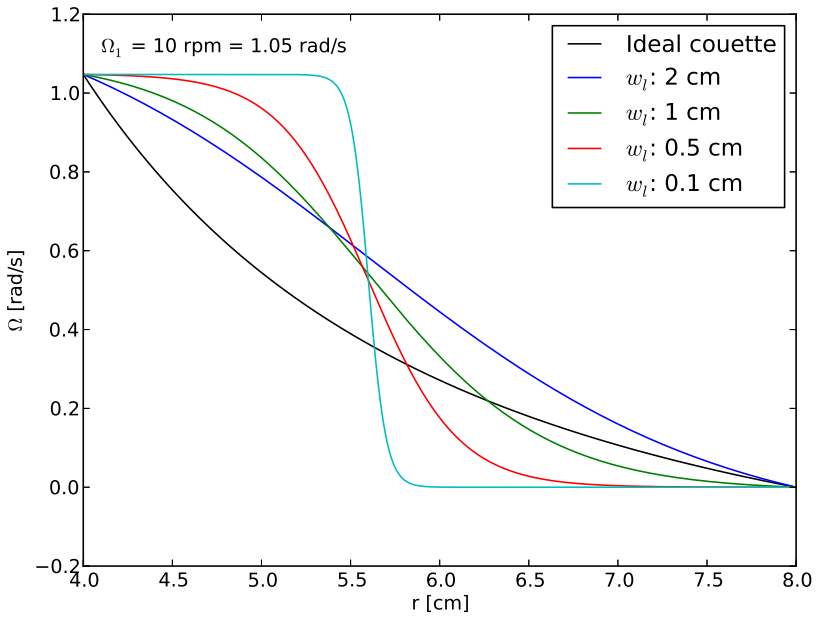

Figure E.1: Profiles of Ω for linear stability calculations of a free shear layer in the PROMISE-2 geometry

$\Omega_1 = 0.05 - 10$ rpm $= 5.24 \times 10^{-3} - 1.05$ rad/s,	$\nu = 2.98 \times 10^{-3}$ cm^2/s,
$\Omega_2 = 0$ rpm $= 0$ rad/s,	$\eta = 2.57 \times 10^{3}$ cm^2/s,
$r_1 = 4.0$ cm,	$\rho = 6.36$ g/cm^3,
$r_2 = 8.0$ cm,	$B_0 = 0$ Gauss,
$r_l = 5.6$ cm,	$w_l = 0.05 - 2$ cm,
$k = 0$ cm^{-1},	$m = 0 - 8$,
$N = 8000$ grid cells,	Conducting boundaries.

Growth rates for the Kelvin-Helmholtz instability for varying w_l are shown in Figure E.2. Note that in this geometry, the $m = 1$ and $m = 2$ modes are destabilized almost simultaneously, suggesting that the eigenmode at marginal stability at higher rotation rates may be $m = 2$ or may have a strong $m = 2$ component. Also note that viscous stabilization is important for $\Omega_1 < 1$ rpm, demonstrated further in Figure E.3. PROMISE-2 often runs with $\Omega_1 < 1$ rpm. The eigenmodes at marginal stability at these slower rotation rates would

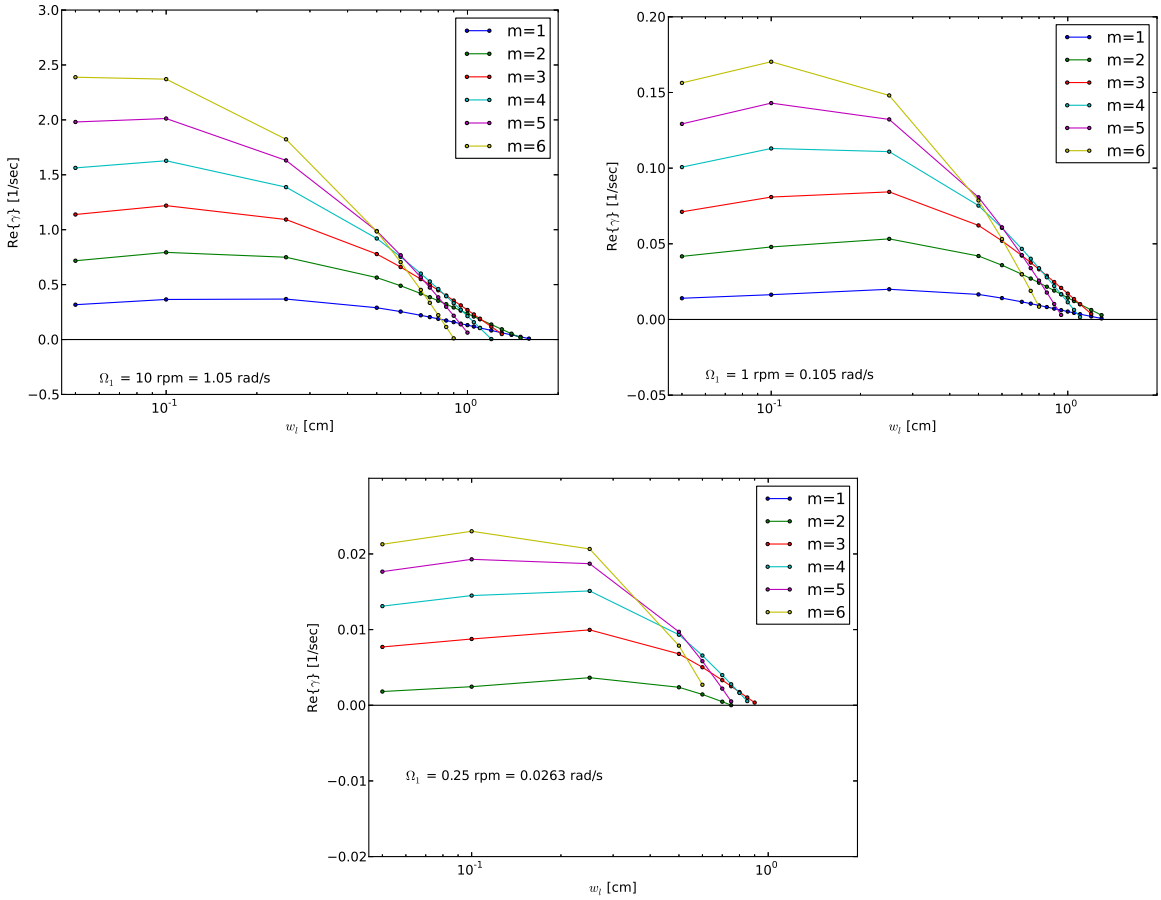

Figure E.2: Unstable growth rates of the Kelvin-Helmholtz instability with different w_l in the PROMISE-2 geometry, all with $\Omega_2 = 0$. *Top left:* $\Omega_1 = 10$ rpm. *Top right:* $\Omega_1 = 1$ rpm. *Bottom:* $\Omega_1 = 0.25$ rpm.

most likely have a larger m, since the lower-m modes may be viscously stabilized.

The marginal eigenmodes, with $w_l = 1.5$ cm, are shown for $m = 1$ and $m = 2$ in Figure E.4. They look very similar to the marginal eigenmodes in the Princeton MRI experiment geometry, with 2 or 4 symmetrical circulation cells filling the radial gap.

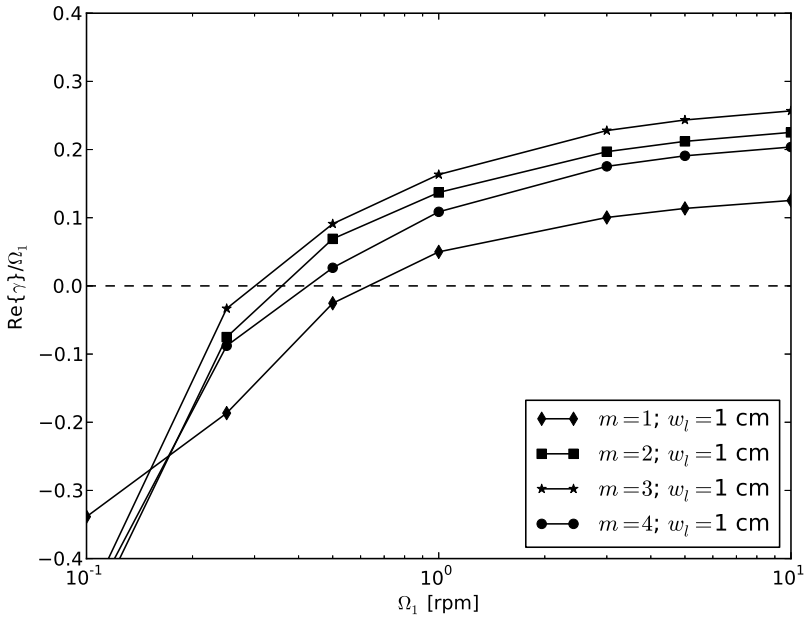

Figure E.3: Growth rate of the Kelvin-Helmholtz versus Ω_1 in the PROMISE-2 geometry with $w_l = 1$ cm for several different azimuthal mode numbers

.

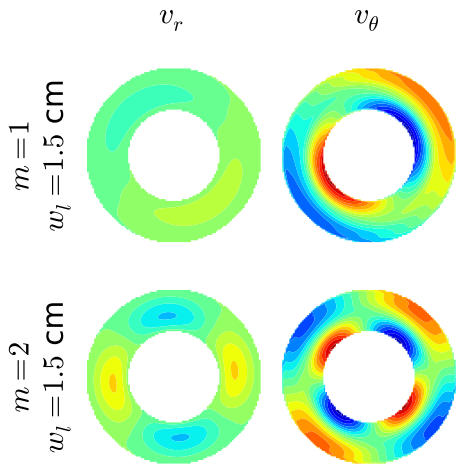

Figure E.4: Marginal eigenmodes of the Kelvin-Helmholtz instability in the PROMISE-2 geometry with $w_l = 1.5$ cm and $\Omega_1 = 10$ rpm. *Top:* $m = 1$. *Bottom:* $m = 2$. The velocity scales are the same for each pair of v_r and v_θ, allowing comparisons of the relative magnitude of each velocity component.

E.2 Centrifugal instability

Calculations of the centrifugal instability were performed with the following parameters:

$\Omega_1 = 0.1 - 20$ rpm $= 1.05 \times 10^{-2} - 2.09$ rad/s,	$\nu = 2.98 \times 10^{-3}$ cm^2/s,
$\Omega_2 = 0 - 30$ rpm $= 0 - 3.14$ rad/s,	$\eta = 2.57 \times 10^{3}$ cm^2/s,
$r_1 = 4.0$ cm,	$\rho = 6.36$ g/cm^3,
$r_2 = 8.0$ cm,	$B_0 = 0 - 2000$ Gauss,
$r_l = 5.6$ cm,	$w_l = 0.1$, 0.5, 1 cm,
$k = 0.001 - 1000$ cm^{-1},	$m = 0$,
$N = 8000$ grid cells,	Conducting boundaries.

As in the MRI geometry, the addition of B_0 or nonzero Ω_2 for constant $\Omega_1 - \Omega_2$ leads to damping of the centrifugal instability, as shown in Figure E.5. As before, these curves are parametrized by a $k_{\rm peak}$ and peak Re$\{\gamma\}$, giving the coordinates of the peak of the growth rate curve, as well as a $k_{\rm max}$ which gives the largest unstable k. These parameters are plotted versus B_0 for various Ω_1 in Figure E.6, and versus Ω_2 for various $\Delta\Omega$ in Figure E.7.

As in the case of the Princeton MRI experiment geometry, the transitions occur at a constant Λ in the case with $B_0 \neq 0$ and Ro in the case with $\Omega_2 \neq 0$. The scaling of the geometrical dependence discussed in Chapter 6 leads to roughly the same $\Omega_{2,\rm crit}$ and $B_{0,\rm crit}$ in the PROMISE-2 geometry as in the Princeton MRI experiment geometry, since the effects due to the change in r_l and the change in the required w_l for the Kelvin-Helmholtz instability nearly cancel each other.

E.3 Summary

If provisions could be made to measure the azimuthal and/or radial velocity, we would expect the Kelvin-Helmholtz instability to be measurable in the PROMISE-2 experiment with $\Omega_1 = 10$ rpm, $\Omega_2 = 0$, and an axial magnetic field larger than $B_{0,\rm crit} \sim 600$ Gauss. As

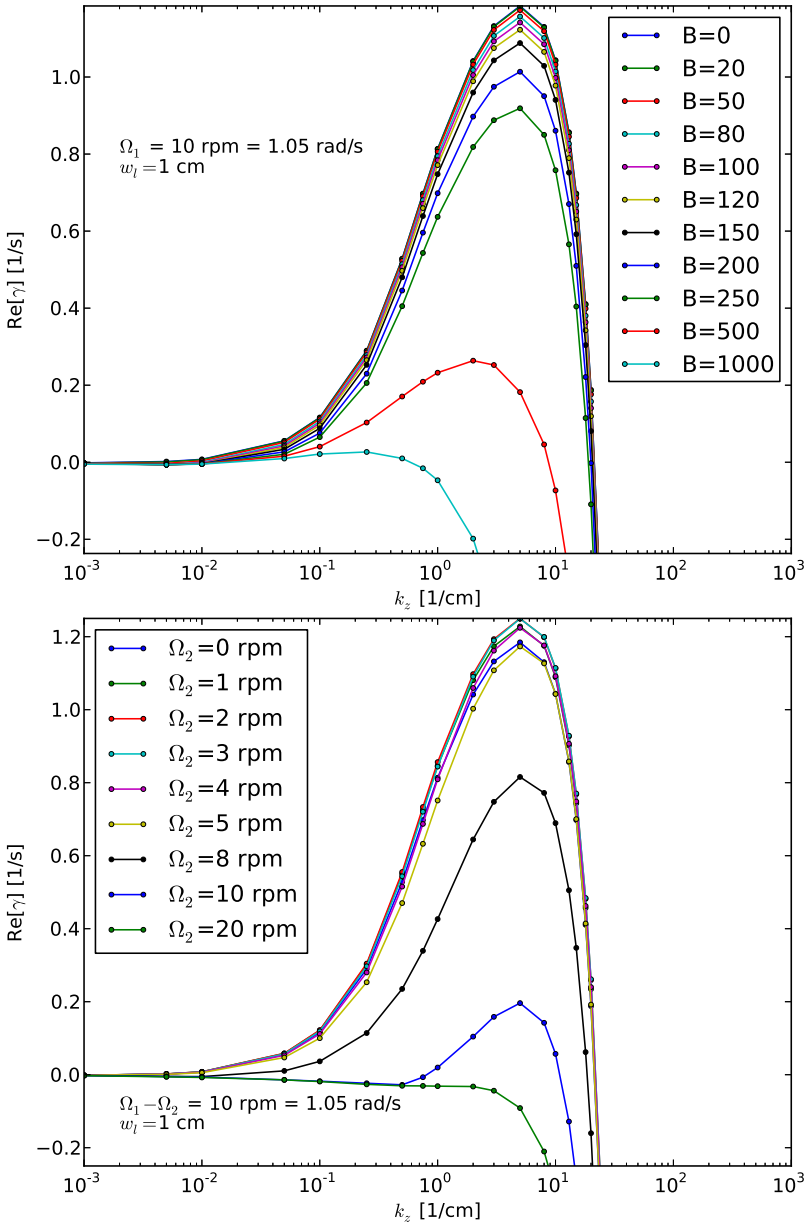

Figure E.5: Damping of centrifugal instability with $B_0 \neq 0$ (*top*) or with $\Omega_2 \neq 0$ (*bottom*) in the PROMISE-2 geometry. All calculations are with $\Omega_1 - \Omega_2 = 10$ rpm and $w_l = 1$ cm.

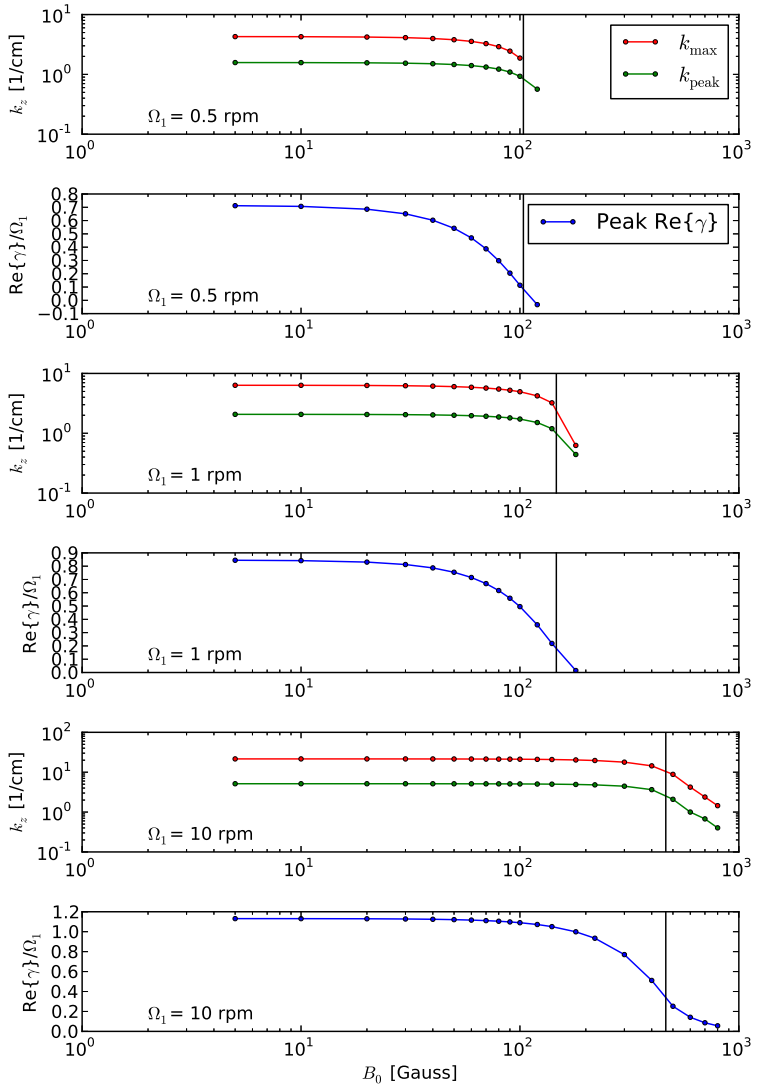

Figure E.6: Plots of k_{peak}, $k_{\max}$ and peak Re$\{\gamma\}$ versus B_0 for various values of Ω_1 in the PROMISE-2 geometry. Plots are arranged in pairs, with the first plot at each speed showing the k values, and the second plot showing the growth rate. The vertical lines are drawn at $\Lambda = 1$.

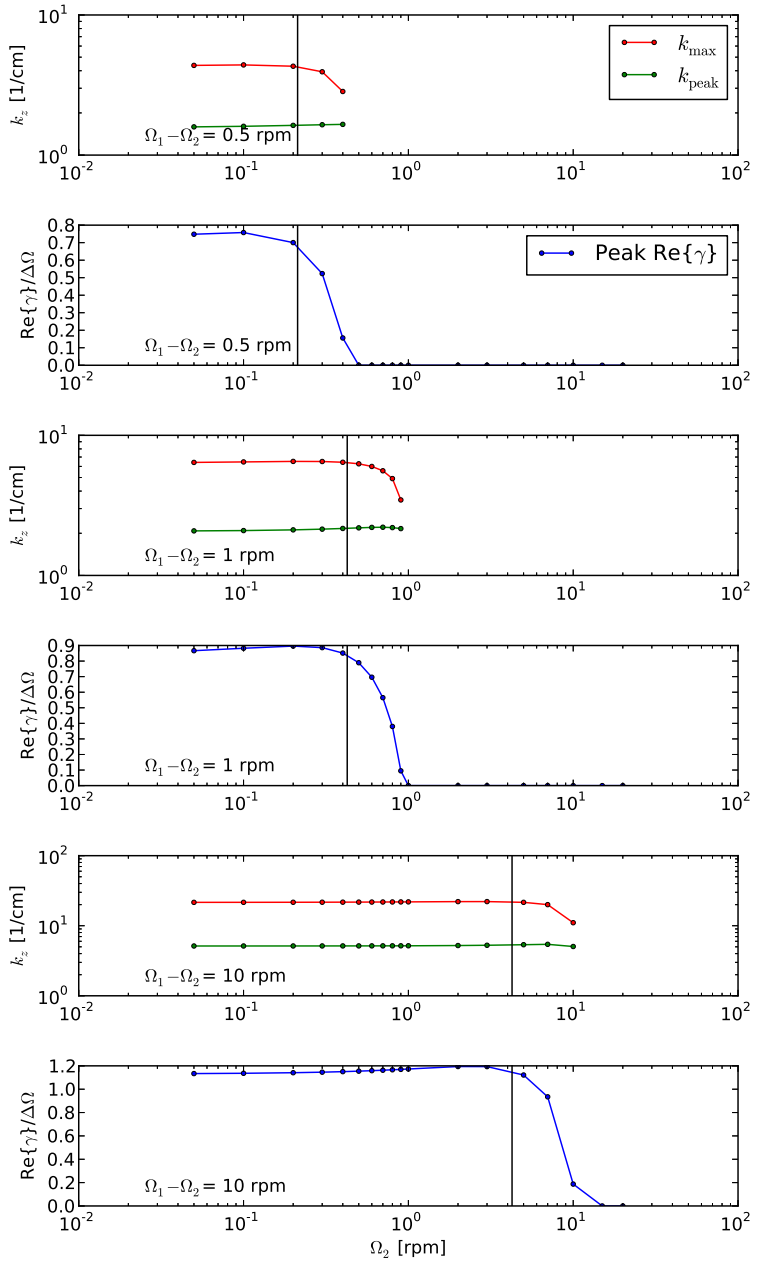

Figure E.7: Plots of k_{peak}, k_{max} and peak Re$\{\gamma\}$ versus Ω_2 for various values of $\Delta\Omega$ in the PROMISE-2 geometry. Plots are arranged in pairs, with the first plot at each speed showing the k values, and the second plot showing the growth rate. The vertical lines are drawn at $Ro = 2.35$.

in the Princeton MRI experiment, we would also expect vigorous instability in the cyclonic regime, with $\Omega_1 = 0$.

At the fastest Ω_1 for the PROMISE-2 experiment, we would expect the mode at marginal stability to have an $m = 1$ or $m = 2$ structure, or possibly a combination of the two, since both are destabilized nearly simultaneously with decreasing shear layer width. The faster growth rate of the $m = 2$ mode in the unstable regime may make its appearance more likely. At slower rotation rates, larger-m modes may always be the most unstable because of the viscous stabilization of the smaller-m modes.

It would be interesting to see the effect on the appearance of the Kelvin-Helmholtz instability of the relatively large height of the PROMISE-2 experiment compared to the Princeton MRI experiment, in particular whether axial variation of the eigenmode could be observed in that geometry. It might also be interesting to observe the effect of the azimuthal magnetic field that is available in PROMISE-2 on the instability. In this case, we would expect significant damping of the Kelvin-Helmholtz instability because of its non-axisymmetric structure. Perhaps a regime could be accessed in which both the centrifugal instability and the Kelvin-Helmholtz instability are damped by the applied magnetic field, allowing very deep penetration of the free shear layer even for a modest Λ.

References

D. J. Acheson and R. Hide. Hydromagnetics of rotating fluids. *Reports on Progress in Physics*, 36(2):159, 1973. DOI: 10.1088/0034-4885/36/2/002.

C. D. Andereck, S. Liu, and H. L. Swinney. Flow regimes in a circular Couette system with independently rotating cylinders. *Journal of Fluid Mechanics*, 164:155–183, 1986. DOI: 10.1017/S0022112086002513.

E. Anderson, Z. Bai, C. Bischof, S. Blackford, J. Demmel, J. Dongarra, J. Du Croz, A. Greenbaum, S. Hammarling, A. McKenney, and D. Sorensen. *LAPACK Users' Guide*. Society for Industrial and Applied Mathematics, Philadelphia, PA, third edition, 1999. ISBN 0-89871-447-8 (paperback).

S. A. Balbus. Enhanced angular momentum transport in accretion disks. *Annual Review of Astronomy and Astrophysics*, 41(1):555–597, 2003. DOI: 10.1146/annurev.astro.41.081401.155207.

S. A. Balbus and J. F. Hawley. A powerful local shear instability in weakly magnetized disks. I - Linear analysis. II - Nonlinear evolution. *The Astrophysical Journal*, 376:214–233, 1991. DOI: 10.1086/170270.

S. A. Balbus and J. F. Hawley. Numerical simulations of MHD turbulence in accretion disks. In E. Falgarone and T. Passot, editors, *Turbulence and Magnetic Fields in Astrophysics*, volume 614 of *Lecture Notes in Physics, Berlin Springer Verlag*, pages 329–348, 2003.

S. A. Balbus and J. F. Hawley. Instability, turbulence, and enhanced transport in accretion disks. *Reviews of Modern Physics*, 70:1–53, 1998. DOI: 10.1103/RevModPhys.70.1.

E. R. Benton. Nonlinear hydrodynamic and hydromagnetic spin-up driven by Ekman-Hartmann boundary layers. *Journal of Fluid Mechanics*, 57(02):337–360, 1973. DOI: 10.1017/S0022112073001199.

R. Betchov and A. Szewczyk. Stability of a shear layer between parallel streams. *Physics of Fluids*, 6(10):1391–1396, 1963. DOI: 10.1063/1.1710959.

S. Braginskii. Magnetohydrodynamics of weakly conducting liquids. *Soviet Physics JETP*, 10(5):1005–1014, 1960.

D. Brito, H.-C. Nataf, P. Cardin, J. Aubert, and J.-P. Masson. Ultrasonic Doppler velocimetry in liquid gallium. *Experiments in Fluids*, 31:653–663, 2001. DOI: 10.1007/s003480100312.

M. Burin, H. Ji, E. Schartman, R. Cutler, P. Heitzenroeder, W. Liu, L. Morris, and S. Raftopolous. Reduction of Ekman circulation within Taylor-Couette flow. *Experiments in Fluids*, 40:962–966, 2006. DOI: 10.1007/s00348-006-0132-y.

F. H. Busse. Shear flow instabilities in rotating systems. *Journal of Fluid Mechanics*, 33 (03):577–589, 1968. DOI: 10.1017/S0022112068001539.

S. Chandrasekhar. *Hydrodynamic and hydromagnetic stability*. Oxford University Press, 1961. ISBN 0-486-64071-X. Reprinted by Dover Publications, Mineola, NY, 1981.

C. Collins, N. Katz, J. Wallace, J. Jara-Almonte, I. Reese, E. Zweibel, and C. B. Forest. Stirring unmagnetized plasma. *Physical Review Letters*, 108:115001, 2012. DOI: 10.1103/PhysRevLett.108.115001.

M. M. Couette. Études sur le frottement des liquides. *Annales de chimie et de physique*, 21:433–510, 1890.

A. Cramer, C. Zhang, and S. Eckert. Local flow structures in liquid metals measured by ultrasonic Doppler velocimetry. *Flow Measurement and Instrumentation*, 15(3):145 – 153, 2004. DOI: 10.1016/j.flowmeasinst.2003.12.006.

J. Dongarra, J. Du Croz, I. Duff, and S. Hammarling. A set of Level 3 Basic Linear Algebra Subprograms. *ACM Trans. Math. Soft.*, 16(1):1–17, 1990. DOI: 10.1145/77626.79170.

R. J. Donnelly and D. R. Caldwell. Experiments on the stability of hydromagnetic Couette flow. *Journal of Fluid Mechanics*, 19:257–263, 5 1964. DOI: 10.1017/S0022112064000696.

R. J. Donnelly and M. Ozima. Hydromagnetic stability of flow between rotating cylinders. *Physical Review Letters*, 4:497–498, May 1960. DOI: 10.1103/PhysRevLett.4.497.

R. J. Donnelly and M. Ozima. Experiments on the stability of flow between rotating cylinders in the presence of a magnetic field. *Proceedings of the Royal Society of London. Series A.*, 266(1325):272–286, 1962. DOI: 10.1098/rspa.1962.0061.

P. Drazin and W. Reid. *Hydrodynamic stability*. Cambridge University Press, 1981. ISBN 0-521-22798-4.

S. Eckert and G. Gerbeth. Velocity measurements in liquid sodium by means of ultrasound Doppler velocimetry. *Experiments in Fluids*, 32:542–546, 2002. DOI: 10.1007/s00348-001-0380-9.

P. R. Fenstermacher, H. L. Swinney, and J. P. Gollub. Dynamical instabilities and the transition to chaotic Taylor vortex flow. *Journal of Fluid Mechanics*, 94(01):103–128, 1979. DOI: 10.1017/S0022112079000963.

W.-G. Früh and P. L. Read. Experiments on a barotropic rotating shear layer. Part 1. Instability and steady vortices. *Journal of Fluid Mechanics*, 383:143–173, 1999. DOI: 10.1017/S0022112098003930.

P. A. Gilman. Instabilities of the Ekman-Hartmann boundary layer. *Physics of Fluids*, 14 (1):7–12, 1971. DOI: 10.1063/1.1693290.

P. A. Gilman and E. R. Benton. Influence of an axial magnetic field on the steady linear Ekman boundary layer. *Physics of Fluids*, 11(11):2397–2401, 1968. DOI: 10.1063/1.1691829.

C. Gissinger, H. Ji, and J. Goodman. Instabilities in magnetized spherical Couette flow. *Physical Review E*, 84(2):026308, 2011. DOI: 10.1103/PhysRevE.84.026308.

C. Gissinger, J. Goodman, and H. Ji. The role of boundaries in the magnetorotational instability. *Physics of Fluids*, 24(7):074109, 2012. DOI: 10.1063/1.4737657.

M. Gonzalez, E. Audit, and P. Huynh. HERACLES: a three-dimensional radiation hydrodynamics code. *Astron. Astrophys.*, 464:429–435, 2007. DOI: 10.1051/0004-6361:20065486.

J. Goodman and H. Ji. Magnetorotational instability of dissipative Couette flow. *Journal of Fluid Mechanics*, 462:365–382, 2002. DOI: 10.1017/S0022112002008704.

J. Hartmann. Hg dynamics I: Theory of the laminar flow of an electrically conductive liquid in a homogeneous magnetic field. *Mathematisk-fysiske Meddelelser*, 15(6), 1937.

J. F. Hawley, C. F. Gammie, and S. A. Balbus. Local three-dimensional magnetohydrodynamic simulations of accretion disks. *The Astrophysical Journal*, 440:742, 1995. DOI: 10.1086/175311.

J. F. Hawley, S. A. Balbus, and W. F. Winters. Local hydrodynamic stability of accretion disks. *The Astrophysical Journal*, 518:394–404, 1999. DOI: 10.1086/307282.

E. Hecht. *Optics*. Addison Wesley, San Francisco, CA, fourth edition, 2002. ISBN 0-8053-8566-5.

R. Hide and C. W. Titman. Detached shear layers in a rotating fluid. *Journal of Fluid Mech.*, 29(01):39–60, 1967. DOI: 10.1017/S002211206700062X.

R. Hollerbach. Instabilities of the Stewartson layer Part 1. The dependence on the sign of *Ro*. *Journal of Fluid Mechanics*, 492:289–302, 2003. DOI: 10.1017/S0022112003005676.

R. Hollerbach. Magnetohydrodynamic flows in spherical shells. In C. Egbers and G. Pfister, editors, *Physics of Rotating Fluids*, volume 549 of *Lecture Notes in Physics*, pages 295–316. Springer Berlin / Heidelberg, 2000. ISBN 978-3-540-67514-3. DOI: 10.1007/3-540-45549-3˙17.

R. Hollerbach. Non-axisymmetric instabilities in magnetic spherical Couette flow. *Proc. R. Soc. A*, 465:2003–2013, 2009. DOI: 10.1098/rspa.2009.0004.

R. Hollerbach. Magnetohydrodynamic Ekman and Stewartson layers in a rotating spherical shell. *Proceedings of the Royal Society of London. Series A.*, 444(1921):333–346, 1994. DOI: 10.1098/rspa.1994.0023.

R. Hollerbach and A. Fournier. End-effects in rapidly rotating cylindrical Taylor-Couette flow. *AIP Conference Proceedings*, 733(1):114–121, 2004. DOI: 10.1063/1.1832141.

R. Hollerbach and G. Rüdiger. New type of magnetorotational instability in cylindrical Taylor-Couette flow. *Physical Review Letters*, 95:124501, 2005. DOI: 10.1103/PhysRevLett.95.124501.

R. Hollerbach and S. Skinner. Instabilities of magnetically induced shear layers and jets. *Proc. R. Soc. A*, 457(2008):785–802, 2001. DOI: 10.1098/rspa.2000.0692.

R. Hollerbach, B. Futterer, T. More, and C. Egbers. Instabilities of the Stewartson layer Part 2. Supercritical mode transitions. *Theoretical and Computational Fluid Dynamics*, 18:197–204, 2004. DOI: 10.1007/s00162-004-0125-5.

J. C. R. Hunt and J. A. Shercliff. Magnetohydrodynamics at high Hartmann number. *Annual Review of Fluid Mechanics*, 3(1):37–62, 1971. DOI: 10.1146/annurev.fl.03.010171.000345.

J. D. Jackson. *Classical Electrodynamics*. John Wiley and Sons, Hoboken, NJ, third edition, 1999. ISBN 0-471-30932-X.

H. Ji, J. Goodman, and A. Kageyama. Magnetorotational instability in a rotating liquid metal annulus. *Monthly Notices of the Royal Astronomical Society*, 325(2):L1–L5, 2001. DOI: 10.1046/j.1365-8711.2001.04647.x.

H. Ji, M. Burin, E. Schartman, and J. Goodman. Hydrodynamic turbulence cannot transport angular momentum effectively in astrophysical disks. *Nature*, 444(7117):343–346, 2006. DOI: 10.1038/nature05323.

K. Julien and E. Knobloch. Magnetorotational instability: recent developments. *Philosophical Transactions of the Royal Society A*, 368(1916):1607–1633, 2010. DOI: 10.1098/rsta.2009.0251.

A. Kageyama, H. Ji, J. Goodman, F. Chen, and E. Shoshan. Numerical and experimental investigation of circulation in short cylinders. *Journal of the Physical Society of Japan*, 73(9):2424–2437, 2004. DOI: 10.1143/JPSJ.73.2424.

I. V. Khalzov, A. I. Smolyakov, and V. I. Ilgisonis. Equilibrium magnetohydrodynamic flows of liquid metals in magnetorotational instability experiments. *Journal of Fluid Mechanics*, 644:257–280, 2010. DOI: 10.1017/S0022112009992394.

B. Lehnert. An instability of laminar flow of mercury caused by an external magnetic field. *Proc. R. Soc. A*, 233(1194):299–302, 1955. DOI: 10.1098/rspa.1955.0265.

R. B. Lehoucq, D. C. Sorensen, and C. Yang. *ARPACK User's Guide: Solution of Large Scale Eigenvalue Problems by Implicitly Restarted Arnoldi Methods*. Society for Industrial and Applied Mathematics, Philadelphia, PA, 1998.

W. Liu. Numerical study of the magnetorotational instability in Princeton MRI Experiment. *The Astrophysical Journal*, 684(1):515, 2008a. DOI: 10.1086/590366.

W. Liu. Magnetized Ekman layer and Stewartson layer in a magnetized Taylor-Couette flow. *Physical Review E*, 77:056314, 2008b. DOI: 10.1103/PhysRevE.77.056314.

W. Liu. *Axisymmetric numerical and analytical studies of the magnetorotational instability in a magnetized Taylor-Couette flow*. PhD thesis, Princeton University, 2007.

W. Liu, J. Goodman, I. Herron, and H. Ji. Helical magnetorotational instability in magnetized Taylor-Couette flow. *Physical Review E*, 74:056302, 2006. DOI: 10.1103/PhysRevE.74.056302.

W. Liu, J. Goodman, and H. Ji. Traveling waves in a magnetized Taylor-Couette flow. *Physical Review E*, 76:016310, 2007. DOI: 10.1103/PhysRevE.76.016310.

D. E. Loper and E. R. Benton. On the spin-up of an electrically conducting fluid Part 2. Hydromagnetic spin-up between infinite flat insulating plates. *Journal of Fluid Mechanics*, 43(04):785–799, 1970. DOI: 10.1017/S0022112070002744.

P. Luebbers and O. Chopra. Compatibility of ITER candidate materials with static gallium. In *Fusion Engineering, 1995. SOFE '95. 'Seeking a New Energy Era'., 16th IEEE/NPSS Symposium*, volume 1, pages 232 –235 vol.1, 1995. DOI: 10.1109/FUSION.1995.534210.

D. Lynden-Bell and J. Pringle. The evolution of viscous discs and the origin of the nebular variables. *Monthly Notices of the Royal Astronomical Society*, 168:603–637, 1974.

N. B. Morley, J. Burris, L. C. Cadwallader, and M. D. Nornberg. GaInSn usage in the research laboratory. *Review of Scientific Instruments*, 79(5):056107, 2008. DOI: 10.1063/1.2930813.

M. Nagata. Shear flow instability of rotating hydromagnetic fluids. *Geophysical and Astrophysical Fluid Dynamics*, 33(1-4):173–184, 1985. DOI: 10.1080/03091928508245428.

Lord Rayleigh. On the dynamics of revolving fluids. *Proceedings of the Royal Society of London. Series A*, 93(648):148–154, 1917. DOI: 10.1098/rspa.1917.0010.

M. S. Paoletti and D. P. Lathrop. Angular momentum transport in turbulent flow between independently rotating cylinders. *Physical Review Letters*, 106:024501, 2011. DOI: 10.1103/PhysRevLett.106.024501.

J. Proudman. On the motion of solids in a liquid possessing vorticity. *Proceedings of the Royal Society of London. Series A*, 92(642):408–424, 1916. DOI: 10.1098/rspa.1916.0026.

D. Richard and J.-P. Zahn. Turbulence in differentially rotating flows. What can be learned from the Couette-Taylor experiment. *Astronomy and Astrophysics*, 347:734–738, 1999.

A. H. Roach, E. J. Spence, C. Gissinger, E. M. Edlund, P. Sloboda, J. Goodman, and H. Ji. Observation of a free-Shercliff-layer instability in cylindrical geometry. *Physical Review Letters*, 108:154502, 2012. DOI: 10.1103/PhysRevLett.108.154502.

P. H. Roberts. Singularities of Hartmann layers. *Proceedings of the Royal Society of London. Series A.*, 300(1460):94–107, 1967. DOI: 10.1098/rspa.1967.0159.

N. Schaëffer and P. Cardin. Quasigeostrophic model of the instabilities of the Stewartson layer in flat and depth-varying containers. *Physics of Fluids*, 17(10):104111, 2005. DOI: 10.1063/1.2073547.

E. Schartman. *Laboratory study of angular momentum transport in a rotating shear flow.* PhD thesis, Princeton University, 2008.

E. Schartman, H. Ji, and M. J. Burin. Development of a Couette-Taylor flow device with active minimization of secondary circulation. *Review of Scientific Instruments*, 80(2): 024501, 2009. DOI: 10.1063/1.3077942.

E. Schartman, H. Ji, M. J. Burin, and J. Goodman. Stability of quasi-Keplerian shear flow in a laboratory experiment. *Astronomy and Astrophysics*, 543:A94, 2012. DOI: 10.1051/0004-6361/201016252.

N. I. Shakura and R. A. Sunyaev. Black holes in binary systems. Observational appearance. *Astronomy and Astrophysics*, 24:337–355, 1973.

J. A. Shercliff. Steady motion of conducting fluids in pipes under transverse magnetic fields. *Mat. Proc. Cambridge Philos. Soc.*, 49(01):136–144, 1953. DOI: 10.1017/S0305004100028139.

DOP3000 series user's manual. Signal Processing, S.A., 2012. Available as a part of the UDOP software package from http://signal-processing.com/download.php.

D. R. Sisan, N. Mujica, W. A. Tillotson, Y.-M. Huang, W. Dorland, A. B. Hassam, T. M. Antonsen, and D. P. Lathrop. Experimental observation and characterization of the magnetorotational instability. *Physical Review Letters*, 93(11):114502, 2004. DOI: 10.1103/PhysRevLett.93.114502.

E. J. Spence, A. H. Roach, E. M. Edlund, P. Sloboda, and H. Ji. Free magnetohydrodynamic shear layers in the presence of rotation and magnetic field. *Physics of Plasmas*, 19(5): 056502, 2012. DOI: 10.1063/1.3702006.

F. Stefani, T. Gundrum, G. Gerbeth, G. Rüdiger, J. Szklarski, and R. Hollerbach. Experiments on the magnetorotational instability in helical magnetic fields. *New Journal of Physics*, 9(8):295, 2007. DOI: 10.1088/1367-2630/9/8/295.

F. Stefani, G. Gerbeth, T. Gundrum, J. Szklarski, G. Rüdiger, and R. Hollerbach. Results of a modified PROMISE experiment. *Astron. Nachr.*, 329(7):652–658, 2008. DOI: 10.1002/asna.200811023.

F. Stefani, G. Gerbeth, T. Gundrum, R. Hollerbach, J. Priede, G. Rüdiger, and J. Szklarski. Helical magnetorotational instability in a Taylor-Couette flow with strongly reduced Ekman pumping. *Physical Review E*, 80:066303, 2009. DOI: 10.1103/PhysRevE.80.066303.

K. Stewartson. On almost rigid rotations. *Journal of Fluid Mech.*, 3(01):17–26, 1957a. DOI: 10.1017/S0022112057000452.

K. Stewartson. Magneto-hydrodynamics of a finite rotating disk. *Q J Mechanics Appl. Math*, 10:137–147, 1957b. DOI: 10.1093/qjmam/10.2.137.

T. H. Stix. *Waves in Plasmas*. Springer-Verlag, New York, NY, 1992. ISBN 0-88318-859-7.

J. M. Stone and M. L. Norman. ZEUS-2D: A radiation magnetohydrodynamics code for

astrophysical flows in two space dimensions. I - The hydrodynamic algorithms and tests. *The Astrophysical Journal Supplement Series*, 80:753, 1992a. DOI: 10.1086/191680.

J. M. Stone and M. L. Norman. ZEUS-2D: A radiation magnetohydrodynamics code for astrophysical flows in two space dimensions. II - The magnetohydrodynamic algorithms and tests. *The Astrophysical Journal Supplement Series*, 80:791, 1992b. DOI: 10.1086/191681.

J. Szklarski and G. Rüdiger. Ekman-Hartmann layer in a magnetohydrodynamic Taylor-Couette flow. *Physical Review E*, 76:066308, 2007. DOI: 10.1103/PhysRevE.76.066308.

Y. Takeda. Velocity profile measurement by ultrasonic Doppler method. *Experimental Thermal and Fluid Science*, 10(4):444 – 453, 1995. DOI: 10.1016/0894-1777(94)00124-Q.

Y. Takeda. Development of an ultrasound velocity profile monitor. *Nuclear Engineering and Design*, 126(2):277–284, 1991. DOI: 10.1016/0029-5493(91)90117-Z.

Y. Takeda, W. E. Fischer, and J. Sakakibara. Measurement of energy spectral density of a flow in a rotating Couette system. *Physical Review Letters*, 70:3569–3571, 1993a. DOI: 10.1103/PhysRevLett.70.3569.

Y. Takeda, W. E. Fischer, J. Sakakibara, and K. Ohmura. Experimental observation of the quasiperiodic modes in a rotating Couette system. *Physical Review E*, 47:4130–4134, 1993b. DOI: 10.1103/PhysRevE.47.4130.

Y. Tasaka, Y. Takeda, and T. Yanagisawa. Ultrasonic visualization of thermal convective motion in a liquid gallium layer. *Flow Measurement and Instrumentation*, 19(34):131 – 137, 2008. DOI: 10.1016/j.flowmeasinst.2007.06.003.

G. I. Taylor. Motion of solids in fluids when the flow is not irrotational. *Proceedings of the Royal Society of London. Series A*, 93(648):99–113, 1917. DOI: 10.1098/rspa.1917.0007.

G. I. Taylor. Stability of a viscous liquid contained between two rotating cylinders. *Philosophical Transactions of the Royal Society of London. Series A.*, 223(605-615):289–343, 1923. DOI: 10.1098/rsta.1923.0008.

E. Velikhov, A. Ivanov, S. Zakharov, V. Zakharov, A. Livadny, and K. Serebrennikov. Equilibrium of current driven rotating liquid metal. *Physics Letters A*, 358(3):216 – 221, 2006. DOI: 10.1016/j.physleta.2006.05.020.

E. P. Velikhov. Stability of an ideally conducting liquid flowing between cylinders rotating in a magnetic field. *Journal of Experimental and Theoretical Physics (U.S.S.R.)*, 36: 1398–1404, 1959. Translated in *Soviet Physics JETP*, 36:995-998, 1959.

S. Vempaty and D. E. Loper. Hydromagnetic free shear layers in rotating flows. *Zeitschrift für Angewandte Mathematik und Physik (ZAMP)*, 29:450–461, 1978. DOI: 10.1007/BF01590766.

X. Wei and R. Hollerbach. Instabilities of Shercliffe and Stewartson layers in spherical Couette flow. *Physical Review E*, 78:026309, 2008. DOI: 10.1103/PhysRevE.78.026309.